Diss. ETH No. 12961

Discovery potential of the Standard Model Higgs in CMS at the LHC

A dissertation submitted to the
Swiss Federal Institute of Technology, Zurich
for the degree of
Doctor of Natural Sciences

presented by
Katri Lassila-Perini
dipl. phys. from Helsinki University of Technology
born 25th August 1965
in Hämeenlinna, Finland

accepted
on the recommendation of
Prof. Dr. F. Pauss, examiner, and
Prof. Dr. H. Hofer, co-examiner

1998

Abstract

This thesis presents the discovery potential of the Standard Model Higgs boson in the CMS experiment at the LHC.

Detailed studies have been carried out to evaluate the detector performance in the difficult $H \rightarrow \gamma\gamma$ channel. The electromagnetic crystal calorimeter is of main importance in this channel and it has been designed according stringent performance requirements. Test beam data of lead tungstate crystals have been analysed and it is shown that the performance of the crystals can meet the requirements.

The Higgs decay into two photons has been studied with full detector simulation and the Higgs mass has been reconstructed. A potential danger for the photon measurement are the photon conversions in the detector material in front of the electromagnetic calorimeter. Different methods to recover these converted photons are developed and it is shown that including the recovered conversions does not degrade the Higgs mass resolution.

To complete the full Standard Model Higgs discovery range, studies of the other decay channels are reviewed and updated taking into account the next to leading order corrections to the cross-sections. A new study for the $H \rightarrow ZZ \rightarrow 2\ell 2\nu$ channel shows that it can give an important contribution above $m_H = 400$ GeV.

An estimate of the integrated luminosity needed for an observable Higgs signal is derived. It is shown that a fast discovery (integrated luminosity less than 10 fb^{-1}) can be expected if the Higgs mass is in the range of 130 – 550 GeV. The most difficult regions are the low mass range ($m_H < 120$ GeV) and the very high mass range ($m_H > 600$ GeV). With 100 $\text{fb}^{-1}$of integrated luminosity the full mass range can be covered.

Zusammenfassung

Die vorliegende Arbeit beschreibt das Entdeckungspotential des Standardmodell Higgsboson im CMS Experiment am LHC.

Genaue Untersuchungen werden durchgeführt, um die Möglichkeiten des Detektors im schwierigen Kanal $H \to \gamma\gamma$ zu bewerten. Das elektromagnetische Kristallkalorimeter ist von grosser Bedeutung in diesem Kanal und wurde nach strengen Leistungsanforderungen entwickelt. Die Teststrahldaten der Bleiwolframatkristalle werden analysiert und es wird gezeigt, dass das Verhalten der Kristalle den Anforderungen entspricht.

Der Higgszerfall in zwei Photone wird mit Hilfe einer vollständigen Detektorsimulation untersucht und die Higgsmasse wird rekonstruiert. Eine mögliche Gefahr für den Photonennachweis sind Photonenkonversionen im Detektormaterial, dass vor dem elektromagnetischen Kalorimeter steht. Verschiedene Methoden, um diese konvertierten Photonen zurückzugewinnen werden entwickelt, und es wird gezeigt, dass das Einbeziehen der erhaltenen Konversionphotonen die Higgsmassenauflösung nicht beeinträchtigt.

Um den möglichen Entdeckungsbereich des Standardmodell Higgsboson zu vervollständigen, wurden Untersuchungen in anderen Zerfallskanälen durchgeführt und auf den neuesten Stand gebracht, unter Berücksichtigung der Korrekturen zweiter Ordnung des Wirkungsquerschnitts. Eine neue Untersuchung für $H \to ZZ \to 2\ell 2\nu$ zeigt, dass dieser Kanal einen wichtigen Beitrag zum Higgsnachweis für Higgsmassen höher als $m_H = 400$ GeV geben könnte.

Eine Schätzung der integrierten Luminosität wird abgeleitet, die zum Nachweis eines Higgssignales notwendig ist. Es wird nachgewiesen, dass eine rasche Entdeckung (integrierte Luminosität kleiner als 10 fb^{-1}) zu erwarten ist, falls die Higgsbosonmasse im Bereich zwischen 130 und 550 GeV liegt. Die schwierigsten Gebiete findet man bei niedrigen Massen ($m_H < 120$ GeV) und bei den höchstmöglichen Massen ($m_H > 600$ GeV). Mit 100 fb^{-1}integrierter Luminosität kann der ganze Massebereich abgedeckt werden.

Contents

Chapter 1

Introduction

The Standard Model of strong, weak and electromagnetic interactions beautifully describes the experimental results obtained up to date. The model contains a theoretical description of the fundamental interactions in the language of the local gauge invariance: quantum chromodynamics for the strong interaction and the electroweak model for the weak and electromagnetic interactions. However, the mechanism that causes the mediators of forces in the unified electroweak theory to differ in mass — the massless photon and the very massive Z and W bosons — is still unexplained. Some fundamental new physics must appear to shed light on this mystery at the energies which will be reached by the Large Hadron Collider (LHC) at CERN. The spontaneous symmetry breaking by the Higgs mechanism as described by the Standard Model can explain the origin of the W and Z boson masses, and an observable consequence of this would be the Higgs particle. This work describes the discovery potential of the Higgs particle in the CMS experiment at the LHC.

Chapter 2 answers the questions such as why, according to the Standard Model, the Higgs particle is needed and what would be its experimental signature if it exists. A short overview is given of the Higgs mechanism and the present understanding of its experimental consequences i.e. the width and the decay modes of the Higgs particle. The production cross-sections of the Higgs particle and its possible discovery channels at the LHC are discussed.

In Chapter 3 the LHC machine and the environment in which the experiments will have to function are described.

Chapter 4 introduces the CMS experiment, and the physics requirements that have led to its design. It explains how we are going to find the Higgs particle, or something else if it does not exist. The electromagnetic crystal calorimeter which will be the main tool in one of the most challenging Higgs discovery channels is described in detail.

The identification and energy measurement of electrons and photons with this extremely precise crystal calorimeter are explained in Chapter 5. Beam test data on crystals are analysed and simulation results used for the optimisation of the detector design are reviewed.

Chapter 6 shows the discovery potential of the CMS experience in the different decay channels of the Higgs boson. Where needed, detailed simulation studies are used to estimate the performance of the detector.

Finally, the conclusion summarises the thesis.

Chapter 2

Neither Schwinger nor I had the foggiest idea of what produced the W-boson's mass and removed the perfect symmetry between weak and electromagnetic interactions. It was a most nettlesome question, and probably led Schwinger to abandon his quest for an electroweak synthesis and pursue other fields of research. I didn't have that option. I had a thesis to write.

— Sheldon Glashow, "Interactions", 1988

Standard Model and Higgs mechanism

To reveal the unified description of the fundamental forces of nature is the ultimate goal for particle physics. Electric and magnetic forces were understood to be of the same origin and described by the classical electromagnetic theory in the nineteenth century. The success of quantum electrodynamics and its formulation in the language of the locally gauge invariant field theory in the end of 1940's inspired theorists to describe the weak forces with the same method and this led to the spectacularly successful electroweak theory. Although the forces and their mediators — a massless photon and massive Z and W bosons — look very different, this unification was reached and the differences in masses were explained by the spontaneous symmetry breaking. Adding the third group of fundamental processes, the strong interaction of quarks and gluons described by the gauge theory of quantum chromodynamics, we have the Standard Model description of fundamental particles and interactions. It is remarkable how three manifestly very different interactions can be described with the same principle of the local gauge invariance. The particles and interactions in the Standard Model are summarised in table 2.1.

In the following, the Higgs mechanism as the model for the spontaneous symmetry breaking is reviewed. To do this, the concept of the local gauge invariance is presented in the context of the electromagnetic interactions. Then, the formulation of the gauge invariant theory for the electroweak interactions is reviewed. The difficulties encountered in this formulation and the ingenious solutions to these problems are discussed. The main

Particles			
Spin-1/2 fermions and antifermions:			
Leptons	e^-	μ^-	τ^-
	ν_e	ν_μ	ν_τ
Quarks	d	s	b
	u	c	t
+ their antiparticles			
Spin-1 gauge bosons:			
Massless electroweak boson		γ	
Massive electroweak bosons		W^+, W^-, Z^0	
Eight coloured gluons		g	
Spin-0 Higgs boson:			
Higgs boson		H	
Interactions			
The electromagnetic interaction of the photon			
The weak interaction of W^+, W^-, Z^0			
The strong interaction of the gluons with the quarks and gluons			

Table 2.1: The particles and interactions of the Standard Model.

item is precisely the Higgs mechanism which allows the symmetry breaking in the local gauge theory of electroweak interactions. Having formulated the theory, some predictions of the Standard Model are compared with the recent experimental data.

The major ingredient of this model, the Higgs boson, has not yet been experimentally observed. The mass of this boson is not specified by the theory, but its couplings to the fermions and other bosons are functions of their masses. Therefore, the Higgs production cross-section, its decay modes and its width are known and they will be discussed in the following.

Finally, notwithstanding its success in describing the actual experimental data, the Standard Model is theoretically unsatisfactory. Some proposals for a more complete theory are briefly described.

2.1 Quantum electrodynamics and local gauge invariance

As an example how the local gauge invariance can be applied let us consider a free electron of mass m and charge q. The field of this electron is described as ψ and it transforms in a local gauge transformation like

$$\psi \rightarrow \psi' = e^{iq\Lambda(x)}\psi$$

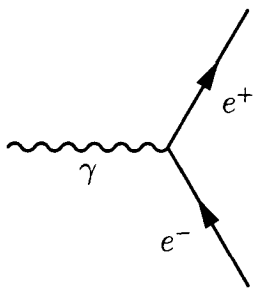

Figure 2.1: Electromagnetic interactions $j^\mu A_\mu$.

Here the parameter Λ depends on the value of the space-time point x. Were the transformation global, the parameter Λ would be constant. The Lagrangian

$$\mathcal{L} = i\bar{\psi}\gamma^\mu\partial_\mu\psi - m\bar{\psi}\psi$$

where $i\bar{\psi}\gamma^\mu\partial\psi$ is the kinetic energy term and $m\bar{\psi}\psi$ is the mass term would be invariant for a global transformation but due to the x-dependence of the derivative it is not invariant in the local transformation:

$$\partial_\mu\psi \rightarrow \partial_\mu\psi' = e^{-iq\Lambda(x)}(\partial_\mu\psi(x) - iq(\partial_\mu\Lambda(x))\psi) \neq \partial_\mu\psi$$

To define a Lagrangian which is invariant in this transformation the dependence of $\partial_\mu\Lambda$ has to be removed. This can be done by introducing a *gauge field* $A_\mu(x)$ and substituting the derivative ∂_μ with a new *covariant derivative* D_μ

$$D_\mu = \partial_\mu - iqA_\mu(x)$$

Requiring that the derivative $D_\mu\psi$ undergo the same transformation as the field itself

$$D_\mu\psi \rightarrow (D_\mu\psi)' = e^{iq\Lambda(x)}D_\mu\psi$$

dictates the transformation of the gauge field under the local gauge symmetry

$$A_\mu(x) \rightarrow A'_\mu(x) = A_\mu(x) + \partial_\mu\Lambda(x)$$

The new Lagrangian

$$\begin{aligned}\mathcal{L} &= i\bar{\psi}\gamma^\mu D_\mu\psi - m\bar{\psi}\psi \\ &= i\bar{\psi}\gamma^\mu\partial_\mu\psi - m\bar{\psi}\psi - qA_\mu\bar{\psi}\gamma^\mu\psi\end{aligned}$$

is locally gauge invariant. The last term is the interaction term between the vector field A_μ and the electromagnetic current $j^\mu = q\bar{\psi}\gamma^\mu\psi$. The new field A_μ is thus the photon field and the interaction term appearing in the Lagrangian due to the local gauge invariance describes the electromagnetic interactions mediated through photons. A Feynman diagram of this interaction is shown in figure 2.1.

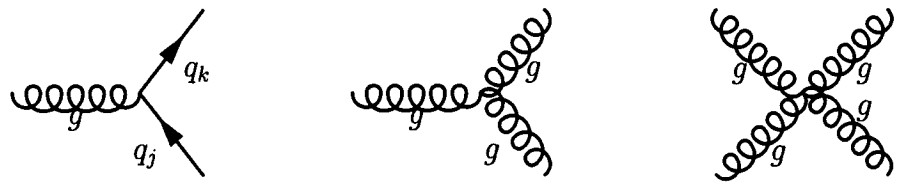

Figure 2.2: Quark-gluon and gluon-gluon interactions.

To complete the QED Lagrangian one has to add the kinetic energy term for the photon formulated by the gauge invariant tensor $F_{\mu\nu} = \partial_\mu A_\nu - \partial_\nu A_\mu$:

$$\mathcal{L} = \bar{\psi}(i\gamma^\mu \partial_\mu - m)\psi - j^\mu A_\mu - \frac{1}{4} F_{\mu\nu} F^{\mu\nu}$$

There are some important remarks to be made:

- The photon is introduced in the theory because of the requirement of the local gauge invariance.
- The form of the interaction is specified by the theory.
- It would be impossible to introduce a mass term for a photon without destroying the local phase invariance. Therefore the photon mass in the theory must be zero.

The here described formalism is the Abelian U(1) gauge group formed by the transformations $\psi \rightarrow \psi' = e^{iq\Lambda(x)}\psi$. In an Abelian group the transformations of the group commute with each other. The generator of the group is the electric charge and the local gauge invariance requires the existence of a corresponding gauge boson, the photon. More generally, the local gauge invariance under a symmetry group requires as many massless gauge bosons as there are generators in the group: three for the SU(2) symmetry, eight for SU(3), etc. In this manner, the strong interactions of quarks can be described by the non-Abelian group SU(3) where transformations are those of the quark colour fields. Accordingly, the local gauge invariance requires the introduction of eight vector fields and the corresponding eight gluons. Again, the theory requires the gluons to be massless. On the contrary to quantum electrodynamics, due to the non-Abelian nature of the symmetry, self-interactions between the gluons are allowed as shown in figure 2.2. The gluons mediate the force between colour charged objects and carry the colour charge themselves whereas the photon couples only to electrically charged particles but are chargeless themselves, thus no self-interactions among photons exist. This causes the phenomenological difference between the electromagnetic and strong interactions.

2.2 Unification of the electromagnetic and weak interactions

Based on the ideas of Glashow[1], Weinberg and Salam proposed the electroweak theory with massive weak bosons in 1967 [2],[3]. At the time, only the electromagnetic interactions, such as $\pi^0 \rightarrow \gamma\gamma$, and charge-changing weak interactions, for example $n \rightarrow pe^-\bar{\nu}_e$

or $K^+ \rightarrow \pi^0\mu^+\nu_\mu$, were known in the electroweak sector and the new proposal required the existence of the neutral weak current. In 1971, 't Hooft showed that the theory is renormalizable[4]. Soon after, many predictions of this theory — including the existence of the neutral weak current — were experimentally verified. The quest for anomalies in its predictions still continues. The electroweak theory has gained the Nobel Prize in physics in 1978 for Glashow, Weinberg and Salam for its formulation and for Rubbia and Van Der Meer in 1984 for the experimental discovery of the W and Z bosons.

2.2.1 $SU(2)_L \times U(1)_Y$ electroweak interaction

The first technical problem of an unified electroweak theory is the choice of the symmetry group. At the time when the theory was first formulated a natural choice would have been SU(2) which could accommodate the electromagnetic and charge-changing weak interactions[5]. This was a major step forward as it introduced the idea of vector bosons as mediators of the weak interaction. Two of the three gauge bosons required by the three independent rotations of the local SU(2) symmetry could be identified with W^+ and W^-. This hypothesis requires an additional uncharged gauge particle W_3 that gives rise to neutral-current interactions. Could this gauge boson be identified as photon? This arrangement did not take into account the important difference between the electromagnetic and weak interactions: the parity is not conserved in the weak charged current interactions which is a consequence of the fact that weak charged current couples only with fermion with positive helicity ("left-handed" fermions). Thus the neutral current arising from the SU(2) symmetry cannot be assigned to the electromagnetic current.

The SU(2) symmetry was required to involve only left-handed particles and denoted $SU(2)_L$ and an additional U(1) symmetry was added to include the electromagnetic interaction in the theory. This new U(1) symmetry cannot be directly the one describing the electromagnetic current as its transformations do not leave the SU(2) sector undisturbed (W^+ and W^- have electromagnetic charge). The symmetry was found to be that of the *weak hypercharge*. It introduces an additional gauge boson B. This may have looked confusing: instead of the photon the theory requires *two* unknown gauge bosons. Glashow [1] proposed that the photon could be a linear combination of the two new bosons. However, the other linear combination of these bosons describes a weak neutral current where a fermion — even the chargeless neutrino — interacts with matter without changing its identity, and processes such as $\nu_\mu p \rightarrow \nu_\mu p$ or $\nu_\mu e^+ \rightarrow \nu_\mu e^+$ should exist. Such interactions had not been observed by the time of the first proposal of this idea in 1961. It was only in 1973 when the weak neutral currents were experimentally observed at CERN [6].

The quantum numbers that characterise the $SU(2)_L \times U(1)_Y$ symmetry are the weak isospin I of $SU(2)_L$ and the weak hypercharge Y which is defined by

$$Q = I_3 + \frac{1}{2}Y$$

The quarks and leptons can be arranged in multiplets under the $SU(2)_L \times U(1)_Y$ symmetry and the local symmetry defines the interactions between the fermion field and gauge fields: the three isospin currents couple with a strength g to a weak isospin triplet of vector gauge bosons W, and the weak hypercharge current couples with strength $g'/2$ (the factor 1/2

is a convention) to a vector gauge boson B. The $SU(2)_L \times U(1)_Y$ multiplets and their quantum numbers are given in table 2.2 for the first generation fermions consisting of the neutrino, the electron and the u and d quarks, and for the gauge bosons.

Multiplets		Weak isospin I_3	Weak hypercharge Y	Electric charge Q
Quarks				
SU(2) doublet	$\begin{pmatrix} u \\ d \end{pmatrix}_L$	$1/2$ $-1/2$	$1/3$ $1/3$	$2/3$ $-1/3$
SU(2) singlets	u_R d_R	0 0	$4/3$ $-2/3$	$2/3$ $-1/3$
Leptons				
SU(2) doublet	$\begin{pmatrix} \nu_e \\ e \end{pmatrix}_L$	$1/2$ $-1/2$	-1 -1	0 -1
SU(2) singlet	e_R	0	-2	-1
Gauge field				
SU(2) triplet	$\begin{pmatrix} W^+ \\ W_3 \\ W^- \end{pmatrix}$	1 0 -1	0 0 0	1 0 -1
SU(2) singlet	B	0	0	0
Higgs field				
SU(2) doublet	$\begin{pmatrix} \phi^+ \\ \phi^0 \end{pmatrix}$	$1/2$ $-1/2$	1 1	1 0

Table 2.2: Multiplets and quantum numbers in the $SU(2)_L \times U(1)_Y$ electroweak theory.

Let us first consider the interaction term of the electroweak Lagrangian. In QED this was of the form $j^\mu A_\mu$ where the electromagnetic current $j^\mu = q\bar{\psi}\gamma^\mu\psi$ couples to the vector boson A_μ. The weak charged current can be described in the SU(2) weak isospin symmetry group with

$$j_\mu^\pm = \bar{\chi}_L \gamma_\mu \tau_\pm \chi_L$$

where $\tau_\pm$ are the raising and lowering operators constructed from Pauli matrices τ

$$\tau_1 = \begin{pmatrix} 0 & 1 \\ 1 & 0 \end{pmatrix}, \qquad \tau_2 = \begin{pmatrix} 0 & -i \\ i & 0 \end{pmatrix}, \qquad \tau_3 = \begin{pmatrix} 1 & 0 \\ 0 & -1 \end{pmatrix}$$

$$\tau_+ = \frac{1}{2}(\tau_1 + i\tau_2) = \begin{pmatrix} 0 & 1 \\ 0 & 0 \end{pmatrix}$$

$$\tau_- = \frac{1}{2}(\tau_1 - i\tau_2) = \begin{pmatrix} 0 & 0 \\ 1 & 0 \end{pmatrix}$$

Pauli matrices are the generators of SU(2) group and χ_L is a fermion doublet in the $SU(2)_L \times U(1)_Y$ symmetry group as in table 2.2. This form states that the weak charged

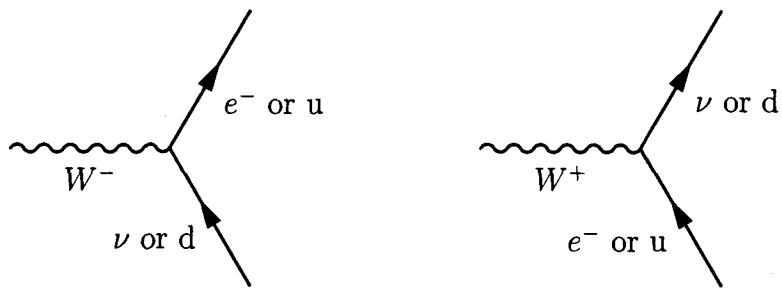

Figure 2.3: Weak charged current interactions.

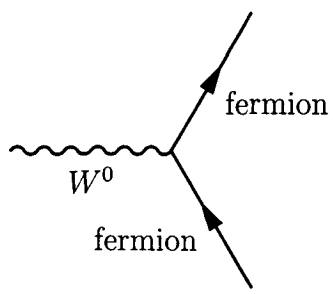

Figure 2.4: Weak neutral current interactions of the gauge boson W_0.

current changes left-handed electron to a left-handed neutrino, or a left-handed up quark to a left-handed down quark, or vice-versa, as shown in figure 2.3. The third isospin current completes the weak isospin triplet of currents

$$j_\mu^3 = \bar{\chi}_L \gamma_\mu \frac{1}{2} \tau_3 \chi_L$$

This current describes the interaction of the boson W_3 with left-handed fermions where the fermions do not change their identity as shown in figure 2.4.

The weak hypercharge current is of the form

$$j_\mu^Y = 2j_\mu^{em} - 2j_\mu^3 \equiv \bar{\chi} \gamma_\mu Y \chi$$

The hypercharge operator Y does not change the identity of the states on which it operates but it gives their hypercharge quantum numbers. The electromagnetic current couples to both left and right-handed fermions while the isospin current couples only to the left-handed fermions.

Now, to combine the weak and electromagnetic interactions, two terms are needed: the triplet weak isospin currents $\boldsymbol{j}$, as described above, coupled to the three vector bosons $\boldsymbol{W}$ and a weak hypercharge current j_μ^Y coupled to the fourth boson B^μ. The interaction is then of the form

$$-i(g\boldsymbol{j}_\mu \cdot \boldsymbol{W}^\mu + \frac{g'}{2} j_\mu^Y B^\mu)$$

The scalar product gives

$$\begin{aligned} g\boldsymbol{j}_\mu \cdot \boldsymbol{W}^\mu &= g(j_\mu^1 W^{\mu 1} + j_\mu^2 W^{\mu 2} + j_\mu^3 W^{\mu 3}) \\ &= g\chi_L \gamma_\mu (1/2)(\tau_1 W_1 + \tau_2 W_2 + \tau_3 W_3)\chi_L \\ &= g\chi_L \gamma_\mu (1/2) \begin{pmatrix} W_3 & W_1 - iW_2 \\ W_1 + iW_2 & W_3 \end{pmatrix} \chi_L \end{aligned}$$

With the definition of the charged currents $j_\mu^\pm = \bar{\chi_L}\gamma_\mu \tau_\pm \chi_L$ and the fields $W^{\mu\pm} = \frac{1}{\sqrt{2}}(W^{\mu 1} \mp iW^{\mu 2})$ the expression can be divided in charged current and neutral current parts as

$$g\boldsymbol{j}_\mu \cdot \boldsymbol{W}^\mu = \underbrace{\frac{g}{\sqrt{2}}(j_\mu^+ W^{\mu +} + j_\mu^- W^{\mu -})}_{\text{charged current}} + \underbrace{g j_\mu^3 W^{\mu 3}}_{\text{neutral current}}$$

The neutral current sector is then presented by

$$-i(g j_\mu^3 W^{\mu 3} + \frac{g'}{2} j_\mu^Y B^\mu)$$

The physical particles mediating the weak neutral interactions (Z^0) and electromagnetic interaction (the photon) can be found as linear combinations of the neutral gauge particles W_3 and B

$$\begin{aligned} A &= B\cos\theta_W + W_3 \sin\theta_W \\ Z^0 &= B\sin\theta_W - W_3 \cos\theta_W \end{aligned}$$

The mixing of the gauge particles to give the physical particles is a consequence of the fact that $SU(2)_L \times U(1)_Y$ is a broken symmetry. The weak mixing angle θ_W is generally called the Weinberg angle although it was first proposed by Glashow [1]. Written out as a composition for the photon field and neutral weak current field the neutral interaction term becomes

$$\begin{aligned} &-i(g j_\mu^3 W^{\mu 3} + \frac{g'}{2} j_\mu^Y B^\mu) = \\ &\quad -i(g\sin\theta_W j_\mu^3 + g'\cos\theta_W \frac{j_\mu^Y}{2})A^\mu - i(g\cos\theta_W j_\mu^3 - g'\sin\theta_W \frac{j_\mu^Y}{2})Z^\mu \end{aligned}$$

The electromagnetic interactions are described by the first term. If this theory should describe them correctly the first term imposes that

$$q = g\sin\theta_W = g'\cos\theta_W \Rightarrow \tan\theta_W = \frac{g'}{g}$$

Here, the definition of the weak isospin and the weak hypercharge in terms of the electric charge ($Q = I_3 + \frac{1}{2}Y$ or, for the currents, $j_\mu^{em} = j_\mu^3 + \frac{1}{2}j_\mu^Y$) have been used. The value of θ_W is not fixed by the theory but its experimental measurements can be used as a consistency check for the theory as all the phenomena of the electroweak interactions should lead to the same numerical value of θ_W.

To build a gauge invariant electroweak Lagrangian we start by writing the Lagrangian for a left-handed fermion doublet and right-handed singlet as

$$\mathcal{L}_{gb+f} = i\bar{\psi}_L\gamma^\mu\partial_\mu\psi_L + i\bar{\psi}_R\gamma^\mu\partial_\mu\psi_R$$

This Lagrangian will describe the fermion and gauge boson kinetic energies and their mutual couplings. Left-handed particles transform under infinitesimal $\mathrm{SU}(2)_L$ transformation as

$$\psi_L(x) \rightarrow \psi_L(x)' = (1 - ig\boldsymbol{\Lambda}(x)\cdot\boldsymbol{\tau}/2)\psi_L(x)$$

while right-handed particles remain unchanged

$$\psi_R(x) \rightarrow \psi_R(x)' = \psi_R(x)$$

The infinitesimal $\mathrm{U}(1)_Y$ transformations for the left and right-handed particles are the same

$$\begin{aligned}\psi_L(x) &\rightarrow \psi_L(x)' &&= (1 - i(g'/2)\lambda(x)Y)\psi_L(x)\\ \psi_R(x) &\rightarrow \psi_R(x)' &&= (1 - i(g'/2)\lambda(x)Y)\psi_R(x)\end{aligned}$$

The functions $\boldsymbol{\Lambda}(x)$ and $\lambda(x)$ are arbitrary functions of space-time and $\boldsymbol{\tau}/2$ (Pauli matrices) and $Y/2$ are the generators of the $\mathrm{SU}(2)_L$ and $\mathrm{U}(1)_Y$ groups, respectively, as described above. The Lagrangian can be made invariant if a covariant derivative

$$D_\mu = \partial_\mu + ig\boldsymbol{\tau}/2\cdot\boldsymbol{W}_\mu + i(g'/2)YB_\mu$$

is introduced. The last term is analogous to the field appearing in the electromagnetic U(1) symmetry and the second term is required by the x-dependence of the SU(2) transformation. As in U(1), by requiring that the derivative of the fermion field transforms in the same way as the fermion field itself one obtains that the gauge fields W_μ and B_μ must transform as

$$\begin{aligned}SU(2)_L &\quad \begin{cases}\boldsymbol{W}_\mu \rightarrow \boldsymbol{W}'_\mu = \boldsymbol{W} + \partial_\mu\boldsymbol{\Lambda}(x) + g\boldsymbol{\Lambda}(x)\times\boldsymbol{W}_\mu\\ B_\mu \rightarrow B'_\mu = B_\mu\end{cases}\\ U(1)_Y &\quad \begin{cases}\boldsymbol{W}_\mu \rightarrow \boldsymbol{W}'_\mu = \boldsymbol{W}_\mu\\ B_\mu \rightarrow B'_\mu = B_\mu + \partial_\mu\lambda(x)\end{cases}\end{aligned}$$

To complete the electroweak Lagrangian the kinetic energy terms of the gauge fields, $-\frac{1}{4}\boldsymbol{W}_{\mu\nu}\cdot\boldsymbol{W}^{\mu\nu}$ and $-\frac{1}{4}B_{\mu\nu}B^{\mu\nu}$ are added. Here, the U(1) field

$$B_{\mu\nu} = \partial_\mu B_\nu - \partial_\nu B_\mu$$

is of the same form as in the electromagnetic U(1) group and the gauge invariance of the SU(2) weak isospin symmetry requires

$$\boldsymbol{W}_\mu = \partial_\mu\boldsymbol{W}_\nu - \partial_\nu\boldsymbol{W}_\mu - g\boldsymbol{W}_\nu\times\boldsymbol{W}_\nu$$

The last term in this expression describes the self-couplings of the weak isospin boson and it is a consequence of the fact that the generators of the SU(2) do not commute (i.e. SU(2) is a non-Abelian symmetry). This is the main new feature introduced by the SU(2) symmetry.

Thus the gauge invariant electroweak Lagrangian is

$$\mathcal{L}_{gb+f} = \bar{\psi}_L \gamma^\mu (i\partial_\mu - g\boldsymbol{\tau}/2 \cdot \boldsymbol{W}_\mu - (g'/2) Y B_\mu)\psi_L + \bar{\psi}_R \gamma^\mu (i\partial_\mu - (g'/2) Y B_\mu)\psi_R - \frac{1}{4}\boldsymbol{W}_{\mu\nu} \cdot \boldsymbol{W}^{\mu\nu} - \frac{1}{4} B_{\mu\nu} B_{\mu\nu}$$

It describes the kinetic energies of the fermions and the gauge bosons and the couplings between them. It is time for some remarks:

- The requirement of local gauge invariance defines the interaction terms in the electroweak Lagrangian.
- The self-couplings of the weak isospin boson $\boldsymbol{W}$ are introduced by the gauge invariance under SU(2).
- Mass terms cannot be added to this Lagrangian without destroying the gauge invariance. However, we know that the W and Z bosons are massive!

2.2.2 The spontaneous symmetry breaking by the Higgs mechanism

There is an obvious contradiction with the principles of the local gauge invariance: the masses of the gauge bosons should be zero as it is the case for the photon and the gluons in QED and QCD respectively. The solution has been anticipated in table 2.2 where the Higgs field is introduced as a doublet of the weak isospin SU(2) symmetry. The Higgs field contains four real scalar fields ϕ:

$$\phi = \begin{pmatrix} \phi^+ \\ \phi^0 \end{pmatrix} = \frac{1}{\sqrt{2}} \begin{pmatrix} \phi_1 + i\phi_2 \\ \phi_3 + i\phi_4 \end{pmatrix}$$

The Higgs mechanism is invoked by requiring that the invariant Lagrangian of these fields is

$$\mathcal{L}_{gb+h} = D_\mu \phi^\dagger D^\mu \phi - \mu^2 \phi^\dagger \phi - \lambda (\phi^\dagger \phi)^2$$

where D_μ is the covariant derivative of the $SU(2)_L \times U(1)_Y$ Lagrangian. This term is to be added to the $SU(2)_L \times U(1)_Y$ invariant Lagrangian for the fermion fields. With the previous choice of the derivative D_μ, the Lagrangian is invariant under the local transformations of $U(1)_Y$ and $SU(2)_L$.

The potential term in the Higgs field Lagrangian is

$$V(\phi) = \mu^2 \phi^\dagger \phi + \lambda (\phi^\dagger \phi)^2$$

with $\mu^2 < 0$ and $\lambda > 0$. μ^2 being negative, the term $\mu^2 \phi^\dagger \phi$ cannot be directly interpreted as the mass term although it has the correct form. The minima of this Higgs potential

are found where

$$\frac{\partial V}{\partial \phi^\dagger \phi} = \mu^2 + 2\lambda\phi^\dagger\phi = 0 \qquad \Rightarrow \qquad \phi^\dagger\phi = -\frac{\mu^2}{2\lambda}$$

Explicitly,

$$\phi^\dagger\phi = \frac{1}{2}\begin{bmatrix} \phi_1 + i\phi_2 & \phi_3 + i\phi_4 \end{bmatrix}\begin{bmatrix} \phi_1 - i\phi_2 \\ \phi_3 - i\phi_4 \end{bmatrix} = \frac{1}{2}(\phi_1^2 + \phi_2^2 + \phi_3^2 + \phi_4^2)$$

This is a four-dimensional equivalent to a circle where the coordinates can vary to satisfy the minimum condition. One is free to choose a set of coordinates that satisfies the above condition, for example

$$\phi_1 = \phi_2 = \phi_4 = 0, \qquad \phi_3^2 = -\frac{\mu^2}{2\lambda} \equiv \frac{v^2}{2}$$

This is the spontaneous symmetry breaking. The minimum of the potential does not appear at $\phi_i = 0$, but at a manifold of values from which a set of values can be chosen without loosing generality, but with breaking the symmetry. As the potential has a non-zero minimum value, it is reasonable to describe the field itself as deviations θ_1, θ_2, θ_3 and $H(x)$ from its value at minimum

$$\phi = \frac{1}{\sqrt{2}}\begin{pmatrix} \theta_2 + i\theta_1 \\ v + H(x) - i\theta_3 \end{pmatrix}$$

If this expression is introduced in the Lagrangian, the vector bosons do get a mass term, but a problem arises. With the words of Salam[3]:

> *"Now all this is beautiful, but there was the suspected difficulty with this theory that held people back for a long time. This was the fear of Goldstone mesons. What one feared was that whenever you have such a theory Goldstone boson sits like a snake in the grass ready to strike. According to Goldstone's theorem a number of massless particles must arise in any such theory."*

What Goldstone's theorem [7] shows is that the spontaneous symmetry breaking of a *global* symmetry generates massless scalar boson. Indeed, in terms of the field ϕ as written above the Lagrangian acquires the mass terms for the gauge bosons through coupling with the Higgs field but it also acquires terms for the fields θ.

However, as discovered by Higgs[8], in a *local* symmetry the unwanted fields can be gauged away. For small variations, the previous expression is equal to

$$\begin{aligned}
\phi &= e^{i\boldsymbol{\tau}\cdot\boldsymbol{\theta}(x)/v}\frac{1}{\sqrt{2}}\begin{pmatrix} 0 \\ v + H(x) \end{pmatrix} \\
&\approx \frac{1}{\sqrt{2}}(1 + \frac{i}{v}(\tau_1\theta_1 + \tau_2\theta_2 + \tau_3\theta_3))\begin{pmatrix} 0 \\ v + H(x) \end{pmatrix} \\
&= \frac{1}{\sqrt{2}}\begin{pmatrix} 1 + \frac{i}{v}\theta_3 & \frac{1}{v}(\theta_1 - i\theta_2) \\ \frac{i}{v}(\theta_1 + i\theta_2) & 1 - \frac{i}{v}\theta_3 \end{pmatrix}\begin{pmatrix} 0 \\ v + H(x) \end{pmatrix} \\
&\approx \frac{1}{\sqrt{2}}\begin{pmatrix} \theta_2 + i\theta_1 \\ v + H(x) - i\theta_3 \end{pmatrix}
\end{aligned}$$

Due to the local gauge invariance one can choose the phase $\boldsymbol{\theta}$ to be zero without loosing generality and

$$\phi = \frac{1}{\sqrt{2}} \begin{pmatrix} 0 \\ v + H(x) \end{pmatrix}$$

can be inserted to the Lagrangian describing the couplings between the Higgs field and the gauge bosons.

$$\begin{aligned}
\mathcal{L}_{gb+h} &= (D_\mu \phi)^\dagger D_\mu \phi - V(\phi) \\
&\text{Here the derivative can be written explicitly} \\
D_\mu \phi &= (\partial_\mu + ig\boldsymbol{\tau}/2 \cdot \boldsymbol{W}_\mu + i(g'/2) Y B_\mu)\phi \\
&= \begin{pmatrix} \partial_\mu + \frac{i}{2}(-gW_\mu^3 + g'B_\mu) & \frac{ig}{2}(W_\mu^1 - iW_\mu^2) \\ \frac{ig}{2}(W_\mu^1 + iW_\mu^2) & \partial_\mu - \frac{i}{2}(-gW_\mu^3 + g'B_\mu) \end{pmatrix} \begin{pmatrix} 0 \\ \frac{1}{\sqrt{2}}(v+H) \end{pmatrix} \\
&= \begin{pmatrix} \frac{ig}{2\sqrt{2}} W_\mu^+ (v+H) \\ \partial_\mu v + \partial_\mu H - \frac{i}{g\sqrt{2}}(-gW_\mu^3 + g'B_\mu)(v+H) \end{pmatrix}
\end{aligned}$$

and when this expression is substituted to the Lagrangian it becomes

$$\begin{aligned}
&= \frac{g^2}{4} W_\mu^+ W^{\mu -} (v^2 + 2vH + H^2) \\
&+ (\partial_\mu v + \partial_\mu H)(\partial^\mu v + \partial^\mu H) \\
&+ \frac{1}{8}(g'B_\mu - gW_\mu^3)(g'B^\mu - gW^{\mu 3})(v^2 + 2vH + H^2) - V(H)
\end{aligned}$$

It is the coupling to the non-zero vacuum value v of the Higgs field that gives the mass term to the bosons W^+ and W^-:

$$\frac{1}{2} m_W^2 = \frac{g^2 v^2}{4} \qquad \Rightarrow \qquad m_W = \frac{gv}{2}$$

To find a mass term for the Z^0 boson — and to see that there is no such term for the photon — we can study the last but one term of the expression. Substituting B_μ and W_3 with the linear combinations in terms of Z_μ and A_μ

$$\begin{pmatrix} A_\mu \\ Z_\mu \end{pmatrix} = \begin{pmatrix} \cos\theta_W & \sin\theta_W \\ -\sin\theta_W & cos\theta_W \end{pmatrix} \begin{pmatrix} B_\mu \\ W_3 \end{pmatrix} \Rightarrow \begin{pmatrix} B_\mu \\ W_3 \end{pmatrix} \begin{pmatrix} \cos\theta_W & -\sin\theta_W \\ \sin\theta_W & cos\theta_W \end{pmatrix} \begin{pmatrix} A_\mu \\ Z_\mu \end{pmatrix}$$

and using $g \sin\theta_W = g' \cos\theta_W$ we obtain

$$\begin{aligned}
g'B_\mu - gW_\mu^3 &= \frac{g \sin\theta_W}{\cos\theta_W}(\cos\theta_W A_\mu - \sin\theta_W Z_\mu) - g(\sin\theta_W A_\mu + \cos\theta_W Z_\mu) \\
&= gZ_\mu(-\frac{\sin^2\theta_W}{\cos\theta_W} - \cos\theta_W) \\
&= -\frac{gZ_\mu}{\cos\theta_W}
\end{aligned}$$

Thus, what remains is the mass term for Z^0:

$$m_Z = \frac{gv}{2\cos\theta_W}$$

Why then the photon remains massless? The non-zero component of the vacuum value of the Higgs field was chosen to be the neutral, weak isospin $I = -1/2$ field ϕ^0 (see table 2.2). When the electric charge operator acts on it

$$Q\phi_0 = (I_3 + \frac{1}{2}Y)\phi_0 = 0$$

which means that the vacuum value of the Higgs field is invariant under the electromagnetic U(1). Thus the subgroup of $SU(2)_L \times U(1)_Y$, the electromagnetic U(1), is unbroken by the spontaneous symmetry breaking with the Higgs mechanism and the corresponding gauge boson, the photon, remains massless.

The interactions of the Higgs field with the massive gauge bosons are described by terms proportional to vH and H^2. We shall return to the strength of this couplings when discussing the Higgs decay modes.

Finally, to complete the electroweak Lagrangian, one should add the couplings between the fermion fields and the Higgs field. We will see that the same mechanism that gives masses to the gauge bosons is able to generate the masses of the fermions. However, this is done in a less satisfactory way: the masses themselves are not defined by the theory, they are just arbitrary free parameters. The Higgs field couples to the left-handed doublets and right-handed singlets of fermions (denoted f_i and f_j)

$$\mathcal{L}_{h+f} = -(g_{f_i}\bar{L}\phi R_{f_i} + g_{f_j}\bar{L}\phi_c R_{f_j} + \text{ Hermitian conjugate})$$

Here, the conjugate Higgs doublet ϕ_c has been introduced such that after the symmetry breaking it becomes

$$\phi_c = \frac{1}{\sqrt{2}}\begin{pmatrix} v+H \\ 0 \end{pmatrix}$$

For the leptons, in the absence of the right-handed neutrinos, this becomes

$$\begin{aligned} \mathcal{L}_{h+l} &= -\frac{g_e}{\sqrt{2}}\left(\begin{pmatrix} \bar{\nu}_e & \bar{e}_L \end{pmatrix}\begin{pmatrix} 0 \\ v+H \end{pmatrix} e_R + \bar{e}_R \begin{pmatrix} v+H & 0 \end{pmatrix}\begin{pmatrix} \nu_e \\ e_L \end{pmatrix}\right) \\ &= -\frac{g_e v}{\sqrt{2}}(\bar{e}_L e_R + \bar{e}_R e_L) - \frac{g_e}{\sqrt{2}}(\bar{e}_L e_R + \bar{e}_R e_L)H \end{aligned}$$

Thus the electron acquires a mass of $m_e = g_e v/\sqrt{2}$ and interacts with the Higgs field with the coupling of $g_e/\sqrt{2} = m_e/v$. For the quarks

$$\begin{aligned} \mathcal{L}_{h+q} &= -\frac{g_d}{\sqrt{2}}\left(\begin{pmatrix} \bar{u}_L & \bar{d}_L \end{pmatrix}\begin{pmatrix} 0 \\ v+H \end{pmatrix} d_R + \bar{d}_R \begin{pmatrix} v+H & 0 \end{pmatrix}\begin{pmatrix} u_L \\ d_L \end{pmatrix}\right) \\ &\quad -\frac{g_u}{\sqrt{2}}\left(\begin{pmatrix} \bar{u}_L & \bar{d}_L \end{pmatrix}\begin{pmatrix} v+H \\ 0 \end{pmatrix} u_R + \bar{u}_R \begin{pmatrix} 0 & v+H \end{pmatrix}\begin{pmatrix} u_L \\ d_L \end{pmatrix}\right) \\ &= -\frac{g_d v}{\sqrt{2}}\bar{d}d - \frac{g_d}{\sqrt{2}}\bar{d}dH - \frac{g_u v}{\sqrt{2}}\bar{u}u - \frac{g_u}{\sqrt{2}}\bar{u}uH \end{aligned}$$

Here again, the quark masses can be identified as $m_i = g_i v/\sqrt{2}$ and the coupling to the Higgs field are proportional to the masses $g_i/\sqrt{2} = m_i/v$.

The complete electroweak Lagrangian is

$$\mathcal{L} = \mathcal{L}_{gb+f} + \mathcal{L}_{gb+h} + \mathcal{L}_{h+f}$$

The couplings of this Lagrangian are used to compute the cross-sections and decay widths of the processes at the Born approximation. However, the couplings are modified by second order processes like radiated photons or virtual photon loops in QED, weak corrections to the vector boson part or QCD corrections. It was shown by t' Hooft[4] that the theory is renormalizable i.e. it does not have lowest order divergences and including the corrections to *all* orders does not give meaningless results in the computations. Indeed, what was shown by t' Hooft was that to be renormalizable, a theory must have a local gauge invariance. This was the main building block of the theory in the beginning!

2.3 The experimental verification of the Standard Model

The Standard Model has been remarkably successful in describing the data from the high energy physics experiments. As an input, the precise electroweak measurements of the Fermi constant G_F (measured from muon decay) giving the strength of the weak interactions, the electromagnetic fine-structure constant α (measured from the quantum Hall effect) giving the strength of the electromagnetic interactions and the Weinberg angle $\sin^2\theta_W$ (measured from m_Z and other Z pole observables, m_W and neutral-current processes) are used. Furthermore, as the measurements are sensitive to the radiative corrections, a fit to the Standard Model calculations including these corrections can predict or constrain the values m_W, m_t and m_H.

Helicity effects play an important role in the Z boson production and decays in e^+e^- machines. It is possible to measure asymmetries such as the forward-backward asymmetry for $e^+e^- \to f^+f^-$

$$A_{FB} = \frac{\sigma_F - \sigma_B}{\sigma_F + \sigma_B}$$

where σ_F is the cross-section for the negative fermion to travel forward and σ_B to travel backward in the e^- direction. In the vicinity of the Z pole, where the $Z - \gamma$ interference vanishes $A_{FB} = (3/4)A_eA_f$ where

$$A_{f/e} = \frac{2g_{A(f/e)}g_{V(f/e)}}{g^2_{A(f/e)} + g^2_{V(f/e)}}$$

are defined in terms of vector and axial-vector chiral couplings. The left-right asymmetry

$$A_{LR} = \frac{\sigma_L - \sigma_R}{\sigma_L + \sigma_R} = A_e$$

where σ_L is the cross-section for a left-handed and σ_R for a right-handed incident electron requires the knowledge of the beam polarisation. The Stanford Linear Collider (SLC) uses polarised beam and such a measurement has been done by the SLD collaboration. At LEP, the charged decays of τ leptons provide a final state polarisation analyser. The

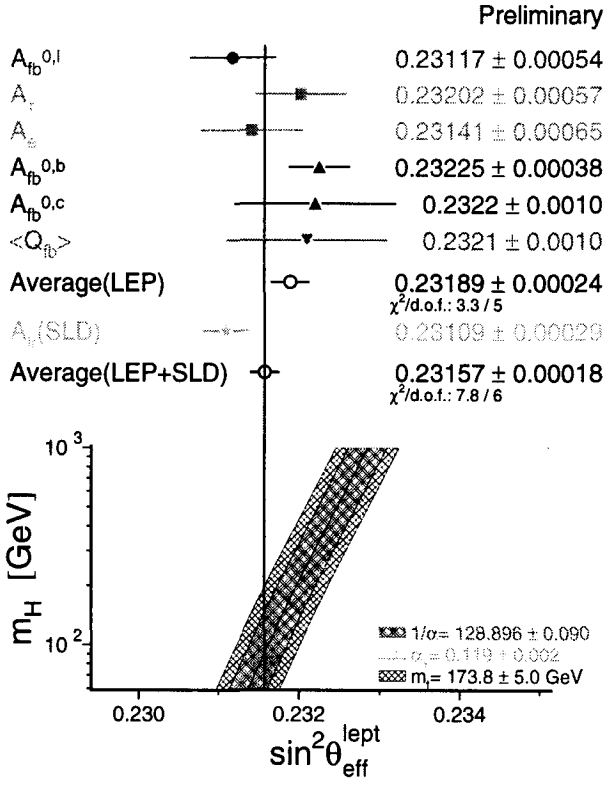

Figure 2.5: Comparison of several determinations of $\sin^2\theta_W$ *from asymmetries. The lower part of the plot shows the Standard Model prediction as a function of* m_H *[9].*

chiral coupling constants g_V and g_A can be derived from the measured asymmetries and the effective electroweak mixing angle $\sin^2\theta_W = (1 - g_V/g_A)/4$ can be determined. Figure 2.5 shows the comparison of $\sin^2\theta_W$ from several measurements and the agreement is good[9], however two most precise determinations (SLAC measurement of A_{LR} and LEP measurement of A_{FB}) are on opposite sides of the average.

Parameter $R_b = \Gamma_b/\Gamma_{had}$ and b and c asymmetries describe the heavy flavour sector where the largest deviations from the Standard Model predictions have appeared. Some comparisons with recent data[9] are shown in figure 2.6. For the Standard Model fit, the direct determinations of m_W and m_t are included. All data measured at Z pole show good agreement with the Standard Model. It is remarkable that if all precision data except the direct measurement of m_t are used, the predicted value of m_t results $m_t = 161^{+8}_{-7}$ GeV which is in agreement with the observed value of 173.8 ± 5.0 GeV.

2.4 Higgs boson as an observable

The search for the Higgs particle is pursued at CERN with the Large Electron-Positron (LEP) Collider. The experiments at LEP have been able to exclude a certain mass range and it seems probable that the LHC will be the instrument to study the Higgs sector, or to find an alternative explanation if no Higgs boson will be discovered.

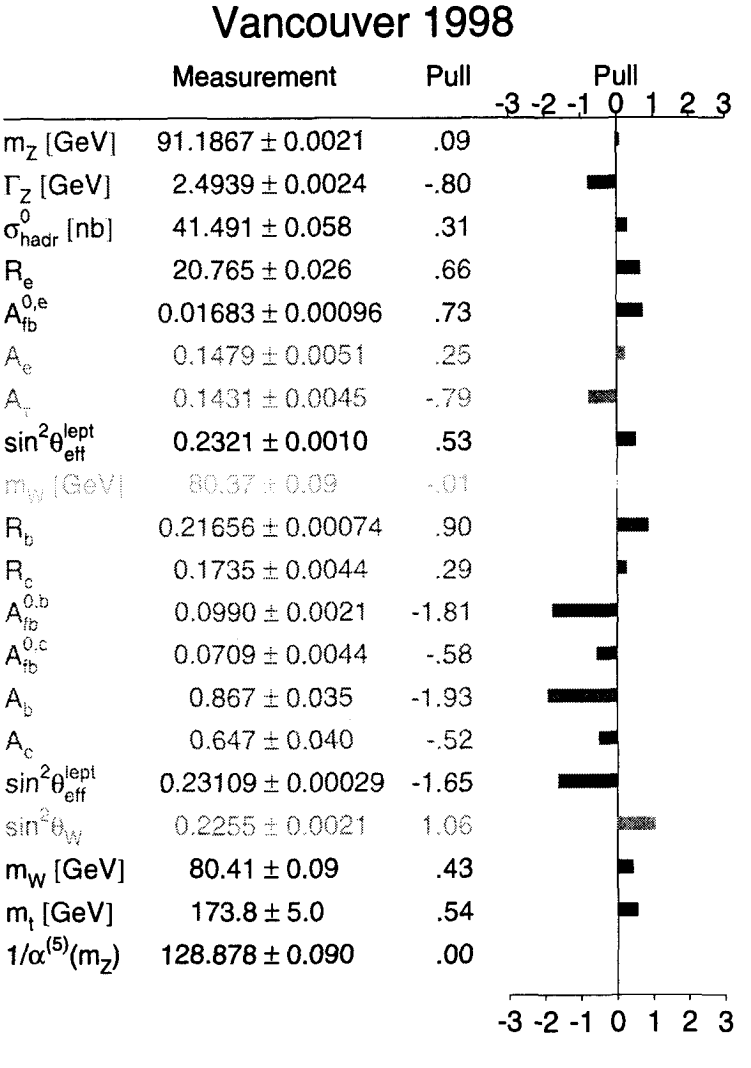

Figure 2.6: Deviations between the measurements of the electroweak parameters and the fit to the Standard Model including direct determinations of m_W and m_t[9]. The deviation is given as a pull which is defined as the difference of the measurement to the SM prediction divided by the measurement error.

In this section, the experimental features — mass, decay modes and width — of the Higgs bosons are covered. The production mechanisms and the cross-sections depend on the colliding particles and their energy, and they will be discussed with respect to the LHC, i.e. considering colliding protons with the centre of mass energy of 14 TeV.

2.4.1 Higgs decays and width

In general, the decay rate for a particle of mass m and 4-momentum p in its rest frame can be computed from

$$\Gamma = \frac{1}{2m}|\bar{\mathcal{M}}|^2 \int \frac{d^3\boldsymbol{p}_1}{(2\pi)^3 2E_1}\frac{d^3\boldsymbol{p}_2}{(2\pi)^3 2E_2}\cdots\frac{d^3\boldsymbol{p}_n}{(2\pi)^3 2E_n}(2\pi)^4\delta^4(p-p_1-p_2-\cdots-p_n)$$

where $i = 1\cdots n$ refers to the momenta of the decay products. $|\bar{\mathcal{M}}|^2$ is the interaction term in the Lagrangian squared, summed over final spins and colours and averaged over initial spins and colours. Accordingly, the Higgs decays are determined by the couplings to the fermions and gauge bosons in the Lagrangian of section 2.2.2:

$$\begin{aligned} g_{Hff} &= \frac{m_f}{v} \\ g_{HWW} &= \frac{g^2 v}{2} = g m_W = \frac{2m_W^2}{v} \\ g_{HZZ} &= \frac{g^2 v}{4\cos^2\theta_W} = \frac{g m_Z}{2\cos\theta_W} = \frac{m_Z^2}{v} \end{aligned}$$

Here, the coupling constant g has been expressed in terms of the vector boson masses. The couplings are proportional to the masses of the fermions and to the square of the masses of the gauge bosons. The calculation of the decay width into a fermion-antifermion pair[10] gives

$$\Gamma(H \to f\bar{f}) = N_c \frac{G m_f^2 m_H}{4\pi\sqrt{2}}(1-4x_f)^{3/2}$$

where G is the Fermi constant, N_c the number of colours (1 for leptons and 3 for quarks) and $x_f = m_f/m_H$. Above the WW and ZZ thresholds, the decay widths into vector boson pairs are[10]

$$\begin{aligned} \Gamma(H \to W^+W^-) &= \frac{G m_H^3}{8\pi\sqrt{2}}(1-4x_W)^{3/2}(1-4x_W+12x_W^2) \\ \Gamma(H \to ZZ) &= \frac{G m_H^3}{16\pi\sqrt{2}}(1-4x_Z)^{3/2}(1-4x_Z+12x_Z^2) \end{aligned}$$

where $x_W = m_W/m_H$ and $x_Z = m_Z/m_H$. After the WW threshold ($m_H > 160$ GeV) the WW decay is the dominant decay mode, followed by the ZZ decay with approximately half the rate of the WW decay. Before, the preferred decay is into the two heaviest available quark-antiquark pair, i.e. into $b\bar{b}$ pair. The decay into $t\bar{t}$ pair is allowed only after the mass threshold of 350 GeV, in the region where the WW decay dominates due to the m_H^3 dependence.

In addition, the Higgs boson can decay into two gluons through top and bottom quark loops and into two photons through top and bottom quark and W loops.

The total decay width is obtained by summing up all possible decay channels $\Gamma = \sum \Gamma_i$. As shown in figure 2.7[11], the width remains extremely narrow at low Higgs masses (few MeV at $m_H = 100$ GeV) and is ≈ 1 GeV at $m_H = 200$ GeV. At high masses, it becomes broad: $\Gamma > 100$ GeV above $m_H = 600$ GeV .

The branching ratio of a decay channel is defined by BR $= \Gamma_i/\Gamma$. The branching ratios of the channels as a function of the Higgs mass are shown in figure 2.8[11]. The higher-order corrections to the decay processes have been taken into account in the computations.

2.4.2 Higgs cross-sections and discovery channels at LHC

Production mechanisms and cross-sections

The production mechanisms of the Higgs boson[12] at the LHC proton-proton collisions are

$gg \rightarrow H$	gluon-gluon fusion
$q\bar{q} \rightarrow W^+W^-, ZZ \rightarrow Hq\bar{q}$	WW or ZZ fusion
$q\bar{q} \rightarrow (W,Z) \rightarrow (W,Z) + H$	Higgs Bremsstrahlung from W or Z
$q\bar{q}, gg \rightarrow t\bar{t} + H$	$t\bar{t}$ Higgs radiation from $t\bar{t}$

Figure 2.9 shows the diagrams of these processes. The cross-sections of the processes depend on the mass of Higgs and decrease with increasing Higgs mass as shown in figure 2.10. The leading order (LO) cross-sections are computed from the interaction terms of the Lagrangian presented in section 2.2.2. Some of the processes have significant contributions from the "next to leading order" (NLO) processes. For the dominant signal process, the gluon-gluon fusion, the main contribution is the radiation of a soft gluon which should not change the kinematics of the event substantially. Therefore, these corrections can be included by multiplying the leading order cross-section by a simple factor, the so called K-factor $K = \sigma_{NLO}/\sigma_{LO}$. The cross-sections shown in figure 2.10 contain the contributions from these higher order processes.

The Higgs production from a top quark loop generated in a gluon-gluon fusion is the dominant process over the entire mass range[13]. It is furthermore amplified by the higher order QCD processes: virtual contributions to the $gg \rightarrow H$ process and contributions with an additional parton in the final state[11]. These processes increase the leading order cross-section at LHC by 60% to 90% depending on the Higgs mass[14].

The vector boson[15] fusion gives a significant contribution; it has an order of magnitude smaller cross-section than the gluon-gluon fusion at $m_H = 100$ GeV but its relative contribution increases with the increasing Higgs mass and it becomes as large as the gluon-gluon fusion at $m_H \approx 1$ TeV. The QCD corrections in this case consist only of corrections to the structure functions of the proton as there are no colour transfer between the quark lines (the proton remnant carries no colour and W and Z are colourless). The leading order cross-section is modified by 8%-10%[16].

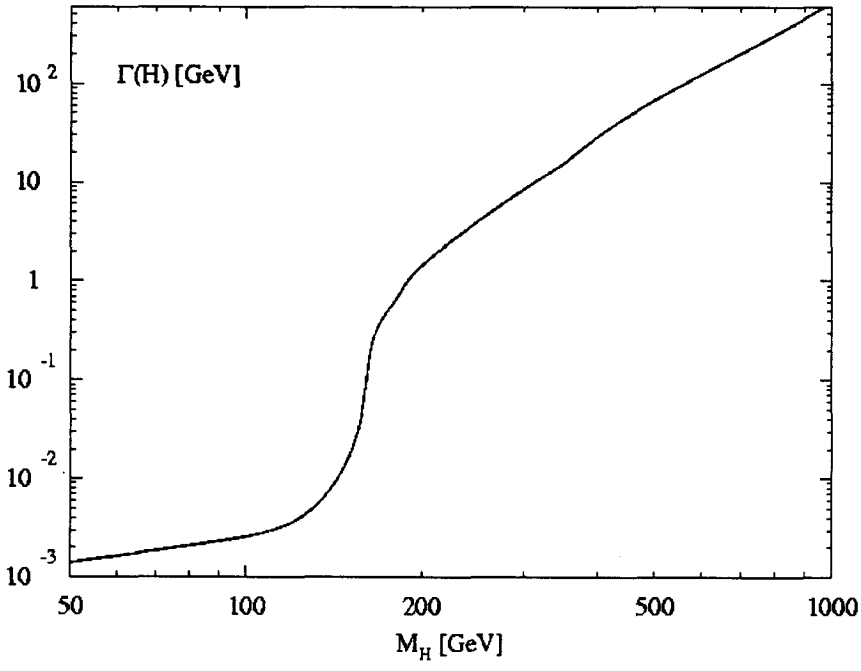

Figure 2.7: The total decay width of Higgs as a function of its mass[11].

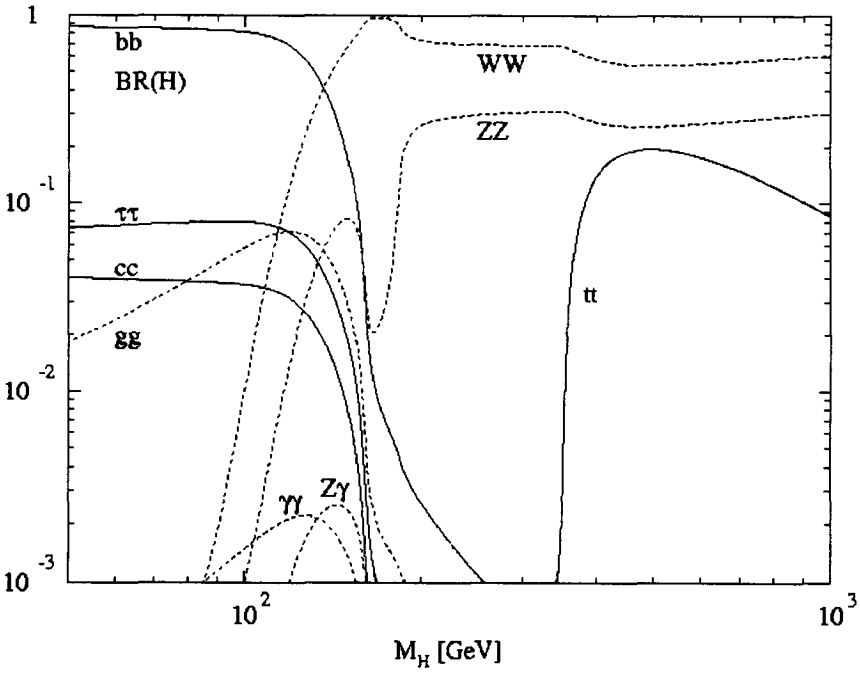

Figure 2.8: The branching ratios of the decay modes of the Higgs boson[11].

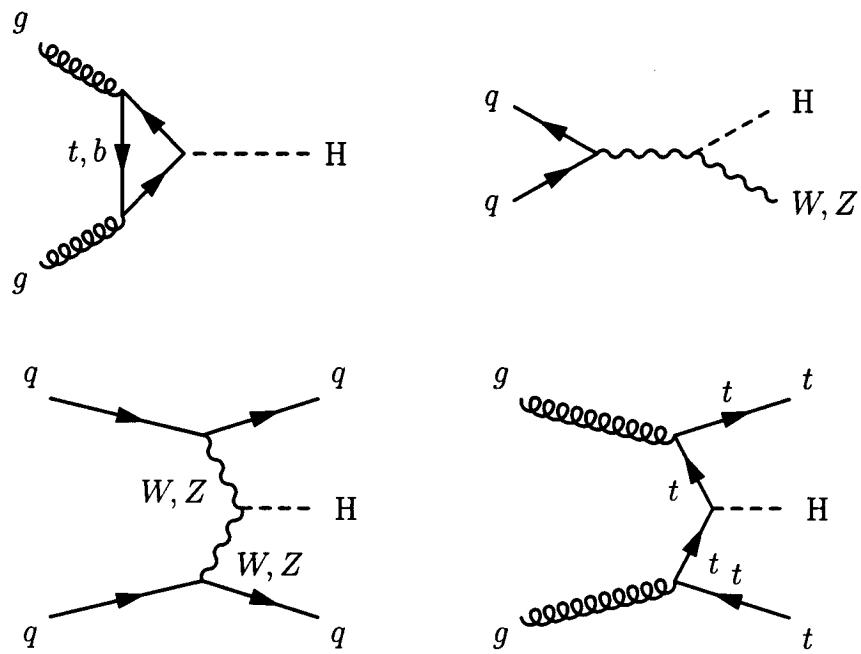

Figure 2.9: The lowest order diagrams for the Higgs production processes.

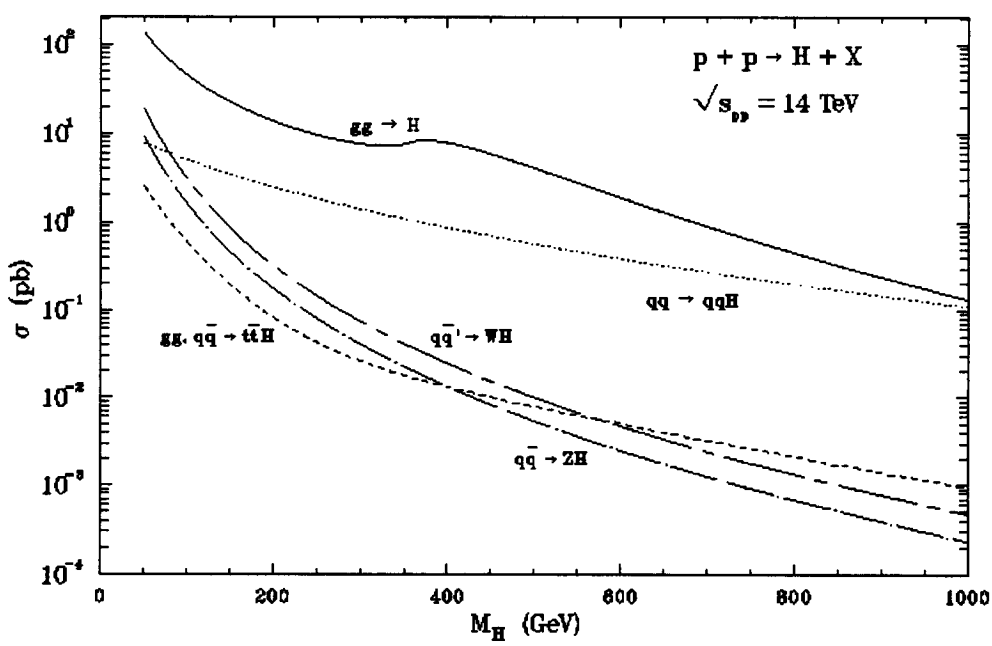

Figure 2.10: The cross-sections of Higgs production processes at LHC as a function of the mass of Higgs including NLO corrections[11].

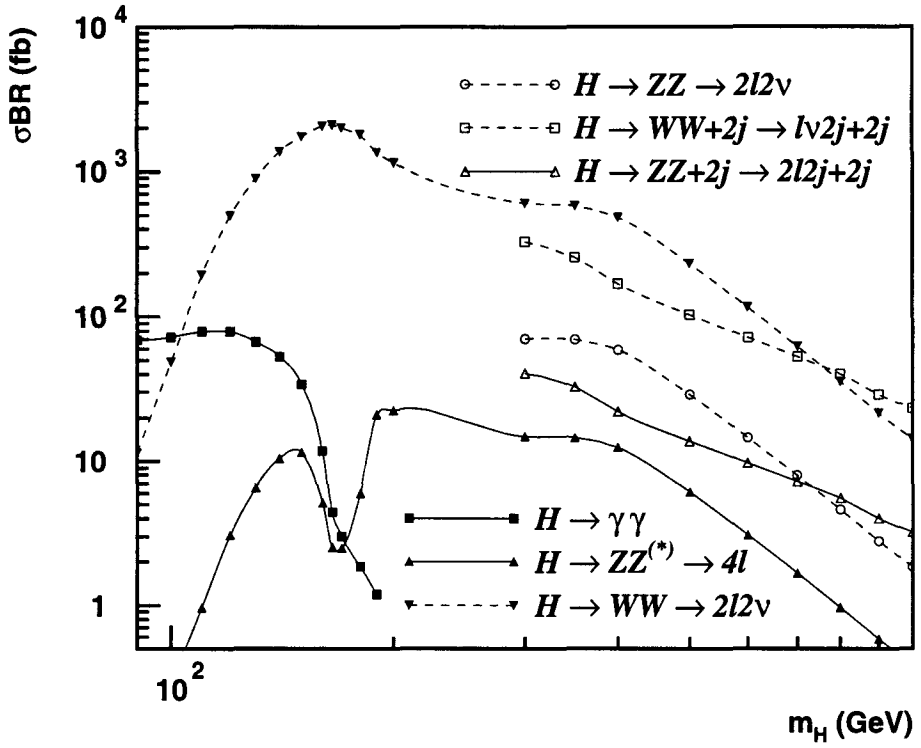

Figure 2.11: Higgs production rates at LHC.

The processes with an associated production of W, Z[17] or a $t\bar{t}$[18] pair give a sizeable rate only at the low mass range of $m_H < 120$ GeV. Although being rare, they may provide an interesting experimental signature if the remaining vector boson or the $t\bar{t}$ pair can be identified. The leading order cross-section for the Higgs radiation from a W or a Z is amplified by 25%-40% by the QCD corrections[19]. The correction for the Higgs radiation from a $t\bar{t}$ fusion has not yet been computed.

Discovery channels

The total cross-section for the Higgs production will be significant over the mass range covered at LHC: at $m_H = 100$ GeV the production rate is approximately 50 pb and at $m_H = 1$ TeV 0.2 pb. If 100 fb^{-1}of integrated luminosity can be accumulated in one year, these rates result in $5{\cdot}10^6$ and 20000 Higgs events per year. However, not all the decay modes provide experimentally distinguishable signatures and the amount of detectable signal is reduced. An estimate of the rates in the different decay channels and with different values of the Higgs mass is given in figure 2.11.

The most promising decay channels as a function of the Higgs mass are shown in figure 2.12. Due to the large background it is believed that the most abundant decay channels at low masses, $pp \rightarrow H \rightarrow b\bar{b}, \tau\tau$, cannot be exploited in hadron colliders. Therefore, the remaining signature will be the decay of Higgs into a photon pair in the mass range of $m_H \approx 90$ GeV to 150 GeV, which gives a signal of two electromagnetic clusters. However, this channel is suppressed by the small branching ratio of the order of 10^{-3}. As shown in

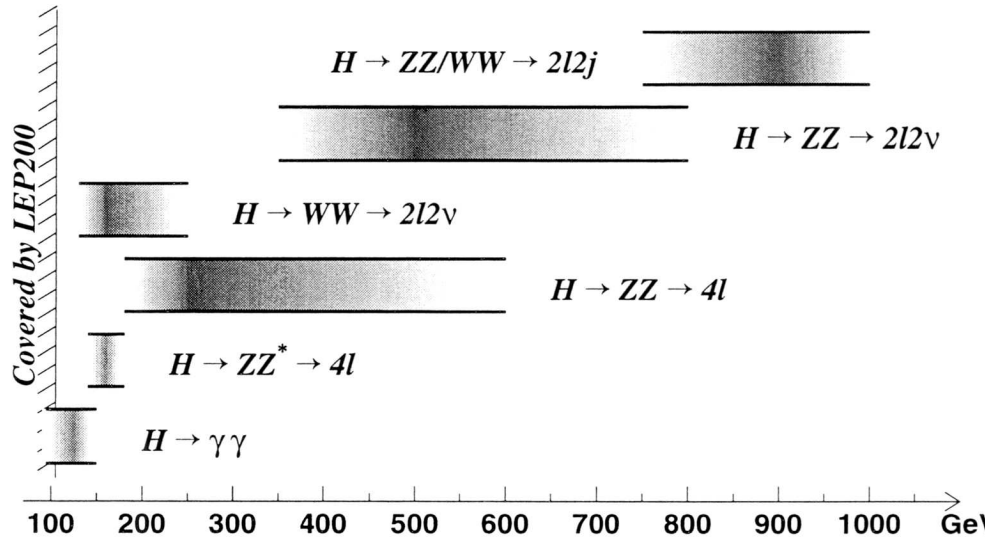

Figure 2.12: The most promising decay channels for Higgs discovery at LHC.

figure 2.8 the natural width of the Higgs boson at this mass range is extremely narrow and in consequence it is possible to detect this channel over the enormous di-photon background with an extremely precise measurement of the mass peak.

Below $m_H \approx 2m_Z$ an important signal is the decay of Higgs to one real and one virtual Z boson (Z*) with Z and Z* bosons decaying into leptons. With masses larger that $2m_Z$, the decays into two real Z's can be exploited given a clean signature if the two Z's decay into electrons or muons. However, the rate of such decays is small as shown in figure 2.11.

The gap between the ZZ* and the ZZ is caused by the opening of the WW channel which reduces the branching ratio of Higgs decays into Z's. There, the decay into two W's decaying into leptons and neutrinos can be exploited. Due to the neutrinos which escape the detector, the mass of the Higgs boson has to be reconstructed indirectly but this is compensated by the size of the signal: the branching ratio of the $H \rightarrow WW$ process is close to one in this region.

The Higgs production cross-section decreases with the increasing Higgs mass and therefore the four lepton mode of the $H \rightarrow ZZ$ becomes difficult at high masses ($m_H > 600$ GeV). There other, more frequent decay modes of Z and W have to be exploited.

The Higgs searches using these different channels are described in detail in chapter 6.

2.4.3 Limits on Higgs mass

Although the Standard Model does not predict the mass of the Higgs boson, constraints on it can be deduced from theoretical arguments.

First, for the internal consistency of the Standard Model, the perturbation approach has to be valid. The processes mediated by the Higgs boson are needed to compensate for the increasing cross-section of the processes including longitudinally polarised W bosons (renormalizability of the theory). However, if $m_H > 1$ TeV, the couplings in the W and Z boson sector become so large that the perturbation theory fails before the processes

including the Higgs boson become effective. Therefore, the consistency requires an upper limit of $m_H < 1$ TeV.

Other bounds can be derived from the energy scale limit up to which the Standard Model can be extended. The Higgs potential is of the form

$$V_0(\phi) = \mu^2\phi^\dagger\phi + \lambda(\phi^\dagger\phi)^2$$

Higher order loop corrections[20] add a term

$$V(\phi) = V_0(\phi) + V_1(\Lambda, m_t, m_H, ...)$$

which can modify the potential. Λ is the renormalization scale which enters in the expression because of the loop corrections. *The vacuum stability* requires that the additional term should not destroy the shape of the potential function and the derivative should not become negative at high values of ϕ driving the potential function down below the original minimum. The vacuum is stable, i.e. the potential curve has an absolute minimum at $\phi^\dagger\phi = v^2/2$, in the region $\phi < \Lambda$ where one requires the theory to be valid if the Higgs mass is high enough to keep the coefficient of $(\phi^\dagger\phi)^2$ positive even after the corrections. Thus the lower limit for the Higgs mass can be deduced.

The Higgs potential written in terms of $\phi_3 = \frac{1}{\sqrt{2}}(v + H)$ becomes

$$V(H) = \text{constant} - v^2\lambda H^2 + \lambda v H^3 + \frac{1}{4}\lambda H^4$$

The quadratic Higgs self coupling increases with the increasing Higgs mass ($m_H = \sqrt{2\lambda}v$) and at a certain point the couplings become infinite[21]. The position of the divergence depends on the Higgs mass and thus a upper limit for the mass can be deduced in the limit up to where the theory is supposed to be valid.

With the now known top quark mass of 175 GeV, the allowed Higgs mass window would be only 130 - 190 GeV if the standard model is required to be valid up to the Planck scale ($\Lambda = 10^{19}$ GeV). However, if the range of validity is required only up to $\Lambda \approx 1$ TeV, the Higgs mass can vary in the range 55 - 700 GeV. The allowed Higgs mass range as a function of the scale is shown in figure 2.13[22].

These theoretical considerations can favour some mass region for the Higgs boson, but depending on many assumptions, they cannot completely exclude the rest. However, if nature has chosen a Higgs boson of 1 TeV we can conclude on the basis of these considerations that something must be very wrong in the Standard Model.

As discussed in section 2.3, the Higgs mass can also be predicted from the electroweak precision measurements. In [9], the upper limit of the Higgs boson mass at the 95% confidence level is found to be 262 GeV. Thus, both the theoretical arguments and the available data favour low mass for the Standard Model Higgs boson.

Up to the summer 1998 the LEP experiments have not found any evidence from a Higgs boson. At LEP, a Higgs would be radiated from a Z boson line and it could be detected in its decay into a b quark or τ lepton pair. The Higgs searches at LEP exclude now the region below $m_H \approx 95$ GeV[23]. When the centre of mass energy of LEP reaches 200 GeV (LEP2) the sensitivity increases to 105 GeV[24].

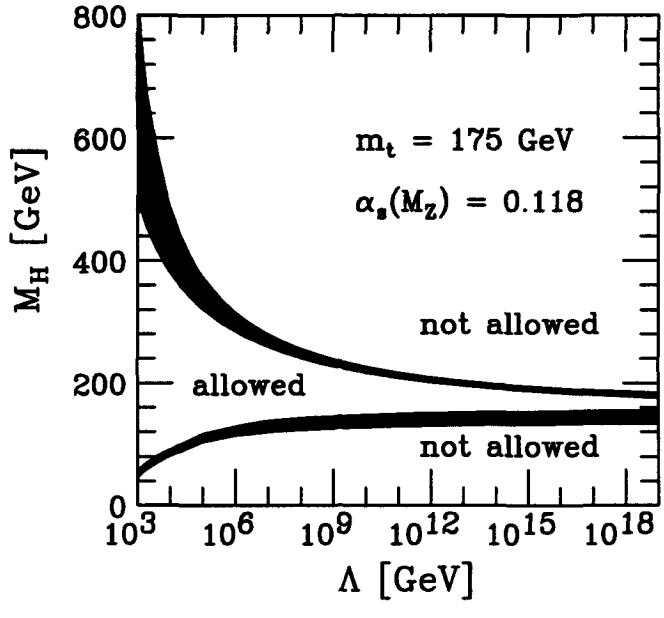

Figure 2.13: The allowed Higgs mass range as a function of the validity limit of the Standard Model[22].

2.5 And if all this is not true

The Standard Model describes the phenomena of physics starting from our everyday electromagnetic interactions down to the scale of strong and weak interactions which have been probed up to energies of 200 GeV. Electromagnetic interactions govern the physical phenomena down to the distances of an atom (10^{-10} m). Then, the strong interaction takes over to hold the protons and neutrons in an atomic nucleus (10^{-14} m) and to keep the quarks in protons and neutrons (10^{-15} m) together . Further down the distance scale (10^{-19} m), the effects of the W and Z bosons, the carriers of the weak interaction, become important. This is where we are now. With the LHC we can hope to gain one more scale in the distance ladder, arriving to energies of the order of TeV, and hopefully discovering the origins of the spontaneous symmetry breaking of the electroweak interactions. At much smaller distances — or at much higher energies — we finally arrive to the Planck scale (10^{19} GeV) where the quantum gravity should become comparable and unified to the other forces. The Standard Model, however, does not include the gravitational force. Our description must be incomplete.

The Standard Model combines the colour forces and the unified electroweak force which is often notated by $SU(3)_c \times SU(2)_L \times U(1)_Y$. The $SU(3)_c$ of QCD, however, is not included in an unified form. One would like to find a grand unified symmetry group which could contain the electroweak group and the colour group. The unification scale M_X can be estimated from the evolution of the running coupling constants of the interactions: the three coupling constants coincide almost at $M_X \approx 10^{15}$ GeV. The symmetry of the unified forces is broken at this value by some mechanism. The Standard Model does not provide a mechanism for this unification.

Furthermore, if the Standard Model were to be valid up to this very large mass scale,

there should be very exact cancellations that remove the divergences in the Higgs mass which are caused by radiative corrections. This is the so called *naturalness* or *hierarchy* problem: incredible fine-tuning is needed up to the highest mass scales to keep the Higgs boson mass small.

There are two ways that propose to solve the naturalness problem[25]: one can avoid the scalar field and construct a new strong force with new vector bosons or one can introduce a new symmetry and new particles that cancel exactly and naturally the divergences. Each of these proposals would have some experimental observables at the energy scale of 1 TeV.

In the case of a new strong force, the electroweak symmetry could be broken by a condensates of new fermions that are attracted by the new strong force like in the technicolour theories[26]. Such a mechanism for the symmetry breaking is also offered for example in the BESS (Breaking Electroweak Symmetry Strongly) model[27]. It would result in three new vector bosons and the Higgs would not be a physical particle. Composite models where the vector bosons and the Higgs are not elementary particles would result in a spectrum of new particles.

Models proposing a new symmetry are extensions of the Standard Model. In E_6 (from the symmetry group E_6) gauge models[28], there is an additional U(1) symmetry arising from the superstring theories. This could result in new heavy gauge bosons Z' and W' at the TeV scale.

The most popular theory extending the Standard Model is Supersymmetry (SUSY)[29] introducing a symmetry between bosons and fermions. Each particle should have a SUSY partner, a *sparticle*, with a spin differing by 1/2. At least two Higgs doublets are required resulting in five observable Higgs particles. The naturalness problem is solved by an exact cancellation between the particle and sparticle contributions.

There is no experimental evidence of any of these models and their existence can only be confirmed — or ruled out — with experiments.

Chapter 3

Large Hadron Collider (LHC)

3.1 LHC machine

The Large Hadron Collider at CERN in Geneva will be the tool to study the phenomenological observables of the electroweak symmetry breaking. It will collide protons on protons with a centre of mass energy of $\sqrt{s} = 14$ TeV and a design luminosity of $\mathcal{L} = 10^{34}$ $\mathrm{cm}^{-2}\mathrm{s}^{-1}$. For an initial period of three years the luminosity is expected to be an order of magnitude lower. The proton-proton collisions will provide a full range of constituent collision energies up to the TeV scale. This is needed at our present knowledge of the theory: the Standard Model does not directly predict the Higgs boson mass and it is argued that whatever breaks the electroweak symmetry must produce some observable consequences for constituent collision energies below ≈ 1 TeV[25].

The LHC will be installed in the existing 27 km long tunnel of the Large Electron-Positron (LEP) collider which is situated across the Swiss-French border west of Geneva at the foot of the Jura mountains. Table 3.1 gives the main parameters of the machine.

The overall layout of the LHC machine and its injection system is shown in figure 3.1. Details on the LHC project can be found in [30]. Here, the main components of the machine are shortly described following the beam from the injection to the end of the fill.

Injection The available CERN infrastructure will be used in the injection system. A small linear accelerator gives the proton beam an initial energy of 50 MeV, then it will be boosted up to 1.4 GeV. The Proton Synchrotron (SP) accelerates the beam up to 25 GeV and it will be injected to the Super Proton Synchrotron (SPS). The 450 GeV protons from SPS are injected to the LHC rings along two new transfer lines.

Vacuum system The beams will run in the stainless steel tube of the LHC vacuum system. The tube is in contact with the super-fluid helium at 1.9 K. Although the synchrotron radiation in hadron colliders is suppressed by the relativistic factor γ of the proton compared to that of the electron in electron colliders, the power emitted by it would be an excessive heat load for a 1.9 K system. Thus there is a special protection, a beam screen, which is maintained at a temperature between 5 K and 20 K and which can absorb the heat from the beam radiation.

Beam and interaction		
Beam energy	(TeV)	7
Luminosity	($cm^{-2}s^{-1}$)	10^{34}
Time between collisions	(ns)	25
Bunch length	(cm)	7.7
Beam radius at interaction point	(μm)	15.9
Technical parameters		
Ring circumference	(m)	26658.9
RF frequency	(MHz)	400.8
Number of bunches		2835
Number of bending dipoles		1232
Magnetic length of the bending dipoles	(m)	14.2
Field of the bending dipoles	(T)	8.386
Bending radius	(m)	2784.3
Temperature of the main magnets	(K)	1.9

Table 3.1: The main LHC parameters.

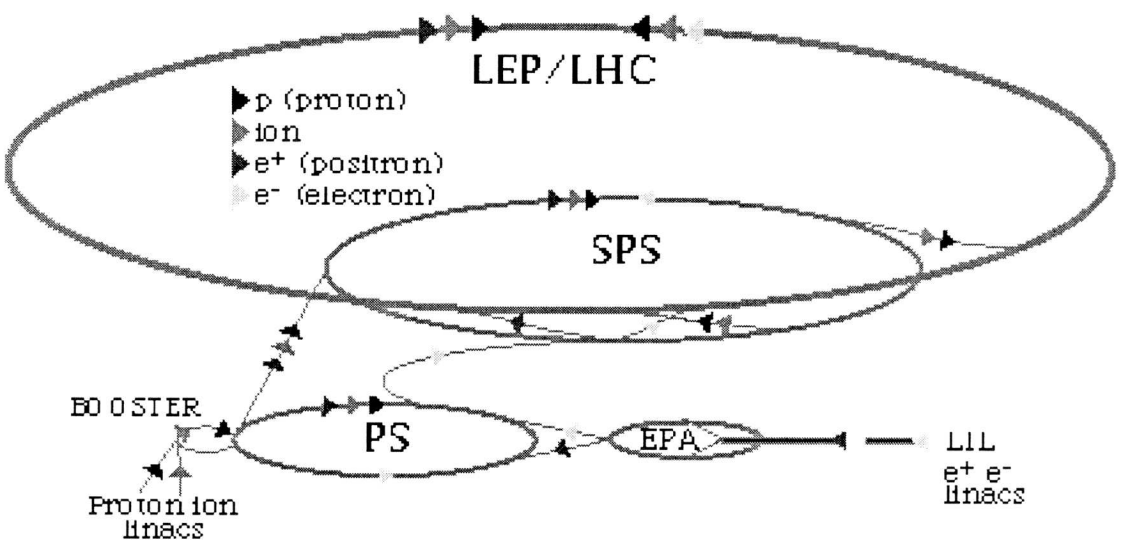

Figure 3.1: The layout of the LHC within the CERN accelerator complex.

Magnets The peak energy in the LHC is defined by the maximum field of the magnets that hold particles in their orbit. The LHC superconducting dipole magnets are designed to reach the field of 8.4 T which will lead to the beam energy of 7 TeV:

$$p_T = 0.3BR = 0.3 \cdot 8.386 \cdot 2784.3 \text{ GeV} = 7.0 \text{ TeV}$$

R (in metres) is the bending radius of each of the eight curved sections which alternate with the straight sections in the LHC ring. High field superconducting magnets are

already in use at Tevatron in Fermilab, USA, with the peak field of 4.4 T giving to the proton beam the energy of 0.9 TeV and at HERA in DESY, Germany, with the peak field of 4.65 T and the proton beam energy of 0.82 TeV.

A beam of antiprotons and the other of protons would have the advantage of single beam channel as the two beams could be guided by the same magnets. However, it is not feasible to produce enough antiprotons to reach the luminosities which are required to fully exploit the physics potential at LHC energies. Therefore, proton-proton collisions are used. The two proton beams circulate in separate magnetic chambers. The chosen solution is a twin bore magnet where the two beam channels are within the same mechanical structure and cryostat. This structure is more compact and more economical than two separate magnets.

Cryogenics To reach this high field of 8.4 T, the superconducting cable must be cooled. The LHC magnets use niobium-titanium conductor which requires the magnets to be cooled down to 1.9 K. This is done by super-fluid helium which features lower viscosity and higher heat conductivity than normal liquid helium (4.2 K).

RF system The radio frequency (RF) system will be installed in one of the eight insertions of the LHC ring. There is an independent RF system for each beam. The frequency of the system will be 400.8 MHz. The time interval between the RF bucket corresponding to this frequency is 2.5 ns and every tenth bucket is filled to obtain bunches separated by 25 ns.

Interaction points There will be two high luminosity interaction points for the two general purpose detectors ATLAS[31] and CMS[32]. Two other points host the injection lines and low luminosity interaction points for the heavy-ion experiment ALICE[33] and the B-physics experiment LHC-B[34].

Beam cleaning Any high luminosity beam acquires a halo of particles that are elastically scattered away from the beam area. These particles are a potential danger for the magnet system as they can deposit their energy as a hadronic shower to the surrounding material. The LHC beam will be cleaned by collimators, which is a block of material parallel to the beam line where the halo particles will be absorbed. The LHC will have two insertions for the beam cleaning.

Beam dump The LHC beam will need to be extracted from the main ring and defocused before dumping. The extraction will be done by a kicker magnet and the beam will be transported to a dump block of graphite surrounded by heavier materials at the end of the 750 m long transfer tunnel. This will allow sufficient dilution of the cascade and shielding for the radiation.

3.2 Overview on the LHC experimental environment

The experimental environment in the LHC is characterised by high luminosity and a short bunch crossing interval.

High luminosity is synonymous with a high collision rate. In a proton-proton collision the interacting objects are the valence quarks, gluons or sea quarks or antiquarks of the proton. The energy available to the collision is determined by the fraction of the total proton energy carried by the colliding parton. Cross-sections for inelastic interactions is such collisions is very large and the cross-sections for interesting events, for example a Higgs, lie orders of magnitude below the rates of the background processes. Figure 3.2 shows the cross-sections of different processes as a function of centre of mass energy in proton-proton and proton-antiproton collisions.

The number of collisions in one bunch crossing can be computed from the luminosity and the cross-section. In the LHC, 2835 out of 3564 bunches are filled. Thus, if the cross-section for an inelastic interaction is $\sigma = 55$ mb[35], at the luminosity of $\mathcal{L} = 10^{34}$ $\mathrm{cm}^{-2}\mathrm{s}^{-1}$ there will be

$$n = \mathcal{L}\sigma\frac{3564}{2835}\tau = 10^{34}\mathrm{cm}^{-2}\mathrm{s}^{-1} \cdot 55\mathrm{mb} \cdot \frac{3564}{2835} \cdot 25\mathrm{ns} = 17.3$$

interactions on the average in one bunch crossing. Every interesting event candidate will have several so called "minimum-bias" events piled up on top of it, resulting in a large particle multiplicity per event. However, this is not an entirely new experimental condition: at Tevatron in the recent runs there are 2.3 events on the average per bunch crossing which is of the same order of magnitude as at the LHC in its initial low luminosity period. Figure 3.3 shows the difference in the sum of the transverse momentum and in the number of tracks in proton-proton collisions at the LHC energy and in proton-antiproton collisions at the Tevatron energy. According to simulations based on theoretical models[36], the average p_T of tracks does not change significantly with the centre of mass energy (0.36 GeV at $\sqrt{s} = 14$ TeV and 0.32 GeV at $\sqrt{s} = 1.8$ TeV). However, it is possible to have some surprises in the years to come, as all the simulations used to estimate the kinematics of a minimum bias events extrapolate from the data at much lower centre of mass energies and we have no guarantee that such an extrapolation is correct. Whatever the nature of the minimum bias events at LHC energies it is clear that they will lead to an enormous particle density in the detector.

The high interaction rate together with the short bunch interval impose stringent conditions on the trigger and data acquisition system of the detectors. The interesting events must be identified and stored in a time which is compatible with the bunch crossing interval of 25 ns. It is not possible to store all the events and therefore the multi-level trigger system has to reduce the data volume from the collision rate of 40 MHz to the level 1 maximum trigger rate of 100 kHz. The trigger observables at the LHC will be isolated leptons, photons or electrons in the electromagnetic calorimeter and muons in the muon system, jets or missing transverse energy in the combined calorimeter system. The first level decision to accept an event will be based on these trigger objects.

The high proton-proton collision rate also implies an intense radiation environment. Most of the collision products are absorbed in the calorimeters, but backscattered particles

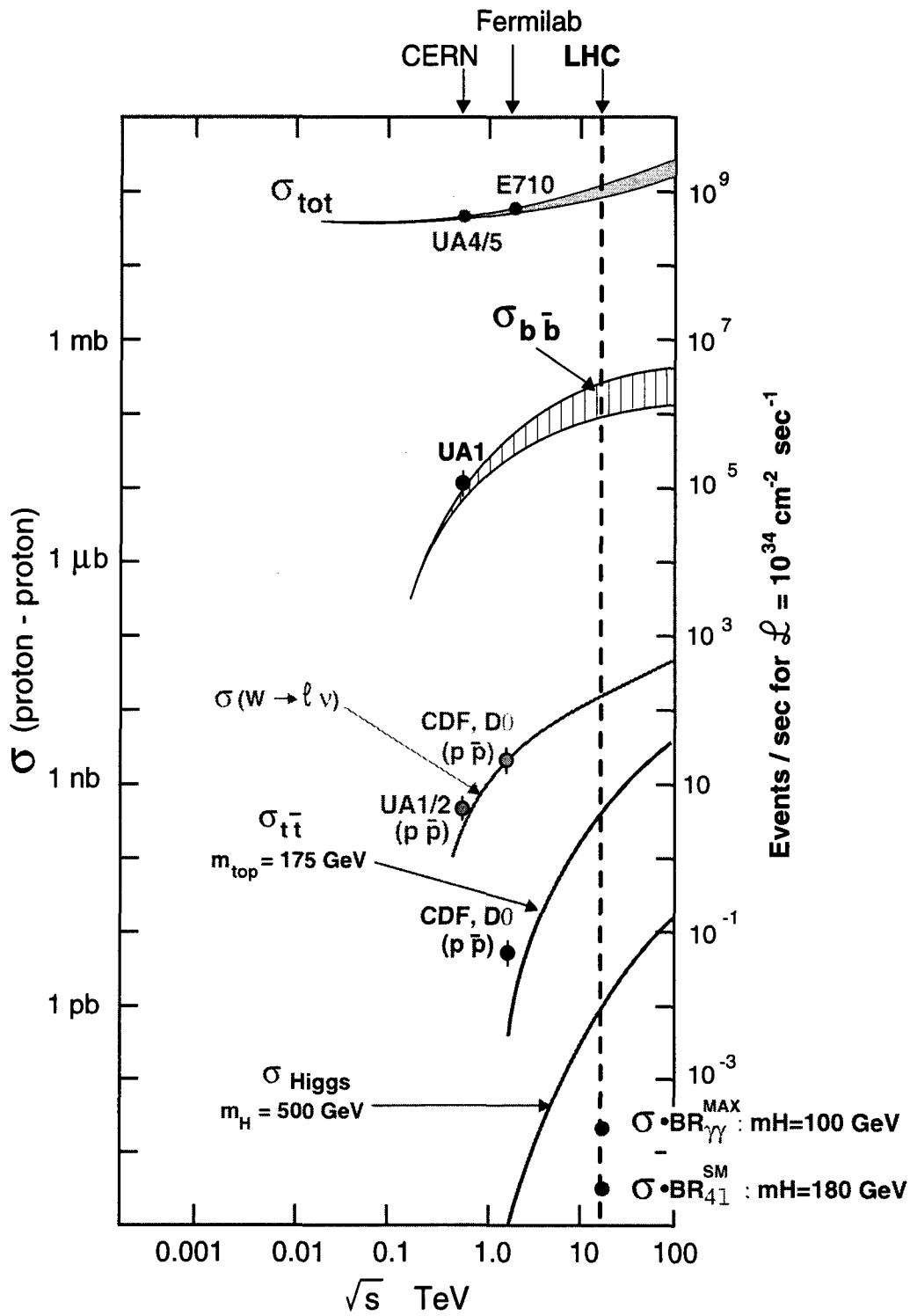

Figure 3.2: Cross-sections and rates in proton-proton and proton- antiproton collisions as a function of centre of mass energy.

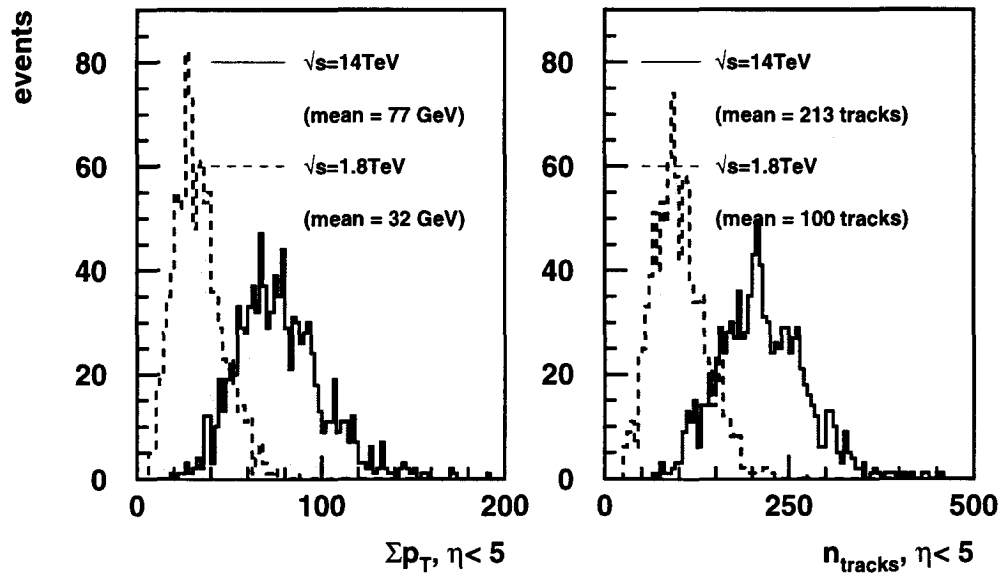

Figure 3.3: The sum of transverse momentum and the number of tracks up to η=5 of the minimum bias events in $\sqrt{s}$ = 14 TeV proton-proton collision (LHC) and in $\sqrt{s}$ = 1.8 TeV proton-antiproton collision (Tevatron)[35].

and shower tails will affect the detector everywhere. The dose rates and particle fluence are at their maximum in the inner detector and in the forward region of the experiment. Radiation resistance is one of the main design requirements of all detector components at the LHC.

Chapter 4

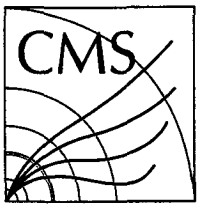

CMS experiment

As described in the previous chapters, the LHC will address one of the main questions in the particle physics today: the origin of the spontaneous symmetry breaking in the electroweak sector of the Standard Model. The observable consequence could be a scalar particle, the Higgs boson, or if the Standard Model is not the complete description of nature, it may also include a variety of new particles like several Higgs bosons, supersymmetric particles, new gauge bosons, technicolour states or leptoquarks. The Compact Muon Solenoid (CMS) experiment is designed to enable the discovery and investigation of all of these possibilities, the Higgs sector being one of the priorities.

In the following, the physics motivation for the CMS design is presented and each subdetector is briefly described.

4.1 Design criteria for CMS

The main characteristics of the LHC experimental environment are

- large particle multiplicity
- short bunch crossing interval
- severe radiation environment.

The physics objectives together with these items dictate the design of the experiment. The basic design criteria of CMS are

- very good muon identification and momentum measurement even in the most difficult experimental conditions

- high resolution electromagnetic calorimeter for the energy measurement of photons and electrons
- powerful inner tracking system that allows reconstruction of particle tracks and precise momentum measurement to reach the two above mentioned criteria.

To achieve these objectives, CMS has chosen a 4 Tesla solenoidal magnet[37] with the inner radius of 2.95 m and the length of 13 m placed after the calorimeter system. It will enable precise and clean environment for the muon measurement, reduce the charged particle multiplicity in the electromagnetic calorimeter barrel and allow good momentum measurement in the inner tracker. A transverse view of CMS with a typical muon track is shown in figure 4.1. The field is parallel to the beam line, thus bending the charged particle tracks in the transverse plane. In such a configuration, the momentum measurement profits from the small size and, therefore, the accurate knowledge of the beam spot in the transverse plane. The field direction after the coil is opposite to the direction inside the coil resulting in a s-shaped muon tracks that are represented in the CMS logo.

To illustrate the effect of the magnetic field on the particle multiplicity, sets of 20 minimum bias events have been simulated and the charged track multiplicity per 2x2 cm^2 (roughly the CMS electromagnetic calorimeter granularity) has been computed with magnetic field values of 0 T, 2 T and 4 T. It can be seen from figure 4.2 and from table 4.1 that a 4 Tesla field cleans the environment at the radius of 130 cm where the electromagnetic calorimeter barrel of CMS starts. The detector material is not included in this study; when the interactions in the material are taken into account the charged track multiplicity increases due to interactions, e.g. Bremsstrahlung of electrons and conversions of photons, in the tracker material. In addition, the actual multiplicity in a given detector cell depends on the detector technology chosen: in some cases it is possible to read out one bunch crossing at the time, in other cases more than one bunch crossing has to be integrated.

Before going to the more detailed discussion of each subdetector one should remark that the chosen field configuration constrains the design of the rest of the detector. From table 4.1 it can be seen that the magnetic field increases the charged track multiplicity at small radii. This is due to the low transverse momentum tracks that spiral in the magnetic field. To cope with the enormous particle density, the inner tracker has to have a very high granularity.

There are technical size limits for a solenoid and therefore the calorimeter system which is placed inside the solenoid has to be compact and provide enough material to avoid hadronic cascades leaking into the muon system. In CMS, the electromagnetic calorimeter consists of very compact and dense crystals. The hadronic sampling calorimeter consists of active scintillator plates and copper absorbers.

4.2 Overview on CMS

A general view of the CMS detector is shown in figure 4.3. The radius of the detector is 7.5 m, the length 21.6 m and the weight is about 12500 t. It will be installed at point 5 of the LHC ring, close to the French village of Cessy 15 kilometres from Geneva.

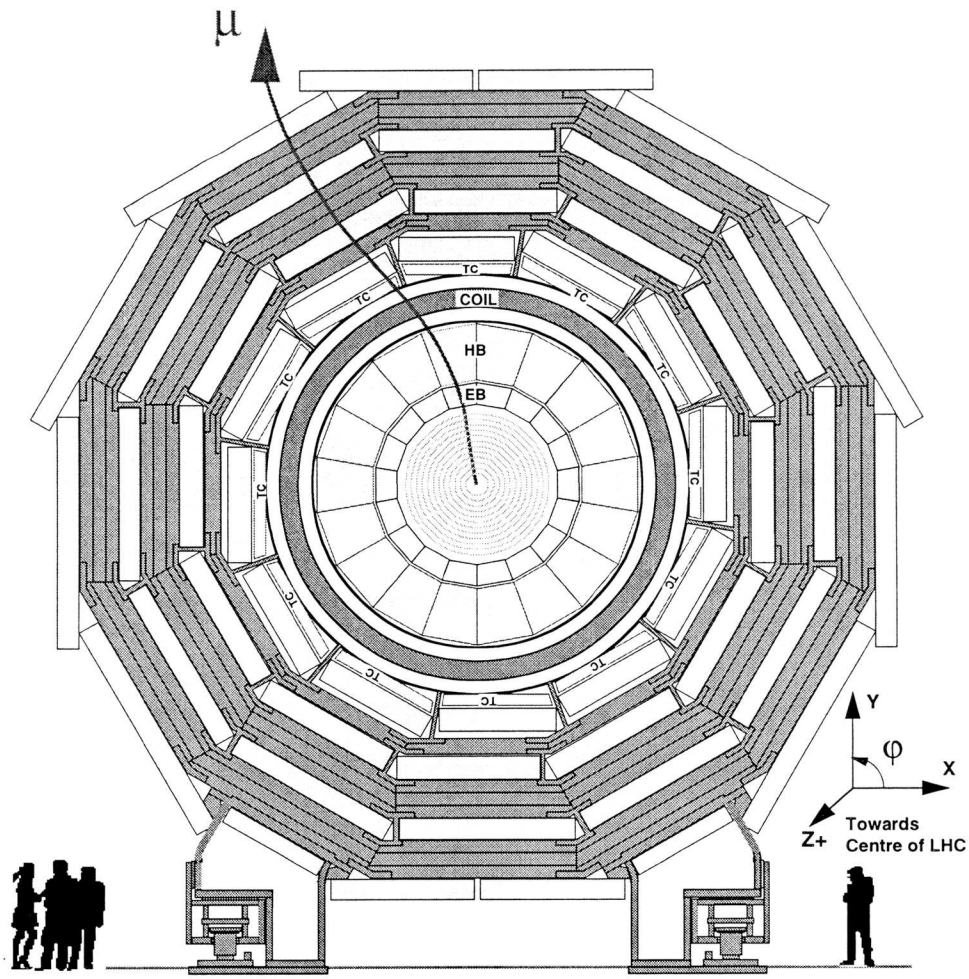

Figure 4.1: Transverse view of the CMS experiment with a typical muon track.

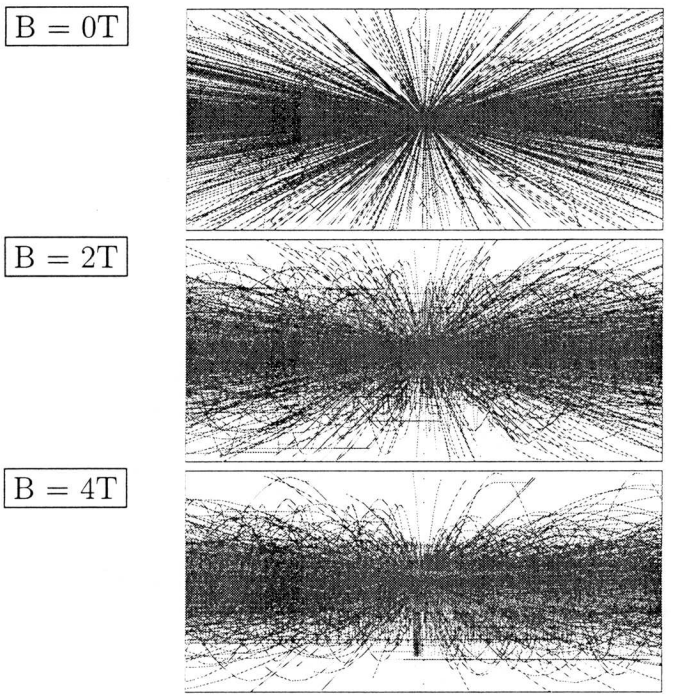

Figure 4.2: Charged tracks of 20 superimposed minimum-bias events in absence of the detector material for the magnetic field strength of 0 T, 2 T and 4 T.

B = 0 T	$\eta = 0$ (r)	7.5 cm	100 cm	130 cm
	No p_T cut	2.23	0.013	0.0078
	$p_T > 1$ GeV	0.21	0.0011	0.0007
	$\eta = 2$ (z)	27 cm	181 cm	290 cm
	No p_T cut	2.62	0.061	0.023
	$p_T > 1$ GeV	0.0036	0.0001	< 0.0001
B = 2 T	$\eta = 0$ (r)	7.5 cm	100 cm	130 cm
	No p_T cut	2.42	0.010	0.0038
	$p_T > 1$ GeV	0.21	0.0011	0.0007
	$\eta = 2$ (z)	27 cm	181 cm	290 cm
	No p_T cut	2.69	0.069	0.027
	$p_T > 1$ GeV	0.0036	0.0001	< 0.0001
B = 4 T	$\eta = 0$ (r)	7.5 cm	100 cm	130 cm
	No p_T cut	3.02	0.0053	0.0013
	$p_T > 1$ GeV	0.21	0.0011	0.0006
	$\eta = 2$ (z)	27 cm	181 cm	290 cm
	No p_T cut	2.98	0.067	0.020
	$p_T > 1$ GeV	0.0035	0.0001	< 0.0001

Table 4.1: Particle multiplicities per 2x2 cm^2 cell of 20 superimposed minimum bias events. The effect of the detector material is not included.

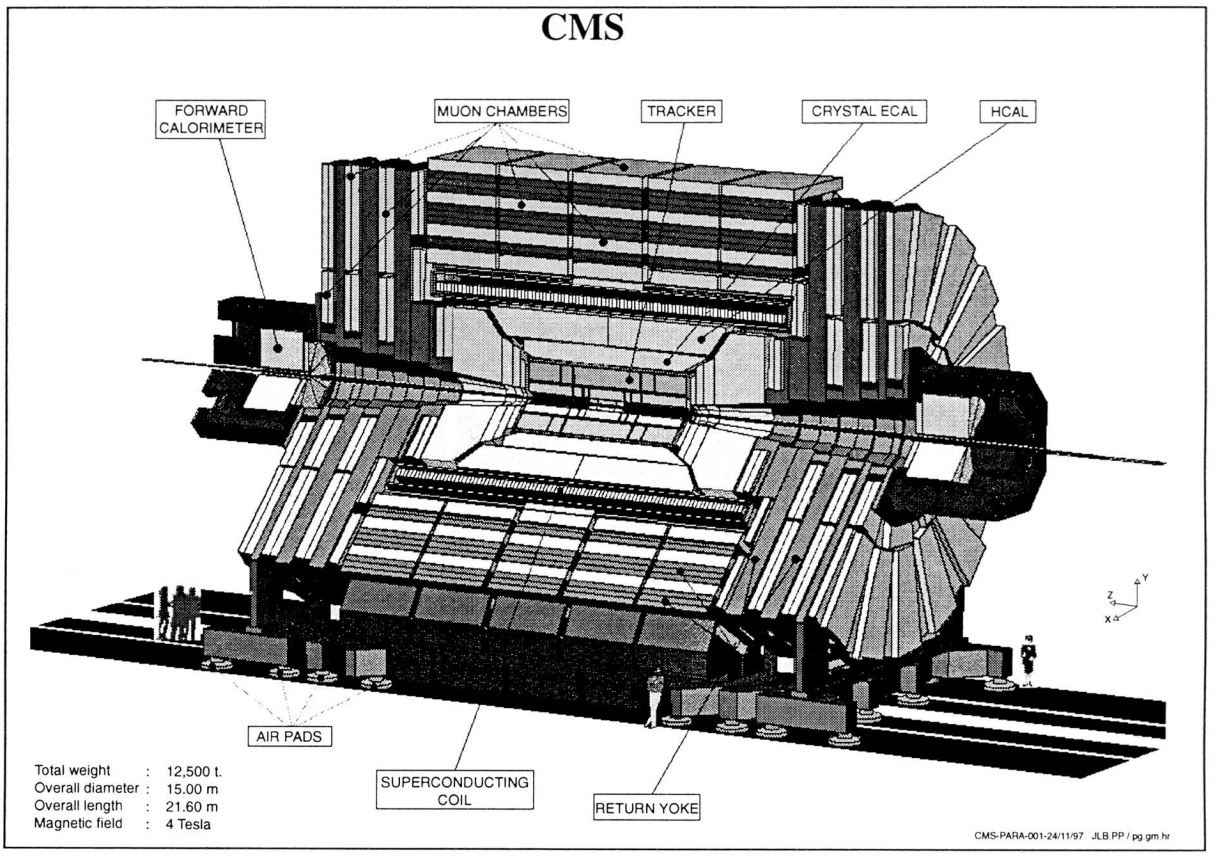

Figure 4.3: Three-dimensional view of the CMS detector.

The preproduction of the detector components will start in 1998 and the assembly in the experimental hall will start in 2003. CMS will be ready for data taking at the LHC start which is foreseen in 2005.

4.2.1 Muon system

Muon detection is of central importance for the Higgs boson searches in the decay channel $H \rightarrow ZZ^{(*)} \rightarrow 4\ell^{\pm}$ where at least two of the leptons are muons. This channel covers most of the Higgs mass range in the Standard Model. Possible extensions of the Standard Model provide signatures like new heavy gauge boson W′ or Z′ decaying in muon and neutrino or two muons respectively. In the supersymmetric scenario, Higgs bosons may decay into muons and the supersymmetric particle themselves decay in cascades including several muons. The decay of supersymmetric Higgs bosons into tau leptons can be explored following the muon from the tau decay.

The tasks of the muon system are identification, triggering and momentum measurement of the muons. The choice of the solenoidal magnet and sufficient amount of material in front of the muon system allows muon identification even at highest luminosities. The muon trigger efficiency does not depend on the hadronic activity. Precise momentum measurement is achieved by several points that define the muon track. In CMS the muon momentum can be defined with independent measurements: with the stand-alone muon system including the vertex point or with the muon system combined with the inner tracker information.

The CMS muon system consists of five wheels surrounding the magnet and two endcaps. The four barrel muon stations and the four endcap muon stations are integrated in the iron return yoke of the magnet. The system will provide coverage over the pseudorapidity range from 0 to 2.4. Different technologies are used in the active devices: in the barrel region, drift tubes are used and the endcaps use cathode strip chambers. These chambers have very good spatial resolution and they will allow the very good momentum measurement which is one of the main design criteria of CMS. In addition, there are resistive plate chambers both in the barrel and in the endcaps. They have an excellent time resolution of 3 ns and will help in the bunch crossing identification and in triggering.

The efficiency for reconstructing a muon track in the stand-alone muon system with at least two track segments is more then 90% below $p_T = 100$ GeV. The momentum resolution of the stand-alone muon system is shown in figure 4.4 and for $|\eta| < 2$, it is 6–20% below $p_T = 100$ GeV and 15–35% at $p_T = 1$ TeV, depending on the angular position as shown in figure 4.4. These resolutions are further improved if the muon chamber measurement is combined with the inner tracker information as shown in figure 4.5 (1-8% for muons below $p_T < 100$ GeV and $|\eta| < 2.4$ and 2-18% at $p_T = 1$ TeV and $|\eta| < 2.4$).

4.2.2 Calorimeters

Hadron calorimeter

The higher end of Higgs mass discovery range will be covered by the signatures including jets and missing energy. In many cases, the Standard Model background can be reduced by

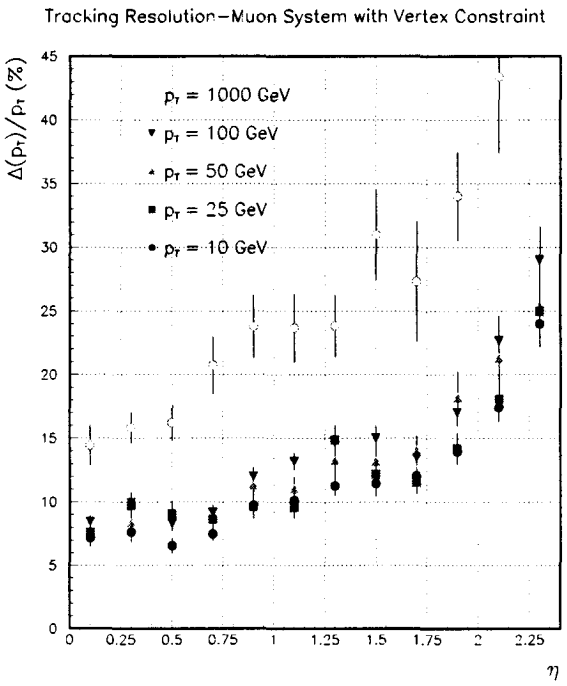

Figure 4.4: Momentum resolution of simulated muon tracks using only hits from the muon system with a vertex constraint.

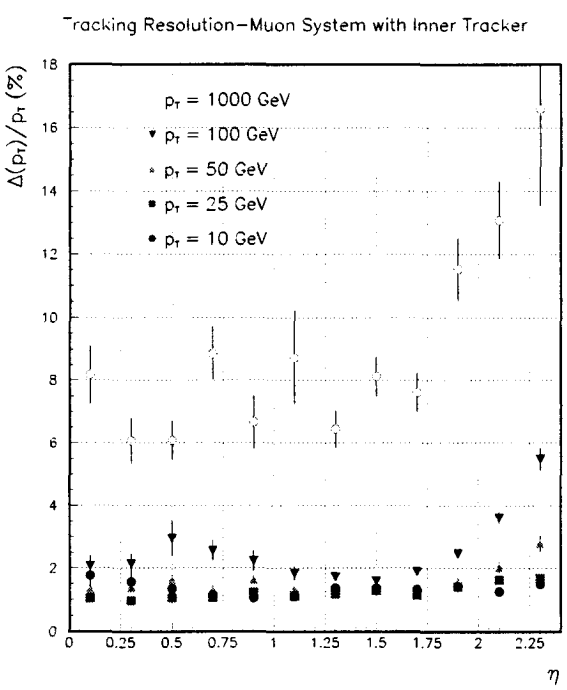

Figure 4.5: Momentum resolution of simulated muon tracks using only hits from the muon system combined with hits from the central tracker.

identifying the forward jets in the signal events. In addition, most of the supersymmetric signatures include missing energy. Thus, a hermetic hadron calorimeter system is required.

The task of the hadron calorimeter is to measure quark and gluon positions and energies by measuring the energies and location of the particle jets. The neutrinos are indirectly identified by the missing energy flow which is reconstructed by measuring all energy deposited in the calorimeter system. These measurements are done with the combined electromagnetic and hadronic calorimeter system. The hadron calorimeter also contributes to the identification of electrons, photons and muons and it provides a trigger signal for jets and missing energy.

The CMS hadron calorimeter is a sampling calorimeter with active plastic scintillator layers and brass absorber layers. It is placed inside the solenoidal magnet, starting from a radius of 1.806 m and ending at 2.95 m in the barrel region ($|\eta| < 1.3$), and starting at $|z|$ of 3.88 m and ending at $|z|$ of 5.77 m in the endcap region. The barrel and endcap sections cover the pseudorapidity range up to 3.0. To ensure an adequate thickness of the calorimeter in front of the muon system there are additional read-out layers embedded in the first muon absorber layer after the magnet system. A separate forward calorimeter extends the pseudorapidity coverage from 3 to 5. It will be placed 6 m downstream from the interaction point and it uses quartz fibres as the active medium in a steel absorber matrix.

Test beam results and simulation studies[37] indicate that the CMS hadron calorimeter will be able to reconstruct single pions with a resolution of $(\sigma/E)^2 = (100\%/\sqrt{E})^2 + (4.3\%)^2$. Simulation studies have been carried out to quantify the jet and missing E_T resolution. For example, a W boson from a 800 GeV Higgs decaying into two jets ($H \rightarrow WW \rightarrow \ell\nu jj$) can be reconstructed with $\sigma = 12$ GeV in the presence of the pile-up events (8 GeV without the pile-up events) as shown in figure 4.6. The same resolution is obtained for a W boson in a top decay ($t \rightarrow Wb \rightarrow jjb$). The missing transverse energy studies show that the real physics missing energy dominates the missing transverse energy measured in the calorimeter system above $\not\!\!E_T > 75$ GeV.

Electromagnetic calorimeter

Electromagnetic calorimeter plays a vital role in most of the Standard Model and supersymmetric Higgs signatures. The detection of Higgs decaying into two photons requires and excellent resolution in order to distinguish the signal from the enormous background. Together with the $H \rightarrow ZZ^{(*)} \rightarrow 4\ell^{\pm}$ channel, these signatures cover almost the entire discovery range. In addition, cascade decays of supersymmetric particles can include several electrons and new heavy gauge bosons can decay in electron states.

It is therefore one of the CMS main design objectives to construct the best possible electromagnetic calorimeter. Excellent energy measurement will be achieved by a homogeneous lead tungstate ($PbWO_4$) crystal calorimeter. The crystals are arranged in the barrel starting at the radius of 129 cm and in the endcaps starting at $|z| = 317$ cm. There is a preshower device in front of the endcaps to provide additional information for separation of neutral pions from photons.

More details on the crystals, the electronics and the structure of the electromagnetic calorimeter are given in section 4.3. The calorimeter performance is described in detail

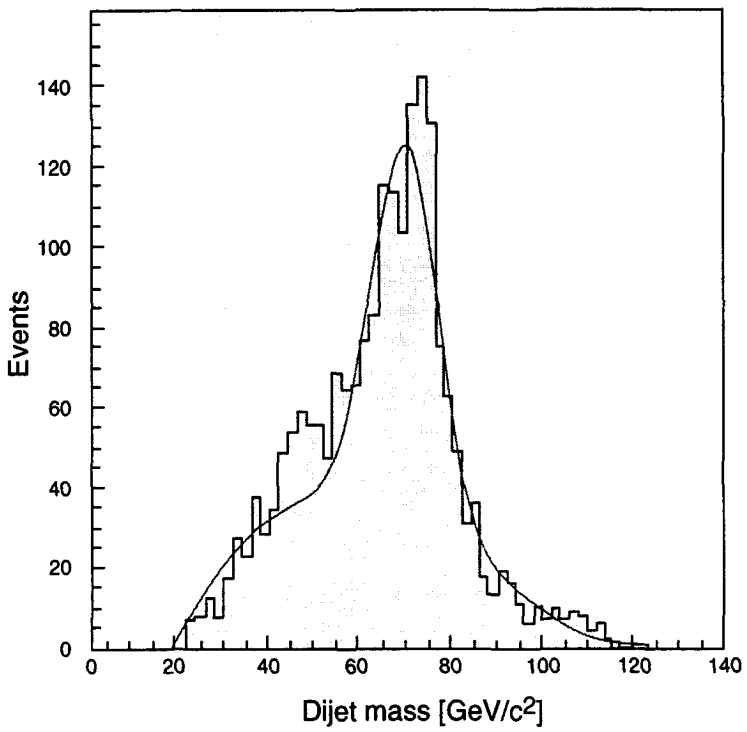

Figure 4.6: Reconstructed jet-jet mass resolution for $t \rightarrow Wb$ with $W \rightarrow jj$ without the minimum bias pile-up.

in chapter 5.

4.2.3 Inner tracking

Inner tracking provides the momentum measurement for all Higgs signals where the decay products are charged leptons. It will be used to establish that the leptons and photons are isolated and thus to suppress the background in most of the Higgs discovery channels. It is used also for the vertex location in the $H \rightarrow \gamma\gamma$ channel.

The task of the inner tracking is to reconstruct high p_T tracks which are isolated or within jets with a good efficiency over the rapidity range of $|\eta| < 2.6$. It will provide a tool for the calibration of the electromagnetic calorimeter and will be used to tag the presence of b-quarks in jets. It will need to cope with an enormous track density and survive in a very hostile radiation environment.

The CMS tracker consists of two layers of silicon pixel detectors surrounded by 5 barrel layers and 10 endcap wheels of silicon microstrip devices which are followed by 6 barrel layers of and 11 endcap wheels of microstrip gas chambers (MSGC). The cell size in the pixel detectors is 150x150 μm^2. The expected hit resolutions are between 10 μm and 20 μm. For the silicon detector, the strip length is 12.5 cm and the pitch ranging from 61 μm to 244 μm depending on the type of the device. The hit resolution varies from 15 μm to 70 μm. In the MSGCs which are in the lower occupancy region of the tracker, the strip length varies from 10 to 25 cm and the pitch between 200 μm and 400 μm. The corresponding hit resolution is between 35 μm and 100 μm.

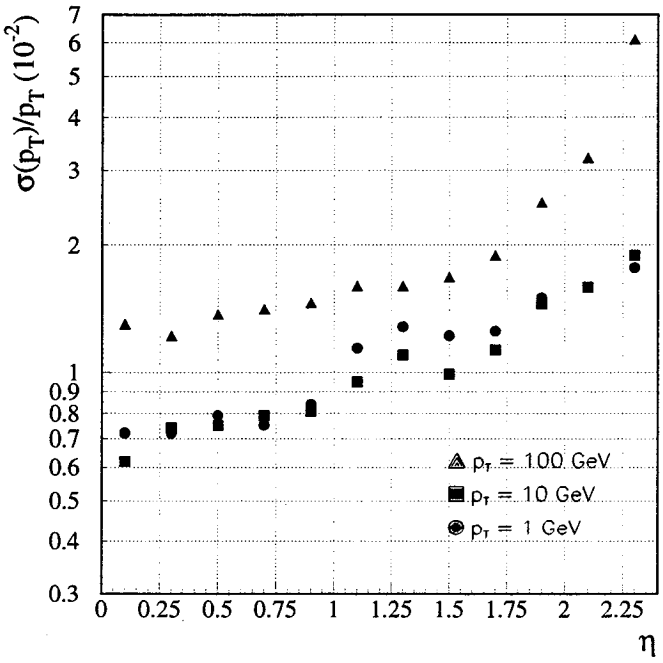

Figure 4.7: Stand-alone transverse momentum resolution in the inner tracking as a function of η, for muons of p_T = 1, 10 and 100 GeV, without beam constraint.

Detailed simulation studies[37] have shown that isolated muon tracks above $p_T = 1$ GeV can be reconstructed with an efficiency better than 98% over the full η range. High energy electrons ($p_T > 10$ GeV) can be reconstructed with an efficiency above 90%. The momentum resolution for muons in the stand-alone tracker system is shown in figure 4.7 The b quark tagging efficiency is the central pseudorapidity region is 50% or better (40% in the forward region), with the mistagging probability of 1–2% as shown in figure 4.8.

4.3 Electromagnetic crystal calorimeter

The task of the electromagnetic calorimeter is to measure the energy and location of the electromagnetic showers and to contribute to the measurement of hadron showers and missing energy in combination with the hadron calorimeter. The calorimeter system should also be capable of distinguishing between showers initiated by neutral pions ($\pi^0 \rightarrow \gamma\gamma$) and photons, or charged pions and electrons.

Energy resolution

The best possible energy resolution can be achieved in a calorimeter of homogeneous material: all energy deposit in the calorimeter material can in principle be detected and there is no contribution from the sampling i.e. the fluctuation in the energy deposit in the active and passive detector material. This has led the CMS collaboration to choose a crystal calorimeter. The resolution of an electromagnetic calorimeter can be parameterised

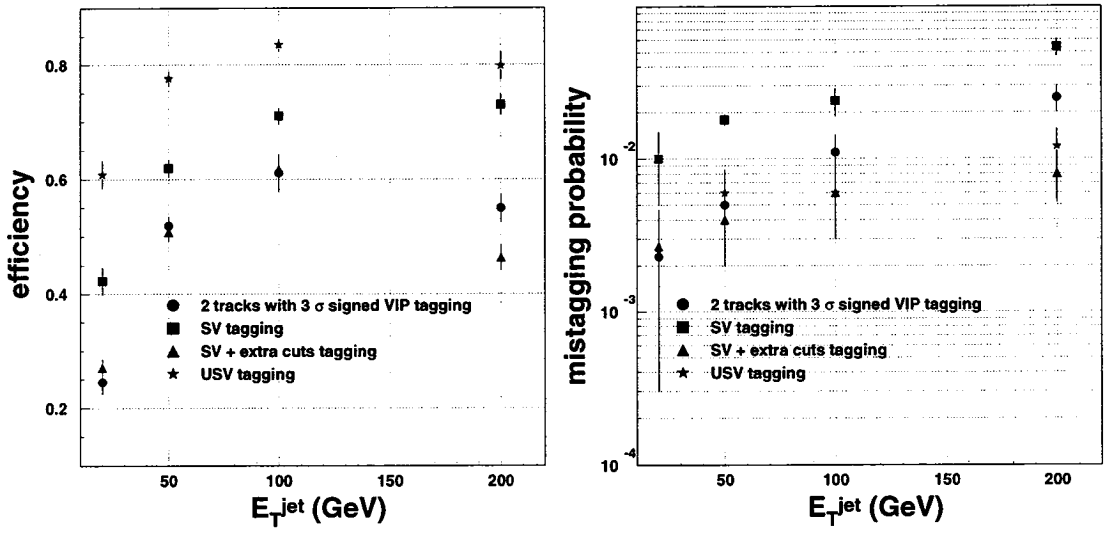

Figure 4.8: b-tagging efficiency and mistagging probability as a function of jet E_T, using four different approaches.

as[38]

$$(\frac{\sigma}{E})^2 = (\frac{a}{\sqrt{E}})^2 + c^2 + (\frac{b}{E})^2$$

where a is the *stochastic term* corresponding to the statistical fluctuations in the number of the primary processes that generate the signal in the measuring volume, b is the *noise term* including the energy equivalent of the electronic noise and the fluctuations in the energy carried to the measuring volume by the particles which are not the ones that are being measured, and c is the *constant term* accounting for the fluctuation in the amount of energy leakage from the active measuring volume, inter-calibration errors and non-uniformity in the generation or collection of the signal. The different contributions to the energy resolution as a function of the measured energy are shown in figure 4.9.

Spatial resolution

The position of the electromagnetic shower in a homogeneous material can be measured with the centre of gravity computed from the energy deposit in the calorimeter cells, or with a preshower detector placed after some absorber material, or with a separate position detector placed between two samplings of the calorimeter. The CMS crystal calorimeter consists of small lateral size crystals (2.2x2.2 cm^2 in barrel) providing high granularity which allows sufficiently precise location of the electromagnetic showers from the shower centre of gravity. To measure the *direction* of a photon, two measurements are needed. It is foreseen to use charged tracks of the same event to identify the event vertex. With the vertex point and the shower location in the electromagnetic calorimeter the direction of the photon can be reconstructed.

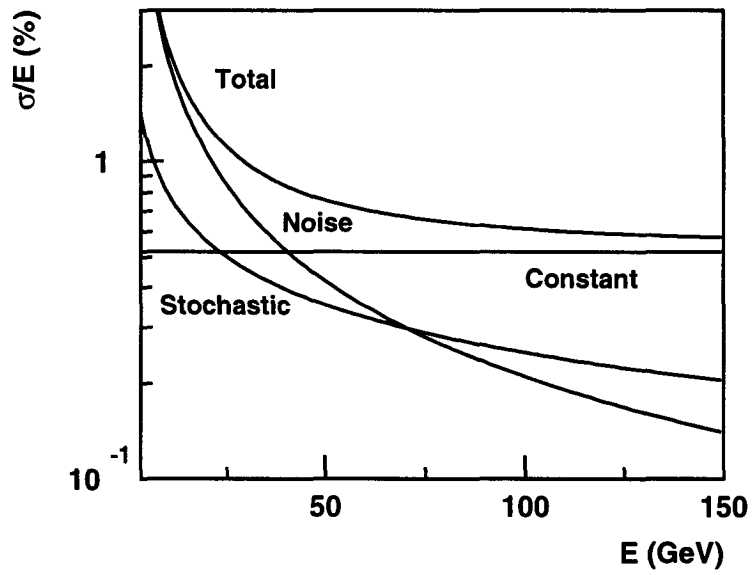

Figure 4.9: Contributions to the energy resolution with the stochastic term a = 2.5%, the constant term c = 0.52%, and the noise term b = 210 MeV.

Lepton-hadron separation

A high energy pion may fake an electron in the electromagnetic calorimeter. However, hadronic showers have larger lateral and longitudinal dimensions than purely electromagnetic showers. The CMS crystal calorimeter profits from the high granularity and a hadron shower can be distinguished from an electron shower by the shower size in the electromagnetic calorimeter or by the energy leakage to the hadron calorimeter. The electron-pion separation is further improved by matching the energy measurement in the calorimeter with the momentum measured in the tracker (E/p matching).

A neutral pion decaying into two photons may fake a single photon in the electromagnetic calorimeter. Again, the high granularity of the crystals allows to distinguish two photon showers from a single photon. The separation between the two decay photons decreases with increasing p_T and the π^0-rejection becomes less effective (see section 5.4.4). The granularity is not high enough in the CMS electromagnetic calorimeter endcaps, and a preshower device with higher granularity will be used.

Timing resolution

The 25 ns bunch crossing interval of the LHC machine requires very fast processing of signals. If several bunch crossings must be integrated, there will be an increase in the pile-up noise from the minimum-bias events with the consequent degradation of the energy resolution. The pile-up also decreases the effectiveness of the isolation criteria. The lead tungstate crystals that will be used in the CMS electromagnetic calorimeter have very short decay time and fast preamplifiers will be used.

		NaI(Tl)	BGO	CSI	BaF_2	CeF_3	$PbWO_4$
Density	(g/cm^3)	3.67	7.13	4.51	4.88	6.16	8.28
Radiation length	(cm)	2.59	1.12	1.85	2.06	1.68	0.89
Interaction length	(cm)	41.4	21.8	37.0	29.9	26.2	22.4
Molière radius	(cm)	4.80	2.33	3.50	3.39	2.63	2.19
Light decay time	(ns)	230	60 300	16	0.9 630	8 25	5 (39%) 15 (60%) 100 (1%)
Maximum of emission	(nm)	410	480	315	210 310	300 340	440
Temperature coefficient	(%/°C)	0	-1.6	-0.6	-2/0	0.14	-2
Relative light output		100	18	20	20/4	8	1.3

Table 4.2: Properties of several crystal scintillators.

4.3.1 Lead tungstate crystals

We have seen that the crystal calorimeter can fulfil the CMS design requirements. The properties that has led to the decision in favour of lead tungstate as the scintillator material are

- short radiation length
- small Molière radius
- fast light decay time
- sufficient radiation tolerance

Table 4.2 compares the properties of several crystal scintillators. The above mentioned features compare very favourably with the other crystal scintillator whereas the relative light output is fairly low. In the following, the properties of the lead tungstate are discussed in more detail.

Dimensional issues

The radiation length (X_0) is the mean distance over which a high-energy electron loses (1-1/e) of its energy by Bremsstrahlung. As the energy loss due to Bremsstrahlung dominates the total energy loss of electrons down to energies of MeV scale one can roughly estimate what is the amount of material needed to contain most of the electromagnetic shower:

$$\begin{aligned} x = 0 \quad & E = E_0 \\ x = 1X_0 \quad & E_1 = E_0(1 - 1/e) \\ x = 2X_0 \quad & E_2 = E_1(1 - 1/e) = E_0(1 - 1/e)^2 \\ & \vdots \\ x = nX_0 \quad & E_n = E_0(1 - 1/e)^n \end{aligned}$$

Approximately n=25 radiation lengths are required to contain longitudinally 99% of the energy of the electromagnetic shower. The short radiation length of $PbWO_4$ allows a compact and cost effective calorimeter with only 23 cm corresponding to 25.8 X_0's.

The interaction length is the length scale appropriate for the hadronic showers. Roughly eight interaction lengths are needed to contain 95% of a hadronic shower up to E $\approx$ 500 GeV and eleven to contain 99% of it[39]. With the crystal length of 23 cm in the barrel and 22 cm in the endcaps, the crystal calorimeter contributes approximately one interaction length to the depth of the combined calorimeter system.

The Molière radius R_M is given by

$$R_M = X_0 E_s / E_c$$

where E_s is the scale energy of 21.2 MeV and E_c the critical energy according to the definition where it is considered to be the energy at which the ionization loss per radiation length is equal to the electron energy. For lead tungstate, this energy is 8.6 MeV. The Molière radius sets the scale to the lateral development of the electromagnetic shower: 90% of the energy is contained in a cylinder with radius R_M and 99% is contained in 3.5 R_M. The small Molière radius of the lead tungstate allows the energy measurement in a small crystal array which minimises the electronics and pile-up noise.

Optical properties

The emission of scintillation light in a crystal is possible due to local electronic energy levels in the normally forbidden region between the valence band and conduction band of the material. The ionisation processes in the electromagnetic shower excites an electron from the valence band to the conduction band. The electron may then fall to the intermediate levels. They can be of three different types[40]:

- luminescence level (the transmission to the ground state is accompanied by photon emission)
- quenching level (the excitation energy is dissipated thermally without radiation)
- traps (the electrons may return to the conduction band by acquiring energy from the lattice vibration or fall to the valence band without radiation).

A simplified energy level schema is shown in figure 4.10. These levels are generated by impurity or defect centres in a crystal lattice and one centre may contain luminescence, quenching and trapping levels. In the $PbWO_4$ crystals, the light emission is limited by the strong thermal quenching. This same mechanism allows the very short decay time.

The emission spectrum of $PbWO_4$ crystals [41] is shown in figure 4.11. It is a composite of the two main emission bands, one in the blue region at 420 nm and the other in the green at 500 nm, resulting to an emission curve peaking at 440 nm. The emission band at 420 nm is attributed to regular WO_4^{2-} centres, i.e. excess ions which occupy interstitial positions in the crystal lattice. The green band is caused by a so called F-centres where a negative ion vacancy is compensated by WO_3 and additional electrons.

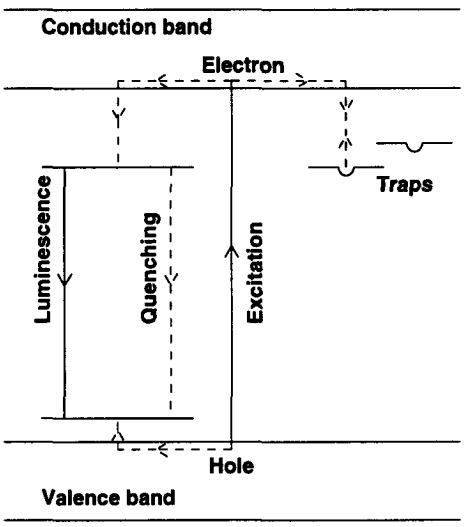

Figure 4.10: Energy bands in a scintillating crystal.

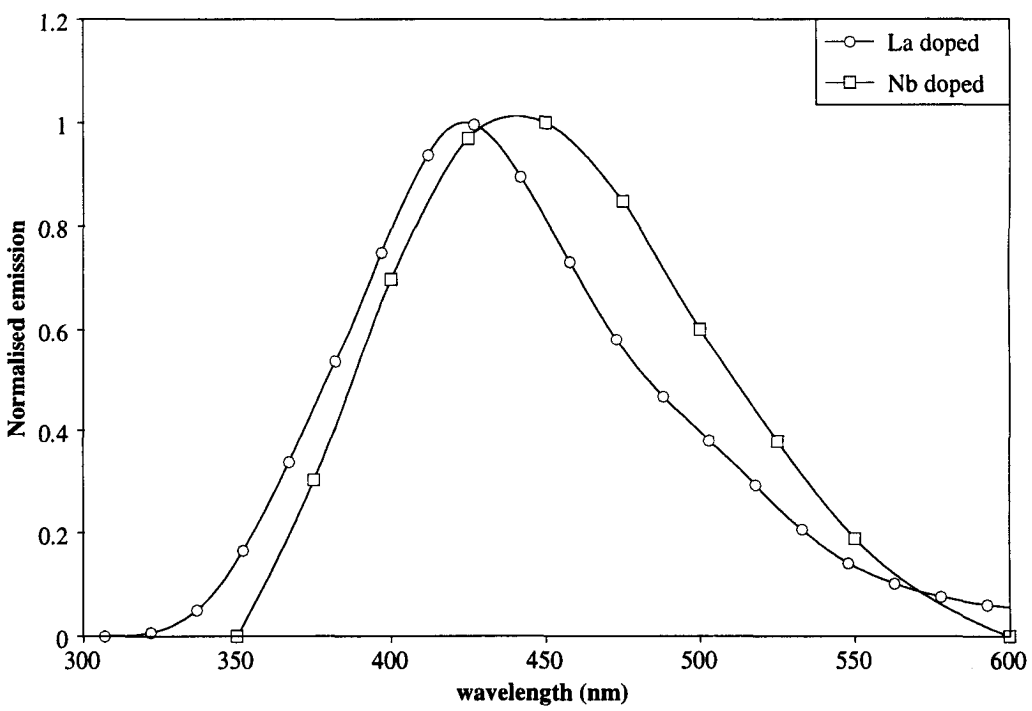

Figure 4.11: Emission spectrum of $PbWO_4$ crystals.

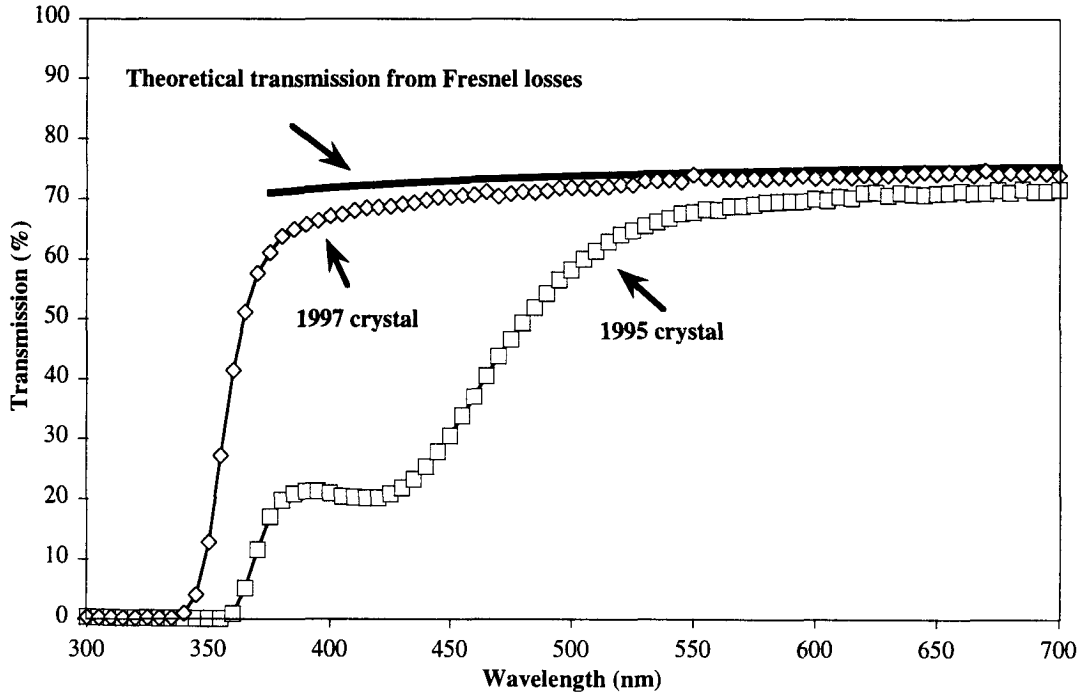

Figure 4.12: Transmission curve of $PbWO_4$ crystals.

The optical transmission capabilities of a crystal may be reduced by macroscopic defects which scatter the light or by impurities which can trap an electron from the conduction band and release it back by reabsorbing the light emitted from the luminescence levels. Thus an absorption band for a certain wavelength is created. This effect can be decreased by doping the crystal, i.e. introducing, during the growth, a small amount of chemical element which can occupy the traps. Figure 4.12 shows the transmission of recent crystals compared to earlier ones with impurities. It can be seen that the transmission for shorter wavelengths is considerably improved by controlling the purity of the crystal and introducing a dopant.

The resulting light yield can be quantified by the number of photoelectrons/MeV observed in a photomultiplier. With the emission spectrum and transmission probability as shown in figures 4.11 and 4.12 the full length $PbWO_4$ crystals yield more than 10 photoelectrons per MeV. This measurement includes the effect of the quantum efficiency of the specific photomultiplier used (XP2262B). In the CMS electromagnetic calorimeter, the crystal will be read out by avalanche photodiodes (APDs) which multiply the primary photoelectrons. The photostatistics contribution to the stochastic term is then

$$a_{pe} = \sqrt{F/N_{pe}}$$

where N_{pe} is the number of primary photoelectrons per GeV released in the photodetector. N_{pe} has been observed to be close to 2000 in beam tests for 5x5 mm^2 APDs[42]. F is the excess noise factor which parameterises the multiplication process in the APD. In the photodiodes used in CMS, its value is close to 2. Two APDs will be used to measure the light and the contribution from the photostatistics with the currently measured light

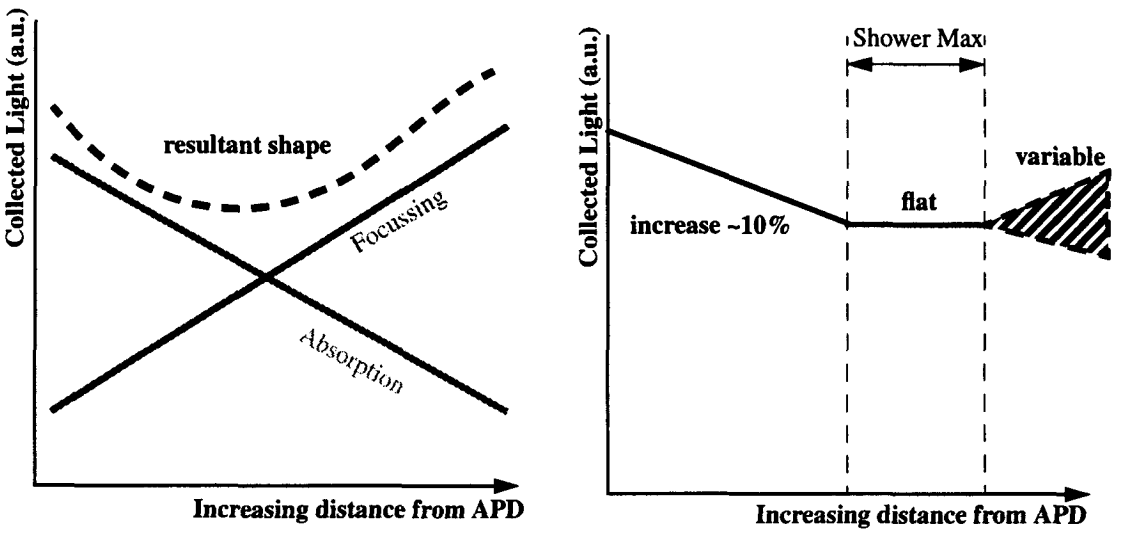

Figure 4.13: Longitudinal light collection curve.

yield will be

$$a_{pe} \approx \sqrt{2.2/4000} = 2.3\%$$

The superposition of the different scintillation mechanisms is apparent in the light decay time of $PbWO_4$. It can be fitted with a sum of three exponentials where the decay times are 5, 15 and 100 ns and their relative fractions 39%, 60% and 1%, respectively. The slow component has been reduced as a result of intensive studies on the effect of the impurities on the decay time [43]. It has been shown that the presence of impurities may cause enhancement of the slow component due to the introduction of impurity centres with traps that may delay the light emission.

Even if the light yield of a crystal is uniform along its longitudinal axis, the longitudinal light collection is not uniform. The probability for light to reach the photodetector is defined by two competing effects. The tapered shape of the crystals focuses the light produced in the front part of the crystal more and it is more likely to reach the photodetector than the light produced in the rear part of the crystal. However, the light coming from the front can be deflected several times and it may be absorbed if the absorption length of the crystal is not long enough. These two effects are illustrated with the longitudinal light collection curve in figure 4.13. The ideal shape of the curve[44] is also shown. The determination of this curve is further discussed in chapter 5. The flat shower maximum region is important in order to keep the constant term of the energy resolution function small. The rise towards the rear of the crystal can compensate for the rear leakage of the showers which start showering late in the crystal. The absorption length of the recently produced crystals is more than one meter and therefore the focusing effect dominates, resulting in a light collection curve that decreases monotonically from the front to the back of the crystal. The ideal shape can be restored by depolishing part of the crystal faces.

Due to the strong thermal quenching, the scintillation mechanism of $PbWO_4$ crystals is temperature dependent. The light yield decreases by $\approx 2\%/C^\circ$ at room temperature.

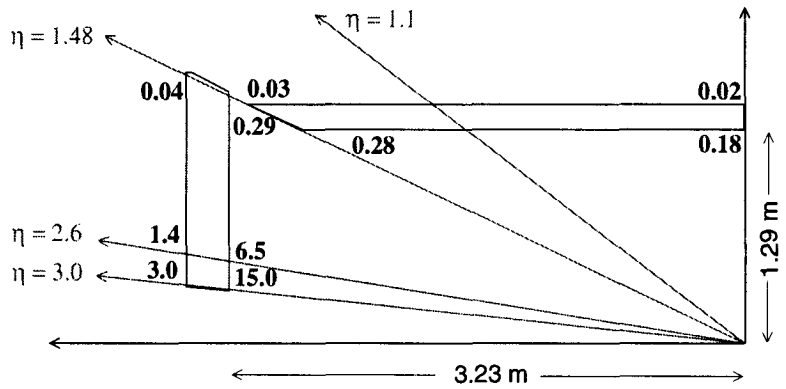

Figure 4.14: Dose rates in Gy/h in different parts of the CMS electromagnetic calorimeter for a luminosity of 10^{34} $cm^{-2}s^{-1}$.

Therefore, the temperature of the crystals must be stabilised very precisely: the operating temperature of the crystal and photodiode entity will be stabilised within 16±0.05° in the final CMS assembly[45].

Radiation tolerance

Ionising radiation has several possible effects on a scintillating crystal. If the luminescence centres are affected, the scintillation mechanism and, in consequence, the light yield is affected. If the radiation generates new colour centres (negative ion vacancies where the missing electric charge is compensated by an electron localised in the vicinity) the absorption length of the crystal may be reduced due to traps that absorb the light emitted from the scintillation process.

The irradiation tests have been performed to reproduce the LHC radiation conditions in the different parts of the electromagnetic calorimeter (see figure 4.14) and to accumulate dose corresponding to the integrated dose of several years of LHC operation (ranging from 10^3 Gy in the barrel to 10^5 Gy in the endcap). It has been concluded from these tests that the structure and the scintillation mechanism of the $PbWO_4$ crystals in unaffected by radiation. This is shown by the fact that the emission spectrum[46] and the resolution[42] of the crystals remain unchanged after irradiation. The irradiation affects the absorption length which is visible from the decrease in the light yield under the irradiation in the beam test with the dose rates corresponding to the LHC conditions. The decrease saturates quickly at a level that depends on irradiation rate. This effect is attributed to the formation of colour centres and their destruction through room temperature annealing[47]. The centres are formed in the existing defects in the crystal lattice and thus the damage can be limited by controlling the growth conditions or by introducing a dopant. The degradation of the light yield under irradiation can currently be limited to few percent from the original level. The change in the light yield will be followed by a light monitoring system as explained in section 4.3.4.

4.3.2 Mechanical structure

An ideal mechanical structure holds detector elements in their place without leaving voids between the active elements. The readout and voltage cables and cooling system should be brought in and out without disturbing the measurement. The structure should allow easy handling of the detector elements before assembly and enable access to the single detector elements in case of failure of a component.

In the CMS electromagnetic calorimeter, the support structure of the crystals will be attached to the surrounding hadron calorimeter and the weight of the detector is transmitted to the hadron calorimeter front face. Therefore, all the heavy support structure and cabling lies behind the crystals and only a light-weight alveolar structure holds the crystals and readout electronics against the stainless steel back plate.

The crystals are arranged in barrel and endcaps. A three-dimensional view of the calorimeter is shown in figure 4.15. The barrel consists of 2×18 supermodules each of which contains 20 crystals in ϕ and 84 crystals in η. In both detector halves in η, the supermodules are divided in 4 support structures called baskets. The baskets require no cabling and can be assembled in regional centres and then transported to CERN. The supermodule with its cabling is assembled at CERN where it will be calibrated and installed.

There are 17 different crystal types in the barrel: each crystal has a length of 230 mm (25.8 X_0) and a front face area close to 22×22 mm^2, exact dimensions depending on crystal type, giving a granularity of $\Delta\eta \times \Delta\phi = 0.0175 \times 0.0175$. The crystals are tapered and they axes have a constant off-pointing angle of 3° with respect to the nominal vertex position in both η and ϕ to avoid gaps that are pointing to the interaction region. The barrel coverage extends over the pseudorapidity range $|\eta| < 1.48$.

The endcap is arranged in two halves ("Dees") which contain supercrystals of 5×5 individual crystals arranged in array in (x-y) direction as shown in figure 4.16. Each Dee contains 134 identical supercrystals and 32 incomplete supercrystals to complete the inner and outer perimeter. The endcap crystals are supported by a back plate which also provides a shield to the electronics equipment which is located behind the back plate. The endcaps are bolted to the hadron calorimeter endcap front face.

All the endcap crystals have the same dimensions of 28.6×28.6 mm^2 front face, 30.0×30.0 mm^2 rear face and the length of 220 mm. The gaps pointing to the interaction region are avoided by an off-point as in the case of the barrel crystals. The endcaps cover the pseudorapidity range of $1.48 < |\eta| < 3.0$.

The preshower detector is present in front of the endcaps. It consists of two layers of 2 X_0 and 1 X_0 thickness including lead absorber, active layers of silicon strips with a pitch of 1.9 mm, electronics and cooling. The preshower covers the pseudorapidity range of $1.65 < |\eta| < 2.61$. It is supported by a flange of aluminium at $\eta = 3$ attached to the hadron calorimeter endcap.

4.3.3 Electronics chain

The electronics readout chain transmits the detector signal to the counting room. It provides the digital sums to the trigger system each bunch crossing. The readout chain

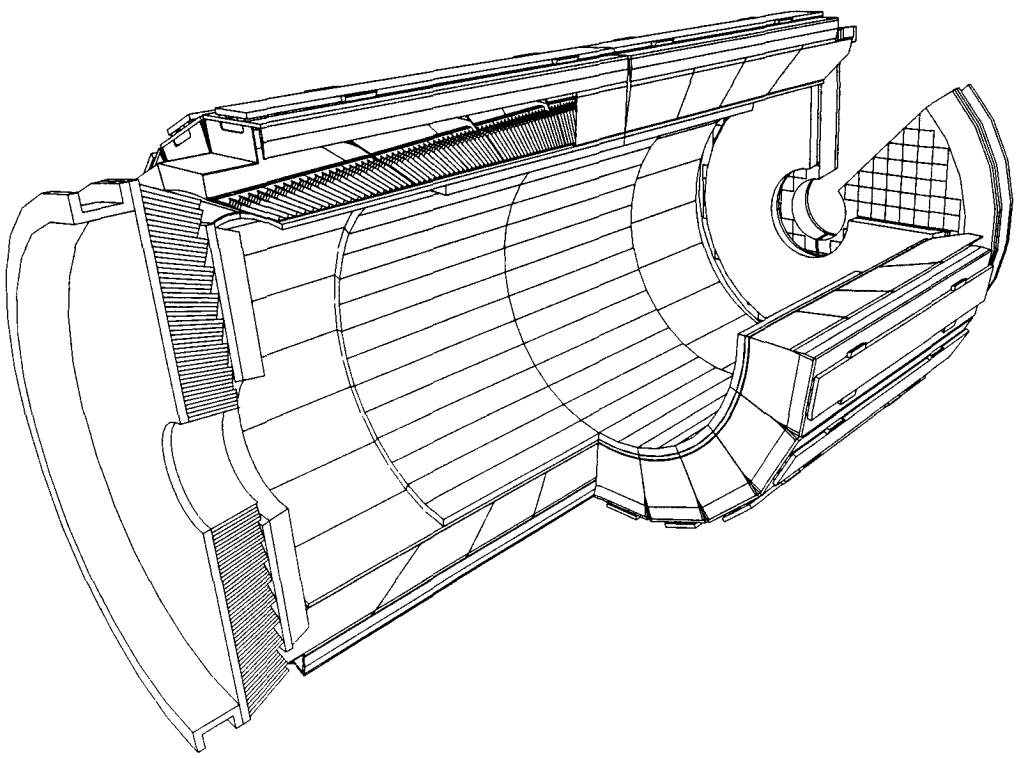

Figure 4.15: Three-dimensional view of the CMS electromagnetic calorimeter.

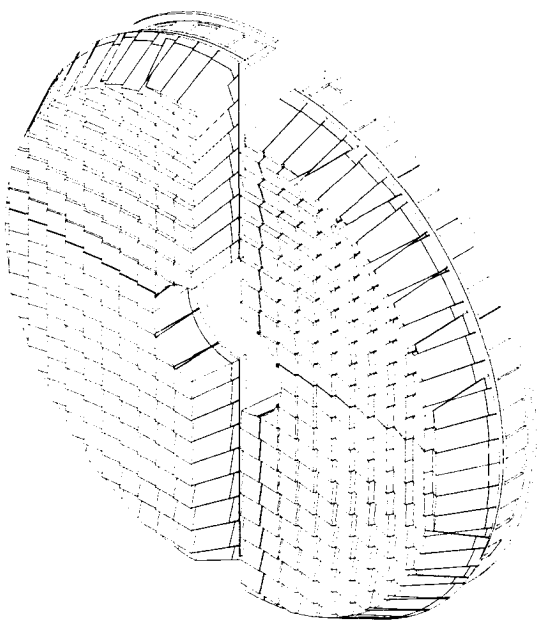

Figure 4.16: The CMS electromagnetic calorimeter endcap.

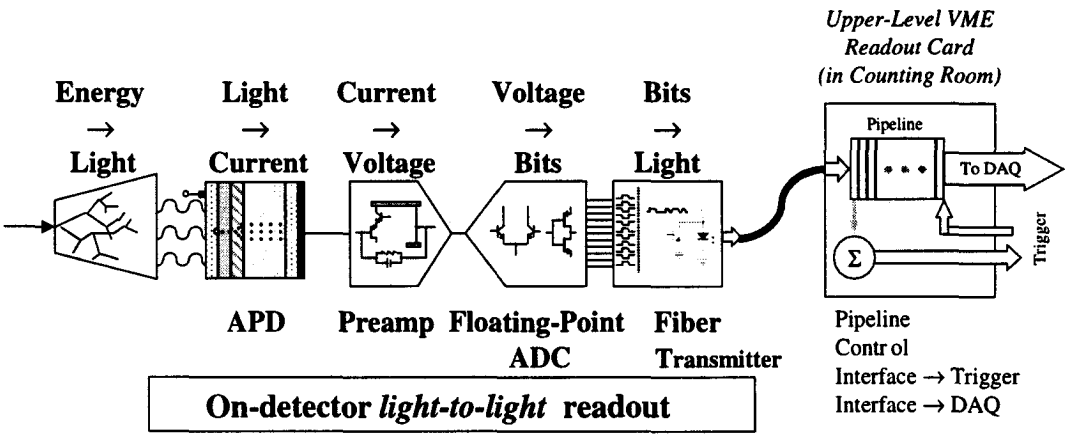

Figure 4.17: Readout chain of the CMS electromagnetic calorimeter.

should

- have a dynamic range up to energies of order 2 TeV
- have a low noise contribution
- have radiation hard components inside the detector volume
- be capable of sampling the signal with the 40 MHz frequency of the LHC bunch crossing.

The readout chain is shown schematically in figure 4.17. The light produced in the crystals is detected in the photodetector which converts the light into a current. Due to the low light yield of the crystal the current is relatively small and a preamplifier is needed to amplify the signal before converting it into a voltage. The voltage is then converted into a digital form by an analog-to-digital converter. This signal is transmitted to the counting room via optical fibres where the upper-level digital readout forms the energy sums for the trigger, stores the data during the trigger latency and transmits the accepted data to the data acquisition system. This approach allows easy access to the readout elements and does not require the upper level electronics components to be radiation hard as it would be the case were the digital readout electronics inside the detector volume.

Photodetectors

The experimental environment behind the crystals reduces the choice of the photodetectors. An avalanche photodiode (APD) is a device which

- amplifies the low light signal of the crystals
- has a fast response
- is radiation tolerant
- works in a magnetic field.

It is a solid state device which consists of a p^{++} layer, followed by a p^{+}-n^{+} junction with a field, drift area and a n^{++} layer (+ or ++ denote the amount of doping resulting in very high or even higher conductivity). The primary photon generates a photoelectron which is then accelerated in a electric field where it generates an avalanche of electrons as illustrated in figure 4.18. A gain of 50 can be reached with a bias voltage below 500

V. The quantum efficiency of such devices in the peak region of the $PbWO_4$ scintillating light is 80%. The area of currently available APDs is 25 mm^2 which is small compared to the crystal rear face of 625 mm^2. Therefore, it is foreseen to use two APDs per crystal.

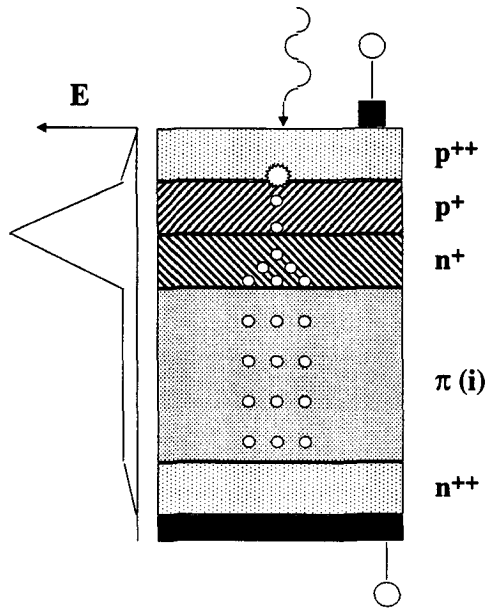

Figure 4.18: Avalanche photodiode.

The stability of APDs depends on the stability of the gain which is affected by the voltage and the temperature. The R&D goal is to optimise the parameters so that the variation due to the voltage at the gain of 50 is less than 2%/V. The temperature dependence is due to the free mean path of the electrons in the material. Currently, the coefficient is found to be -2.3%/°C. It is therefore important to arrange a cooling system which is able to dissipate the electronics heat and keep the temperature of the APDs and the crystals constant.

The characteristics of the APD have a number of effects on the performance of the calorimeter. First, the multiplication of the light signal is a non-Poissonian process, thus affecting the photostatistics contribution to the stochastic term. This effect can be quantified by the excess noise factor $F = \sqrt{1 + (\sigma_M/M)^2}$ where σ_M is the variation in gain for a photoelectron at a gain M. The photostatistic term is then modified by this factor ($a_{pe} = \sqrt{F/N_{pe}}$) as discussed in section 4.3.1. Second, the preamplifier noise has a component which is proportional to the capacitance of the APD. Third, there may be leakage current flowing on the surface of the device (I_s) or flowing through the device ("bulk current" I_b). In the first case, the current does not undergo multiplication while in the second case it does. These currents enter in the noise term proportional to $\sqrt{I_s}/M$ and $\sqrt{FM^2I_b}/M$.

Radiation may cause damage which increases the leakage currents. The main damage comes from the neutron irradiation which creates defects in the silicon lattice. The current arises due to the new energy levels between the conduction and valence band of the semiconductor and it increases linearly with the concentration of the defects. After irradiation, the semiconductor recovers from the radiation damage and the leakage cur-

rent decreases. The estimated noise as a function of the LHC operation time is shown in figure 4.19. The upper curve shows the noise evolution were there no recovery present.

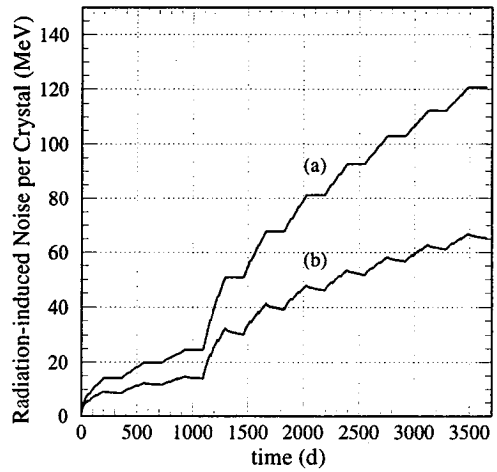

Figure 4.19: The noise per crystal from the leakage current induced by radiation (a) with no recovery, and (b) with a realistic recovery parameters.

The lower curve includes realistic parameters for the radiation damage recovery.

In the endcap, the radiation levels behind the crystals are two orders of magnitude higher than in the barrel, and APDs are not sufficiently radiation hard for this environment. A vacuum phototriode (VPT) is a device is capable of working in an axial or quasi-axial magnetic field. It has a a radiation hard glass face plate. A typical VPT is illustrated in figure 4.20. Photoelectrons are generated on the photocathode and part of them passes through the anode mesh and impacts on the dynode where the secondary electron cascade arises. The secondary electrons are attracted back to the anode mesh which captures a large fraction of them. The quantum efficiency of these devices for the peak wavelength is 15% and their sensitive area of roughly 300 mm^2. The total efficiency is thus of the same order as in the APDs. The gain of the VPTs in a 4 T magnetic field is of order of 7 compared to 50 of APDs.

The temperature stability of VPTs is $\leq 0.2\%/°C$ and they are very insensitive to the bias voltage variation ($< 0.1\%/V$). VPTs have a low capacitance and there are no effects such as the leakage current of solid state devices. The excess noise factor of the currently available VPTs is 1.5–2.0.

Preamplifier and ADC converter

The photocurrent is amplified with different gains resulting in a $\times 1$, $\times 4$, $\times 8$ or $\times 32$ amplification. Thus, saturation can be avoided by choosing the largest signal below a certain threshold, i.e. if the $\times 32$ amplification rises the pulse above the highest possible value of the readout, $\times 8$ amplification for that part of the pulse is used instead. The pulse is then stored in a digitised word with the gain values.

The noise in the preamplifier is defined by the *equivalent noise charge* ENC by $\sigma/E = ENC/(qN_{pe}M)$ where q is the electric charge, N_{pe} the number of the photoelectrons

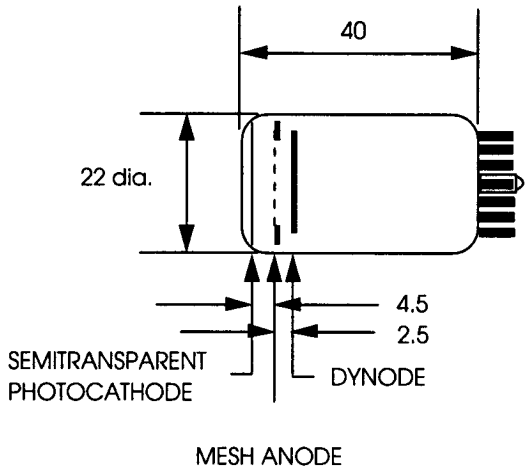

Figure 4.20: Vacuum phototriode.

generated in APD and M the APD gain. ENC depends mainly on the capacitance seen by the preamplifier input, the noise current, the shaping time and the gain of the preamplifier. As the full-scale energy is adjusted as a function of η in the detector (2 TeV at $\eta = 0$, rising up to 4.5 TeV at $\eta = 1.5$ and staying constant 4.5 TeV at higher values) the noise is given in E_T for the barrel and in E in the endcaps. It results to $E_T = 30$ MeV/crystal in the barrel and $E = 150$ MeV/crystal in the endcaps.

Upper level readout

The signal is transmitted to the counting room through a high speed (800 Mb/s) interface of optical fibres. There is one transmission channel per crystal which permits some flexibility in design of the upper level readout and makes the system less vulnerable to a component failure. The upper level readout does not need to be radiation hard.

The upper level readout interprets the signal stored in a form of a digitised word and subtracts the pedestal, pipelines the data while waiting for the trigger decision, forms the sums of the trigger towers and extracts the trigger signal. It provides the data for the data acquisition system in case of a positive trigger decision.

4.3.4 Calibration and monitoring

Due to the excellent intrinsic resolution of the $PbWO_4$ crystal the resolution of the energy measurement at high energies is dominated by the effects that contribute to the constant term (see figure 4.9). The main contribution to the constant term is the calibration error.

The calibration of the CMS electromagnetic calorimeter will be done in two phases:

1. precalibration of supermodules in the test beam

2. in situ calibration with $Z \rightarrow e^+e^-$ events and other electron sources using E/p matching with the tracker measurement.

The test beam calibration will provide an initial set of calibration constants. The in situ intercalibration starts with these predefined calibration constant and can reach a precision of 0.3%.

In addition, the possible short-term variations due to the radiation are monitored by laser light pulses which are transmitted to each crystal by optical fibres. The fibres are embedded in the moderator plate in front of the crystals.

Chapter 5

Photon and electron identification and measurement

Detailed detector simulations have been carried out to study the performance of the electromagnetic calorimeter and to optimise its design. This chapter will concentrate on the results of these studies. Test beam data have been analysed and compared to the corresponding simulation to verify that the detailed behaviour of crystal matrices is fully understood. The results are shown for the light yield non-uniformity, the energy resolution of the crystals and the lateral size of the electromagnetic showers. The emphasis is then put on the simulation of the photon measurement. Some of the results are presented in terms of the reconstructed Higgs mass for a 100 GeV Higgs decaying into two photons. This important channel has been used as a benchmark in the CMS electromagnetic calorimeter performance studies as it covers the Higgs mass range where the Higgs boson can be detected only with an excellent electromagnetic calorimeter.

5.1 Simulation tools

The CMSIM[48] package is a GEANT[49] based detector simulation tool. It includes a detailed description of all of the CMS subdetectors including the cables and the mechanical support structures. It propagates the input particles in the detector material, simulates their interactions and secondary particles and produces the output signal in the form of data banks. It provides also some reconstruction tools, for example track finding and electromagnetic clustering.

The electromagnetic calorimeter structure in the simulation program is identical to the one described in chapter 4. A cross-section of the geometry used in the simulation is shown in figure 5.1. The main parameters of the structure are summarised in table 5.1

As will be discussed in the following sections, the presence of material in front of the crystals affects the energy measurement of the electromagnetic clusters. Therefore, an accurate description of the tracker material is required. The tracker description used in these simulation studies is the Version 4 described in CMS Tracker TDR [37]. The CMSIM geometry includes all the material: the active layers, support structures, cooling systems and cabling. Figure 5.2 shows the conversion points in the tracker material for

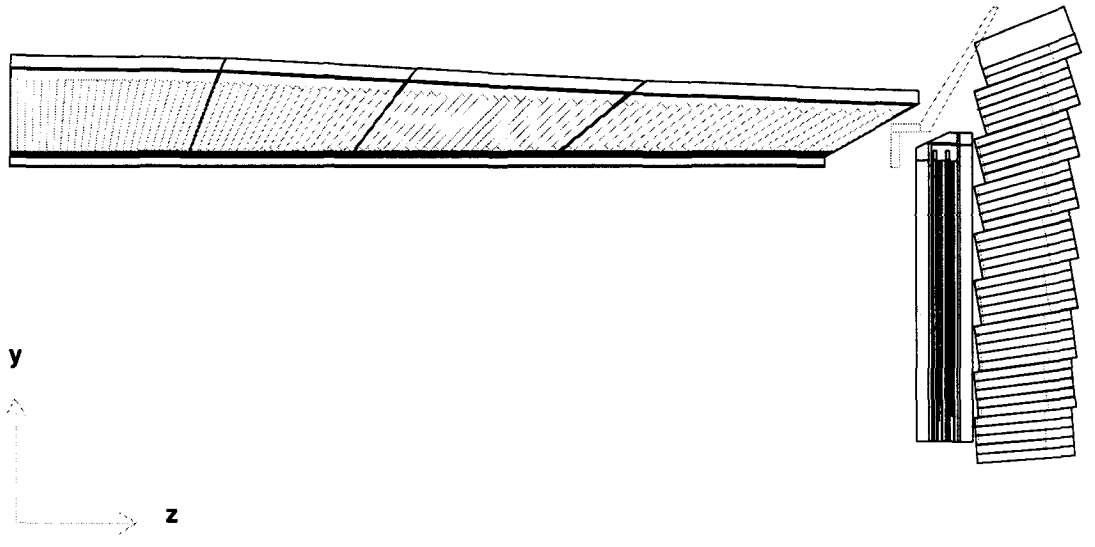

Figure 5.1: Cross-section of the electromagnetic calorimeter description in CMSIM.

		Barrel	Endcaps
η-coverage		0.0 – 1.48	1.48 – 3.0
Granularity	$(\Delta\eta \times \Delta\phi)$	0.0175×0.0175	0.0175×0.0175 – 0.05×0.05
Crystal front face	(mm^2)	22×22	28.6×28.6
Crystal length	(mm)	230	220
	(X_0)	25.8	24.7 (27.7 with preshower)
Modularity		Baskets 18 in ϕ 2×4 in η	Supercrystals containing 5×5 crystals
Distance from crystal-to-crystal	(mm)	0.5	0.5 at the front opening towards the back
Distance from crystal-to-crystal over a module crack	(mm)	6.0	1.5 at the front opening towards the back
Number of crystals		61200	16000

Table 5.1: Main parameters of the electromagnetic calorimeter structure.

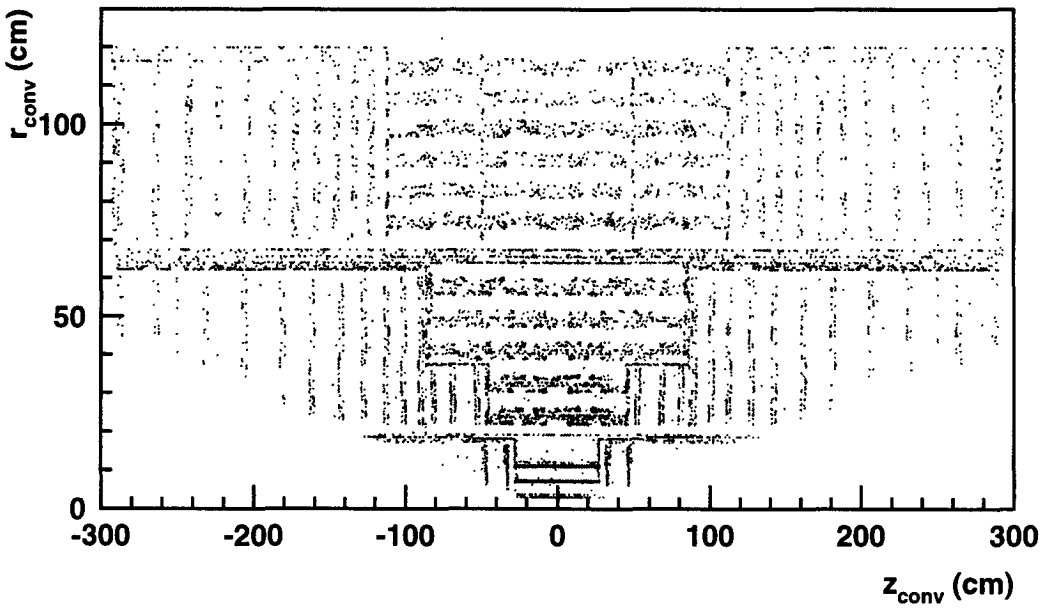

Figure 5.2: Photon conversion points in the tracker material.

photons from $H \rightarrow \gamma\gamma$ decays. The beam pipe and the two pixel layers are clearly visible, followed by the silicon system and the MSGC layers.

5.2 Contributions to the energy resolution

In the shower simulation the output is the local energy deposit in the material. Thus the resolution obtained by the simulation includes the spatial fluctuations in the energy deposit and the geometrical effects, which contribute 1.0% to the stochastic term and 0.16% to the constant term when the energy is measured in a 5x5 array of crystals. The shower simulation results do not contain any contribution from whatever happens to the energy after the deposit, and therefore the particular properties of signal propagation in the crystal material and in the electronics chain are added to the simulation output.

In crystals, the local energy deposit produces scintillation light which propagates in the crystal and part of it arrives to the photodetector. In the photodetector the photons generate photoelectrons which are then amplified and generate the signal. This photostatistic chain and its effect on the original energy deposit is considered by adding 2.3% to the stochastic term.

The preshower device in front of the endcap crystals adds an additional sampling contribution of 5% to the stochastic term. It is caused by the fluctuations in the energy deposit in the preshower material and is fully reproduced in the shower simulation.

The calibration errors and non-uniformity in the light collection in the shower maximum region contribute to the constant term. The non-uniformity contribution has been studied to be less than 0.3% if the non-uniformity slope in the shower maximum region is required to be less than $0.35\%/X_0$[44]. This will be a requirement for the acceptable

	Barrel	Endcap
Stochastic term		
Shower containment	1.0%	1.0%
Photostatistics	2.3%	2.3%
Sampling	–	5%
Total	2.5%	5.6%
Constant term		
Shower containment	0.16%	0.16%
Non-uniformity	0.3%	0.3%
Calibration errors	0.4%	0.4%
Total	0.52%	0.52%
Noise		
Preamplifier noise	150 MeV	750 MeV
Leakage current (low $\mathcal{L}$)	30 MeV	–
Pile-up noise (low $\mathcal{L}$)	30 MeV	175 MeV
Total (low $\mathcal{L}$)	155 MeV	770 MeV
Leakage current (high $\mathcal{L}$)	110 MeV	–
Pile-up noise (high $\mathcal{L}$)	95 MeV	525 MeV
Total (high $\mathcal{L}$)	210 MeV	915 MeV

Table 5.2: The contributions to the energy resolution in a 5x5 crystal array[37].

crystals in the production. The calibration errors are estimated to be 0.4%.

The noise in the energy measurement comes from the preamplifier and from the pile-up energy deposit as discussed in section 4.3.3. The preamplifier noise is estimated to be $E_T = 30$ MeV per channel in the barrel and $E = 150$ MeV in the endcaps. In the barrel, the neutron irradiation on APDs can induce a leakage current. This current contributes to the preamplifier noise and it is shown in figure 4.19 in chapter 4. This contribution can be estimated to be 6 MeV/channel averaged over the initial three-year low luminosity period and 22 MeV/channel during the first year of the high luminosity operation. The pile-up noise is added to the clusters by sampling from histograms giving the pile-up noise in different size crystal clusters as a function of η. These histograms have been generated by PYTHIA[50] with default settings for minimum bias events[51]. The contributions to the energy resolutions are summarised in table 5.2.

In addition, the light collection in the crystal is not uniform along its length as discussed in chapter 4. In the simulation, an ideal light collection curve is applied: the response is flat in the shower maximum region and rises up to 10% towards the end of the crystal. The rise towards the end of the crystal compensates a part of the rear leakage of the showers which start late in the crystal.

5.3 Comparison of the simulation with the test beam

As the optimisation of the electromagnetic calorimeter relies partly on the simulation it is important to verify that the test beam data is fully understood with simulation studies. The data used in this comparison was taken in in H4 test beam in 7x7 crystal matrix. The test beam apparatus in described in appendix A.

The simulation program used in these studies (H4sim96) describes the 1996 beam test setup. All details are given in reference [52].

5.3.1 Non-uniformity studies

An important contribution to the constant term c is the longitudinal non-uniformity of the light collection[42]. As the energy resolution at high energies is dominated by the constant term, it is mandatory to understand and control the factors that affect its size. In the following, the simulation studies on the effects of the non-uniformity are summarised. This section relies on the work done in the references [44] and [53].

Laboratory measurements

The light collection uniformity has been studied with sources in regional centres and at CERN, and using proton beam at the Paul Scherrer Institute (PSI) in Villigen. At PSI, low momentum protons were scanned along the longitudinal axis of the crystal and the response was measured by a photomultiplier on the rear face of the crystal. The measurements have been repeated using APDs to better correspond to the beam conditions. CERN measurements were done using a radioactive source and a photomultiplier readout. The light collection uniformity curves from these measurements have been used as an input to the simulation.

Simulation studies

In the simulation program H4sim96, each crystal is divided longitudinally in 100 volumes. Energy deposit in each of these volumes is recorded and can be weighted afterwards with different light collection curves. Showers were generated with 50 GeV and 120 GeV electrons incident uniformly over a 4x4 mm^2 area in the centre of the central crystal.

First, the energy resolution of a crystal with a uniform longitudinal light collection was simulated. Then, the simulated energy deposit in 100 longitudinal slices was weighted with a measured non-uniformity curve. Thus, the contribution to the resolution due to the non-uniformity could be estimated subtracting quadratically the resolution of the uniform case from that of the non-uniform case.

The ideal light collection curve has been defined by varying the gradients of the uniformity curve in the rear, central and front parts of the crystal by varying the weight of the energy deposit on the longitudinal divisions, and finding the values which minimise the additional contribution to the resolution. The ideal shape was found to have a flat shower maximum region (5 – 10 X_0 from the crystal front), and 10% rise towards the rear of the crystal as was shown in figure 4.13. Varying the gradient of the slope in the front part of the crystal has little effect on the response.

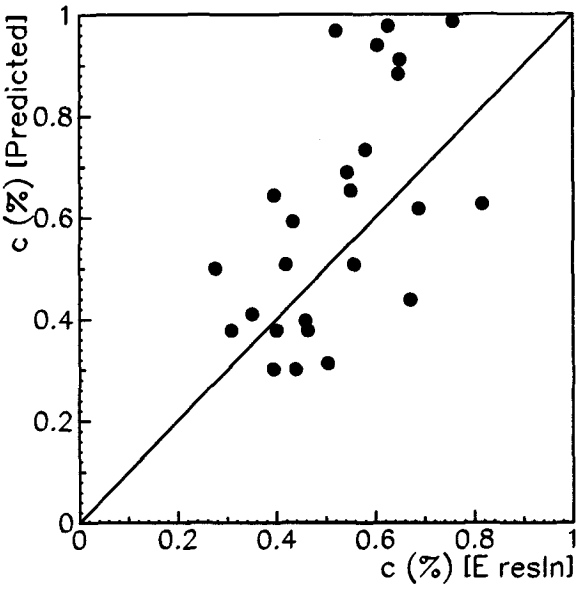

Figure 5.3: The constant term predicted from the simulation versus the constant term from a fit to the test beam data for crystals with a different light collection non-uniformity curve[42].

Comparison with the test beam data

The measured non-uniformity curves of the crystals were used in the simulation and the resolution was extracted. The figure 5.3 shows the so predicted constant term versus the constant term fitted in the test beam analysis[42]. It can be seen that there is a correlation between the two estimates.

Conclusions on the non-uniformity

The longitudinal non-uniformity of the light collection can be the dominant contribution to the constant term of the energy resolution. An ideal light collection curve (figure 4.13 has been defined by the simulation and it has been shown that the crystals with such a curve give a good energy resolution due to their small constant term. This curve has been achieved consistently with recent crystals which show an average constant term of 0.35% including all other effects which may affect the constant term in the test beam environment[54].

5.3.2 Resolution

The Higgs discovery potential in the $H \rightarrow \gamma\gamma$ channel depends crucially on the resolution of the electromagnetic calorimeter. The reliability of the significance estimates of this channel depend how closely the simulation studies can reproduce the energy resolution of the crystals. It is therefore important to verify that all possible contributions to the energy resolution are included in the simulation. This has been done by comparing the

resolution obtained from the test beam data and from the corresponding simulation setup. In the following, the data analysis used to define the resolution from the beam test data is described. Then, the results are compared with those from the simulation.

Test beam data and analysis

This analysis uses the data taken in H4 test beam in September, 1996. The runs foreseen for the energy resolution studies were preceded by calibration runs with 50 GeV electrons. All crystals were scanned with the beam, and the calibration constants were extracted from the pulse height of the signal. For the resolution studies, the crystals were then scanned with 15, 35, 50, 80, 120, and 150 GeV electrons. The data are calibrated with the calibration constants and the pedestal noise is subtracted from the data.

The resolution for each energy is defined from a Gaussian fit to the energy measurement in 3x3 crystal array. The fit is limited to $\pm 1.5\sigma$ from the mean value. The beam is required to be in the centre of the crystal by choosing the events with the beam chamber coordinates corresponding to the central 4x4 mm^2 of the crystal front face. As the crystals are tilted by 3 degrees in the two coordinate directions, a nominal centre is found corresponding to the maximum response to the beam. It is defined from a fit to the pulse height as a function of the beam chamber coordinates. The energy resolution as a function of energy is obtained by fitting the squared values of the measured resolution, stochastic and constant terms by straight line

$$(\sigma/E)^2 = a^2(1/E) + c^2$$

The measured noise term $(b/E)^2$ was subtracted from the resolution before fitting. As the crystals were monitored by a LED system, the photostatistic contribution to the stochastic term a can be estimated from the LED signal with

$$a_{led} = \sqrt{\frac{\sigma_{led}^2 - \sigma_{noise}^2}{\mu_{led}}}$$

where σ_{led} and μ_{led} are the Gaussian width and mean of the LED signal and σ_{noise} is the width of the noise. The stochastic term then becomes $a^2 = a_{led}^2 + a_{cont}^2$ where a_{cont}^2 comes mainly from the shower containment in the 3x3 crystal array.

Beam test results

The energy resolution is shown here for two central crystals 1315 and 1350, both read out with EG&G APDs with an excess noise factor F of 2.2. The light yield of these crystals as measured with a photomultiplier is 14.8 and 12.6 pe/MeV, respectively. The uniformity measurement for these crystals is shown in figure 5.4.

Figure 5.5 shows the resolution curves as a function of E for crystals 1315 and 1350. There is a large difference in the constant terms (0.37% and 0.50%) which is mainly due to the different longitudinal non-uniformity as will be discussed below.

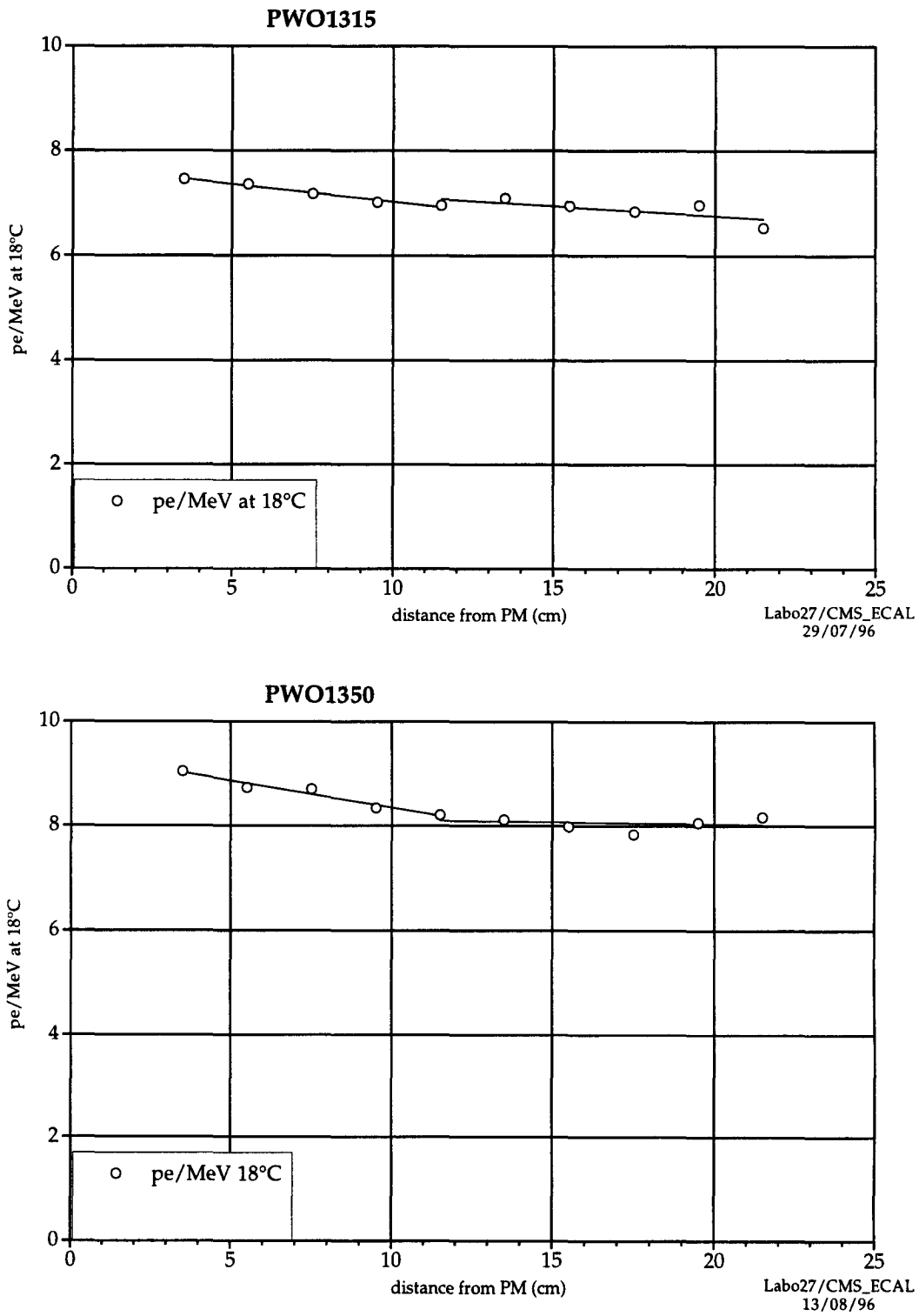

Figure 5.4: The longitudinal light collection curve for the crystals 1315 and 1350.

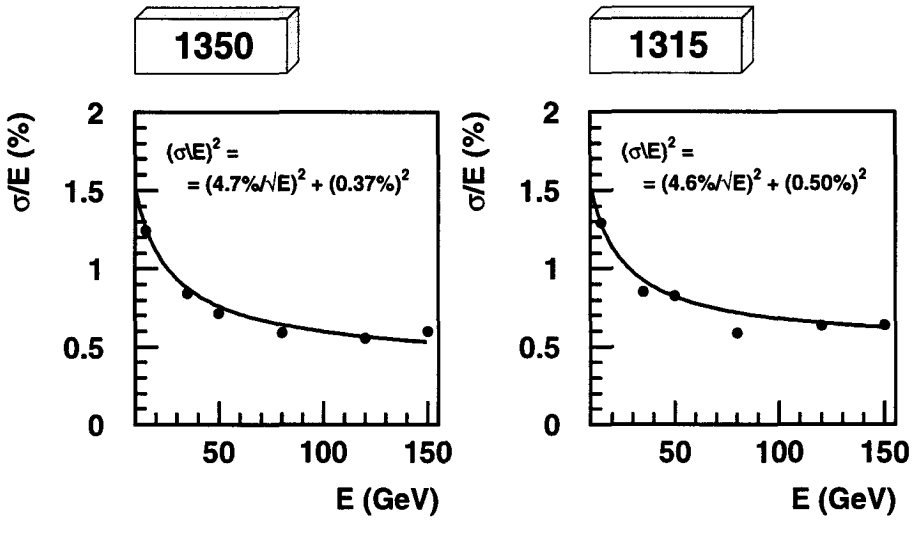

Figure 5.5: Energy resolution as a function of energy for crystals 1315 and 1340 from the test beam data.

Simulation results

The energy resolution of the crystals has been measured from the simulation results of the test beam setup. The crystals have the nominal size and are tilted by 3° in ϕ and η as in the test beam setup. Electrons incident to a 4x4 mm^2 beam spot corresponding to the effective centre of the central crystal in a 3x3 array crystal have been generated. The incident particles were electrons with energies of 15, 25, 35, 50, 80, 120 and 150 GeV. The simulation cuts were set at 100 keV.

The resolution is extracted with the same method that is used in the test beam data analysis described above. Figure 5.6 shows the fit of the resolution function in the absence of the photostatistics or non-uniformity effects. The stochastic term is found to be 1.85% and the constant term 0.17%.

The photostatistics contribution can be estimated from the LED signal in the beam test as explained above. The contributions for the two crystals 1315 and 1350 are found to be $a_{led,1315} = 3.4\%$ and $a_{led,1350} = 3.6\%$. In the beam test, one APD per crystal was used. In the final assembly, it is foreseen to use two APDs per crystal thus decreasing the photostatistics contribution to 2.3% as discussed in section 4.3.1.

The non-uniformity contribution is estimated by measuring the slope of the longitudinal light collection curves shown in figure 5.4 in the shower maximum region (5 – 10 X_0 corresponding to 14.1 – 18.55 cm in the figure 5.4). Four measurement points (13.5, 15.5, 17.5. and 19.5 cm) are included in a linear fit to obtain an estimate of the slope. As shown in reference [44] and explained in the previous section, the additional width of the energy resolution due to the non-uniformity of a crystal can be estimated by simulating the corresponding non-uniformity slope and comparing it to a uniform crystal. The non-uniformity of the two crystals is found to be $0.25\%/X_0$ and $0.49\%/X_0$[55] for 1350 and 1315, respectively, corresponding to an additional width of $\approx$ 0.2% and 0.35%.

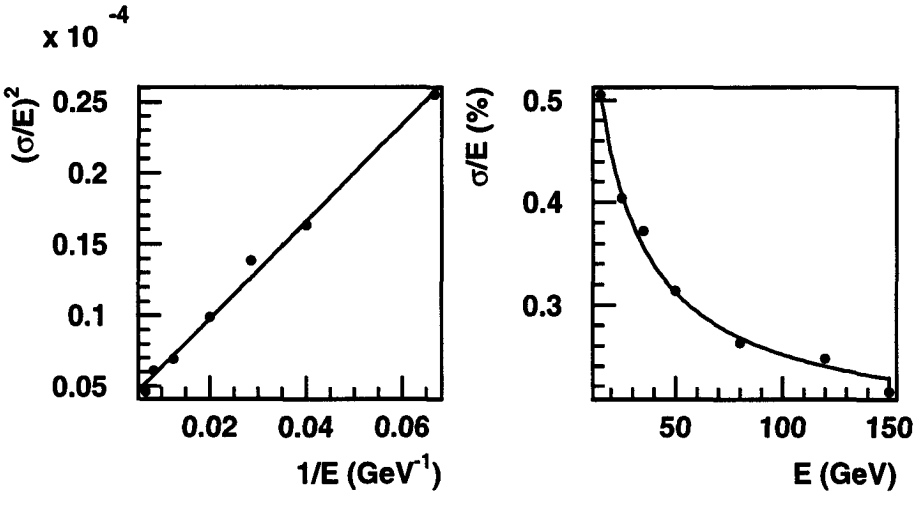

Figure 5.6: Energy resolution in 3x3 crystal array obtained from the simulation. The stochastic term is 1.85% and the constant term 0.17%. No effects from the photostatistics, non-uniformity or intercalibration errors are included.

	Data	Simulation			
Crystal	a_{fit}	a_{sim}	a_{led}		Sum
1315	4.6%	1.85%	3.4%		3.9%
1350	4.7%	1.85%	3.6%		4.0%
	c_{fit}	c_{sim}	c_{n-u}	beam	Sum
1315	0.50%	0.17%	0.35%	0.15%	0.42%
1350	0.37%	0.17%	0.2%	0.15%	0.30%

Table 5.3: Energy resolution obtained from the simulation when the effects of the photostatistics and non-uniformity are taken into account.

The beam spread in the H4 beam line is calculated to be 0.17% for 150 GeV collimator settings and 0.15% for other energies[42].

Table 5.3 summarises all these contributions. The resolution obtained in the test beam is rather well reproduced in the simulation. The simulation results with all the above mentioned effects are slightly better than those of the real data. The difference can be attributed to the calibration errors, shower leakage in the APDs and non-uniformity effects not taken into account in the estimate which has been carried out. The two crystals that have been studied here are presentative examples from the September 1996 test beam matrix. Since then, some progress has been made, for example in the uniformisation of the crystals and in the electronics noise, and better results have been obtained. Figures 5.7 show the stochastic and constant terms for different crystals achieved in the beam test 1997[54].

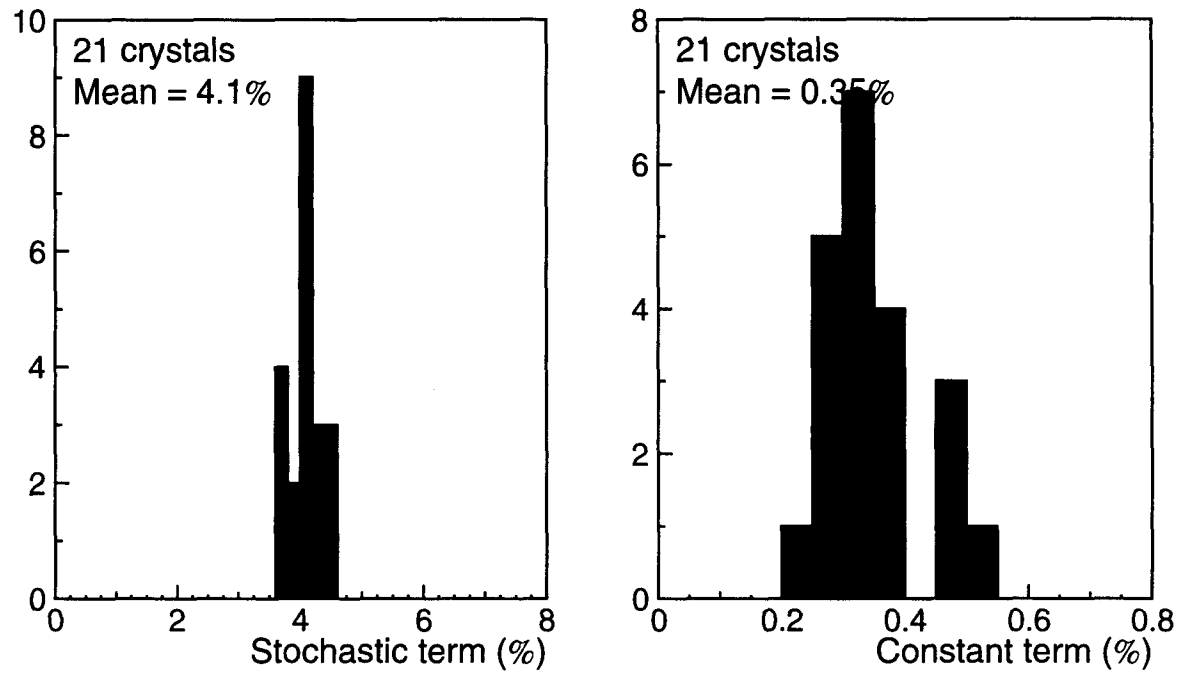

Figure 5.7: Stochastic (left) and constant (right) terms of the energy resolution for 21 crystals in the 1997 beam test.

Conclusions on the resolution studies

It has been shown that the contributions to the energy resolution of the crystals are understood in the test beam data and in the simulation. The magnitude of the effects that have to be added in the simulation results has been estimated from the independent measurements and the resulting resolution agrees with the test beam data.

5.3.3 Lateral width of the showers

Many of the effects that are studied with the simulation programs are directly connected to the lateral dimensions of the electromagnetic showers, e.g. the choice of the number of crystals in an electromagnetic cluster, the measurement of the shower centre of the gravity and the side leakage of the energy deposit outside of the chosen cluster size. The definition of the electromagnetic clusters, isolation criteria and π^0 rejection depend on these quantities. Therefore, it is important to understand how well the lateral dimensions are reproduced in the simulation.

First, the method used to extract the information from the test beam data is briefly described. Then, the simulation setup and the effect of variation of some parameters are explained. The results[56] are compared and the errors in the procedure are estimated.

Test beam data and analysis

The data used in this comparison were taken in September, 1996, in H4 test beam in 7x7 crystal matrix. As the expected difference between the simulation and the data is small,

it was decided to use the data from a single crystal rather than from a bigger matrix to avoid any ambiguities due to the intercalibration of the crystals. The data were taken in 50 GeV e^-beam with a 20x20 mm^2 wide trigger. In the analysis the impact point giving the maximum energy deposit in the central crystal was found in x- and y-direction in terms of the beam chamber hit position. Then the y-value was allowed to range ± 2 mm around the maximum (essentially giving no variation to the containment) and the energy contained in the crystal was plotted as a function of the hit x position. Several crystals were studied to estimate the difference from crystal to crystal.

Simulation setup

The simulation program H4sim96[52] used in this study allows a variation of several parameters, such as the crystal size, the tilt angle and the gap between the crystals. Electrons of 50 GeV were generated uniformly in the area corresponding to the accepted beam chamber values in the data. The GEANT cuts in the simulation were set to 10 keV (rising them to 100 keV does not change the results). The presence of δ-rays is important in this measurement, and this process was switched on for the simulation.

The nominal values for the crystal geometry were used:

- the length of crystal 23 cm
- the lateral dimension of the crystal front face 20.5 mm
- the tilt in ϕ and θ 3°
- the gap between the crystals 0.5 mm.

To estimate the effect of the possible uncertainties of these values, the simulation events were also generated with the gap distances of 0.3 and 0.7mm, and with the tilt angles of 2.5° and 3.5°. Each simulation sample contained 10000 events.

Results

The energy containment as a function of the impact point is shown in figure 5.8. The centre of the x-axis is the impact point giving the maximum signal in the central crystal (due to the tilt, this value does not correspond to the centre of the front face of the crystal). The signal is normalised to the maximum value. The data from 9 different crystals are shown with markers (each point corresponding to a x-y-area of 1x4 mm^2) and the simulation result is shown by the continuous line. In the central part of the distribution where the impact point varies $\pm$ 6 mm from the central point, data and simulation agree very well. This part corresponds to the events where the narrow central core of the electromagnetic shower is contained in the central crystal. When the impact point differs more than $\pm$ 6 mm from the central point, slight deviation can be observed. Here the shower core starts to leak to the neighbouring crystal. The data points indicate a better containment in the central crystal than the simulation values. Therefore, the shower dimensions in the simulation seem to be somewhat larger than in the data.

The difference in the lateral shower dimension can be estimated in two independent ways. First, the lateral crystal dimension in the simulation is increased by 3% - 9%. The

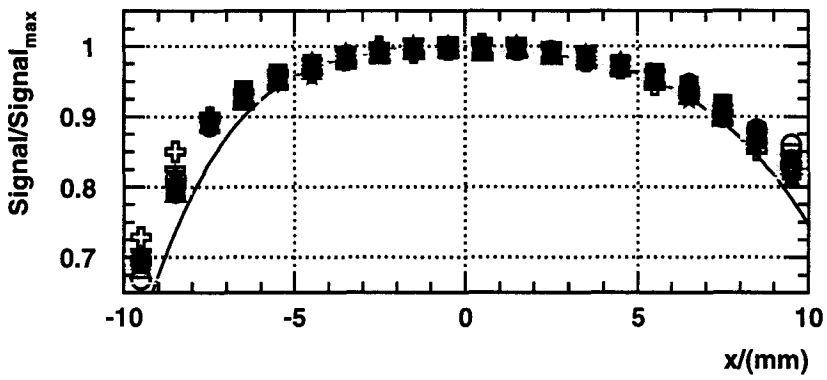

Figure 5.8: The energy containment as a function of the impact point. The symbols are the data from nine crystals and the continuous line is the curve obtained from the simulation. Each symbol corresponds to one crystal, for most of the data points the symbols are overlaid. The asymmetry is due to the tilt of the crystals.

results are shown in figure 5.9. The dimension of the x-axis is scaled correspondingly for the simulation curves: for example, for a 3% increase, 1 mm in the scale corresponds to 1.03 mm. A good agreement with the data is obtained with a 6% increase. For the sake of clarity, the mean of the 9 data points is computed and the error bar presents the RMS error of these points.

The effect of the shower width can be estimated also from a functional shape of a electromagnetic shower. The lateral shape of the shower can be described with a sum of two exponentials [57]:

$$f(r) = a_1 e^{-r/b_1} + a_2 e^{-r/b_2}$$

The containment in the central crystal as a function of the impact point can be obtained by integrating this expression

$$E_{\text{central Xtal}} = \int_0^{r_l} f(r)dr + \int_0^{r_r} f(r)dr$$

where r_l and r_r are the crystal borders to the left and to the right. These can be estimated to be 11 mm (at the shower maximum) for the impact point giving the maximum signal in the central crystal and correspondingly $r_l = 11 + x$ and $r_r = 11 - x$ when $x \neq 0$ as shown in figure 5.10.

The integrated function gives the shower containment in the central crystal. A set of parameters can be found to fit one side of the test beam data curve. Because of the tilt, the two sides of the crystal are not equal as the inclined shower will leak to the neighbouring crystal by a different amount at different depths on the two sides. A possible set of parameters ($a_1/a_2 = 1$, $b_1 = 2.5$ mm, and $b_2 = 20$ mm) is compared with

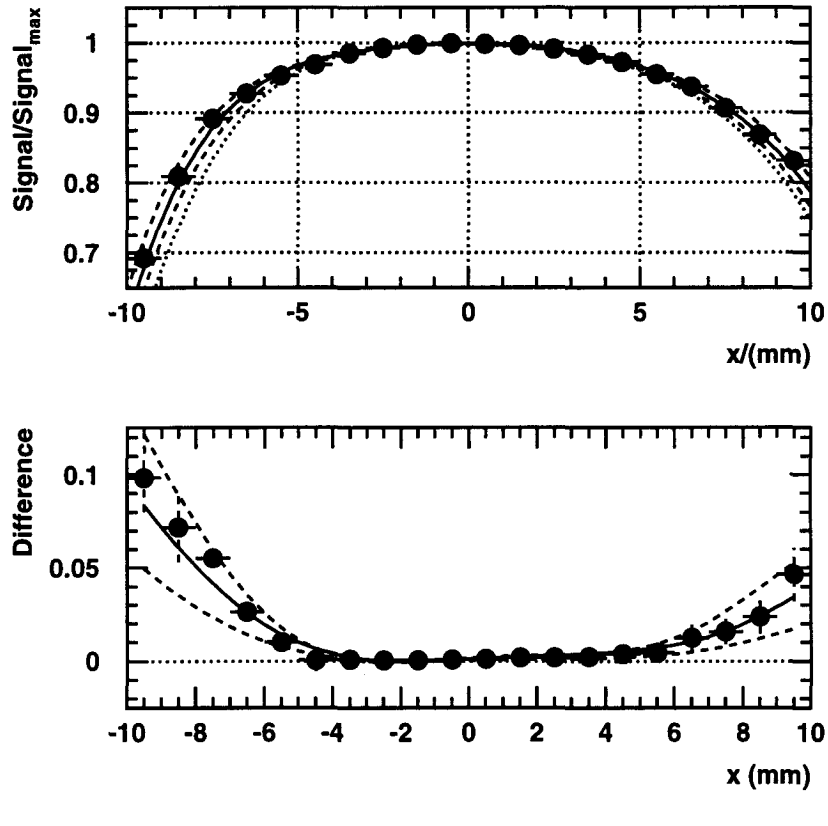

Figure 5.9: The energy containment as a function of the impact point. The dots are the mean value of the data points and the curves are from the simulation. The lateral dimensions of the crystals in the simulation have been increased by 0% (dotted line), 3% (dashed line) ,6% (continuous line) and 9% (dashed line). The plot below shows the same as the difference from the simulation results with the nominal crystal width.

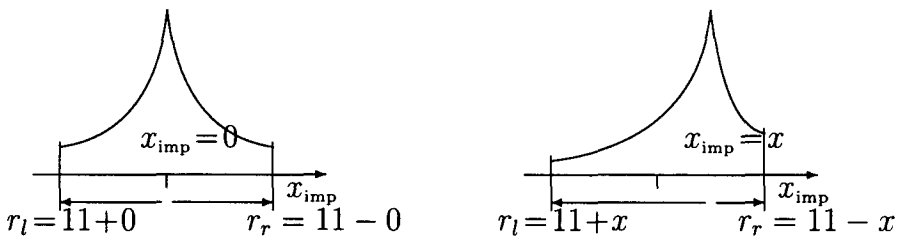

Figure 5.10: The limits of integration of the shower shape function for different impact points.

the data in figure 5.11. The same parameters can describe the simulation results if the integration limits are decreased to (100/1.06)%·11 mm instead of 11 mm to effectivly widen the distribution. This indicates that the simulation showers are indeed 6% wider than in the data. However, to verify that the set of parameters used really describes the data, the deposit in the neighbouring crystals should be considered also as the parameters depend on the shower shape further away from the central core.

The variation of the response due to the geometry has been studied with simulation. The possible variations due to the gap size between the crystals are shown in figure 5.12a. The results with the nominal 0.5 mm wide crystal gap are compared with the cases where the gap width has been set to 0.3 and 0.7 mm. The lines with 3%, 6% and 9% increases in crystal size are also shown as a reference. The effect of the tilt angle imprecision of ± 0.5° is shown in figure 5.12b. Again, the results with the nominal 3.0° angle are compared with those with 2.5° and 3.5° and the 3%, 6% and 9% wider crystal lines are shown as a reference. In both cases, the variation from the nominal value curve is smaller than that of 3% wider crystals.

The lateral sizes of the crystals in the test beam matrix were measured to have a mean of 99.9% of the nominal size with an r.m.s variation of 0.4%.

The method described here is very sensitive to the lateral width of the showers. In the analysis of the final CMS data, the measurements which can be affected by the lateral width are, for example, the ratio of the energy deposit of the central crystal to that of the surrounding crystals. This type of ratios have been studied in [58] where ratios of energy deposit in 4x4 mm^2 and larger areas were compared. These values have been reproduced for nominal size and 6% larger crystal and it is shown[59] that the small difference is not visible in the ratios. Table 5.4 shows the mean values of these ratios for different areas. However, it should be further verified by comparing the simulation and the test beam data that, for example, the π^0 rejection algorithms are not sensitive to this discrepancy.

Conclusions on the lateral width

There is a small disagreement between the test beam data and the simulation in the lateral dimensions of the electromagnetic shower. The simulation showers in $PbWO_4$ crystal are shown to be 6% ± 3% wider than the real showers. However, this small discrepancy is visible only in very detailed studies on the width of the central part of the shower and it does not affect the validity of the GEANT simulation results for the CMS electromagnetic

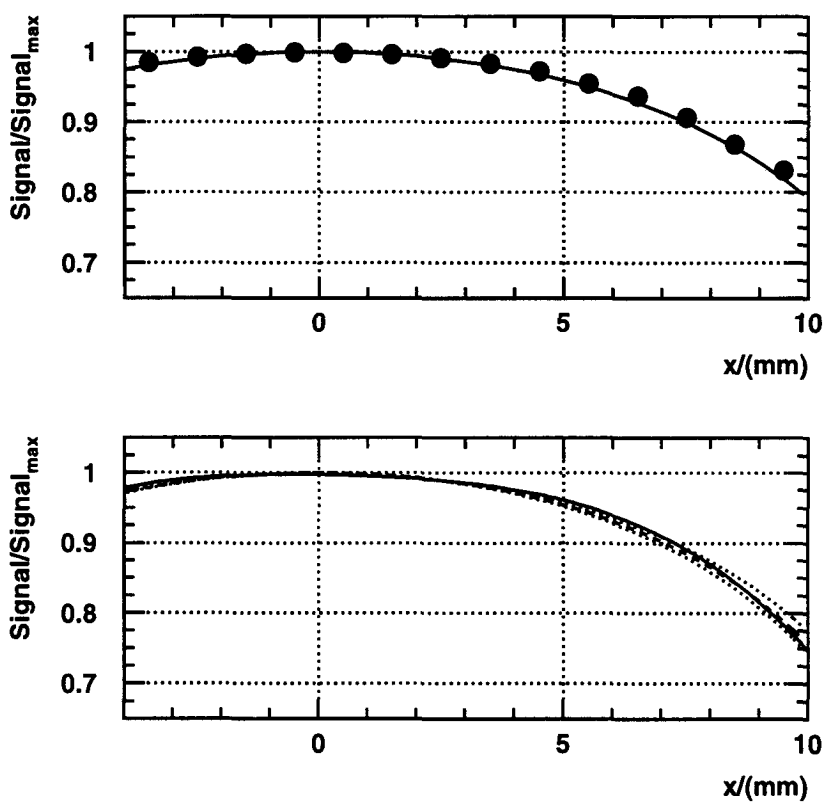

Figure 5.11: The energy containment as a function of the impact point. In the upper plot, the dots are the mean value of data points and the dashed line corresponds to the computed shower containment for a functional shower shape intergrated from r = 0 mm to r = 11 mm. In the plot below, the continuous line is the simulation curve and the dashed line corresponds to the computed shower containment integrated from r = 0 mm to r = (100/1.06)%·11 mm. For comparison, the computed containment corresponding to 9% and to 3% wider showers (dotted lines) are shown.

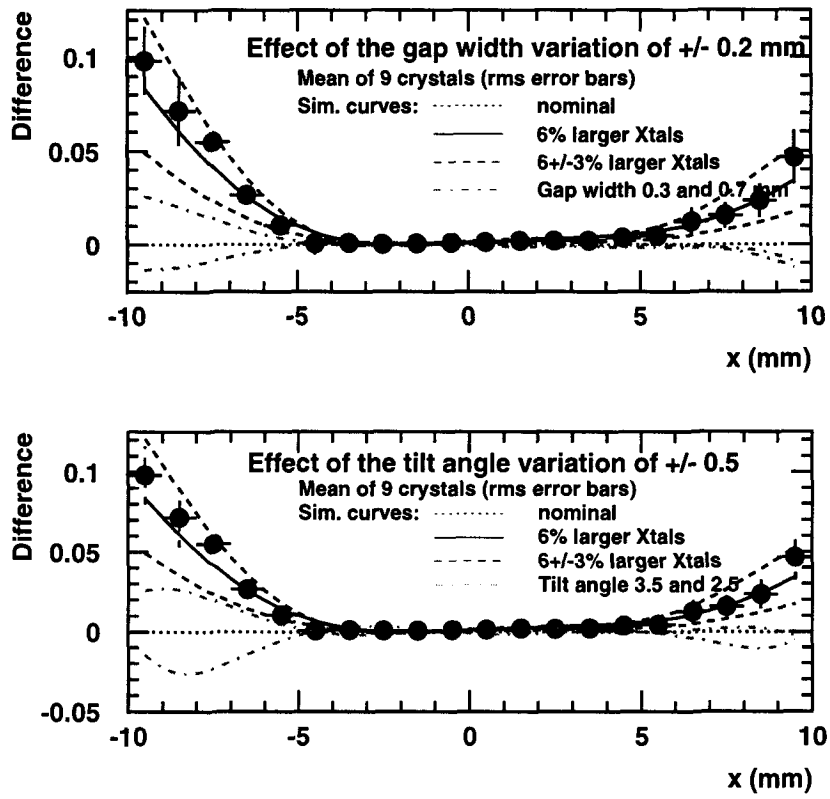

Figure 5.12: a) The effect of varying the width of the gap between the crystals: the dotted line corresponds to the nominal width and the dot-dash lines correspond to widths of 0.3 and 0.7 mm. The continuous line shows the results from 6% wider crystals and the dashed line from 3% and 9% wider crystal. The data is shown by markers. b) The effect of varying the tilt angle: the dotted line corresponds to the nominal angle and the dot-dash lines correspond to angles of 2.5° and 3.5°. The 6%±3% wider crystals and the data are as above.

Ratio (mm^2)	Nominal size	6% larger
4x4/6x6	1.004	1.004
4x4/8x8	1.010	1.011
4x4/10x10	1.021	1.021
4x4/15x15	1.066	1.066
4x4/20x20	1.189	1.190

Table 5.4: Ratios of the energy deposits in dirrefent areas for nominal size and 6% larger crystals.

calorimeter.

5.3.4 Conclusion on the test beam data

The test beam data of $PbWO_4$ crystals have been analysed and different aspects of the electromagnetic cascades have been studied. The importance of the shape of the longitudinal light collection curve has been studied by a detailed simulation and the crystals in the recent beam tests confirm that a good constant term can be achieved (see figure 5.7) when the crystals are carefully uniformised. The lateral shape of the showers has been studied and it is shown that although a disagreement exists between the data and the simulation, it is small and not visible in the quantities that are used in the final data analysis. The resolution has been extracted from two presentative crystals of the 1996 beam test. The results indicate that when the APD sensitive area is increased (by using two ADPs per crystal) the performance of the crystals is adequate for the final CMS assembly. Since 1996, the average light yield of crystals and the APD performance have improved, the crystals are less sensitive to low dose radiation damage and there is less variation from crystal to crystal. Excellent resolution has been obtained consistently for crystals in the 1997 beam test matrix[54].

5.4 Photons

A photon can be identified as a concentrated energy deposit in the electromagnetic calorimeter with no corresponding track in the inner detector. Due to the small Molière radius of $PbWO_4$, 96% of the electromagnetic shower is contained in an array of 5x5 crystals corresponding to an area of 11×11 cm^2.

The magnetic field has no effect on the photon track and it has only a minor effect on the resulting electromagnetic cascade in the crystal material. Figure 5.13 illustrates the difference between the shower width in the presence of a 4 T field along the z-axis and in the absence of field and it can be calculated from the r.m.s. value of the energy deposition that the field widens the shower in the ϕ-direction by 7%.

A photon can convert to an electron-positron pair in the presence of material. The mean free path λ before a conversion can be estimated to be $\lambda = 9X_0/7$ where X_0 is the radiation length of the material. The probability for a photon to travel a distance x without a conversion is

$$P_{\text{no conv}} = e^{-x/\lambda} = e^{-\frac{7}{9}\frac{x}{X_0}}$$

The probability for a conversion is then

$$P_{\text{conv}} = 1 - P_{\text{no conv}} = 1 - e^{-\frac{7}{9}\frac{x}{X_0}}$$

The amount of radiation lengths and the corresponding conversion probability per photon in front of the CMS electromagnetic calorimeter is shown in figure 5.14. In CMS with a complete high luminosity tracker, 34% of the photons convert before reaching the calorimeter. To reach a high photon reconstruction efficiency, these photons should not be discarded. However, if their measurement worsens the overall photon resolution which

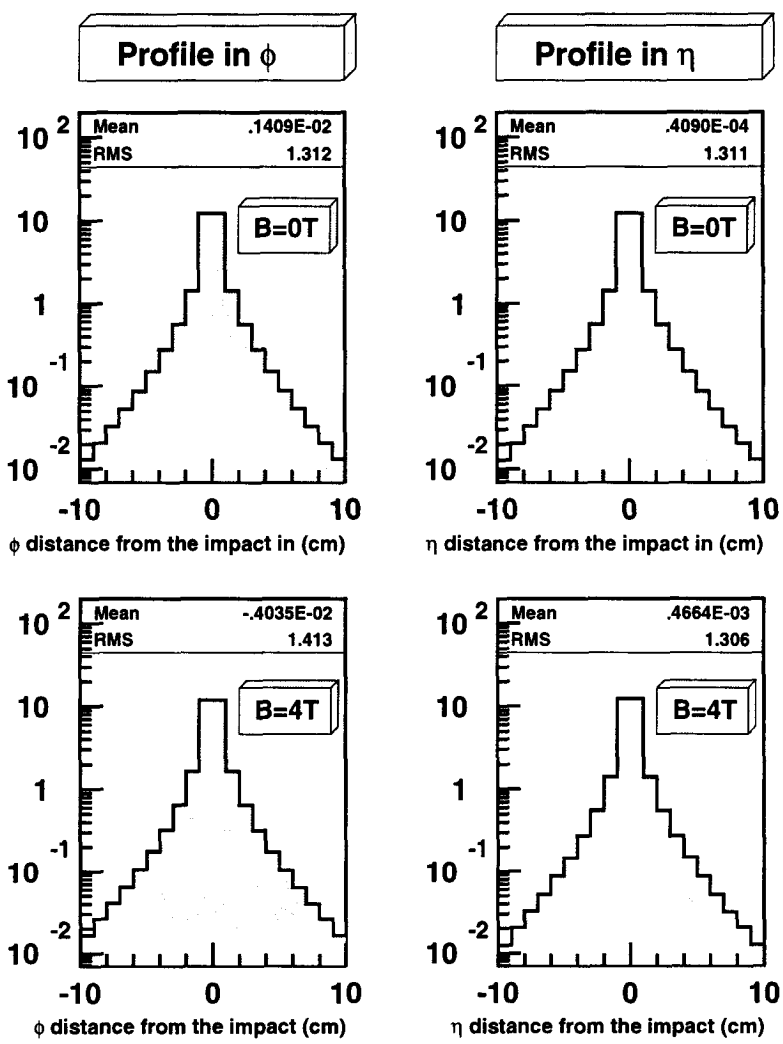

Figure 5.13: The effect of the magnetic field in the electromagnetic cascade in the lead tungstate.

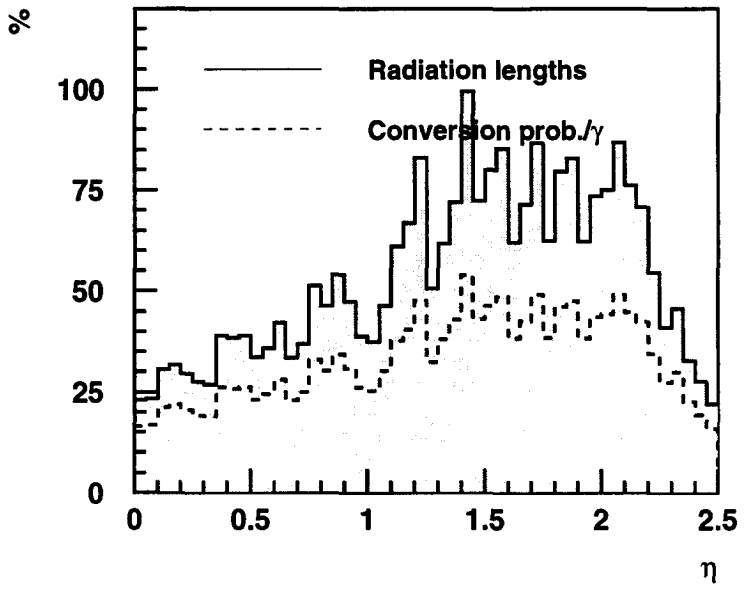

Figure 5.14: The amount of material in front of the crystal and the conversion probability per photon (tracker V4 in phase II, i.e. complete detector).

may be the case when the conversion happens very early or if it is very asymmetric, they should be identified and removed from the studied event sample.

In the following, the performance of the CMS electromagnetic calorimeter is quantified using the $H \rightarrow \gamma\gamma$ channel as a benchmark[60]. The two photons from the Higgs decay are passed through a full GEANT simulation, using the calorimeter geometry described in CMSIM. Particles of the underlying event are not simulated but they are recorded for the vertex reconstruction. Including these particles in the simulation would have little effect on the results, the two photon clusters in the signal event are isolated and losses due to the isolation criteria are included in the study of $H \rightarrow \gamma\gamma$ significance. Furthermore, in the following, the pile-up noise is included. The cutoff values in the simulation are set to 100 keV. It has been verified that lowering the cutoff value to 10 keV does not change the results.

For the Higgs mass reconstruction, the energy and the direction of the two decay photons have to be measured. The energy measurement is described in section 5.4.1. It can be done in a different way for the non-converted and converted photons depending on the available tracker information. If the conversion happens before the last but one measuring layer of the tracker, it is assumed that the conversion can be identified with the track segments. In this case an optimised algorithm can be used to measure the energy of the converted photon. If the conversion happens after, it will not be visible in the tracker. These invisible conversions must be treated like non-converting photons. The tracker layout has been optimised so that the invisible conversions cause no significant damage to the energy measurement. These optimisation studies are described in section 5.6. The conversion probabilities in front of the barrel and the endcaps are summarised in table 5.5

	No conversion	Invisible conversion	Visible conversion
Barrel ($\|\eta\| < 1.48$)	71.6%	2.9%	25.5%
Endcap ($1.48 < \|\eta\| < 3.0$)	61.3%	5.7%	33.0%

Table 5.5: Conversion probability for photons before the ECAL with the tracker V4, phase II, i.e. complete detector.

The direction of the photons is given by two measured points: the vertex of the Higgs event and the impact point of the photon on the crystals. Their measurement is described in section 5.4.2.

5.4.1 Energy measurement

No conversions before the ECAL

When the two photons from Higgs decay do not convert in the sensitive part of the tracker, the photon energy is summed in 5x5 crystals around the maximum energy deposit (a 5x5 crystal array contains approximately 96% of the photon energy).

The fluctuation in the energy measurement given by the GEANT simulation is only due to the front, side and back leakage from the area where the energy is measured. The fluctuations in the light generation, transmission and detection or calibration are added by smearing the energy deposition obtained after simulation with $2.3\%/\sqrt{E} \oplus 0.5\%$ as discussed in section 5.2. All the noise terms are added and if not mentioned separately the figures correspond to the initial low luminosity period ($\mathcal{L} = 10^{33}\text{cm}^{-2}\text{s}^{-1}$).

At high η, towards the end of the barrel, less energy is contained in the 5x5 crystal array, and a simple correction depending on the η direction of the photons is applied. The energy measurement can be further improved by additional corrections, e.g. a correction for the side leakage depending on the impact point on the crystal front face and the vertex point. This has not been included in the barrel. In the endcap, where the gaps between the crystals are significant the side leakage effect is more important and a correction is applied. The variable as a function of which the correction is applied is the ratio of the sum of all 25 crystals in the array to the energy of the central crystal.

In the barrel, if the maximum energy deposit is in either of the two crystal rows adjacent to a basket border, the energy measurement may degrade. A correction is applied to a certain class of these clusters and, if the degradation is too large, the cluster is discarded. The correction is done as a function of the ratio of the energies on each side of the basket border which effectively measures the position. Figure 5.15 shows the reconstructed energy in 5x5 crystal array as a function of the correction variable $\log(E_1/E_2)$ before and after the correction. The reconstructed energy is normalised to the initial energy of the photon. The correction is applied in the shaded area and the region between the corrected areas is excluded. Figure 5.15 shows the correction over the basket borders in η, a similar correction is applied to the basket borders in ϕ. The fraction of the photons which are excluded because of the cracks in the barrel is 2.9%. Figure 5.16 shows

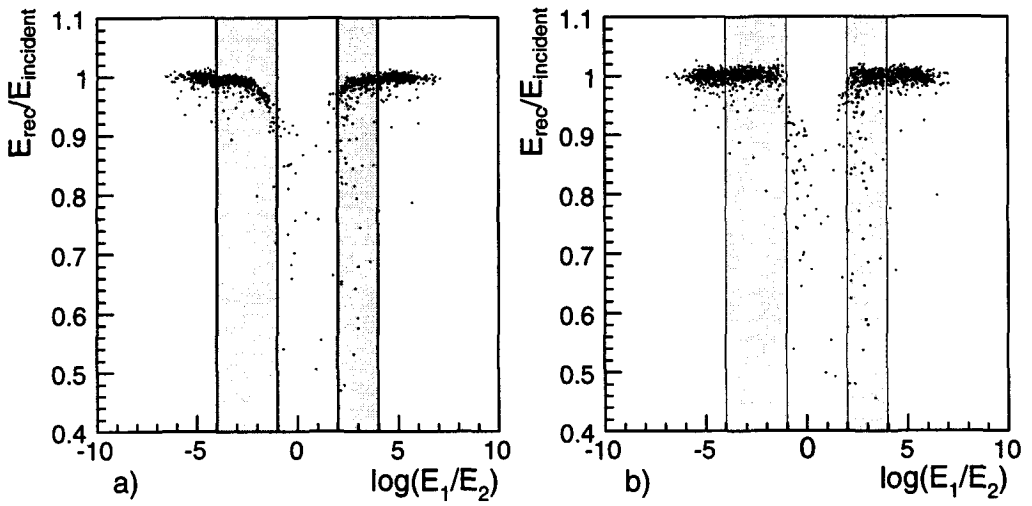

Figure 5.15: Correction over the basket borders in η, the correction is applied to the shaded range of the variable $\log(E_1/E_2)$ and the reconstructed cluster energy is shown before correction (a) and after correction (b).

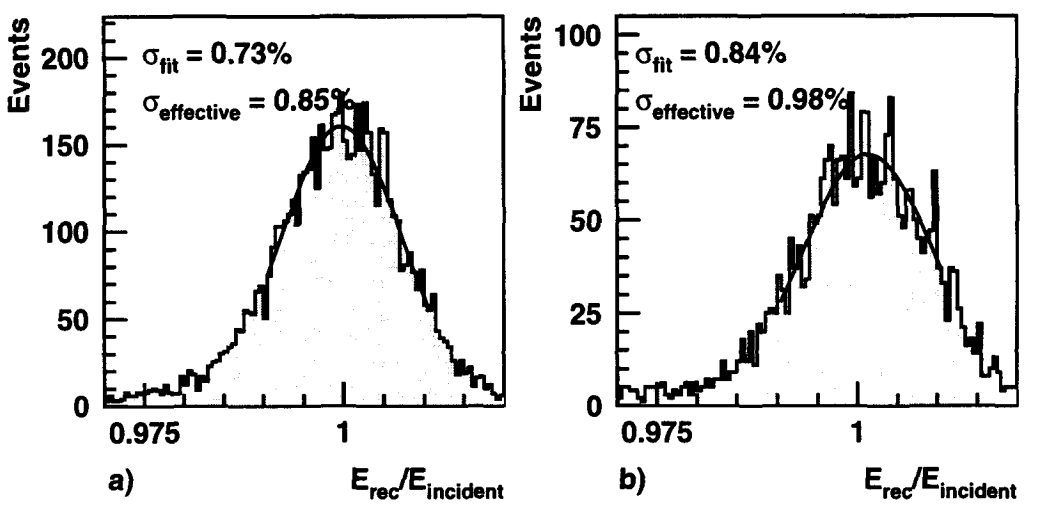

Figure 5.16: Energy resolution[1] of the photon clusters which do not cross any basket border cracks (a) and of the photons clusters where a basket border correction has been applied (b).

the energy resolution of the clusters not crossing the basket border crack compared to the energy resolution of the clusters where the basket border correction has been applied. The photons are generated from a $H \rightarrow \gamma\gamma$ decay ($m_H = 100$ GeV) and the reconstructed energy is normalised to the initial energy of the photon.

In the endcaps, the energy measurement in the crystals is corrected with the signal

[1] σ_{fit} is the sigma of a Gaussian fit to the peak, σ_{eff} is the effective root mean square i.e. half of the minimum width which contains 68.3% of the events. For a perfect Gaussian distribution, $\sigma_{fit} = \sigma_{eff}$.

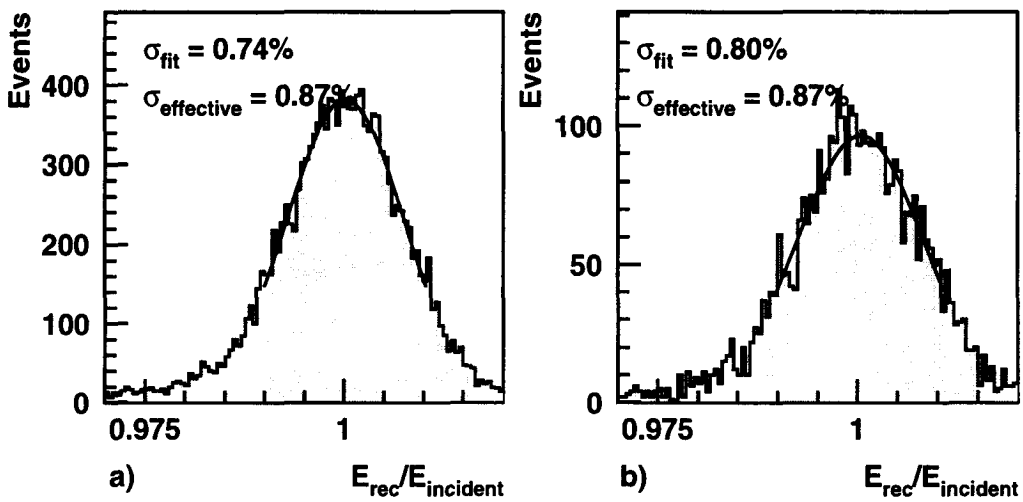

Figure 5.17: Energy resolution of the non-converted photons from $H \rightarrow \gamma\gamma$ (m_H = 100 GeV) in the barrel (a) and in the endcaps (b).

from the preshower device. Figure 5.17 shows the energy measurement for the photons in the barrel including the basket border correction and for the endcaps including the side leakage correction and the preshower signal correction.

Invisible conversions

The tracker layout has been optimised so that the invisible conversions in the last layers, in the outer cables or in the support structure of the tracker do not affect the energy resolution significantly (see section 5.6). This is shown in figure 5.18 for the photons from 100 GeV $H \rightarrow \gamma\gamma$ in the barrel. The energy resolution is even narrower for invisible conversions. This is due to the fact that the electromagnetic shower induced by a photon starts when the photon converts. If the photon does not convert in the material in front of the crystal, it may continue few centimetres in the crystal before showering (for example, in 1 cm of $PbWO_4$ the conversion probability is $P_{conv} = 1 - e^{-7\cdot1/(9\cdot0.89)} = 58\%$). This may cause leakage from the back end of the crystal degrading the energy resolution. Such leaking showers are not present in the sample containing photons that convert before the crystals.

Visible conversions

When a photon converts in the tracker the energy deposit pattern in the crystals is different from that of non-converting photons and different algorithms should be used to measure the photon energy. Only the photons converting before the last but one tracker layer are considered (giving at least two measured points per track) as only in these cases can the two electrons be recognised as a conversion using the tracker information. It should be noted that in this study 100% efficiency is assumed for the identification of the electron track segments which is certainly an optimistic assumption. Further detailed

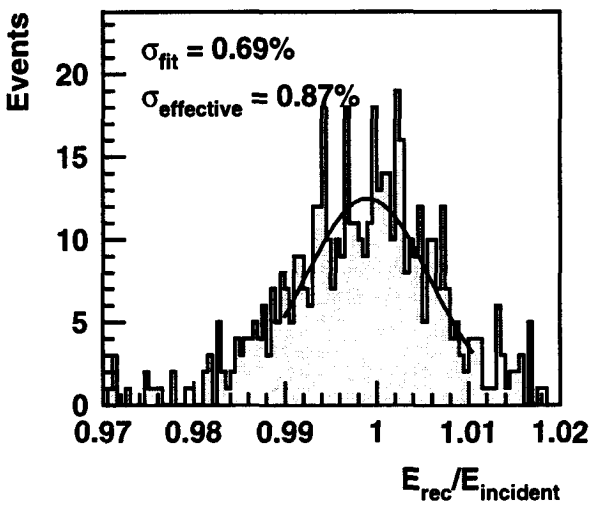

Figure 5.18: Reconstructed energy of photons from $H \rightarrow \gamma\gamma$ ($m_H = 100$ GeV) for photons converting after the last but one tracker layer in the barrel.

studies are needed to estimate the track finding efficiency of the converted photons.

The electron and positron paths bend in the magnetic field and they arrive on the calorimeter front face some distance from each other in ϕ direction (figure 5.19). For the conversion in the pixel layers, the most probable distance between the impacts is 3.5 crystals ($\Delta\phi = 0.06$) and for those in the silicon support tube at r$\approx$ 65 cm it is one crystal ($\Delta\phi = 0.0175$). The radius of curvature of the track depends on the electron energy. As Bremsstrahlung photons are emitted mainly along the electron trajectory any photon radiated from the electron will arrive on the crystals between the electron and positron impact points. Therefore the area of energy deposition of the converted photon is limited by the distance between the two electron and positron impact points.

In the barrel, two different algorithms are used to measure the energy of converted photons. A simple algorithm measures the energy in a 5x9 crystal array around the crystal with the maximum energy deposit in the direction of the e^+e^- pair ("5x9 algorithm"). This algorithm is applied if the impact points have less than $\Delta\phi = 0.05$ between them. In this study, the impact points are taken from the simulation. In the real data, if the conversion can be identified with the track segments, the impact points will be known. The 5x9 algorithm recovers conversions where the energy deposit is concentrated in a small area. It recovers 53.9% of the converted photons in the barrel.

When the criterion for applying the simple algorithm is not satisfied a dynamic algorithm is used. It finds the local maxima between the two impacts ($E_{dep} > 1$ GeV) and sums around these maxima in 5x5 crystals if the local maximum is larger than 20 GeV and in 3x3 crystals in the other cases as schematically shown in figure 5.20. If the number of crystals in the cluster becomes large, the noise contribution increases. Using this algorithm, the average number of crystals in the cluster is 31.1 (less than 45 crystals in the 5x9 algorithm) so the contribution of noise will not increase compared to the 5x9 algorithm. The energy measurement is optimised when the number of summed crystals

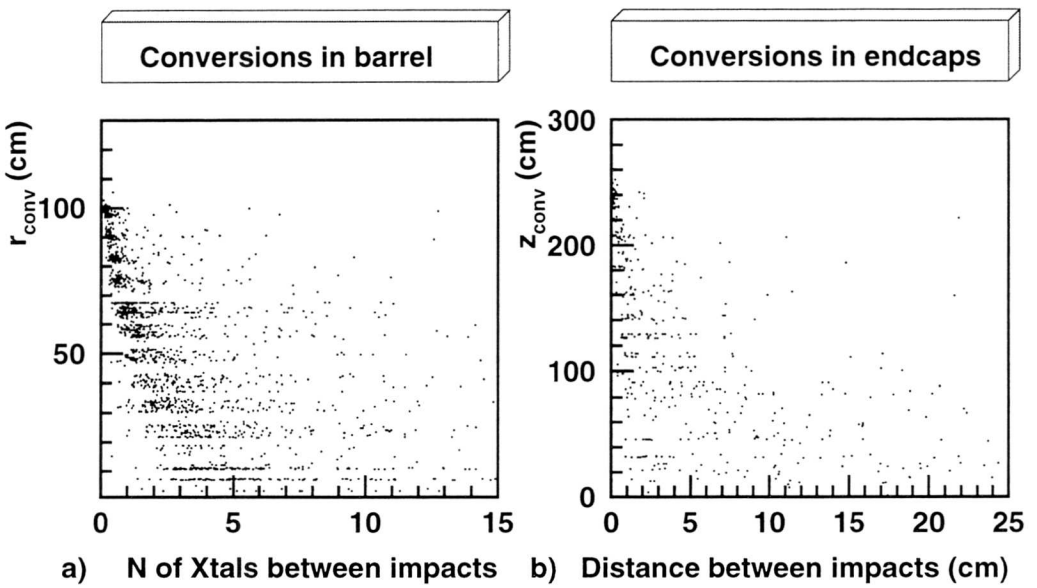

Figure 5.19: (a) The radius of conversion versus the number of crystals in ϕ direction between the e^+ and e^- impact points on the crystal front face in the barrel. The size of the crystal front face in the barrel is $\Delta\eta \times \Delta\phi = 0.0175 \times 0.0175$. (b) The z-coordinate of conversion versus ΔR between the e^+ and e^- impact points in the endcaps.

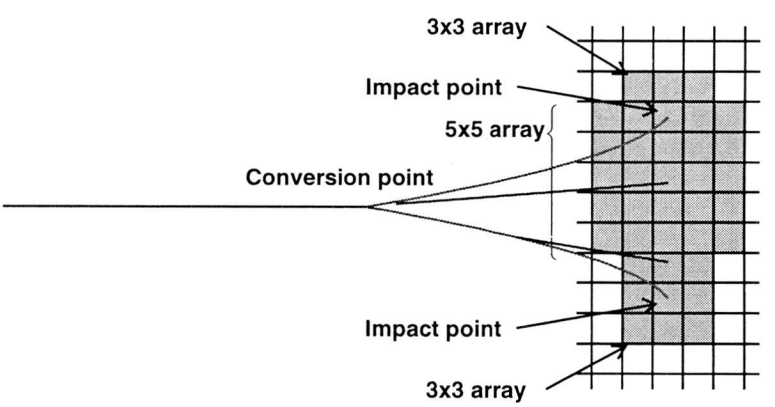

Figure 5.20: Principle of the dynamic algorithm used in recovering clusters from converted photons.

	Barrel	Endcap	All
% of photons	71.5%	23.6%	95.1%
% in barrel cracks	2.9%		2.1%
% lost conversions	7.2%	16.3%	9.0%

Table 5.6: Amount of photons in the barrel and in the endcaps, and the photon efficiency losses with respect to the amount photons in the barrel, in the endcaps, and in total.

is more than 24, therefore events with less than 25 crystals in the cluster are excluded. With these criteria, the dynamic algorithm is used for 16.7% of the converted photons in the barrel. With the two algorithms 71.6% of the converted photons can be measured. The amount of photons which are rejected due to a conversion is thus 7.2% of all photons in the barrel.

The measured energy is corrected using the dependence on the η direction of the photon mentioned previously. When the 5x9 algorithm is applied, a dependence of the energy on the distance between two impacts is corrected. When the dynamic algorithm is used, a correction is applied as a function of the number of summed crystals.

For both algorithms, the noise and the additional fluctuation are added as in the case of the non-converted photons.

The clusters which have a maximum energy deposit in one of the two crystal rows close to a basket border are corrected. In the 5x9 algorithm, the correction is used in the η direction where the number of crystals is the same as for the non-converting photons. In the ϕ direction the opening of the electron and positron tracks due to the magnetic field changes the energy deposit pattern. Therefore, the basket border correction in ϕ in the 5x9 algorithm is less effective and it is not applied. In the dynamic algorithm, the basket border correction is applied to the 5x5 subclusters of the dynamic cluster.

In the endcaps, the distance between the electron-positron impacts is smaller (see figure 5.19) because of the magnetic field direction and no special method is used to recover the conversions. The clusters where the electron positron impact are further apart than 4 cm are excluded. This corresponds to 49.4% of converted photons in the endcaps resulting in rejection of 16.3% of all photons in the endcaps.

The energy resolution of the converted photons in the barrel is shown in figure 5.21. The resolutions for the 5x9 and dynamic clusters are shown separately.

Photon efficiency

The effective area of the electromagnetic calorimeter barrel covers $|\eta| < 1.46$ and the endcaps $1.59 < |\eta| < 2.5$. The gap corresponds to the area where the energy measurement is considerably degraded due to the presence of tracker services exiting in the gap between the barrel and the endcap. 4.9% of the photons from a Higgs ($m_H = 100$ GeV) decay fall into this area. 71.5% of the photons are incident to the barrel area and 23.6% to the endcap area. Table 5.6 summarises the efficiency losses due to cracks and conversions.

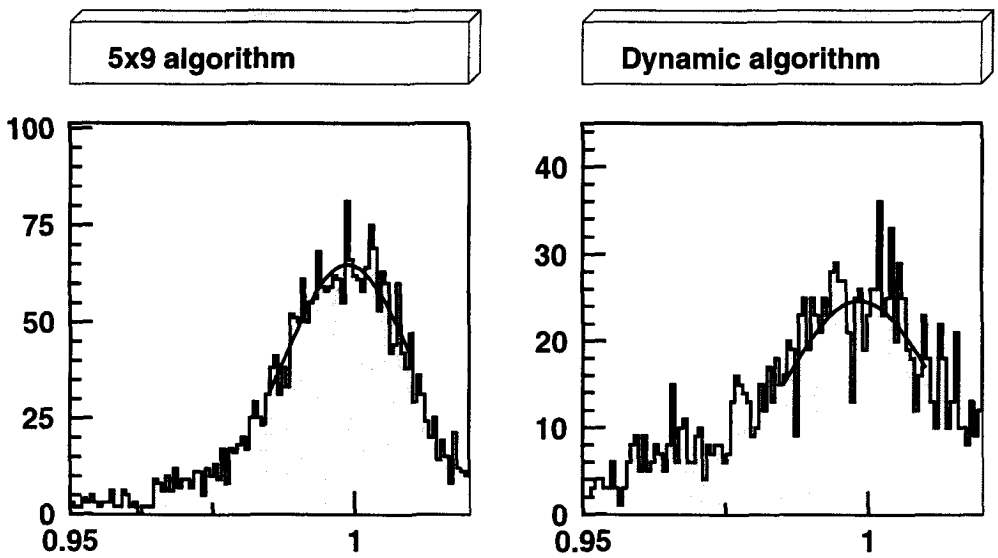

Figure 5.21: Energy resolution of the converted photons for clusters accepted by the 5x9 algorithm and for those measured by the dynamic algorithm.

5.4.2 Angular measurement

The photon direction will be measured from the impact point on the crystals and the vertex point. The impact point is measured using the shower centre of gravity

$$x = \frac{\sum E_i x_i}{\sum E_i}$$

in the two coordinate directions. The shower centre of gravity gives a typical s-curve shown in figure 5.22. If the impact point is to be given at the crystal front face the measurement in ϕ is independent of the vertex but in η the different inclinations of the tracks due to the variation in the vertex point have to be taken into account. If the shower positions is to be measured at the longitudinal shower centre, this vertex dependence can be eliminated[61]. The measurement presented here gives the impact point at the crystal front face. The dependence on the shower centre of gravity can be parameterised as

$$\begin{aligned} x_{c.o.g} &= a\tan(bx_{real} + c) + d \\ \Rightarrow x_{real} &= \frac{1}{b}\left(\text{atan}(\frac{1}{a}(x_{c.o.g} - d)) - c\right) \end{aligned}$$

All parameters a, b, c, and d are constant for the position measurement in ϕ. For the measurement in η, a and d are constant parameters and c and b depend on the cluster position in η and the z-coordinate of the vertex. The following values of the parameters are used (the unit of the coordinates is the fraction of the crystal width from the crystal front face centre, z is the vertex z coordinate):

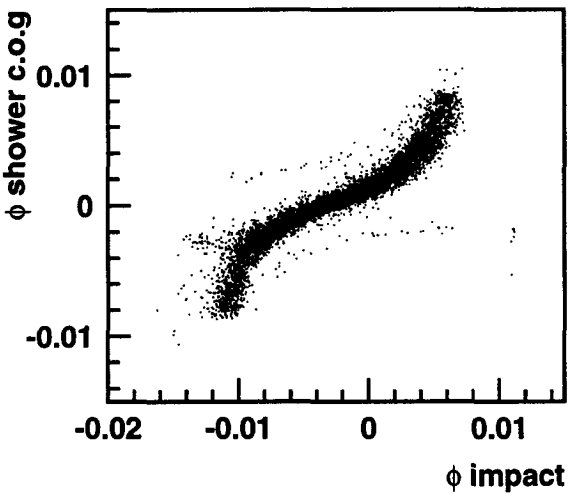

Figure 5.22: The shower centre of gravity versus the real impact.

Coordinate	a	b	c	d
ϕ, $\eta > 0$	-0.2	-2.2	-0.2	0.05
ϕ, $\eta < 0$	-0.2	-2.2	0.2	- 0.05
η, 1st basket	-0.19	$-2.275 + 0.0287 \cdot z$	$0.413 - 0.065 \cdot z$	-0.02
η, 2nd basket	-0.19	$-2.275 + 0.0287 \cdot z$	$0.438 - 0.046 \cdot z$	-0.02
η, 3rd basket	-0.19	$-2.275 + 0.0287 \cdot z$	$0.481 - 0.036 \cdot z$	-0.02
η, 4th basket	-0.19	$-2.275 + 0.0287 \cdot z$	$0.383 - 0.0237 \cdot z + .00119 \cdot z^2$	-0.02

Figure 5.23 shows the impact point resolution obtained by this method in ϕ and η directions in the electromagnetic calorimeter barrel.

In the endcap, the preshower information can be used to measure the impact point.

The vertex of the Higgs is found with the help of additional tracks from the same Higgs event[62]. The Higgs p_T is balanced by the rest of the particles in the event and therefore the tracks associated to a Higgs event are harder than the tracks of a minimum-bias event. The vertex can be identified by the hardest tracks of the bunch crossing. In the simulation, a number of pile-up events is added according to a Poisson distribution around the mean value of 1.7 corresponding to the low luminosity phase of LHC ($\mathcal{L} = 10^{33} cm^{-2} s^{-1}$) or 17.3 corresponding to the high luminosity. The luminosity drop during the run is taken into account by sampling from a luminosity profile which starts from the nominal value and drops to 20% of it during a 20-hour fill. The pile-up events are generated with PYTHIA. The tracks above a luminosity dependent p_T limit are accepted with 95% efficiency and the point on the beam line where maximum number of tracks are pointing ($\sigma_z = 2$ mm) is chosen as the vertex value. This procedure gives a non-Gaussian contribution to the mass resolution: when the correct vertex point is chosen the error is very small but when a wrong vertex from a pile-up event or no vertex is found the error is large. The events with wrong vertex have a reconstructed mass width of about 2.2 GeV

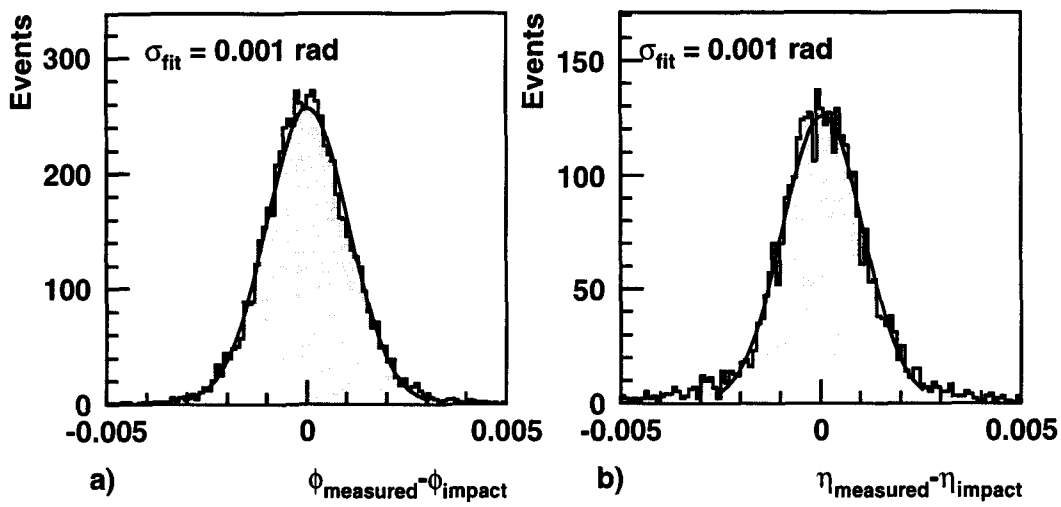

Figure 5.23: Resolution of the impact point measurement in the barrel measured from the shower centre of gravity.

and those with no vertex of about 1.6 GeV.

If a photon converts, it is assumed that its direction can be found using the reconstructed e^+e^- tracks and the error is negligible.

5.4.3 Results on mass resolution of $H \rightarrow \gamma\gamma$

Mass resolution for events with no conversions in the tracker

The mass resolution for the events with no visible conversions in front of the crystals is shown in figure 5.24. The contributions to the mass width are a) fluctuation in the energy deposit in 5x5 crystals, b) the estimated $2.3\%/\sqrt{E} \oplus 0.5\%$ smearing to take into account photostatistics and calibration, c) electronics and pile-up noise in each crystal (see section 5.2), and d) the angular measurement. Taking all these effects into account, the effective root mean squared is found to be 0.75 GeV and the Gaussian σ is 0.56 GeV.

Figure 5.25 shows the Higgs mass resolution when both barrel and endcaps are included for events with no visible conversions. The effective r.m.s. is found to be 0.78 GeV and the Gaussian σ is 0.57 GeV.

Mass resolution for events with conversion in the tracker

In the V4 tracker geometry 45% of events have one or two conversions before the last but one layer in the tracker. The goal is to recover the maximum number of these events without degrading the mass resolution.

If both photons are in the barrel, the fraction of converted events is 42%. First, the 5x9 algorithm is applied and it accepts 52% of the converted events. The dynamic algorithm is applied for the events not satisfying the selection criteria (distance in ϕ between the impacts $\Delta\phi < 0.05$). Accepting only events where the number of summed crystals is more

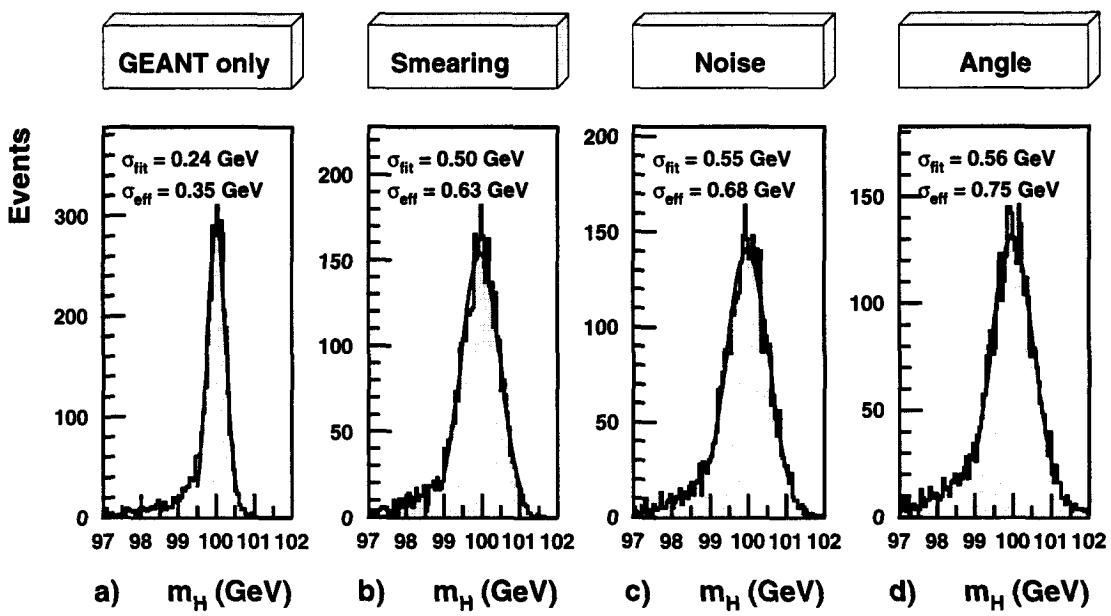

Figure 5.24: Contributions to the Higgs mass resolution in the barrel for the events where there are no visible conversions before the electromagnetic calorimeter: a) fluctuation in the energy deposit in 5x5 crystals, b) smearing to take into account photostatistics and calibration, c) electronics and pile-up noise and d) angular measurement.

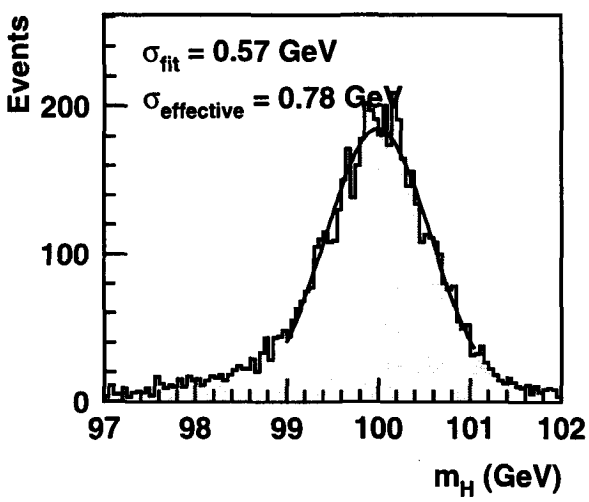

Figure 5.25: Higgs mass resolution (barrel and endcaps) for the events with no visible conversions.

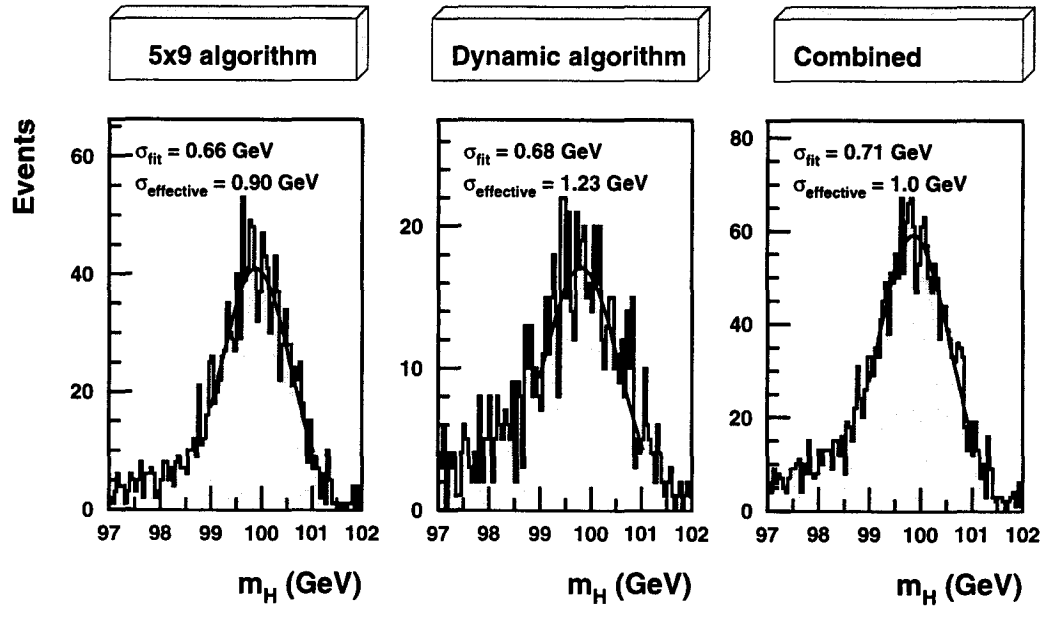

Figure 5.26: Higgs mass resolution in the barrel for the events where at least one photon converts and leaves a track in the tracker. To the left the events accepted by the criteria of 5x9 algorithm (52% of conversions), in the middle the events to which the dynamic algorithm has been applied (34% of conversions), and to the right the two algorithms combined.

than 25 removes events in the low mass tail of the mass distribution. With this cut further 34% of the converted events in the barrel are accepted resulting in a total acceptance of 86% for the two algorithms in the barrel.

In the endcaps, the converted clusters where the electron positron impacts are further away that 4 cm are discarded. With this cut and with the barrel conversion algorithms 80% of all converted events are accepted.

The mass distributions of the converted events are shown in figure 5.26 for both barrel algorithms separately and combined. The Gaussian width of the peak is as narrow as for the events with no conversions in the tracker; nevertheless a small tail at low mass is introduced as shown by the increased effective RMS.

Mass resolution for all events

The effect of including the conversion events in the mass reconstruction is shown in figure 5.27. Table 5.7 shows the effective RMS of the reconstructed Higgs mass when no conversion events, 52% of conversion events and 86% conversion events are recovered in the barrel. Combining the conversion recovery in the barrel and accepting the events where the positron and electron impacts are not further than 4 cm apart in the endcap results to an effective RMS of 0.87 GeV with 80% of the conversion events recovered. Including the conversion events causes only a slight degradation in the mass resolution.

Figure 5.28 shows the Higgs mass resolution in CMS for the low and high luminosity

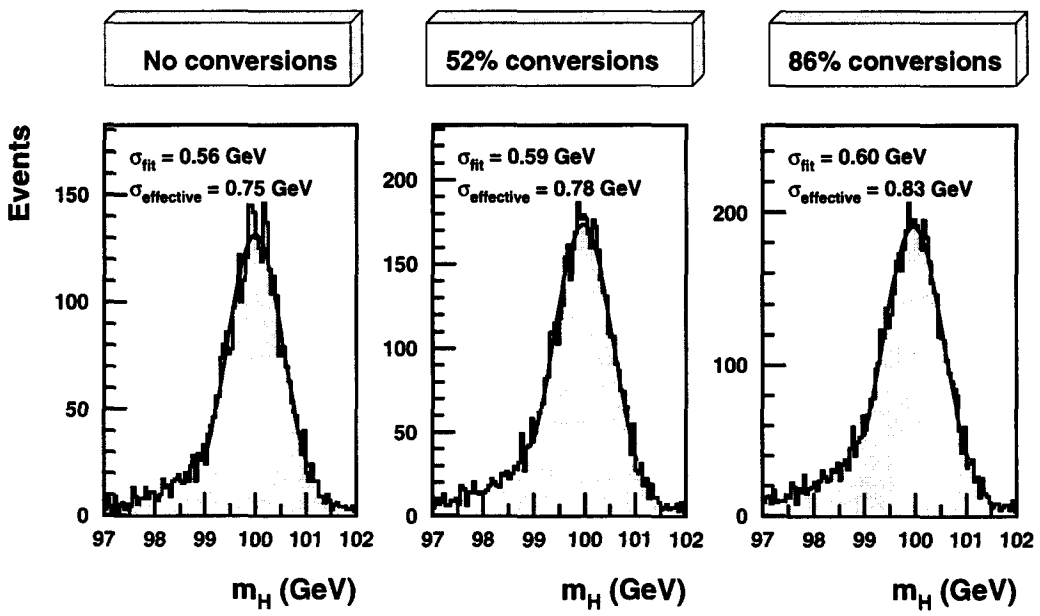

Figure 5.27: Reconstructed m_H in the barrel when all the conversions in the tracker are excluded (to the left), when 52% of conversion events are recovered with the 5x9 algorithm and added to the events with no conversion in the tracker (in the middle), and when additional 34% of conversion events are recovered with the dynamic algorithm (to the right).

Recovery of the converted photons	% of conversion events recovered	Effective RMS
Barrel		
No conversions recovered	0%	0.75 GeV
5x9 algorithm	52%	0.78 GeV
5x9 algorithm + dynamic algorithm	86%	0.83 GeV
Barrel + endcaps		
No conversions recovered	0%	0.78 GeV
5x9 + dynamic in the barrel + close conversions in the endcaps	80%	0.87 GeV

Table 5.7: Mass resolution for Higgs $\rightarrow \gamma\gamma$ with and without conversion events.

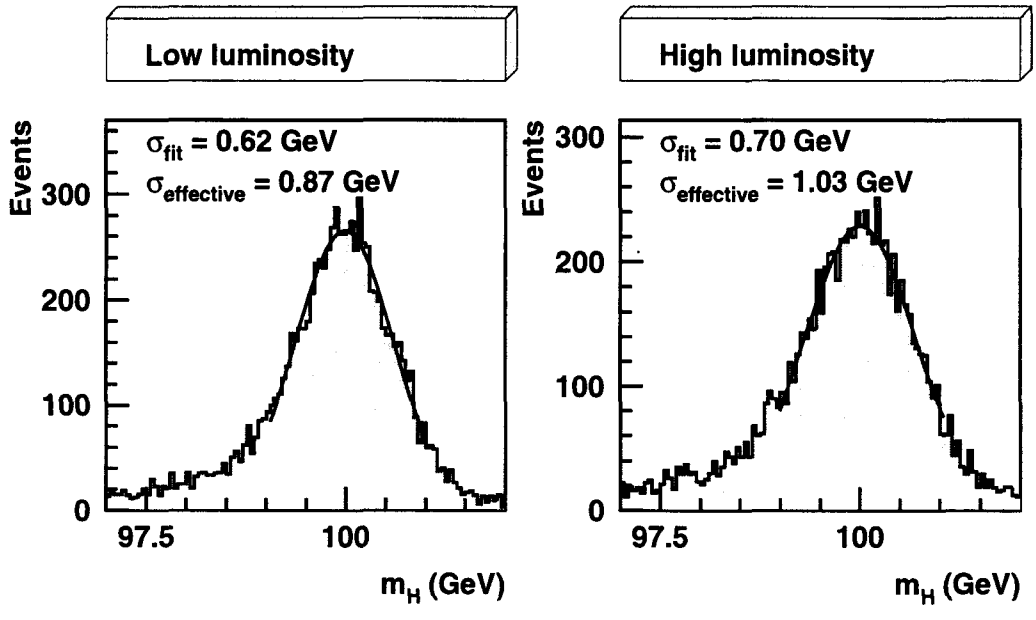

Figure 5.28: Reconstructed m_H with the low and high luminosity phase of LHC. Recovered conversions are included in the event sample.

operation. The effective RMS is found to be 0.87 GeV and 1.03 GeV for the low and high luminosity, respectively.

Any changes in the tracker geometry and material will effect the conversion probability. The opening angle between the two electrons depends on the radius where the photon converts as shown in figure 5.19 and therefore the efficiency of the 5x9 algorithm and the dynamic algorithm will change if the material distribution in the tracker changes.

5.4.4 Rejection of neutral pions

An important background to the $H \rightarrow \gamma\gamma$ channel comes from the events where a neutral pion decaying into two photons carries most of the jet energy and a jet is misidentified as a photon. The π^0 rejection is thus an important task for the electromagnetic calorimeter. It has been studied in [63] and the main results are summarised here.

In the barrel, the minimum separation of the photons from a π^0 of $p_T = 25$ GeV is 15 mm when they strike the crystals. The crystal lateral size being 22 mm, a large rejection factor is feasible using the lateral shower shape measured in 3x3 crystals. The separation, and the rejection factor, decreases with p_T. Figure 5.29 shows the fraction of rejected π^0's in the barrel requiring a photon efficiency of 90%.

In the endcaps, the preshower device is used to identify the neutral pions. The strip pitch of 1.9 mm is small compared to the separation between the photons through all momentum space. The highest signal in preshower strips is compared to the total signal of 21 adjacent strips and the fraction is computed. This value is strongly peaked for the single photons and has a large tail on the lower side for the photons from a π^0. Figure 5.30 shows the percentage of rejected π^0's in the endcaps requiring 90% photon efficiency.

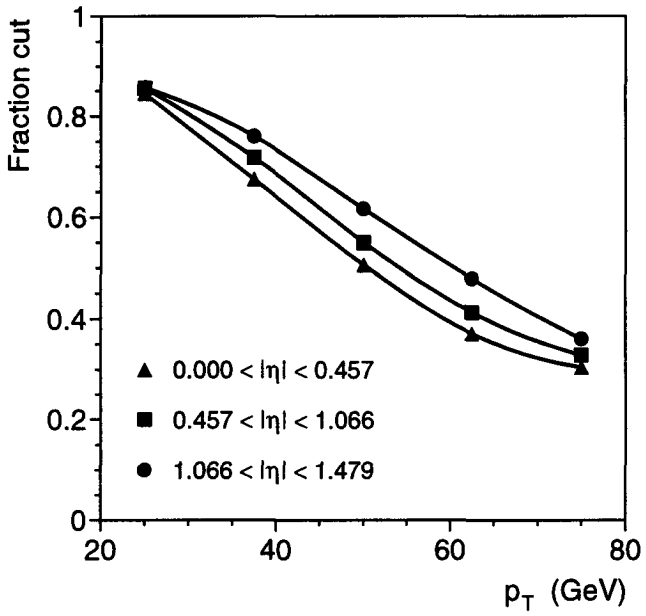

Figure 5.29: π^0 rejection in the barrel, using the lateral shape of the cluster, as a function of p_T, for 90% photon efficiency.

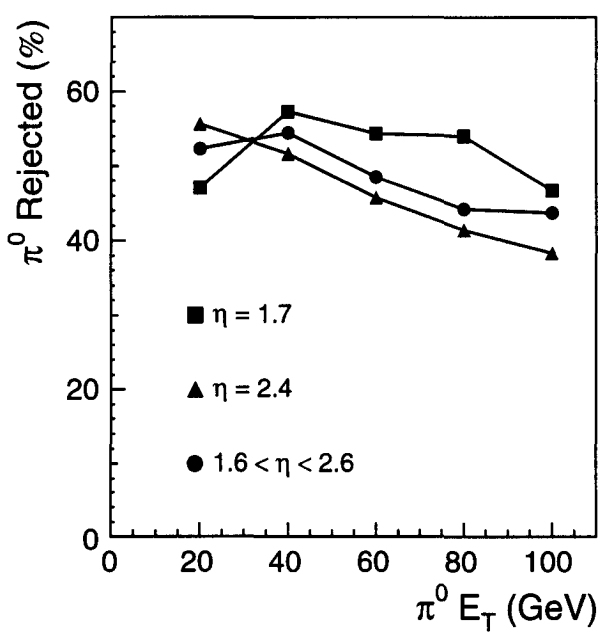

Figure 5.30: π^0 rejection in the endcaps, using the preshower information, as a function of p_T, for 90% photon efficiency.

It can be concluded that a π^0 rejection factor of about 2 can be reached over most of the momentum and pseudorapidity space.

	$1.4 \cdot \sigma_{fit}$	% events in mass window
Low luminosity	1.4·0.62 GeV = 0.87 GeV	72%
No conversions	1.4·0.57 GeV = 0.80 GeV	70%
Barrel only	1.4·0.60 GeV = 0.84 GeV	70%
High luminosity	1.4·0.70 GeV = 1.05 GeV	70%

Table 5.8: Mass windows and efficiencies for $H \rightarrow \gamma\gamma$.

5.4.5 Summary on photon measurement

For the CMS crystal calorimeter the Higgs $\rightarrow \gamma\gamma$ mass resolution for m_H=100 GeV is shown to be 0.77 GeV for the events with no conversions within the central tracker, assuming the low luminosity phase of LHC. The event sample includes the photons that convert late in the tracker cables and they cause only a small degradation in resolution.

Recovering 52% of the 42% of events with a conversion in front of the barrel within the tracker volume with an algorithm measuring the energy of the converted photon in 5x9 crystals increases the mass resolution to 0.78 GeV and recovering an additional 34% of conversions with the help of a dynamic algorithm increases the mass width to 0.83 GeV. Recovering further the conversion events where the impact points are less than 4 cm apart in front of the endcaps increases the mass width to 0.87 GeV. Thus, a good fraction of conversion events can be recovered with only a small degradation of the mass resolution.

For the high luminosity the mass width is found to be 1.03 GeV.

The mass windows and efficiencies that are used for the $H \rightarrow \gamma\gamma$ analysis in chapter 6 are summarised in table 5.8.

It has been shown that the photon measurement in CMS allows an excellent mass resolution for Higgs decaying into two photons. The geometrical effects, such as leakage from the measuring volume, and cracks and gaps in the calorimeter, or the material in front of the ECAL do not degrade the energy measurement if care is taken in the detector design.

5.5 Electrons

An electron can be identified as a concentrated energy deposit in the electromagnetic calorimeter with an associated track of similar momentum in the inner detector. The track is bent in the transverse plane and transverse momentum (in GeV) is computed from

$$p_T = 0.3RB$$

where B is the magnetic field (Tesla) and R the bending radius of the track (metres). The momentum measured in the tracker should match with the energy measured in the calorimeter.

Most of what has been said of the electromagnetic clusters initiated by the photons is valid also for the electron clusters. The main additional feature is the radiation of

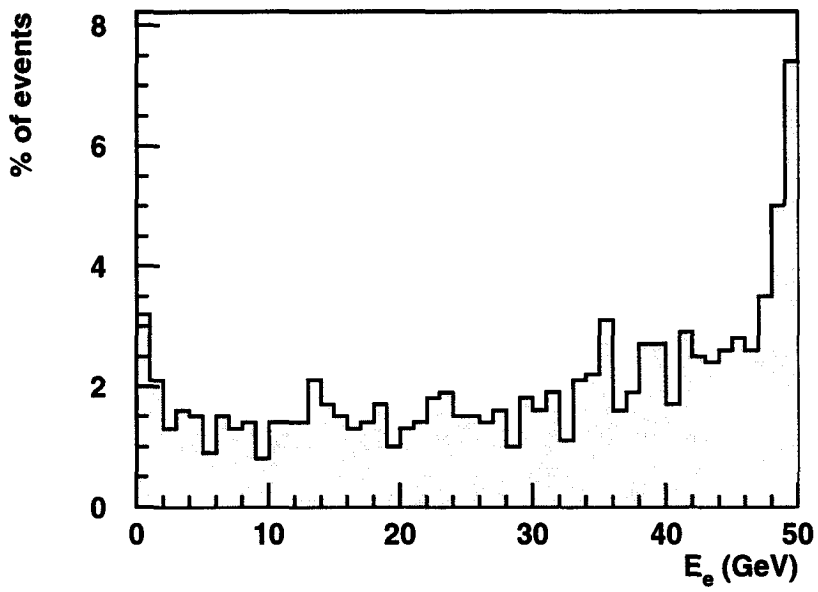

Figure 5.31: Energy distribution on the ECAL front face of 50 GeV electrons which traverse the tracker material at $\eta = 1.0$. Only the energy carried by the electron itself is plotted, excluding all energy carried by Bremsstrahlung photons.

photons (Bremsstrahlung) induced by the material of the inner tracker. On contrary of the conversion of photons which divides the photons in two categories: the non-converted, "good" photons and the converted "bad" photons, electrons radiate all along their path and every electron loses some energy before the electromagnetic calorimeter. Figure 5.31 shows the energy distribution of a 50 GeV electron at $\eta = 1.0$ on the calorimeter front face excluding all energy radiated by photons. It can be seen that most of the electrons lose a considerable fraction of their energy before reaching the calorimeter. However, the radiation is emitted along the tangent of the trajectory and thus, if the electron energy is high enough and consequently the curvature of the track is small enough, the energy emitted arrives to the calorimeter front face close to the original electron. Thus, the effect of the Bremsstrahlung photons is important in the case of rather low energy electrons and in the case of a radiation of a high-energetic photon. The transverse momenta that causes a charged track to deviate from its initial direction by one crystal width is 45 GeV, by two crystal widths is 23 GeV and by three crystal widths is 15 GeV. Therefore, if the radiation is soft, only the measurement of electrons below roughly 15 GeV p_T suffer from Bremsstrahlung. If the radiation is hard, the electron loses a large amount of energy and changes its direction. The spectrum of the Bremsstrahlung photons from a 50 GeV electron is shown in figure 5.32. In this example case, 22% of the electrons radiate one or more Bremsstrahlung photons with more than half of the original electron energy. The actual damage to the energy measurement depends how early the emission happens, the worst case being an emission at small radius: the electron loses its energy and the magnetic field deviates it far from its original path. For such cases, a special algorithm has been developed to recover the Bremsstrahlung photons[64].

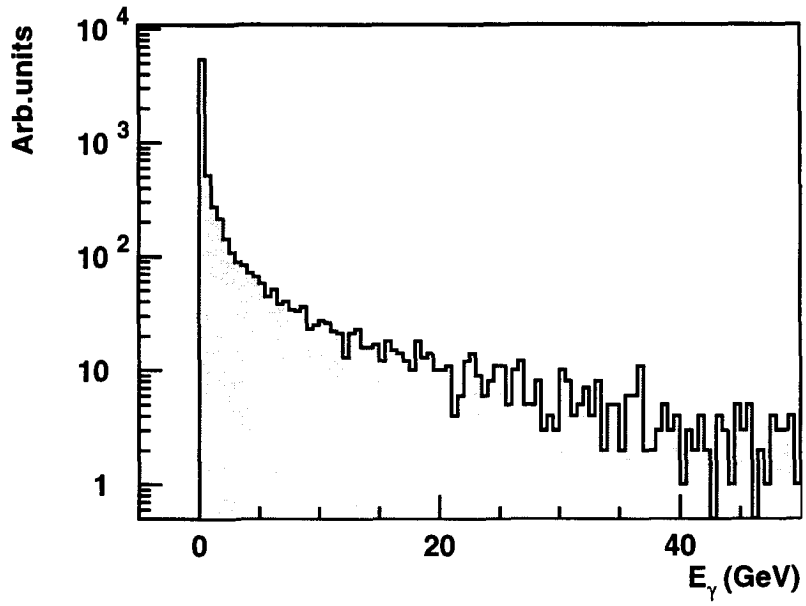

Figure 5.32: Energy distribution of Bremsstrahlung photons emitted from 50 GeV electrons traversing the tracker material at $\eta = 1.0$.

In addition to Bremsstrahlung caused by the material, an electron loses energy by synchrotron radiation due to the curvature of its track in the magnetic field. The effect is less important and can be estimated from the energy loss per revolution of a high-energy electron[65]

$$\delta E_{rev} \text{ (in MeV)} \approx 0.0885(E_T(\text{ in GeV}))^4/R \text{ (in m)}$$

where R is the radius of the curvature of the electron track. In CMS the fraction of the complete revolution of the particle track before the electromagnetic calorimeter barrel is approximately $1.3/(2\pi R)$. This is true for all tracks with a large enough bending radius (e.g. $p_T = 10$ GeV electrons has a bending radius of 8.3 m). With $R = p_T/(0.3B)$, with B = 4 Tesla and with $E_T \approx p_T$ the energy loss of an electron via synchrotron radiation in front of the CMS electromagnetic calorimeter barrel becomes

$$\begin{aligned} \delta E \text{ (in MeV)} &\approx \frac{0.0885(E_T(\text{ in GeV}))^4}{R}\frac{1.3}{2\pi R} \\ &= \frac{1.3 \cdot 0.0885 \cdot (0.3 \cdot 4)^2 (E_T(\text{ in GeV}))^2}{2\pi} = 0.0264(E_T(\text{ in GeV}))^2 \end{aligned}$$

The synchrotron energy loss as a function of the electron transverse momentum is shown in figure 5.33. The photon spectrum is very soft and therefore the overall effect is a bit lower than expected energy response from the calorimeter. However, a part of radiated photons will reach the electromagnetic calorimeter and be included in the cluster. This effect is usually not taken into account in the simulation and is negligible compared to Bremsstrahlung.

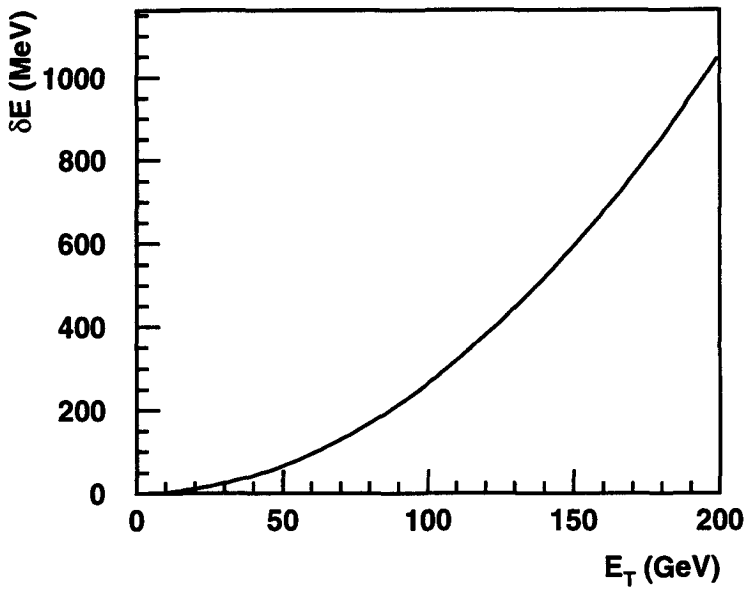

Figure 5.33: The synchrotron energy loss as a function of the electron p_T in front of the CMS ECAL barrel.

5.5.1 Energy measurement

As explained above, an electron radiates Bremsstrahlung photons when traversing the tracker material. These photons are emitted mainly along the electron path and as the photons will continue on a straight line and the electron path is curved in the magnetic field the resulting energy deposit pattern on the calorimeter is asymmetric. Therefore, the energy measurement in a 5x5 fixed window as used for the photons will not be sufficient for electrons. Two algorithms are under study: a 5x7 fixed window which is set asymmetrically to recover the energy of radiated photons[66] and a dynamic algorithm which clusters the energy in the crystals in one cluster as long as the energy in the next crystal is smaller than the previous one[67].

The method for the recovery of radiated photon energy[64] has been implemented and studied[68]. It searches for secondary clusters in an η-ϕ road where the extension in ϕ is computed from the measured E_T of the electron cluster. Detailed simulation studies[68] indicate that the dynamic clusters with the Bremsstrahlung photon recovery give better efficiency than the fixed window in terms of the fraction of events inside $\pm 2\sigma$ or $\pm 3\sigma$ around the peak value for $E_T = 10$ GeV electrons and the two methods are comparable for $E_T = 30$ GeV.

5.5.2 Momentum measurement

The momentum measurement of the electrons is done in the tracker. For the electrons which radiate a hard Bremsstrahlung photon, a recovery procedure is applied[69]. The recovery procedure identifies badly reconstructed electrons by performing a χ^2 fit based on the track and electromagnetic cluster positions and on the E/p estimate. For poorly

reconstructed tracks, the transverse momentum is recalculated using the shower barycentre, the beam constraint and the hit is the first pixel layer. For more than 95% of the reconstructed electrons the E/p ratio is in the range $0.85 < E/p < 1.2$. With the Bremsstrahlung recovery, the efficiency to reconstruct electron with $p_T > 10$ GeV is larger than 90% even in the η region where the tracker material budget is at largest.

5.6 Optimisation of the tracker cable layout

It has been emphasised above that the energy resolution of the electromagnetic calorimeter may deteriorate due to the material after the measuring tracker layers. A photon may convert to an electron-positron pair and lose energy and generate a tail in the photon energy resolution. For the electrons, the effect is somewhat hidden by the radiation of the Bremsstrahlung photons already earlier in the tracker: the methods used to recover the energy of the emitted photons partially recover the damage due to the material after the active elements of the tracker.

To optimise the layout, different cable arrangements have been investigated[70] starting from the tracker description in the technical proposal (TP). In the TP description the tracker cables were drawn out from the tracker cylinder in the space between the tracker and the electromagnetic calorimeter barrel inner radius. Figure 5.34 shows the distribution of the reconstructed energy of photons in three different η ranges for non-converted photons and for late conversions. In this study the late conversions are considered the ones that happen at a radius which correspond to a distance smaller than 29 cm (radially) from the crystal front face. The active tracker layers end at a distance of 24 cm from the crystal front face. The photons have the energy spectrum and rapidity of the decay photons of 100 GeV Higgs and the reconstructed energy has been normalised to the initial energy of the photon. The energy is measured in 5x5 crystals around the crystal with the maximum energy deposit. The degradation of the energy measurement is clearly visible, and it is more pronounced in the high η range where there are more cables and where the photon track in the cable material is longer.

5.6.1 Simulation setup

The simulation study uses CMSIM package, with a detailed description of the tracker as defined in the CMS technical proposal[32] and the crystal geometry[71].

The part defining the cables in the tracker geometry has been modified: three cable geometries have been used to find the optimal solution from the point of view of photon energy resolution. In all cases the cable volume is kept constant. The cable material consists of aluminium, polyethylene, optical fibres and cooling fluids and it is approximated by a uniform mixture with an average atomic weight of A = 18 and an average atomic number of Z = 9. The average density is estimated to be 2.2 g/cm^2 and the radiation length $X_0 = 14.1$ cm.

In the default case the cables are not uniform in ϕ but are combined in 8 segments. From each tracker wheel a new bunch of cables is added to segments. The depth (r_{max}-r_{min}) of the cables is constant in every wheel. The 1.5 cm tracker support lays outside

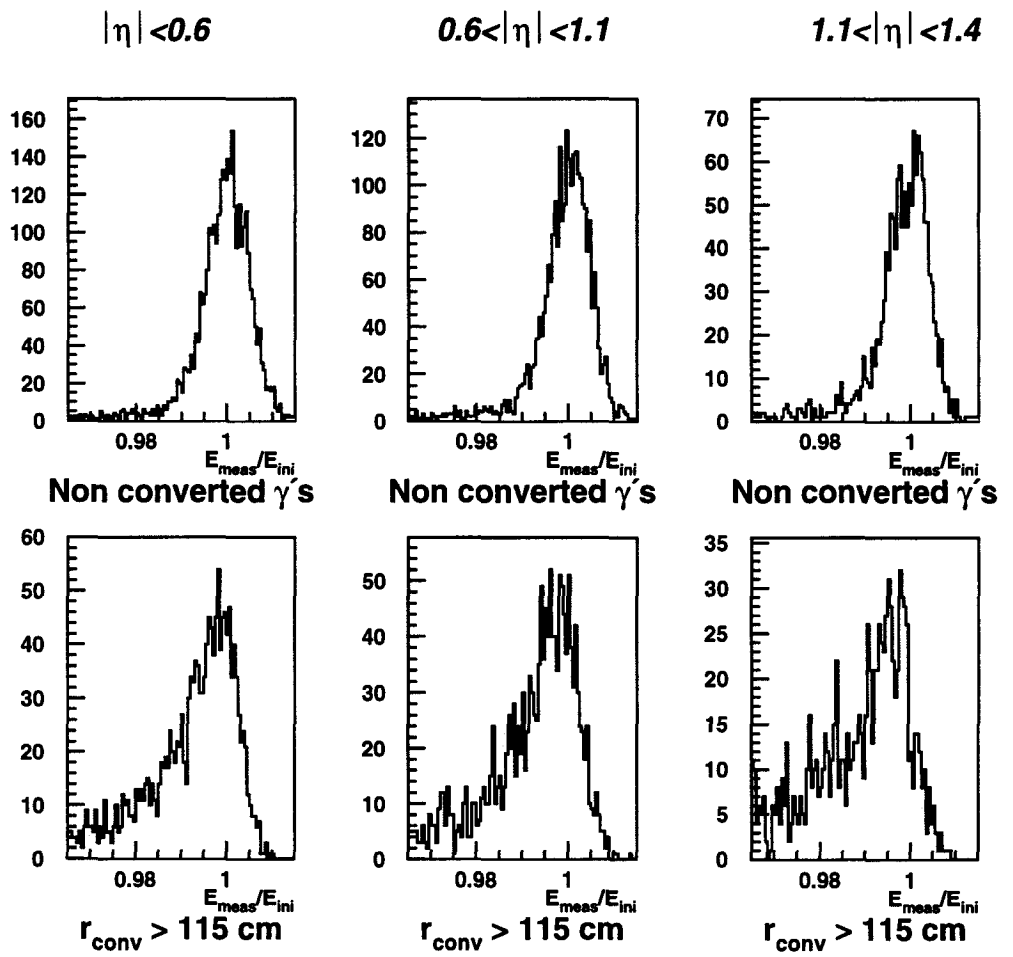

Figure 5.34: The energy distribution normalised to the incident energy of photons from the decay of a Higgs boson with a mass of 100 GeV. The distributions for non-converted photons are shown on the top and the distributions for photons that convert late (less than 5 cm from the end of, or after, the active tracker volume).

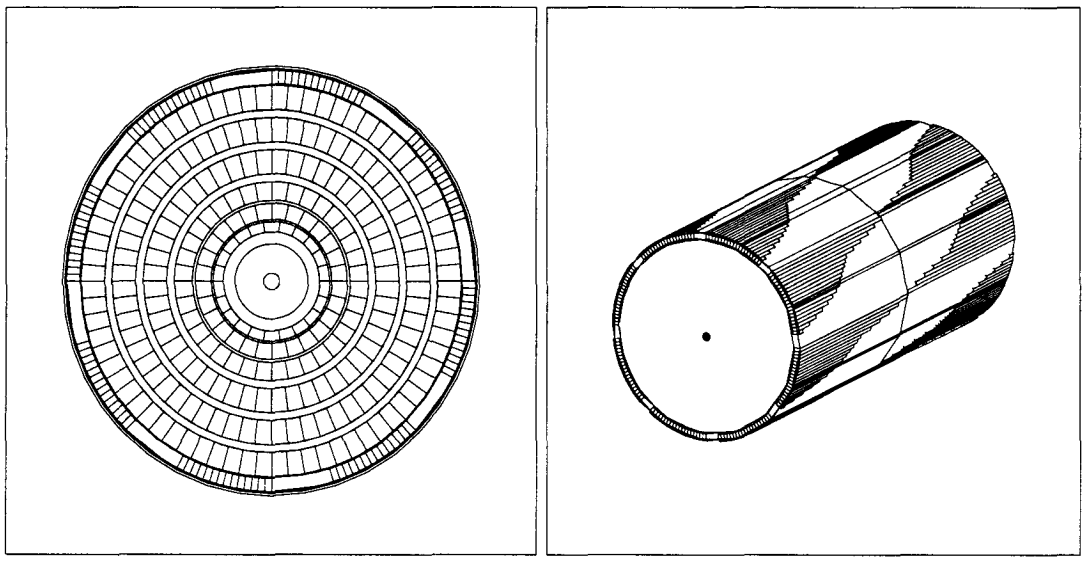

Figure 5.35: The default configuration for the cables.

Distance from crystals		Default	1st modification	2nd modification
Tracker	r_{min}	14.5 cm	24.0 cm	4.5 cm
support	r_{max}	13.0 cm	22.5 cm	3.0 cm
Cables	r_{min}	24.0 cm	22.5 cm	defined by volume
	r_{max}	15.5 cm	defined by volume	4.5 cm

Table 5.9: Main parameters of the three cable geometries studied.

the cables (see figure 5.35).

In the first modification (figure 5.36) the tracker support structure is brought inside the cables. The cables are uniform in ϕ and the maximum radius of the cables at each wheel is defined so that the cable volume stays the same as in the default case.

In the second modification (figure 5.36) the tracker support is brought up to 2 cm from the electromagnetic calorimeter support and the cables are places just inside the support tube. The minimum radius of the cables at each wheel is defined so that the cable volume stays the same as in the default case. The main parameters of the three different options are shown in the table 5.9.

To study the differences, samples 85 GeV photons at $\eta = 1.25$ have been simulated. 85 GeV is the most probable decay photon energy from 100 GeV Higgs around this η value. Only the photons converting in the last 5 cm of the active tracker volume and in the space between the tracker and the ECAL support structure are simulated. The electromagnetic shower is fully simulated with GEANT3.21[49] and the energy cut below which particles are stopped is 100 keV. Using lower cuts would not change the results. The non-uniform longitudinal light transmission in the crystals is taken into account in

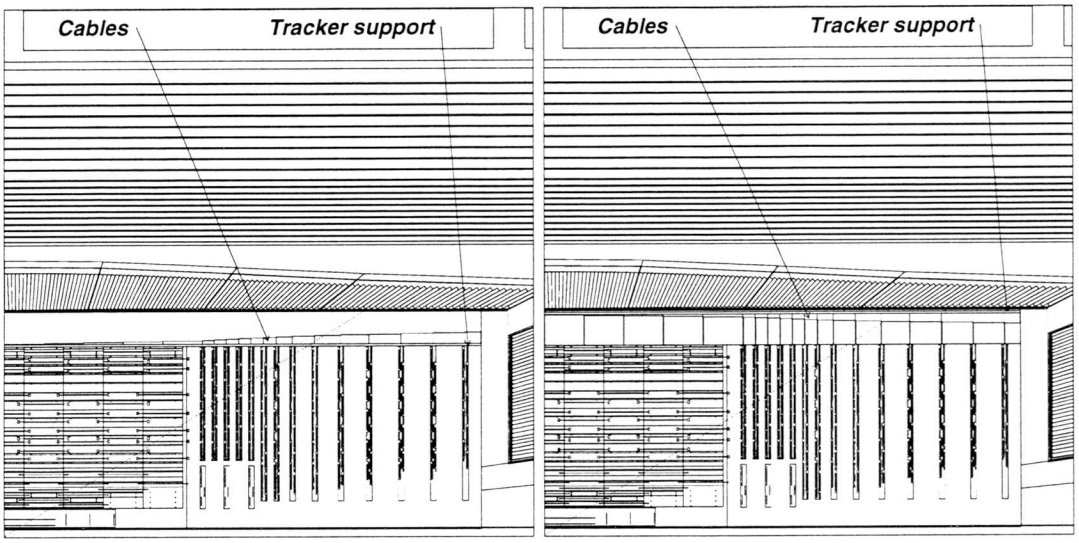

Figure 5.36: The modifications: to the left: 1st modification, cables uniform in ϕ and close to the tracker; to the right: 2nd modification, cables uniform in ϕ and close to the crystals. The line indicates the direction of η=1.25.

the simulation. The noise or the fluctuations due to the light transport are not added to the simulation results. This additional fluctuation is the major contribution to the width of the distribution but, as it has Gaussian form, the tails of the distribution will remain unchanged.

5.6.2 Results

The energy of the converted photons is measured in an array of 5x5 crystals around the one containing the maximum energy deposit. Figure 5.37 shows the photon energy distribution normalised to the incident energy for the three different cable arrangements. The low-energy tail is very pronounced in the default case. In the first modification where the cables are uniform in ϕ but far from the crystals, the tail diminishes but does not disappear. In the second modification where the air gap between the cables and the crystal is reduced, the tail disappears. The fraction of the events contained within $\pm$ 1, 2 and 3 Gaussian σ's of the non-converted photons (σ=0.27%) is shown in table 5.10 for the non-converted photons and for the late conversions in the three cable geometries. The efficiency of the late conversions in the second modification is only slightly worse than that of non-converted photons and clearly better than in the other configurations. The reasons for the improvement is studied by considering the energy deposited in the cables.

The energy deposit in the cables is recorded. The cable is divided into bins in η, each bin with a width of $\Delta\eta = 0.0145$ i.e. the width of the crystal in the TP design. In figure 5.38 the energy deposit in the cables is plotted as a function of the distance in crystal widths from the photon direction. In the default case, the energy deposit is highest in the area where the photon hits the cables but it rises again several crystal widths away from

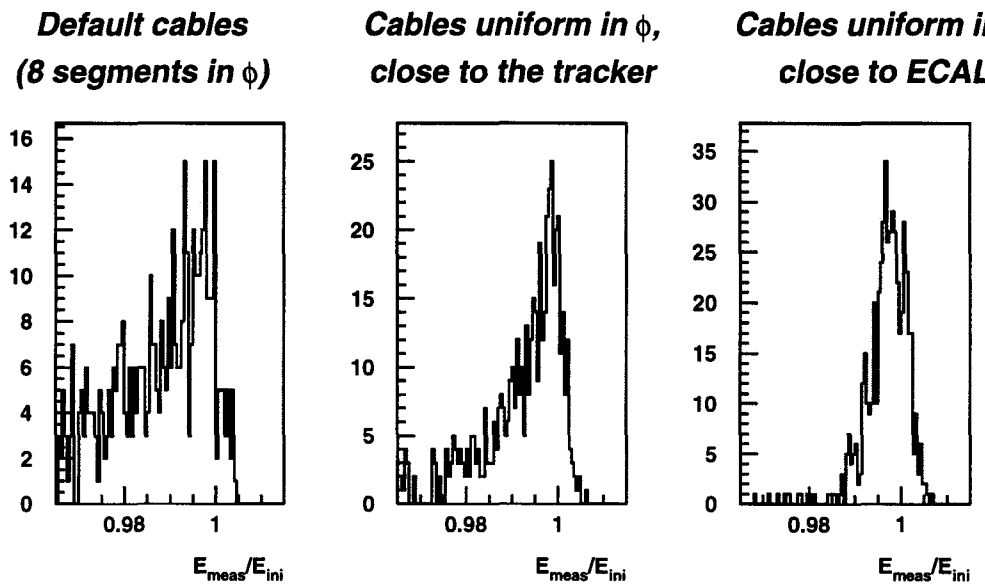

Figure 5.37: The energy distribution of 85 GeV photons at $\eta = 1.25$ converting late in the tracker (less than 5 cm from the end of, or after, the active tracker volume) for three different cable geometries.

	Non converted γ's	Default	1st modification	2nd modification
$\pm 1\sigma$	54.2%	15.1%	32.7%	43.6 %
$\pm 2\sigma$	78.2%	28.2%	48.5%	70.8 %
$\pm 3\sigma$	85.4%	36.6%	59.2%	84.5 %

Table 5.10: Fraction of the events contained within 1, 2 and 3 Gaussian σ's for the non-converted photons and for the late conversions in the three different cable arrangements. In each case σ of the distribution for non-converted photons is used and the window is centred at its mean value.

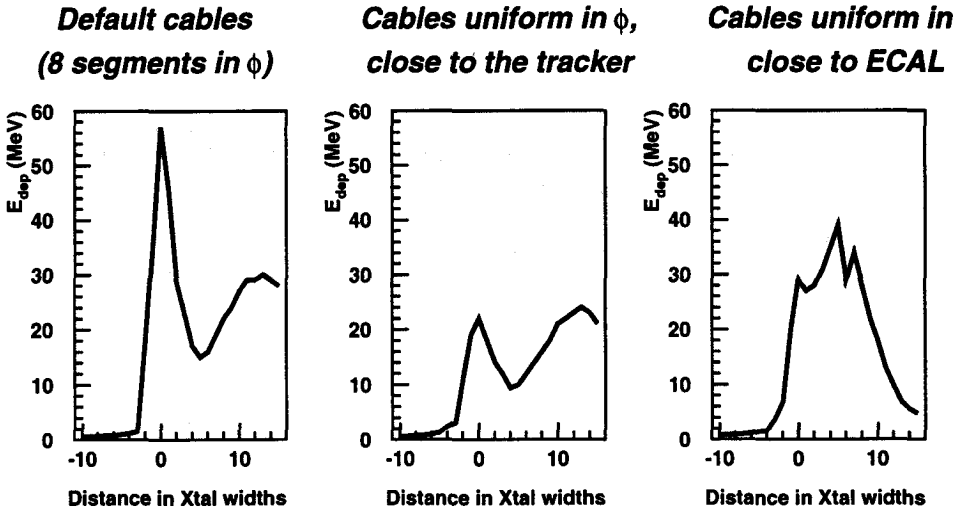

Figure 5.38: The energy deposit of 85 GeV converted photons in the tracker cables. The cables have been divided into η-bins, each bin corresponding to the crystal width. The distance is measured from the photon incident direction and the positive direction of the x-axis corresponds to the increasing η. The total energy deposit in the cables is 0.69 GeV for the default case and 0.45 GeV and 0.44 GeV respectively for the two modifications.

the hit. This is due to the low energy secondary particles generated in the cable material that curl in the air gap due to the 4T magnetic field. If they do not have enough energy to reach the crystals they curl back to the cables and deposit their energy in the cables far away from the incident point.

In the first modification, the energy deposited in the cables is less than in the default case: the total energy deposit is 0.45 GeV instead of 0.69 GeV with the default case. This is due to the fact that the converted photon sees less material as the cables are uniformly distributed in ϕ. However, the energy deposit far from the interaction point is not reduced.

In the second modification, the energy deposit in the cables is concentrated around the impact point and 2–3 crystal widths towards high η. There is much less energy deposit far away from the hit as in the two other cases. This is due to the reduced air gap (2 cm); the secondary particles that curl in the magnetic field will hit the crystals instead of bending back into the cables. The total energy deposit in the cables is 0.44 GeV.

5.6.3 Conclusions on the cable layout

It is shown that the air gap between the tracker cables and the electromagnetic calorimeter has to be as small as possible. Otherwise some secondary particles from the interactions in the cables curl in the magnetic field and their energy will be lost in the cables at a point away from the impact point. The amount of energy lost in the cables can also be reduced by placing the cables uniformly in ϕ, but this is not enough to reduce the leakage towards

high η: the air gap is the main reason for the degradation of the energy measurement.

These considerations have been taken into account in the layout of the region between the electromagnetic calorimeter and the inner tracker[37]. The calorimeter radius has been brought closer to the tracker and the tracker services are brought out in the endcap region where the damage caused to the energy resolution is smaller due to the presence of the preshower.

Chapter 6

Higgs searches

Yesterday's sensation
is today's calibration
and tomorrow's background.

This chapter gives an up-to-date overview of the discovery potential of the Standard Model Higgs boson in CMS. First, the simulation and analysis tools are described. Then, the general kinematics of a Higgs event is discussed. The significance of the main Higgs decay channels is presented: new studies are shown for $H \rightarrow \gamma\gamma$ and $H \rightarrow ZZ \rightarrow 2\ell 2\nu$ channels, for the other channels recent studies are reviewed and some old studies are updated. The next to leading order (NLO) contributions to the signal cross-sections are included. For the background processes, NLO corrections are applied in cases where they are known. The results are then combined to show the significance over the full Higgs mass range.

In some of the processes, the discovery potential is dominated by the detector performance. This is the case for the two photon channel where the natural width of the Higgs boson is very narrow and the performance in the channel is entirely dictated by the precision of the electromagnetic calorimeter measurement. In such cases it is important to estimate the detector performance as precisely as possible. This is done by full shower simulation as described in chapter 5. When, instead, the width of the Higgs particle is large, the dominating effects on the discovery potential are the uncertainties of the physical processes themselves. In these cases, the performance of the detector — as far as it is well understood — has less effect on the physics results and full shower simulation has not been carried out. However, a good missing E_T resolution is essential in the channels where $\not{E}_T$is used in the event selection. In all channels, the efficiencies for the lepton identification are applied to the results.

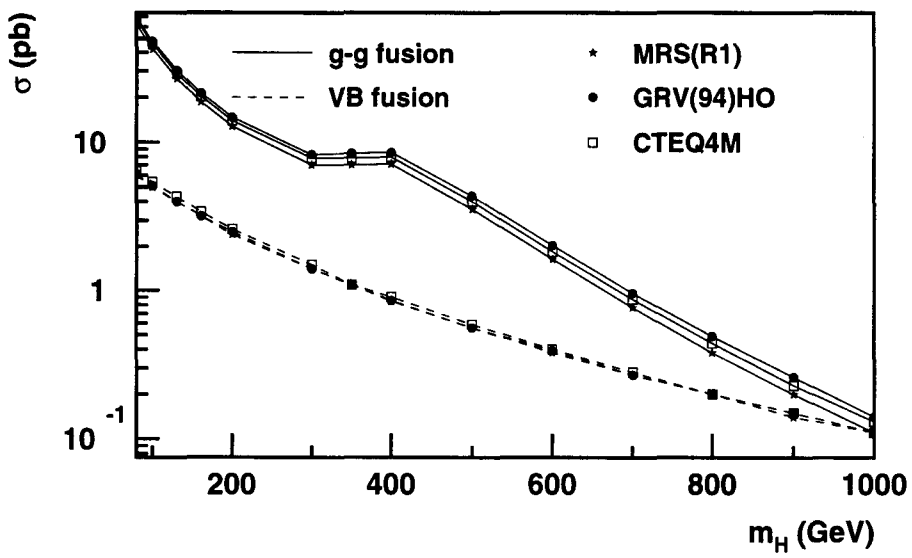

Figure 6.1: Higgs productions cross-sections with MRS(R1), GRV(94)HO and CTEQ4M parton distribution functions including the NLO correction[72].

6.1 Simulation and analysis tools

Simulation

The event kinematics simulation program used to generate the signal and background event samples is PYTHIA[50]. It produces proton-proton events with a required centre of mass energy (14 TeV) by picking up the colliding partons according to the parton distribution functions. It generates the chosen processes and lets the generated final states decay into the allowed decay modes. The secondary quarks and gluons generate jets by hadronization process, and the resulting hadrons or leptons are allowed to decay into stable particles. The user can define the relevant decay modes for all particles.

PYTHIA uses the leading order cross-sections for the processes. As discussed in chapter 2, the next to leading order processes modify the cross-section sometimes considerably. The appropriate NLO corrections are applied as described in [72] and the default parton distribution function of PYTHIA is changed to be compatible with the NLO computations. The difference between some recent parton distribution functions is illustrated in figure 6.1 and is fairly small (5 – 20% depending on the Higgs mass). It should be noted that the effect of the higher order corrections on the event kinematics is not taken into account by such an approach. For the Higgs signal processes, as the most important corrections to the dominating gluon gluon fusion production mechanism are due to soft gluon radiation it is expected that the change in the kinematics is small. For the background processes where the NLO contributions consist of hard scattering the event kinematics can change considerably. However, in the absence of a NLO event generator, these processes are taken into account by applying a K-factor to the LO processes. In the following, the main aspects of the background cross-sections and their simulation are discussed.

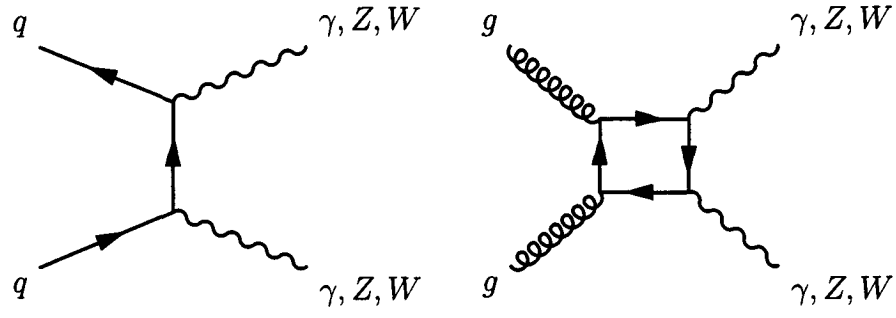

Figure 6.2: The Feynman diagrams for the most important gauge boson pair production processes: Born and box diagrams.

The Standard Model Higgs discovery channels discussed here proceed through a pair of gauge bosons. Therefore, the main background processes to the Higgs particle come from the non-resonant production of photon and vector boson pairs. In addition, there are processes where the final state is misidentified, e.g. a jet is misidentified as a photon or as an electron or missing p_T signal due to the unmeasured jet outside the detector acceptance is misidentified as a neutrino.

Gauge boson pairs are produced through the Born process of quark-antiquark scattering ($q\bar{q} \to \gamma\gamma$, $q\bar{q} \to ZZ$, $q\bar{q} \to W^+W^-$, and $q\bar{q}' \to W^\pm Z$) or through gluon fusion ($gg \to \gamma\gamma$, $gg \to ZZ$, and $gg \to W^+W^-$). Diagrams for the basic contributions of these processes are shown in figure 6.2. In addition, the $t\bar{t}$ production followed by $t \to Wb$ results in a W^+W^- pair.

Recent studies on the background processes are shortly summarised.

Two-photon continuum The leading order process contributing to the two-photon background is

- Born process ($q\bar{q} \to \gamma\gamma$).

However, cross-sections of the same order are obtained from higher order processes such as [73]

- box process ($gg \to \gamma\gamma$)
- single and double photon Bremsstrahlung from an outgoing parton line.

The gluon fusion box diagram is of order $\alpha^2\alpha_s^2$ but due to the large gluon luminosity in hadron collisions it gives a contribution which is comparable to the Born quark-antiquark scattering. The Bremsstrahlung process is a higher order correction but due to the behaviour of the quark fragmentation functions ($\approx \alpha/\alpha_s$, α_s in the denominator cancels one order of α_s in the nominator) which define the photon emission from the parton line, the process is effectively of the same order as the LO contribution of $q\bar{q} \to \gamma\gamma$. The Born and box processes have been implemented in PYTHIA. The photon emission from an incoming or an outgoing quark line is also included.

The other NLO contributions are the remaining order α_s contributions to the Born process. These have been calculated in [74] including

- real gluon emission ($q\bar{q} \to \gamma\gamma g$)

- real photon emission ($gq \rightarrow \gamma\gamma q$)
- virtual one-loop corrections to $q\bar{q} \rightarrow \gamma\gamma$.

Defining the border line between the Bremsstrahlung process where the photon is emitted collinearily from the outgoing quark line and between the hard process of $gq \rightarrow \gamma\gamma q$ is not evident. The same is true for the soft gluon emission. If the NLO contributions are taken into account with a K-factor, care must be taken to avoid double counting of these processes. The details will be discussed together with the $H \rightarrow \gamma\gamma$ channel.

Di-boson production The NLO contributions to the quark-antiquark scattering have been computed and compared to the leading order processes for ZZ in [75], for WW in [76] and for ZW in [77]. The K factors to be applied to the leading order contribution are found to be 1.25, 1.4 and 1.5–1.6 for ZZ, WW and WZ processes, respectively[72].

It should be noted that the kinematics of a vector boson events may change considerably as the most of the NLO contributions result in a jet emission in the event. In the absence of any jets, the vector boson pair has to be back to back, leading to a relatively low p_T spectrum for the di-boson system. If, instead, there is a jet in the event the p_T of the di-boson system has to balance the jet p_T thus giving much higher p_T distribution. It has been shown in [78] that the NLO contributions cause a long tail in the p_T distribution of the ZZ system which is not present in the LO Monte Carlo programs such as PYTHIA.

It should also be noted that the event selection criteria may affect differently the LO and NLO contributions. In [79] it has been shown how the NLO contribution to the background of ZZ, WW and WZ decaying into leptons is removed if a jet veto is applied in the analysis stage. However, this also indicates how easily the validity of any constant K factors may be affected by the event selection criteria.

Due to the complexity of the gluon fusion diagrams, only the leading order contributions have been computed for most of the processes. The gg contribution has been estimated to be 33% of the $q\bar{q}$ rate for the ZZ production[80]. The kinematics of $gg \rightarrow ZZ$ events is similar to $q\bar{q} \rightarrow ZZ$ events. However, as indicated in [80], ZZ pairs from gluon-gluon fusion is produced more centrally than those from quark-antiquark scattering and the tail of the transverse momentum distribution of the Z boson is slightly larger. The QCD corrections for this process are not yet calculated and they may be quite important. The gluon fusion contribution to the WW production is estimated to be 10–13 %[81]. However, the estimate is quoted for $\sqrt{s} = 17$ TeV and for the top mass of 100 GeV. It can be deduced from the results presented for $\sqrt{s} = 40$ TeV and top masses of 100 GeV and 200 GeV that an increased top mass increases the relative importance of the box contribution, especially at high WW invariant masses.

The $t\bar{t}$ production is an important source of WW pairs. Including the NLO contributions gives a total $t\bar{t}$ cross-section of 760 pb[72].

Analysis

In these studies, some identification and isolation criteria are applied. The identification efficiencies for photons, electrons and muons are taken from the estimates of the detailed simulation. An object is identified as a jet if it has a required size, i.e. the resulting

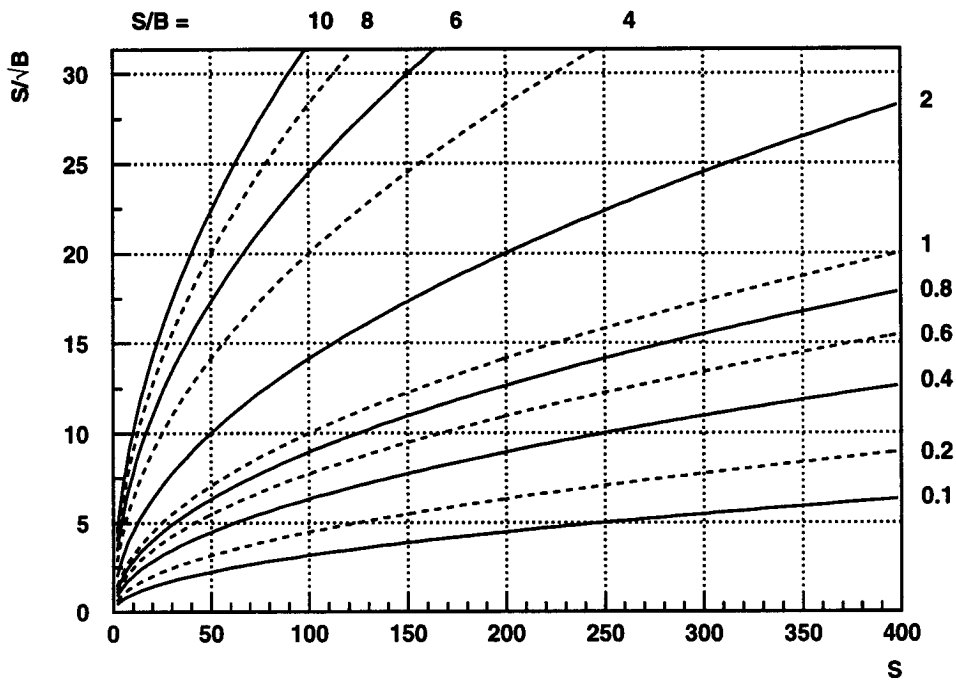

Figure 6.3: The statistical significance as a function of the number of the signal events for different signal to background ratios. This estimate of the significance is valid down to S or $B \approx 20$.

hadrons form a cluster of tracks not further away than a required ΔR cut, ΔR being defined as

$$\Delta R = \sqrt{(\Delta\eta)^2 + (\Delta\phi)^2}$$

The isolation of an electromagnetic cluster, i.e. of photons and electrons, can be based on the calorimeter information when the energy flow close to a certain ΔR cone containing the isolated observable is limited, or on the tracker information when one requires that no charged tracks above a certain p_T limit is allowed in the isolation cone.

The results are presented in terms of the statistical significance $\sigma = S/\sqrt{B}$ where S and B are the amount of signal and background events, respectively. It is assumed that 5 σ significance is needed to claim a discovery. Figure 6.3 shows the behaviour of the statistical significance as a function of the number of the signal events for different signal to background ratios. It can be seen that if the ratio between the signal and background events remains constant, the significance improves if more events can be included in the event sample. It is also obvious that a very good signal to background ratio is needed to reach the 5 σ limit if the amount of signal events is small. To claim a discovery with less than 25 signal events, the signal to background ratio must be bigger than one. It should be noted that $S/\sqrt{B}$ is not an adequate estimator of signal significance when the number of events becomes so small (< 20) that Gaussian statistics can no longer be applied.

The significance is given for a certain amount of integrated luminosity. Three years

of low luminosity running ($\mathcal{L} = 10^{33}$ cm^{-2}s^{-1}) of the LHC machine corresponds to the integrated luminosity of 30 fb^{-1}. This requires 116 full days of LHC running per year. When the design luminosity is reached, a year of running is expected to give 100 fb^{-1} excluding the effect of the luminosity decrease during a fill.

6.2 General kinematics of a Higgs event

Higgs mass

The Higgs mass is reconstructed as the invariant mass of the decay system

$$m_H = \sqrt{(\sum E_i)^2 - (\sum \vec{p}_i)^2}$$

(E_i and $\vec{p}_i$ are the energy and momentum of the decay products) if the decay particles can be directly observed. This is the case for the two photon decay and the decays through a ZZ pair with the Z bosons decaying into electrons, muons or jets. If the decay products include neutrinos ($Z \to \nu\nu, W \to \ell\nu, \tau \to \ell\nu\bar{\nu}$) the Higgs mass can be estimated from the transverse momentum distribution of the observed decay particles or from the *transverse mass* distribution of the decay system defined as

$$m_T = \sqrt{(E_{T,seen} + E_{T,miss})^2 - (\vec{p}_{T,seen} + \vec{p}_{T,miss})^2}$$

The transverse mass distribution results in a broad rising distribution which is abruptly cut at the value of the Higgs mass. The detector effects can smear the distributions considerably.

Two-body decay

All the Higgs decays considered here proceed through two equal particles: γ's, Z or W bosons. With a simple kinematics consideration one can estimate the minimum angle between the decay products. For a massless decay products, the decay angle that produces the minimum angle between the decay products is the one with the decay products perpendicular to the Higgs laboratory momentum in the rest frame of the Higgs particle as shown in figure 6.4. For massive particles also, this is the case for most of the parameter space. Only if one of the decay products flies close to the direction of the Higgs particle and the momentum of the Higgs particle is large enough to boost the backward going decay product in the forward direction, can the angle between the decay products be smaller.

The minimum angle θ between the decay products as a function of the Higgs momentum is shown in figure 6.5 $m_H = 100$ GeV decaying into photons. Even with a very high Higgs momenta the two photons are separated by more than 20°. Therefore, if only the signal event is considered, the two photons from the Higgs decay are isolated.

The final observables in the W and Z decays are fermions or missing E_T due to the unobserved neutrinos. The weak current W_μ couples to the left-handed fermions and right-handed antifermions causing the angle of the decay products to have an angular

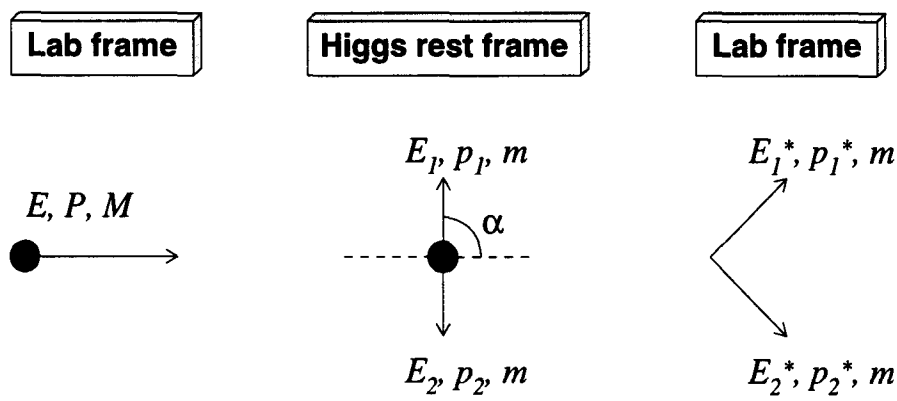

Figure 6.4: Higgs decay kinematics.

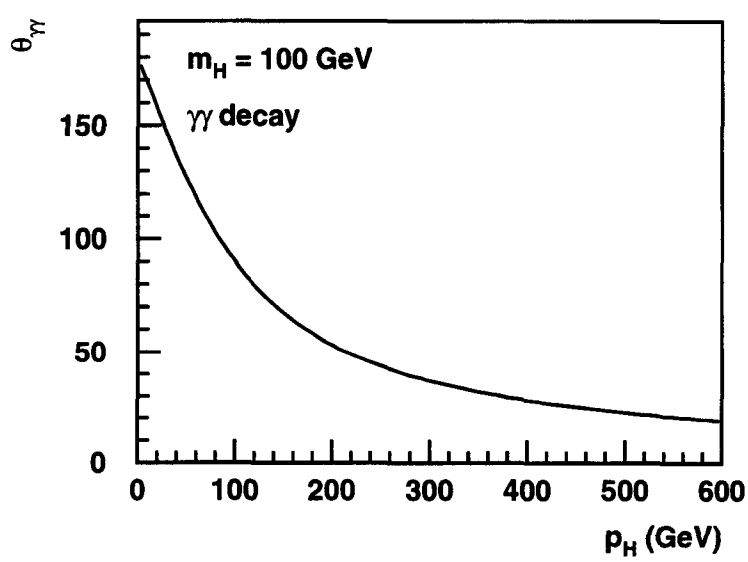

Figure 6.5: The minimum angle between the decay products of the Higgs particle (m_H = 100 GeV) decaying into two photons as a function of the momentum of the Higgs.

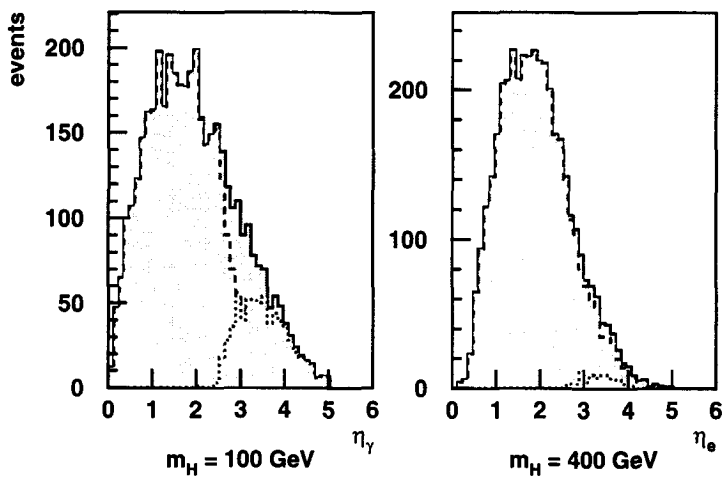

Figure 6.6: The η distribution of the decay product with the highest η in $H \rightarrow \gamma\gamma$ ($m_H = 100$ GeV) and for $H \rightarrow 4e$ ($m_H = 400$ GeV). The dashed line shows the contribution from events where Higgs has a rapidity of $|y| < 2.4$ and the dotted line that from events with Higgs $|y| > 2.4$.

dependence on the vector boson direction. The knowledge of the W or Z boson angle and spin orientations can thus be used to distinguish between the Higgs decay products and the continuum pair production as will be discussed in section 6.3.4.

Kinematics of the Higgs particle

For the final decay products to be observed, they have to fall in the detector acceptance range. For electron, photons and muons the CMS detector covers the pseudorapidity of about $|\eta| < 2.5$ and for the jets and missing E_T measurement $|\eta| < 5$. There is a strong correlation between the direction of the Higgs particle and that of the decay products. A centrally produced Higgs tends to produce central decay products. An example is shown in figure 6.6. To the right, the η distribution of the photon with the highest η from the $H \rightarrow \gamma\gamma$ decay ($m_H = 100$ GeV) is shown. To the left, the η distribution of the electron or positron with the highest η from the $H \rightarrow ZZ \rightarrow 4e^{\pm}$ ($m_H = 400$ GeV) is shown. The dashed lines gives the contribution from the events where the Higgs particle is in the rapidity range of $|y| < 2.4$ and the dotted line gives the contribution from the events with $|y| > 2.4$. For $m_H = 100$ GeV, the events in the η distribution tail which will be excluded due to the detector acceptance limit are entirely due to events with large Higgs rapidity. For higher Higgs masses, the average Higgs rapidity is smaller and the events with $|y| > 2.4$ contribute little to the total event rate.

The Higgs particle can be produced via several mechanisms which have been reviewed in section 2.4.2. The dominating production mechanism is gluon gluon fusion. The two gluons produce a quark loop which then generates the Higgs boson. The p_T distribution of the Higgs boson peaks at low p_T values for all masses although it gets broader for high

m_H	gg fusion	VB fusion
100 GeV	31.7 GeV	87.5 GeV
200 GeV	58.3 GeV	99.1 GeV
400 GeV	101.4 GeV	114.2 GeV
700 GeV	147.3 GeV	116.1 GeV

Table 6.1: Average values of Higgs transverse momentum for different Higgs masses and production mechanisms.

masses. Relatively low p_T of Higgs causes the Higgs decay products to be rather back to back than close to each other in the transverse plane. The Higgs particle has a rapidity below $|y| < 2.4$ in roughly 76% of the events for $m_H \approx 100$ GeV and in more than 90% of events for higher Higgs masses and thus most of the decay products will be covered by the geometrical detector acceptance ($|\eta| < 2.5$ for photons and electrons).

The Higgs production via a fusion of heavy vector bosons is the second important production mechanism. The two vector bosons are radiated from quark lines resulting in slightly higher average p_T for the generated Higgs particle than in gluon-gluon fusion for $m_H < 700$ GeV as shown in figure 6.7. The average values of the Higgs p_T distributions are given in table 6.1. A larger fraction of the events have the Higgs particle rapidity within $y < 2.4$: 89% for $m_H = 100$ GeV and 95%-100% for the higher ones. This will emphasise the relative importance of the vector boson fusion channel especially for the lepton and photon decays as a larger fraction of Higgs events produced by this mechanism is within the detector acceptance. In this channel, it is possible to tag the two forward jets resulting from the outgoing quarks and use these tags to discriminate the signal from background.

The Higgs production via a radiation off the vector boson line (Higgsstrahlung) is important only at low Higgs mass. The main interest of this channel is the remaining vector boson which may be detected in the detector. The p_T and the rapidity distributions of the associated vector boson are shown in figure 6.8. The decay products of the vector boson are within the reach of the experimental pseudorapidity coverage.

The Higgs radiation from $t\bar{t}$ quark line contributes only at Higgs masses below 120 GeV. The attracting feature of this channel is again the possibility of tagging the W boson from $t \rightarrow Wb$. The p_T and the rapidity distributions of these quarks are shown in figure 6.9.

Kinematics of the underlying event

The p_T of the Higgs particle is compensated by the particles of the underlying event which can form jets. Figure 6.10 shows the jet multiplicity of the Higgs events for different Higgs masses for gluon-gluon and vector boson fusion. The jet is defined here as a hadronic shower of $\Delta R < 0.5$ and $p_T > 20$ GeV within pseudorapidity range of $|\eta| < 5$. The shaded histogram shows the multiplicity of a Higgs event alone. At low Higgs masses ($m_H < 200$ GeV) it is hard to make use of the jet system as most of the events have no jets with the above definition. At higher Higgs masses, where in the dominating gluon-

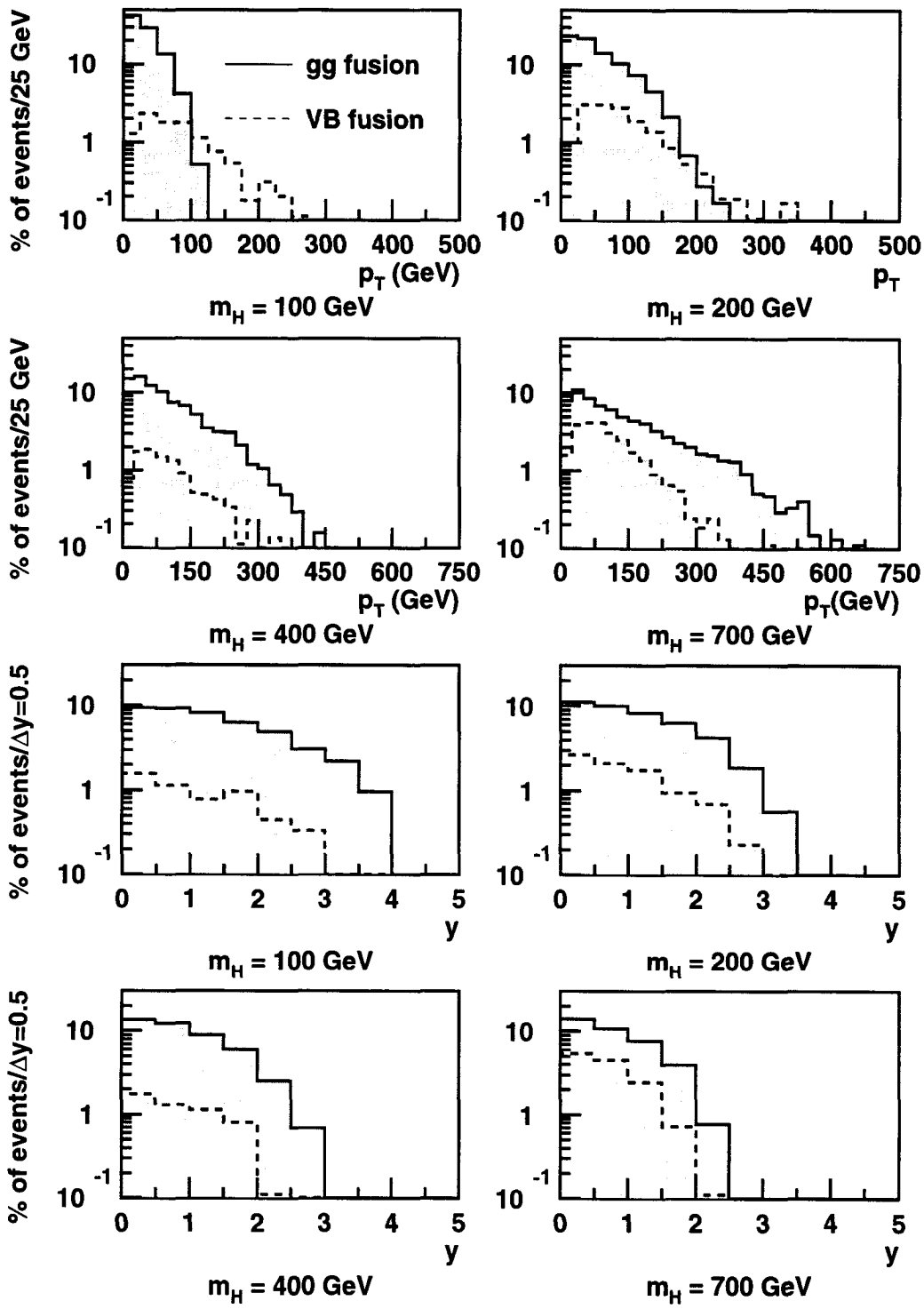

Figure 6.7: p_T and rapidity distributions of a Higgs boson for gluon-gluon fusion (continuous line) and vector boson fusion (dashed line) for different Higgs masses. The histograms are normalised to the total Higgs production cross-section.

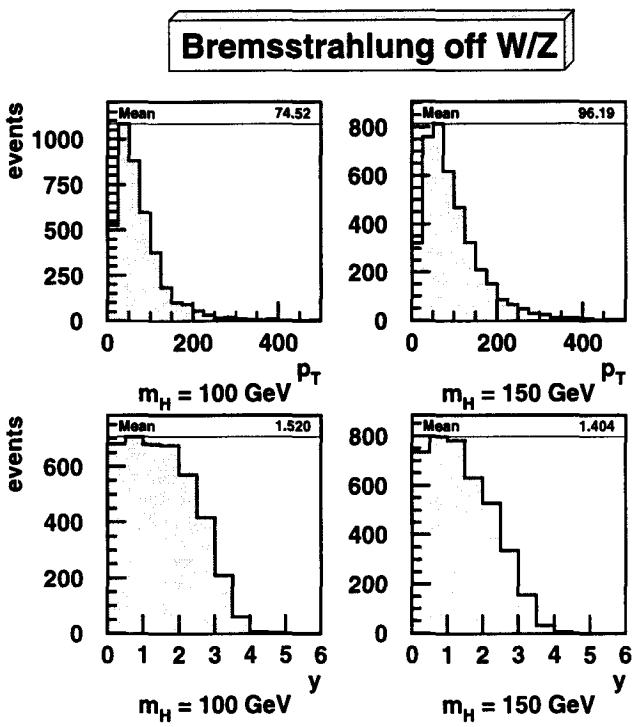

Figure 6.8: p_T and rapidity distributions of the vector boson produced in association with the Higgs particle.

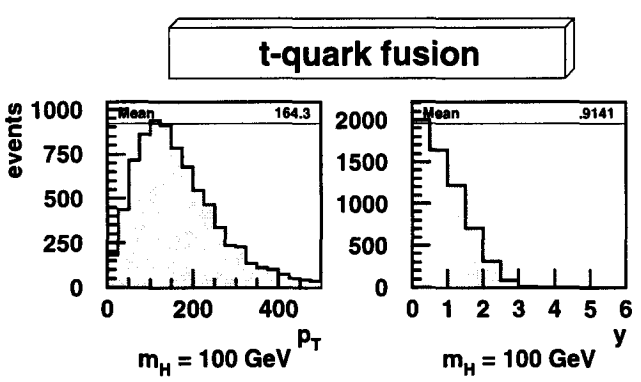

Figure 6.9: p_T and rapidity distribution of the t quarks produced in association with the Higgs particle.

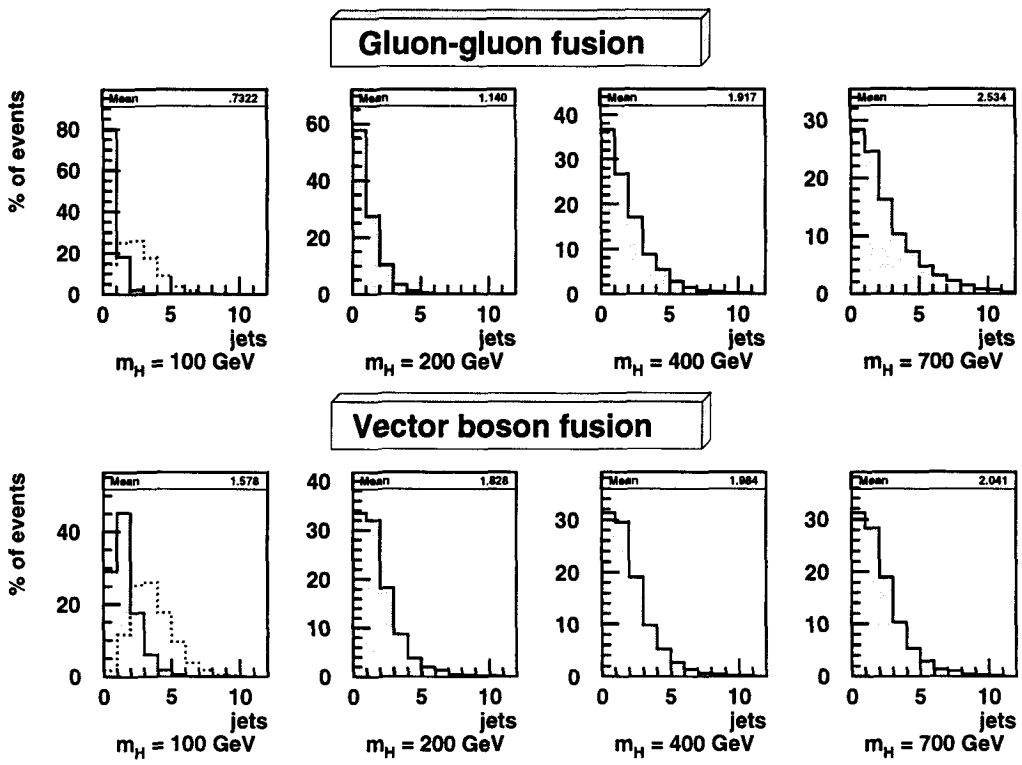

Figure 6.10: The jet multiplicity of the Higgs events for different Higgs masses and for the two most important production mechanisms. The dashed line for $m_H = 100$ GeV shows how the jet multiplicity is changed if 17.3 minimum bias events are included.

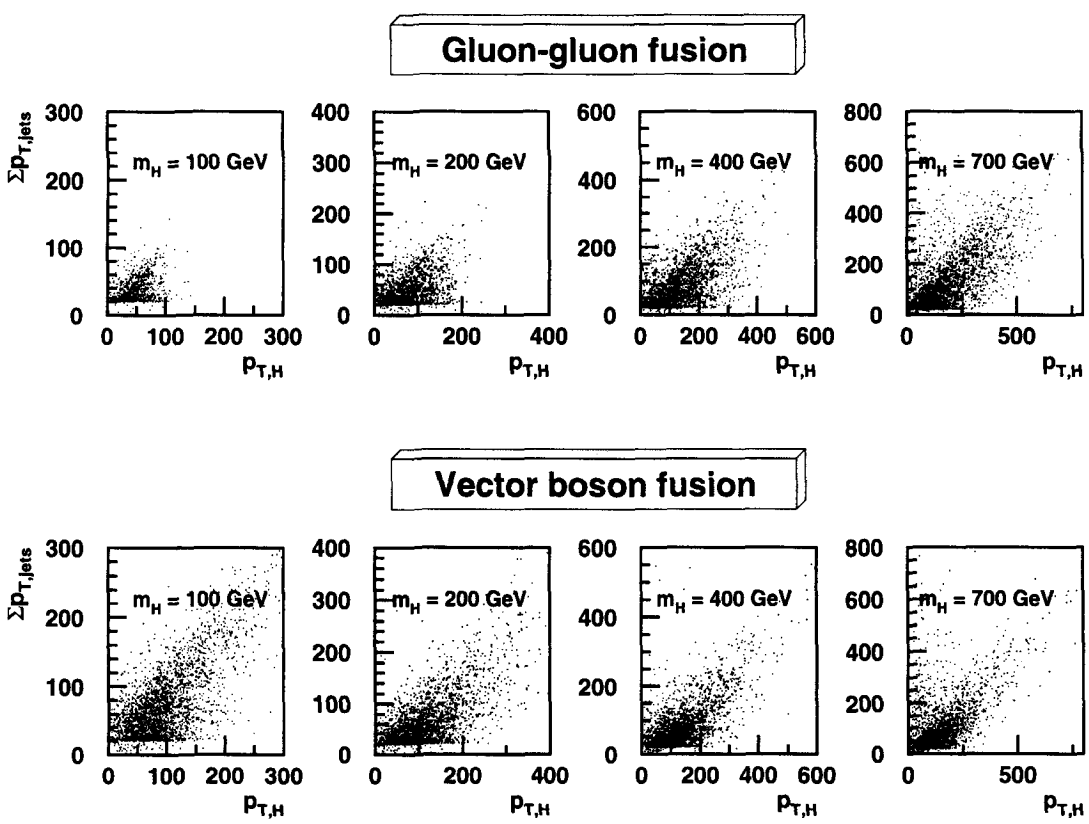

Figure 6.11: Correlation between the transverse momenta of the underlying jet system and the Higgs for different Higgs masses and production mechanisms.

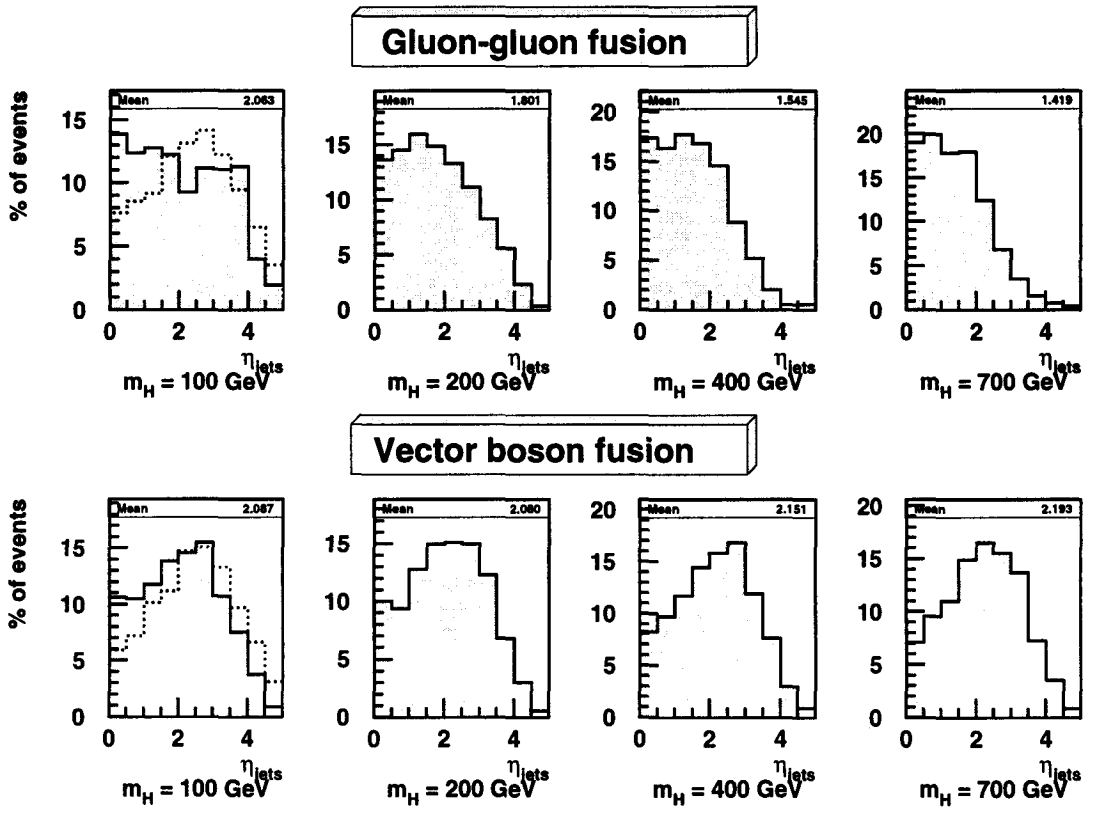

Figure 6.12: The pseudorapidity distribution of jets in the Higgs events with different Higgs masses and for the two most important production mechanisms. The dashed line for m_H = 100 GeV shows how the jet pseudorapidity distribution is changed if 17.3 minimum bias events are included.

gluon fusion process 60-70% of the events have jets one can correlate the Higgs p_T with the p_T of the jet system. This correlation is illustrated in figure 6.11 for gluon-gluon and vector boson fusion mechanisms separately. The vector sum of the jet transverse momenta is shown as a function of the Higgs transverse momentum for different Higgs masses. It can be seen that at high Higgs masses the underlying jet system can provide useful information about the properties of the Higgs particle. This is important especially in the decay modes where the decay products include neutrinos and the Higgs mass cannot be directly reconstructed. The transverse momentum of neutrinos can be defined from the transverse momentum of the visible decay system and that of the underlying jet system.

The presence of pile-up events may modify the jet pattern: as an example, the jet multiplicity when 17.3 pile-up events per bunch crossing are included is shown by the dotted line for m_H = 100 GeV. The pile-up events as produced by PYTHIA rarely contain any jets with the above definition, but their presence may turn some isolated medium energy tracks of the Higgs event into jets by adding energy around them. Therefore, care must be taken that the signal selection criteria are not too sensitive to the jet definition.

Figure 6.12 shows the average pseudorapidity of the jets in an event. Again, the shaded histograms show the pseudorapidity distribution of the jets in a Higgs event alone and the dotted line for m_H = 100 GeV shows how the distribution is modified by the

presence of 17.3 pile-up events per bunch crossing. In the case of vector boson fusion, the pseudorapidity of jets peaks at about $|\eta| = 3$. The events are thus characterised by the presence of jets in the forward direction which can then be used to distinguish the Higgs signal from the background processes. In the gluon gluon fusion events such forward jets are rarely present.

6.3 Signal significances in Higgs decay channels

In the following, the studies of the main Higgs decay channels are presented. The scope is to combine the results over the entire Higgs mass range and estimate what is the integrated luminosity needed for an observable signal as a function of Higgs mass. Care has been taken to use the next to leading order cross-sections for the signal and the background processes. All the signal cross-sections have been normalised to the NLO cross-section given by MRS(R1) structure function. First, two new analyses are presented:

- section 6.3.1 $H \rightarrow \gamma\gamma$
- section 6.3.2 $H \rightarrow ZZ \rightarrow 2\ell 2\nu$.

Then, existing studies for other channels are reviewed:

- section 6.3.3 $H \rightarrow ZZ \rightarrow 4\ell$
- section 6.3.4 $H \rightarrow WW \rightarrow 2\ell 2\nu$
- section 6.3.5 $H \rightarrow WW \rightarrow \ell\nu 2j$ and $H \rightarrow ZZ \rightarrow 2\ell 2j$.

6.3.1 Higgs $\rightarrow \gamma\gamma$

Features of the decay channel

The search for the Higgs in the two photon channel covers the Higgs mass range from 100 GeV to 150 GeV. The main features of this decay channel are

- small branching ratio which suppresses the relatively large cross-section resulting in a signal of order of tens of femtobarns (i.e. for $m_H = 100$ GeV, σ·BR = 52 pb · $1.5{\cdot}10^{-3} = 80$ fb)
- very narrow width of the Higgs particle ($\Gamma \approx$ few MeV)
- clean experimental signature of two isolated photon clusters in the electromagnetic calorimeter
- large background which requires an excellent mass resolution in order to distinguish the signal.

This channel has been investigated in [82] and in the CMS Electromagnetic Calorimeter TDR [37]. Here, a new study including the performance as a function of the isolation criteria and PYTHIA simulation of the formerly neglected γ-jet background is presented.

The signal has been generated with PYTHIA using MRS(R1) parton distribution function and the higher order corrections to the cross-sections have been taken into account by applying the corresponding K-factors (section 2.4.2) to the different production mechanisms (1.80 – 1.65 for the gluon fusion and 0.89 – 0.93 for the vector boson fusion). Higgs radiation from a vector boson line has been included without K-factors as the NLO contribution is relatively small and positive[11].

The mass resolution of the signal has been studied with detailed CMSIM detector simulation as described in section 5.4.

Background processes

The background processes for the $H \rightarrow \gamma\gamma$ channel can be divided into *irreducible* background containing two real photons and *reducible* background:

- Irreducible background
  - two prompt photons: $q\bar{q} \rightarrow \gamma\gamma$ or $gg \rightarrow \gamma\gamma$
  - quark Bremsstrahlung from $qg \rightarrow q\gamma \rightarrow q\gamma\gamma$.
- Reducible background
  - γ-jet events where a leading π^0 of a jet has been misidentified as a photon
  - jet-jet events where both jets have been misidentified as photons.

In the following, the background processes are simulated by PYTHIA using MRS(R1) parton distribution functions.

The γ-jet background is simulated by PYTHIA γ-jet processes. A jet is considered as a photon candidate when a neutral pion passing the basic kinematical selection criteria is found in the event. The Bremsstrahlung events are considered to be those γ-jet events where a second prompt photon is observed. It should be noted that the division between the Bremsstrahlung events and hard scattering is not necessarily the same in PYTHIA and in other theoretical calculations for the two-photon background [74]. As discussed in section 6.1, the initial and final state radiation are included in PYTHIA and therefore, although being a LO Monte Carlo, it includes the soft part of of the photon and gluon emission. These are NLO processes and included in the K-factors estimated for the background [73]. Therefore, it is not evident which is the best method to include the NLO corrections to the PYTHIA simulation. The following considerations should be taken into account:

- If a K-factor is applied to the $q\bar{q} \rightarrow \gamma\gamma$ background, the PYTHIA estimate of the Bremsstrahlung contribution should not be included.
- If no K-factor is applied to $q\bar{q} \rightarrow \gamma\gamma$ background and the Bremsstrahlung rate from PYTHIA is included, hard gluon and photon emission and 1-loop corrections to the quark-antiquark scattering will be omitted.

In this analysis it was decided to use the first approach, i.e. to apply a K-factor to the quark-antiquark scattering and exclude the Bremsstrahlung events from γ-jet event sample. The choice is motivated by the uncertainties in PYTHIA $q \rightarrow q\gamma$ fragmentation rate which has been shown to underestimate the $e^+e^- \rightarrow Z \rightarrow q\bar{q}\gamma$ LEP data [83] by 20% and the afore mentioned ambiguities in dividing the NLO correction into the Bremsstrahlung contribution and the hard NLO processes. Reference [73] reports the signal K factor of 2.11 - 2.34 in the Higgs mass region of 100 - 150 GeV, and the background K factor of 1.91 - 2.01 in the same di-photon mass range. The background K factor (K′ in the following equations) was defined as

$$K' = NLO/LO = (LO + \alpha_s\text{correction})/LO$$

with LO = Born + box + single and double fragmentation. Now, the K-factor to be applied to the quark-antiquark scattering has a different definition (NLO = K·Born + box) and some simple algebra is needed to extract it from the quoted numbers[84]. First, due to differences in structure functions and in the definition of the leading order and next to leading order component the signal K-factor results higher than proposed in [72]. For the sake of consistency, the K-factors are scaled down by 78% which is the ratio between the K-factors used in this analysis and the signal K-factor in [73]. Thus, the reported K-factor of 2 is scaled down to 1.56. The gg contribution is reported to be 35% of the total LO cross-section and Bremsstrahlung contribution less than 10% (here, we assume 10%). Therefore, for the NLO cross-section applies

$$\begin{aligned} K' \cdot LO &= K' \cdot (q\bar{q} + gg + \text{Brem}) \\ &= K' \cdot (0.55 \cdot LO + 0.35 \cdot LO + 0.10 \cdot LO) \\ &= K' \cdot (q\bar{q} + (0.35/0.55) \cdot q\bar{q} + (0.10/0.45) \cdot q\bar{q}) = K' \cdot 1.82 \cdot q\bar{q} = 2.84 \cdot q\bar{q} \end{aligned}$$

	$q\bar{q}$	gg	γ-jet
K-factor	2.33	1.8	1

Table 6.2: K-factors applied to the background processes of the $H \rightarrow \gamma\gamma$ channel.

This is the NLO cross-section expressed in terms of the LO quark-antiquark scattering. The gg contribution of the total NLO cross-section is reported to be 18%. The remaining 82% are attributed to the quark-antiquark scattering and its corrections (Bremsstrahlung contribution and other α_s corrections) and the K-factor for the quark-antiquark scattering can be estimated as

$$K \cdot q\bar{q} = 0.82 \cdot K' \cdot LO = 0.82 \cdot 2.84 \cdot q\bar{q} = 2.33 \cdot q\bar{q}$$

The NLO contributions to gg process are still unknown. As suggested in [73], an educated guess of their magnitude can be done applying the K-factor of $gg \rightarrow H$ to this process.

In the absence of NLO calculations, no K-factors are applied to the γ-jet process. The K-factors applied for the background processes are given in table 6.2 It is assumed that the jet-jet background can be reduced to an insignificant level with the isolation criteria and π^0 rejection[82].

Event selection criteria

Kinematical cuts The experimental signature is required to have two isolated photons with high p_T within the reach of the electromagnetic calorimeter ($|\eta| < 2.5$). The p_T distribution of the photons for these events is shown in figure 6.13 for Higgs masses of 100 and 130 GeV. The p_T distribution of the photons corresponding to $m_{\gamma\gamma}$ windows around 100 and 130 GeV in the irreducible prompt photon background are the lower histograms in figure 6.13. The p_T cuts for the photons are set to be 25 GeV and 40 GeV cutting away part of the soft photon events in the background, and keeping 59% – 73% of the signal events, the percentage of the accepted events rising as a function of the Higgs mass.

A single photon efficiency of 76% will be applied on the event rates. This results from:

- lost conversions 9% (see table 5.6 in section 5.4.1)
- loss in cracks in the fiducial area of the electromagnetic calorimeter 7% (5% in the cracks between the barrel and the endcaps and 2% in the barrel cracks, table 5.6 in section 5.4.1)
- loss due to the π^0 rejection 10% (see section 5.4.4).

If the converted photons were discarded, the loss due to conversions would be 26%. The photon efficiency is also affected by the isolation criteria. This effect is studied in more detail in the following.

Part of the π^0's faking a photon can be rejected using calorimeter or preshower information as discussed in section 5.4.4. The fraction of π^0's which can be rejected depends on the direction and the transverse momentum of the particle. Here, an average π^0 rejection factor of 2 is applied.

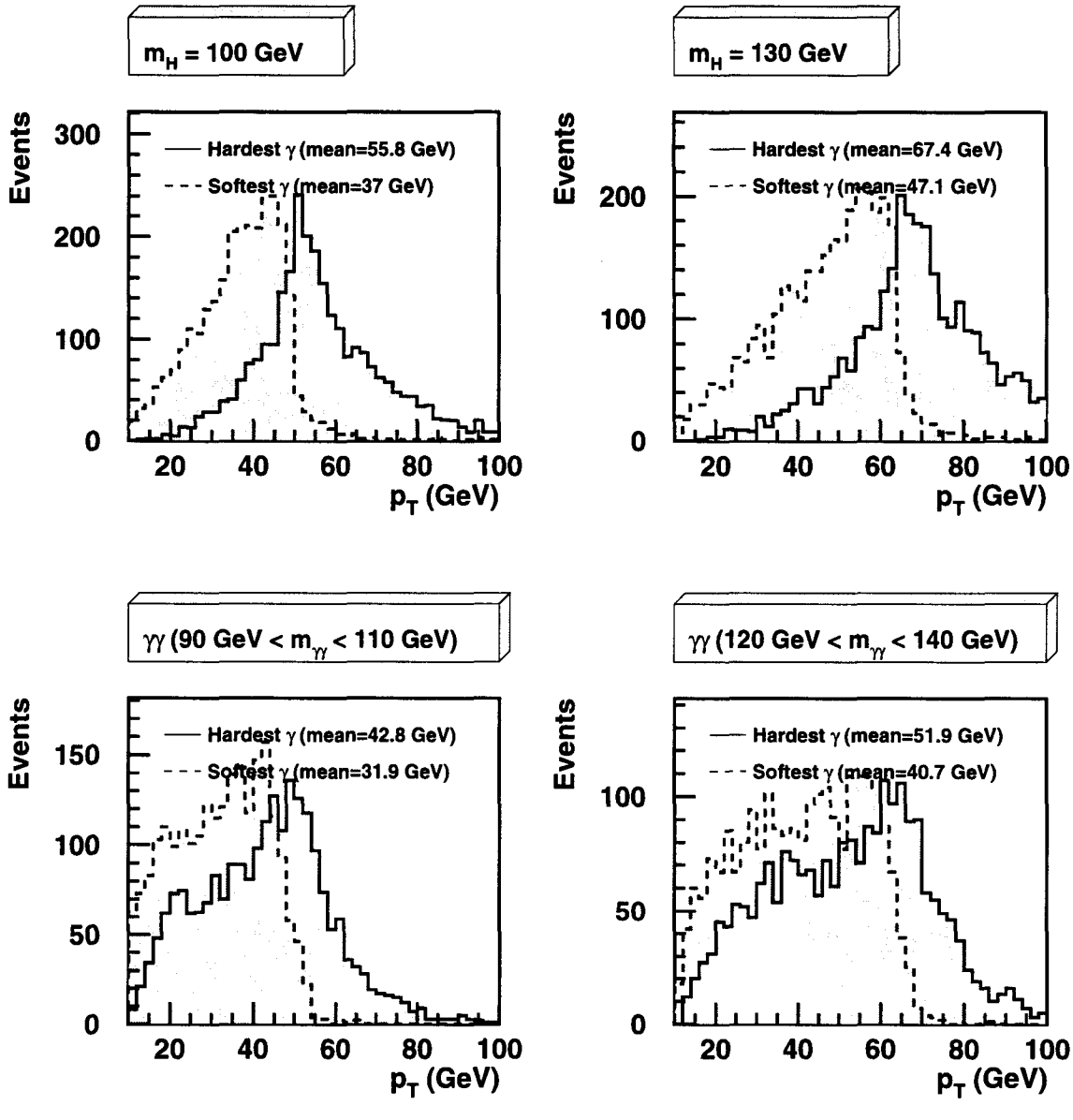

Figure 6.13: The p_T distribution of the two photons in $H \rightarrow \gamma\gamma$ events (m_H = 100 GeV and 130 GeV) and in the irreducible background with a corresponding $m_{\gamma\gamma}$ window. The two photons are required to be within $|\eta| < 2.5$.

Isolation In the signal events, the photons are intrinsically isolated. As discussed in section 6.2, the decay kinematics of the Higgs particle sets a minimum angle between the decay products and the underlying event balances the p_T of the two photon system. In the Bremsstrahlung events, the photon is emitted from the quark and in the majority of events, the angle between the quark and the photon is small. Thus, the isolation criteria cuts away the bulk of the Bremsstrahlung background. In this study, the K-factor applied to the $q\bar{q}$ process corresponds to the case where the energy of partons closer than $\Delta R = 0.255$ is required to be less than 5 GeV[73]. It is assumed that the effect of the isolation cuts on these events is the same as for the events from $q\bar{q}$ background. On the contrary, in the γ-jet background, the photon candidate is surrounded by the rest of the jet particles. Thus, the isolation criteria can be very efficient in reducing the this background while keeping the signal rate high.

In the LHC environment, the isolation is affected by the presence of the pile-up events. Different isolation criteria have been studied by generating pile-up events with PYTHIA together with signal and background processes. Two cases corresponding to the high and low luminosity conditions have been studied: constant 10^{34} cm^{-2}s^{-1}resulting in 17.3 pile-up events per bunch crossing and constant 10^{33} cm^{-2}s^{-1}resulting in 1.7 pile-up events per bunch crossing. The isolation is based on the tracker information i.e. it is required that no charged tracks above the chosen p_T cut pass through the isolation area. The magnetic field is not taken into account in the simulation. Figure 6.14 shows the efficiency of the isolation criteria on the signal and on the γ-jet background events with the photon candidates within $|\eta| < 2.5$ and with p_T of the first and second photon above 40 GeV and 25 GeV, respectively. The efficiency is shown for the number of pile-up events corresponding the low and high luminosity values. For the high luminosity, 90% efficiency is obtained for the signal events with $\Delta R = 0.2$ and the p_T cut 2.5 GeV or larger. For the low luminosity, the signal efficiency is above 95% with $\Delta R = 0.2$ and $p_T > 2$ GeV. For the γ-jet events, the percentage of accepted events is given with respect to the number of non-isolated $\pi^0\gamma$ pairs where the π^0 and the γ pass the general p_T and η cuts. With $\Delta R = 0.2$ and $p_T >$ 2 GeV, the γ-jet events can be reduced to 2% of the non-isolated level.

It may be possible to reduce the event rate of the background by requiring in addition that the energy flow close to the photon candidate is limited. In the absence of pile-up events this would not reduce the efficiency for the signal photons but it could reject such events where the fake photon candidate in a jet is surrounded by many low energy particles. Figure 6.15 shows the efficiency if in addition of requiring no charged tracks above $p_T = 3$ GeV a limit to the energy flow is applied. ΔR_E is the isolation cone for the energy flow and the lines correspond to the charged track isolation cones of $\Delta R = 2$ (continuous line) and $\Delta R = 0.3$ (dashed line). For the high luminosity case, compared to the charged track isolation requiring no charged tracks with $p_T > 2.5$ GeV in a cone of $\Delta R = 0.2$, the number of accepted signal events decreases from 91% to 80% if the energy flow, excluding the energy of the photon candidate, is required to be less than 10 GeV. The γ-jet background is reduced by a factor of 0.75. However, as the signal rate decreases, the reduction in the γ-jet background is not large enough to improve the signal to background ratio. These estimates are to be considered only indicative because the magnetic field and the detector material which certainly modify the energy flow from the soft tracks are not present in the PYTHIA simulation.

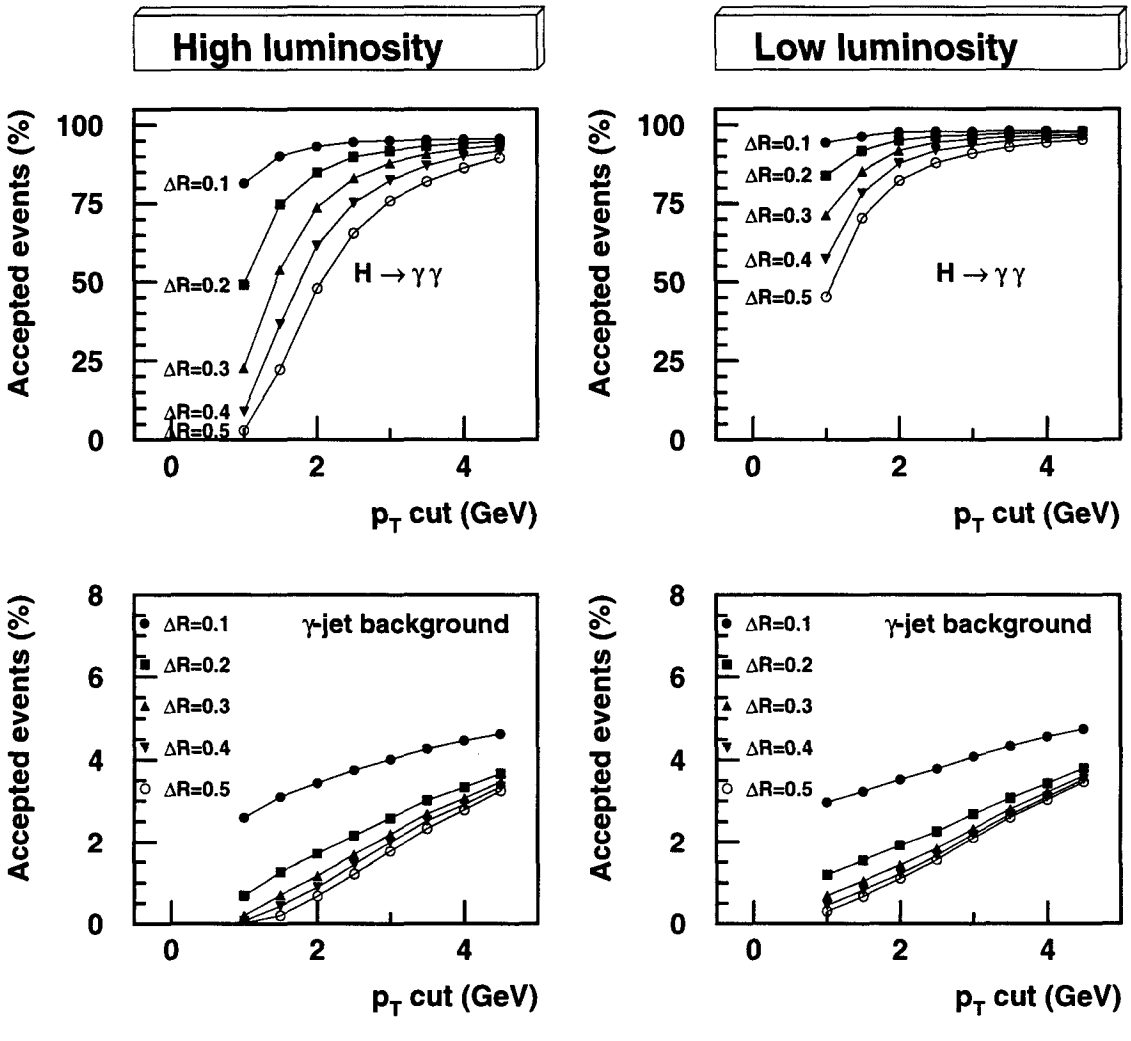

Figure 6.14: The efficiency of the isolation criteria based on the charged tracks in a isolation cone of ΔR for the $H \rightarrow \gamma\gamma$ events ($m_H = 100$ GeV) and the γ-jet background.

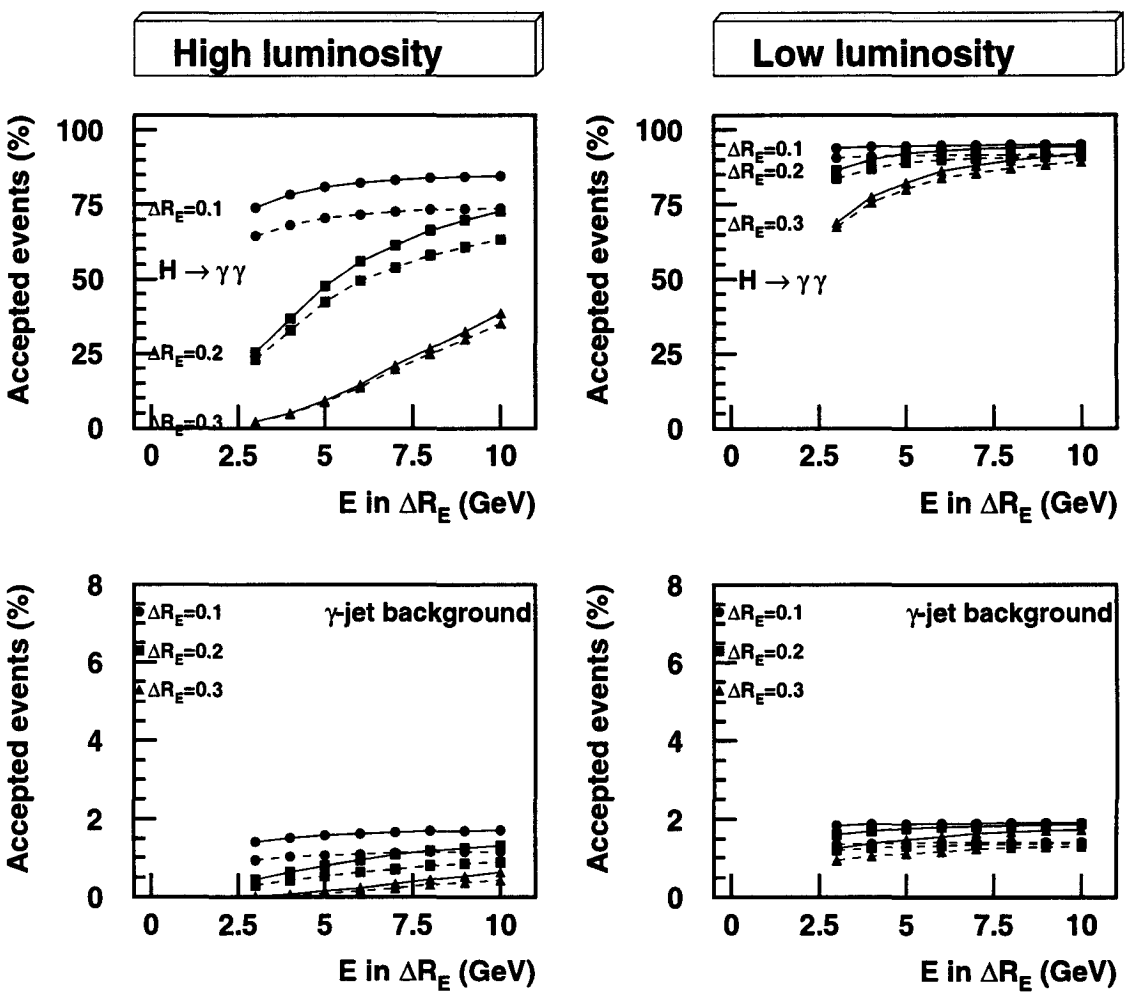

Figure 6.15: The efficiency of the isolation criteria based on the charged tracks in $\Delta R = 0.2$ (continuous line) and $\Delta R = 0.3$ (dashed line) and the energy flow in a isolation cone of ΔR_E for the $H \rightarrow \gamma\gamma$ events ($m_H = 100$ GeV) and the γ-jet background.

Events in $m_{\gamma\gamma} < m_H \pm$ 0.87 GeV for 30 fb^{-1}					
Cuts	m_H	Signal	$q\bar{q}$+h.o.	gg	γ-jet
Isolation: no tracks ($p_T > 2.0$ GeV) in ΔR=0.2	100 GeV	477	6126	4179	3235
	110 GeV	572	5133	3292	2359
	120 GeV	600	4242	2537	1647
	130 GeV	532	3451	1914	1099
	140 GeV	433	2761	1422	715
	150 GeV	290	2173	1063	494

Table 6.3: Event rates for 30 fb^{-1}collected at low luminosity.

Events in $m_{\gamma\gamma} < m_H \pm$ 1.05 GeV for 100 fb^{-1}					
Cuts	m_H	Signal	$q\bar{q}$+h.o.	gg	γ-jet
Isolation: no tracks ($p_T > 2.0$ GeV) in ΔR=0.2	100 GeV	1375	21840	15228	11290
	110 GeV	1696	18462	12004	7668
	120 GeV	1766	15364	9260	4952
	130 GeV	1563	12547	6996	3142
	140 GeV	1287	10011	5211	2238
	150 GeV	840	7754	3997	2241

Table 6.4: Event rates for 100 fb^{-1}collected at high luminosity.

The final isolation criteria are chosen by maximising the signal significance as will be shown below.

Event rates Table 6.4 shows the event rates for the signal and the background with a set of isolation criteria. The background rates have been estimated by simulating a large sample of events, applying the isolation criteria and fitting a curve to the shape of the remaining background.

Significance at CMS

Figure 6.16 shows the significance of the $H \rightarrow \gamma\gamma$ signal (m_H = 100 GeV) as a function of the charged track isolation criteria for 100 fb^{-1}collected at the luminosity of 10^{34} cm^{-2}s^{-1}and for 30 fb^{-1}collected at the luminosity of 10^{33} cm^{-2}s^{-1}. In both cases, the isolation cone of ΔR=0.2 gives the best results. During the low luminosity running, the significance is fairly insensitive to the isolation criteria: p_T thresholds between 1.5 and 3.0 GeV in isolation cones of ΔR=0.2 and 0.3 give essentially the same results. During the high luminosity running, it is preferable to use higher p_T cuts, the best results are obtained with p_T cut larger than 2 GeV in the isolation cone of ΔR=0.2. The isolation criteria are chosen to be p_T cut of 2 GeV in an isolation cone of $\Delta R = 0.2$ for both high and low luminosity running. Figure 6.17 shows the two photon signal from the Higgs

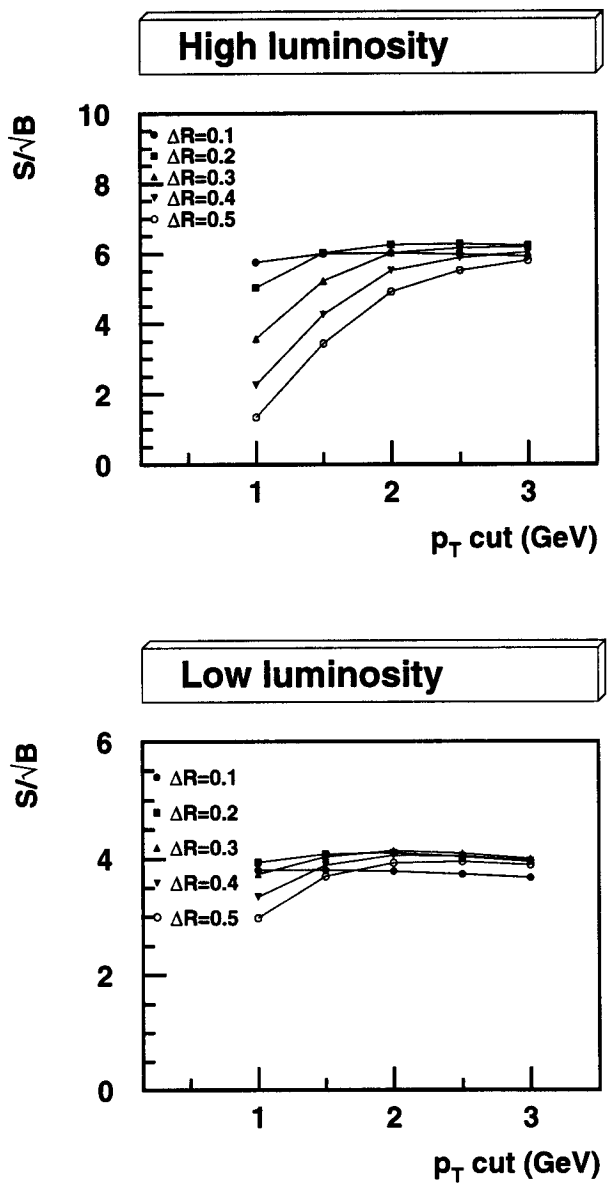

Figure 6.16: Significance as a function of the isolation criteria for $H \rightarrow \gamma\gamma$ ($m_H = 100$ GeV). Isolation is based on the tracker information: no charged tracks above the p_T cut are allowed in the isolation code of ΔR.

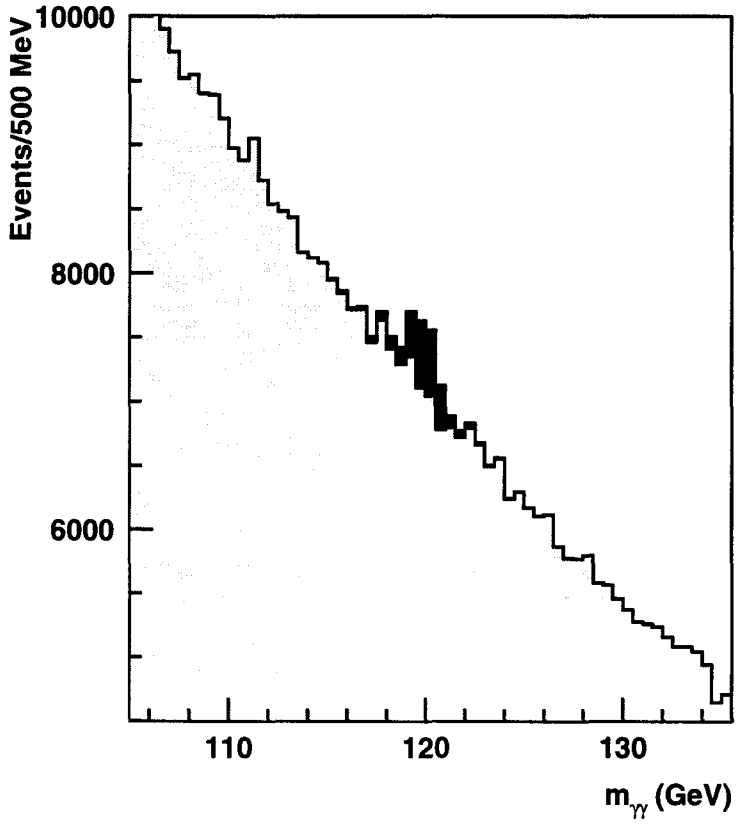

Figure 6.17: $H \rightarrow \gamma\gamma$ (m_H = 120 GeV) signal on the top of the background after 100 fb^{-1} of integrated luminosity.

decay on the top of the background with these selection criteria. With the event rates presented in table 6.4 the following signal to background ratio and significance can be achieved for the integrated luminosities of 30 fb^{-1} and 100 fb^{-1}:

	$\int \mathcal{L}$ = 30 fb^{-1}				$\int \mathcal{L}$ = 100 fb^{-1}				min $\mathcal{L}$
m_H	S	B	S/B	$S/\sqrt{B}$	S	B	S/B	$S/\sqrt{B}$	for 5 σ fb^{-1}
100 GeV	477	13540	0.04	4.1	1375	48358	0.03	6.3	44.6
110 GeV	572	10784	0.05	5.5	1696	38134	0.04	8.7	24.7
120 GeV	600	8426	0.07	6.5	1766	29576	0.06	10.3	17.6
130 GeV	532	6464	0.08	6.6	1563	22685	0.07	10.4	17.1
140 GeV	433	4898	0.09	6.2	1287	17460	0.07	9.7	19.6
150 GeV	290	3730	0.08	4.8	840	13903	0.06	7.1	33.3

The 5 σ discovery limit can be reached with 30 fb^{-1} in the mass range of 105 GeV – 148 GeV. The m_H = 100 GeV signal which requires 45 fb^{-1} at LHC will be in the reach of the Higgs searches at LEP200 and should be found or excluded before the LHC start (see section 2.4.3).

Excluding all visible conversions would result in a loss of efficiency but the mass width would be slightly better. With the 0.80 GeV window including 70% of the events achieved for events without conversions (see table 5.8), the event rate for 30 fb^{-1}at low luminosity would be 306 for the $m_H = 100$ GeV signal and 8635 for the background resulting in a significance of 3.3. Thus, recovering the conversions improves the $H \rightarrow \gamma\gamma$ discovery potential. It should be noted, however, that it is assumed that the conversion track segments can be identified in the tracker. More detailed study would be needed to estimate the track finding efficiency for the converted photons and its effect on the signal significance.

Restricting the coverage to the electromagnetic calorimeter barrel results in a significance of 3.6 with 312 ($m_H = 100$ GeV) signal events and 7733 background events for 30 fb^{-1}at low luminosity.

To enhance the significance, the two photon signal offers little possibilities other than p_T cuts and isolation criteria. However, it is possible to study a smaller subset of events with a particular structure in the underlying events. A part of the $H \rightarrow \gamma\gamma$ signal is thus rejected but the background can be reduced considerably.

The $H \rightarrow \gamma\gamma + jet$ channel has been studied in [85]. The cross-section for the signal is smaller than in the above described $H \rightarrow \gamma\gamma$ mode, but the background can be suppressed to reach signal to background ratio of ≈ 0.5. The authors report the following values for the significance and the signal to background ratio for integrated luminosity of 30 fb^{-1}:

- $m_H = 100$ GeV: $S/\sqrt{B} = 4.3$, $S/B = 0.40$, $S \approx 45$
- $m_H = 120$ GeV: $S/\sqrt{B} = 7.0$, $S/B = 0.55$, $S \approx 90$
- $m_H = 140$ GeV: $S/\sqrt{B} = 6.3$, $S/B = 0.43$, $S \approx 90$

As the signal to background ratio in this channel is far better than in the inclusive diphoton channel, the mass resolution of the calorimeter is less important. This process can thus add an important contribution to the Higgs discovery potential in CMS and further detailed studies would be needed to confirm these preliminary indications. The background estimates and the effect of jet definitions need to be studied in detail and the jet tagging performance must be verified with a detailed simulation study.

The possibility of tagging the two forward jets in the Higgs production through the vector boson fusion has been studied in [86]. A parton level study indicates that the background for the $H \rightarrow \gamma\gamma + 2\ jets$ can be reduced below the signal level. The authors estimate that the statistical significance of 5 σ can be reached with only 10 - 20 fb^{-1}. This channel seems thus very promising and merits a more detailed detector simulation study, including, as for the $H \rightarrow \gamma\gamma + jet$ channel, detailed estimates of the backgrounds, the effects of the jet definition and the jet tagging efficiency.

6.3.2 Higgs $\rightarrow ZZ \rightarrow 2\ell 2\nu$ ($\ell = e, \mu$)

Features of the decay channel

Towards the high Higgs masses the significance of the four lepton channel decreases due to the decrease in the Higgs production cross-section. To fully exploit the discovery potential of CMS, other decay channels need to be studied. The branching ratio of Z into electrons and muons is 3.37% each, and thus requiring that both Z bosons decay in muon and electrons reduces the total signal by a factor of 0.0045. If the Z decay into neutrinos can be included (branching ratio of 20%), the reduction is 0.027. Thus the $H \rightarrow ZZ \rightarrow 2\ell 2\nu$ channel has six times higher rate than the four lepton channel. The main feature of this decay channel are

- a signal of order of tens of femtobarns (i.e. m_H = 500 GeV, $\sigma \cdot$ BR = 4.1 pb $\cdot$ 0.07 = 28.9 fb)
- the Higgs mass cannot be directly reconstructed but it can be estimated from the transverse mass of the system

This process has been studied in reference [87] concentrating on the high mass region and in [88] where the emphasis was put on the $\not{p}_T$resolution of the CMS calorimeter system. Here, an new study is carried out, using a different approach to estimate the missing p_T. The signal has been generated by PYTHIA with MRS(R1) parton distribution function applying the corresponding K-factors to take into account the NLO corrections.

The Z boson is allowed to decay into electron or muon pairs or into neutrinos.

This channel has been studied on particle level, as the natural width of the Higgs particle dominates over the effects of the detector resolution. The lepton efficiency of 90% is assumed for electrons and muons.

Background processes

The main background processes to the $H \rightarrow ZZ \rightarrow 2\ell 2\nu$ channel are

- ZZ, WZ and WW decaying in two leptons and two neutrinos
- $t\bar{t}$ decaying in leptons and neutrinos
- Z-jet production with a leptonic decay of the Z and where part of the jet energy is lost, giving rise to $\not{p}_T$signature.

The background has been generated by PYTHIA with MRS(R1) parton distribution function. The gluon fusion contribution to the WW and ZZ production are included by multiplying the leading order $q\bar{q} \rightarrow WW/ZZ$ production of PYTHIA by 1.1 and 1.33, respectively. The NLO contributions are taken into account by applying K-factors. For the vector boson pair production, the results from [79] are used. As the NLO corrections are more important in the high invariant mass tail than in the low mass region where the cross-section is highest, applying the K-factor extracted from the total cross-section would underestimate the background. Thus, an attempt has been made to to estimate the K-factor as a function of the invariant mass (ZZ) or the transverse mass m_T (WW

$m_{(T)}$	300 GeV	500 GeV	700 GeV	800 GeV
ZZ	1.36	1.46	1.48	1.5
ZW	1.85	1.86	1.9	1.8
WW	1.6	1.8	1.73	1.7

Table 6.5: K-factors applied to the $q\bar{q} \rightarrow ZZ/ZW/WW$ backgrounds in the $H \rightarrow ZZ \rightarrow 2\ell 2\nu$ channel. $gg \rightarrow ZZ/WW$ process is included by multiplying the LO $q\bar{q} \rightarrow ZZ/WW$ contribution by 1.33 and 1.1, respectively. The $t\bar{t}$ production is normalised to NLO cross-section of 760 pb and no K-factor is applied to Z-jet background.

and WZ) of the system[89]. The K-factors are given in table 6.5. However, it should be noted that these K-factors do not account for the large difference between PYTHIA and the higher order corrections for example in the high p_T part of the ZZ spectrum reported in [78]. The total $t\bar{t}$ cross-section is scaled by 1.2 to correspond to the NLO value of 760 pb[72]. In the absence of NLO calculations no K-factor has been applied to the Z-jet background.

The Z boson is allowed to decay into lepton pairs (electrons, muons or taus) or into neutrinos and the W boson is allowed to decay into lepton-neutrino pair ($\ell = e, \mu$ or τ). The Z-jet background has been generated in p_T bins to allow a better estimate of this process in the tail of the p_T distribution.

Event selection criteria

Kinematical and mass cuts The experimental signature of this channel consists two isolated leptons with invariant mass of the Z boson and missing p_T due to the presence of neutrinos. Figure 6.18 shows the p_T distribution of the lepton pair for the signal and the background processes. Both leptons are required to be isolated and to be within $|\eta| < 2.0$, the p_T thresholds are $p_T > 20$ GeV and $p_T > 10$ GeV for the harder and the softer lepton, respectively. Furthermore, the reconstructed mass of the two lepton system should correspond to the Z boson mass ($|m_{\ell\ell} - m_Z| < 6$ GeV). The signal processes result in a harder p_T distribution of the two lepton system and thus the p_T cut is set to 100 GeV. This cut reduces the background by 80–85% and keeps more than 90% of the signal from 500, 700 and 800 GeV Higgs and 64% of the 300 GeV Higgs as shown in table 6.6.

Missing p_T cut The signal process is characterised by the presence of neutrinos. The p_T of the neutrino pair, i.e. of the second Z boson in the case of the signal, can be estimated from the missing p_T measured in the detector as discussed in [88] or from the observed two leptons and the underlying jet system. The correlation between the Higgs p_T and the p_T of the jet system was shown in figure 6.11 and is relatively good for high Higgs masses. Figure 6.19 shows the missing p_T distribution where the missing p_T is defined as

$$\not{p}_T = -\vec{p}_{T,\ell\ell} - \sum_{|\eta|<4.0} \vec{p}_{T,jets}$$

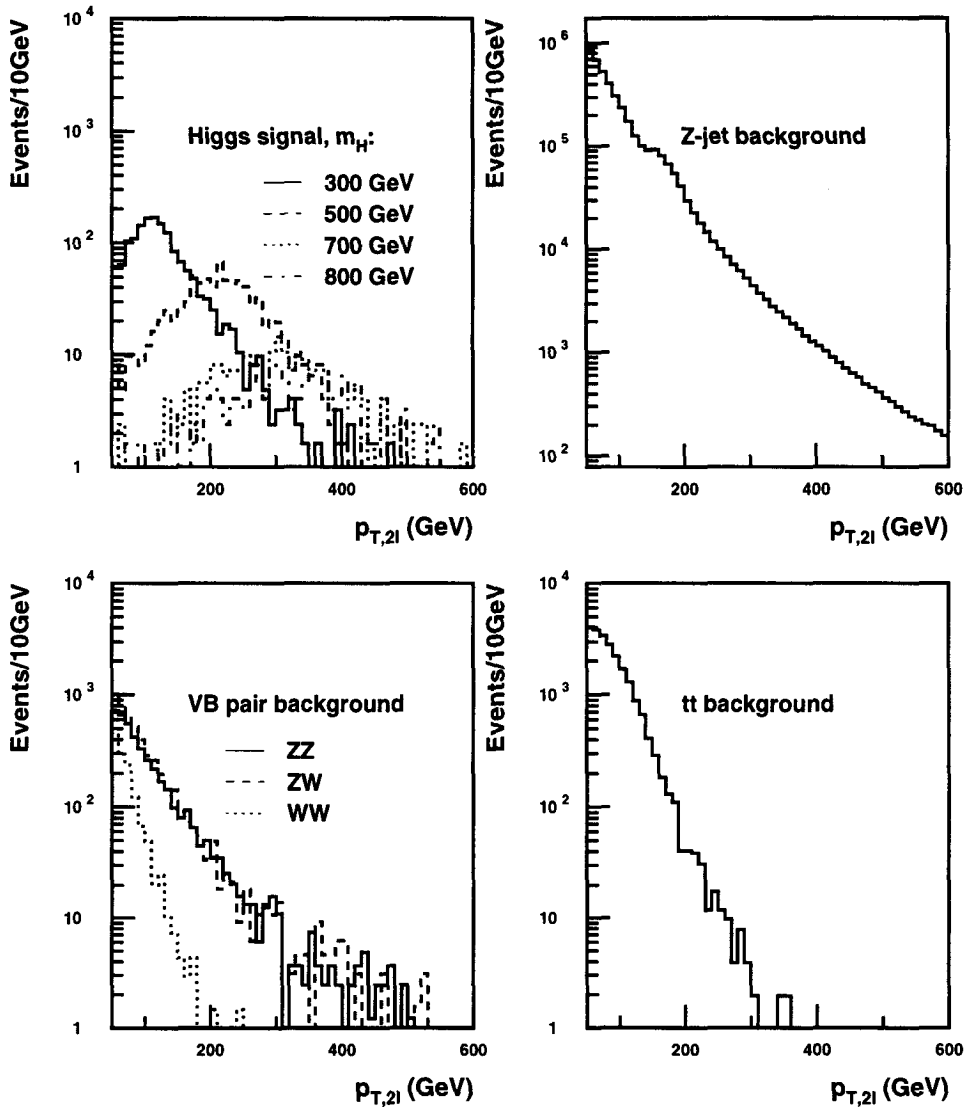

Figure 6.18: p_T of the two lepton system for $H \rightarrow ZZ \rightarrow 2\ell 2\nu$ and for the backgrounds after the basic kinematics and m_Z cuts for 100 fb^{-1}.

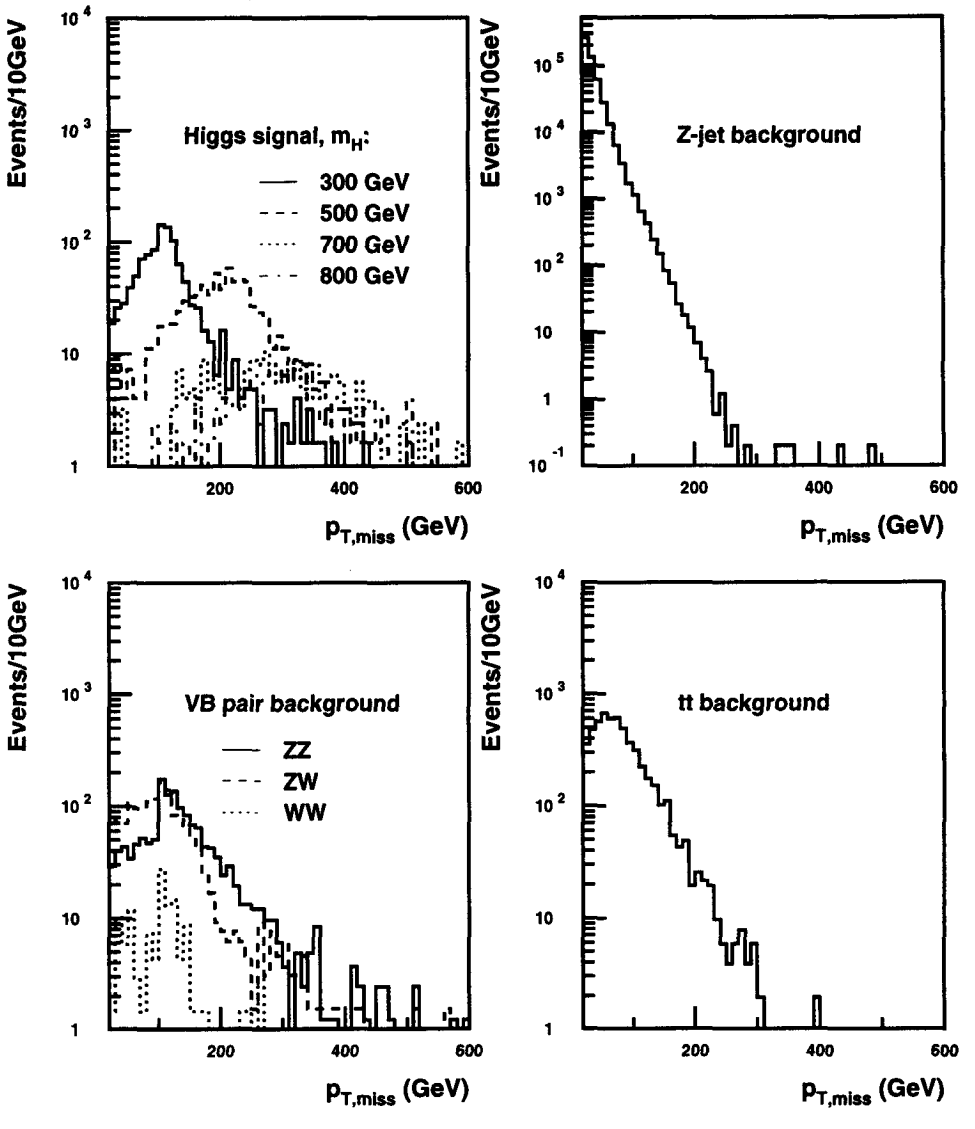

Figure 6.19: Missing p_T distribution for $H \rightarrow ZZ \rightarrow 2\ell 2\nu$ and for the backgrounds after the basic kinematics and m_Z cuts and requiring $p_{T,\ell\ell} > 100$ GeV for 100 fb^{-1}.

A jet is required to have $p_T > 20$ GeV within ΔR=0.5. The missing p_T cut is set at 100 GeV. This reduces the Z-jet background below one per thousand of the initial rate. For the high Higgs masses, the missing p_T cut can be further raised without losing signal events. $\not{p}_T > 150$ GeV is required for $m_H = 500$ GeV, $\not{p}_T > 200$ GeV for $m_H = 700$ GeV, and $\not{p}_T > 250$ GeV for $m_H = 800$ GeV.

Event rates The presence of the Higgs particle can be detected from the p_T distribution of the lepton pair. However, especially at lower Higgs masses, the background after the p_T cuts has an identical shape and it is hardly possible to distinguish the signal from it. More information of the event structure is contained in the transverse mass distribution shown in figure 6.20 for the signal and the background processes. The transverse mass is defined as[90]

$$\begin{aligned} m_T &= \sqrt{(\sqrt{p_{T,\ell\ell}^2 + m_{\ell\ell}^2} + \not{p}_T)^2 - (\vec{p}_{T,\ell\ell} + \vec{\not{p}}_T)^2} \\ &= \sqrt{(\sqrt{p_{T,\ell\ell}^2 + m_{\ell\ell}^2} + \not{p}_T)^2 - \sum_{|\eta|<4.0} \vec{p}_{T,jets}^2} \end{aligned}$$

where the above described definition of $\not{p}_T$ is used.

Table 6.6 shows the event rates after each of these cuts for the integrated luminosity of 100 fb^{-1}. A lepton efficiency of 0.9 is applied to both leptons.

Significance at CMS

Figure 6.21 shows the transverse mass distribution of the signal superimposed to the background for 100 fb^{-1}for different Higgs masses. Good knowledge of the background rate and shape is required as the signal appears as a broad excess over the background. With the event rates presented above in table 6.6 the following signal to background ratio and statistical significance can be achieved for the integrated luminosities of 30 and 100 fb^{-1}:

	$\int \mathcal{L} = 30$ fb^{-1}				$\int \mathcal{L} = 100$ fb^{-1}				min $\mathcal{L}$
m_H	S	B	S/B	$S/\sqrt{B}$	S	B	S/B	$S/\sqrt{B}$	for 5 σ fb^{-1}
300 GeV	109	791	0.14	3.9	362	2635	0.14	7.1	50.3
500 GeV	126	176	0.71	9.5	420	588	0.71	17.3	8.3
700 GeV	28	44	0.63	4.2	92	147	0.63	7.6	43.4
800 GeV	17	20	0.86	3.8	57	66	0.86	7.0	50.8

This channel should be visible between 350 GeV and 650 GeV in 30 fb^{-1}of integrated luminosity and up to 800 GeV for 100 fb^{-1}.

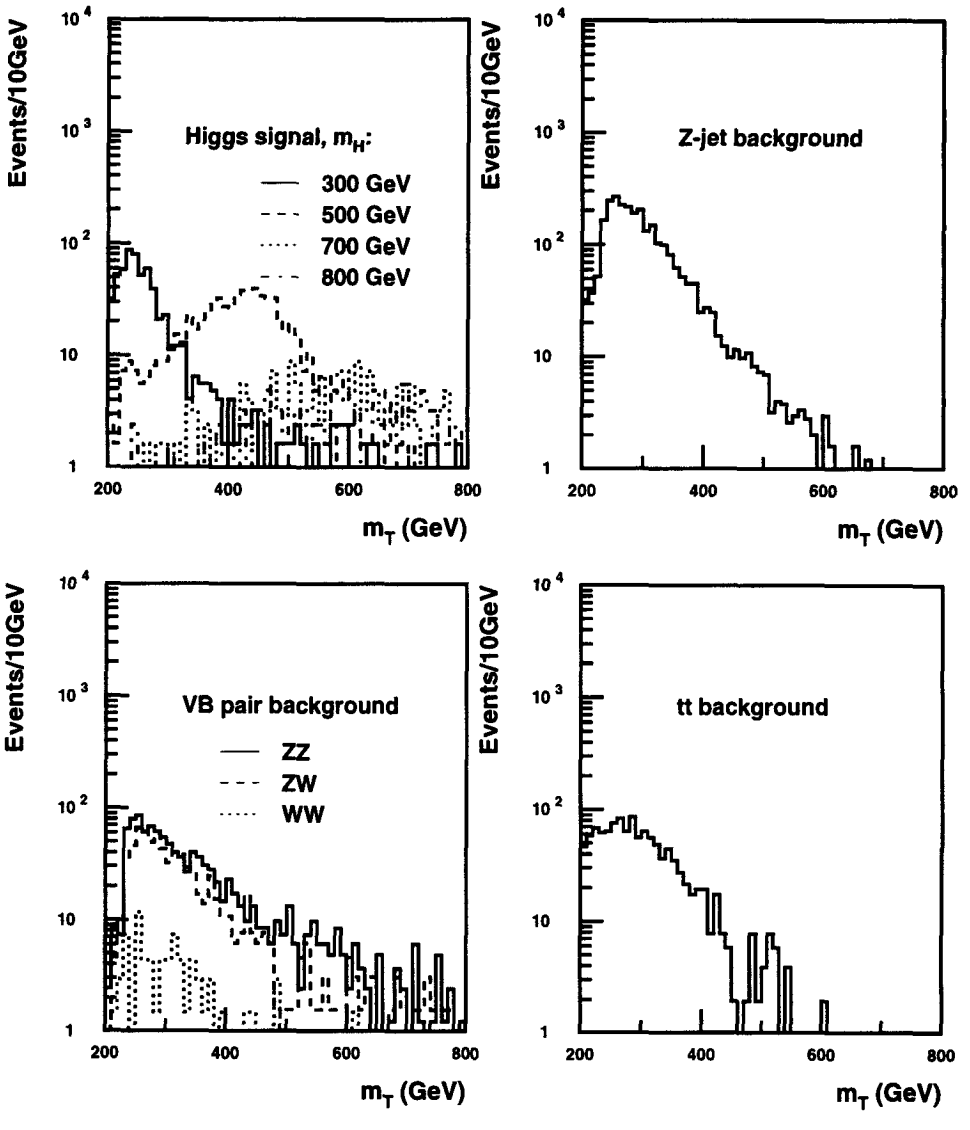

Figure 6.20: Transverse mass distribution of the $H \rightarrow ZZ \rightarrow 2\ell 2\nu$ and the background processes for 100 fb^{-1}.

Events in m_T window for 100 fb^{-1}							
Cuts	m_H	Signal	ZZ	WZ	WW	$t\bar{t}$	Z-jet
Basic kinem.	300 GeV	514	778	608	399	4445	27406
and m_Z	500 GeV	450	468	151	108	1246	2768
cuts	700 GeV	102	157	48	27	140	39
	800 GeV	58	46	35	28	16	11
	300 GeV	450	620	526	37	1137	13451
$p_{T,\ell\ell} > 100$ GeV	500 GeV	449	303	151	17	340	605
	700 GeV	102	124	48	3.0	37	89
	800 GeV	58	45	35	1.4	3.9	11
	300 GeV	362	538	349	32	492	1224
$\not{p}_T > 100$ GeV	500 GeV	447	295	149	16	192	296
	700 GeV	102	116	48	1.5	23	35
	800 GeV	57	45	35	1.4	3.9	10
$\not{p}_T > 150$ GeV	500 GeV	420	267	115	9.0	121	76
$\not{p}_T > 200$ GeV	700 GeV	92	95	42	<1	3.9	5.8
$\not{p}_T > 250$ GeV	800 GeV	57	32	34	<1	<1	<1

Table 6.6: Event rates for 100 fb^{-1} in transverse mass windows of 230 - 300 GeV, 350 - 500 GeV, 500 - 700 GeV, and 600 - 800 GeV corresponding to Higgs masses of 300 GeV, 500 GeV, 700 GeV, and 800 GeV, respectively. $p_T > 40$ GeV is required in the generation of the Z-jet events and in consequence the Z-jet event rates with the basic kinematical cuts may be underestimated. 90% lepton efficiency is assumed.

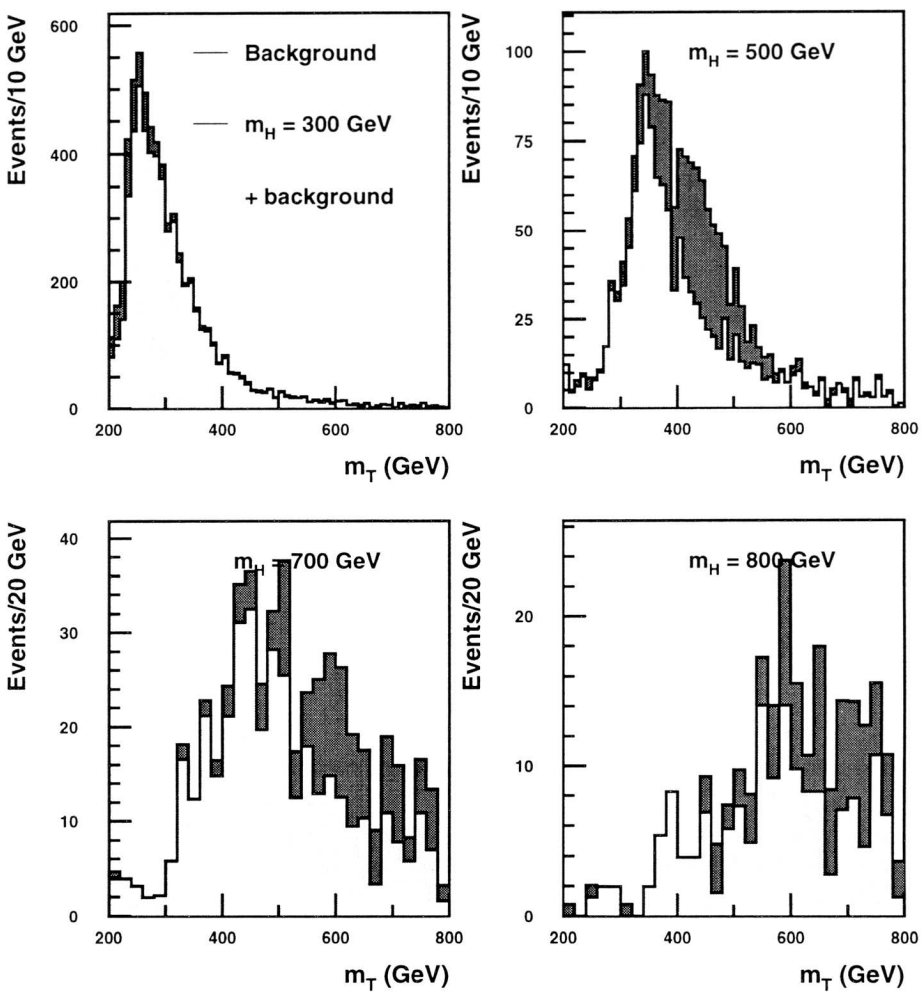

Figure 6.21: Transverse mass distribution of the signals with different m_H and the background assuming 100 fb^{-1} of integrated luminosity.

6.3.3 Higgs $\rightarrow ZZ(^*) \rightarrow 4\ell$ ($\ell = e, \mu$)

Features of the decay channel

The Higgs decay into four leptons (electrons or muons) via two Z bosons can be exploited in the Higgs mass range of 140 GeV $< m_H <$ 600-700 GeV. Below the ZZ pair production threshold of $2m_Z$, the decay proceeds through a ZZ* state where one of the Z bosons is off mass shell. The main features of the channel are

- relatively small branching ratio (10^{-2}–10^{-1} for ZZ* and 0.3 for ZZ, see figure 2.8) which is further suppressed by the branching ratio of Z into e^+e^- or $\mu^+\mu^-$ (3.37% each) resulting in a signal cross-section of about ten femtobarns
- clean experimental signature of isolated electromagnetic clusters or muon tracks
- the presence of internal and external Bremsstrahlung which may reduce the signal efficiency.

The ZZ^* channel has been investigated in [66] where the event selection criteria have been developed and [91] where these criteria are improved by using neural network in the event selection. In these studies, K-factors for the signal processes have not been taken into account.

The ZZ channel has been studied in [92] and [93] up to $m_H \approx 650$ GeV and in [94] where the event selection was optimised to reach even higher m_H values. In [95] it is shown that the polarisation of the Z boson can be used to enhance the signal to background ratio. None of these studies include K-factors, neither for the signal and nor for the background processes.

The results presented in this section rely largely on the work done by Iashvili, Kinnunen, Nikitenko and Denegri in reference [66] and by Bomeštar, Denegri, Kinnunen and Nikitenko in [93]. The results presented for the higher Higgs masses are not included as the significance estimate in this region is difficult due to the next to leading order effects in the background.

The signal was generated with PYTHIA with CTEQ2L parton distribution functions. In the following, the total signal cross-sections are scaled to correspond to the next to leading order values of MRS(R1) parton distribution functions as discussed before. The cross-sections and the scale factors are presented in table 6.7. As the NLO values are given only for gluon fusion and vector boson fusion processes, the total cross-section to which the results are scaled includes NLO values for these processes and LO values for $t\bar{t}$ fusion and radiation from vector boson line. The contribution of the latter processes in the LO cross-section is given in the table.

The internal photon emission was simulated by a dedicated photon radiation program PHOTOS[96].

The lepton momentum resolution has been studied by detailed GEANT simulation[97, 98]. Using the results of these studies, the muon momentum ($\delta p/p < 1.5\%$ for $p_T <$ 100 GeV) was parameterised as a function of momentum and pseudorapidity. The full simulation of the $H \rightarrow ZZ \rightarrow 4e$ channel was performed in [98] and for the background suppression studies, the electron energy resolution was parameterised.

m_H	σBR (fb) PYTHIA LO	(non gg or VB fusion)	σBR (fb) NLO (gg or VB fusion)	Scale
130	2.4	(0.2)	5.2	2.25
150	5.0	(0.3)	9.2	1.90
170	1.3	(0.01)	2.0	1.54
190	10.1	(0.4)	16.7	1.69
200	11.6	(0.5)	18.0	1.59
250	10.2	(0.2)	15.2	1.51
300	8.4	(0.1)	11.8	1.42
350	8.2	(0.1)	11.6	1.43
400	6.5	(0.1)	9.9	1.53
500	3.2	(0.03)	4.9	1.52
600	1.6	(0.02)	2.5	1.56

Table 6.7: Scaling factors for $H \rightarrow ZZ(^*) \rightarrow 4\ell$ from PYTHIA LO results to NLO values.

Background processes

$\mathbf{m_H < 2 \cdot m_Z : H \rightarrow ZZ^* \rightarrow 4\ell}$ The main background for the Higgs mass in this region where one of the Z bosons is off mass shell arises from

- $t\bar{t}$ events where four leptons are produced from W bosons, b-quarks decays and or further cascade decays
- ZZ^* continuum, resulting in an irreducible background spectrum
- $Zb\bar{b}$ decays with 2 leptons from Z decay and two leptons from b-quarks of further cascade decays.

The results presented in [66] are scaled with the available K-factors. The total $t\bar{t}$ cross-section of 600 pb is scaled with K=1.27 to correspond to NLO cross-section of 760 pb[72]. The ZZ^* production in PYTHIA includes only the quark-antiquark scattering. As discussed in section 6.1, the gluon fusion contribution is added by multiplying the LO quark-antiquark scattering by a factor of 1.33. To include the NLO corrections of the quark-antiquark scattering, the PYTHIA cross-section is further scaled by K=1.2[79]. No K-factors are applied to $gg \rightarrow ZZ^*$ and for the $Zb\bar{b}$ production. Thus the results should be considered as optimistic; full NLO corrections are applied for the signal, but the background may be underestimated due to the absence of NLO contributions to some of the processes.

$\mathbf{m_H > 2 \cdot m_Z : H \rightarrow ZZ \rightarrow 4\ell}$ In this Higgs mass range the background is reduced because both of the Z bosons are real. ZZ continuum remains the main background. As above, the $gg \rightarrow ZZ$ contributions is included by scaling the PYTHIA cross-section by K=1.33. From the NLO calculations presented for the leptonic final state of the ZZ pair

$m(ZZ)$ (GeV)	K-factor
190	1.20
200	1.20
250	1.25
300	1.36
350	1.31
400	1.37
500	1.43
600	1.47

Table 6.8: K-factors applied to the $q\bar{q} \rightarrow ZZ$ backgrounds in the $H \rightarrow ZZ \rightarrow 4\ell$ channel. $gg \rightarrow ZZ$ process is included by multiplying the LO $q\bar{q} \rightarrow ZZ$ contribution by 1.33. The $t\bar{t}$ production is normalised to the NLO cross-section of 760 pb and no K-factor is applied to Zbb background.

production[79] it is evident that the NLO contributions are more important towards the higher value of the invariant ZZ mass scale. The K-factors used in this study[99] are given in table 6.8.

Event selection criteria

Kinematical and mass cuts The signal consists of four leptons ($e^+e^-e^+e^-$, $\mu^+\mu^-\mu^+\mu^-$ or $e^+e^-\mu^+\mu^-$) with one (ZZ^*) or two (ZZ) pairs with an invariant mass consistent with the Z boson mass. The p_T of the leptons in one pair are required to be greater than 20 GeV and 10 GeV for muons and greater than 20 and 15 GeV for electrons. In the other pair, $p_T > 10$ GeV is required for electrons and $p_T > 5$ or 7 GeV for muons. Muons are required to be within the pseudorapidity range of $|\eta| < 2.4$ and electrons within $|\eta| < 2.5$.

For the ZZ^* channel one of the lepton pairs is required to have an invariant mass consistent with the Z boson mass, $|m_{2\ell} - m_Z| < 6$ GeV. For the ZZ signal, this is required for both lepton pairs. However, QED radiation of hard and non-collinear photons from the electron or muons ("internal Bremsstrahlung") can reduce the invariant mass of the lepton pair. The fraction of events falling outside the mass window due to internal Bremsstrahlung is 7% for the Z decay into muons and 12% for the decay into electrons when no detector effects are included in the simulation. For the low luminosity in the ZZ^* channel, the results can be improved if the Z mass requirement is dropped.

Isolation Isolation criteria can be used to reduce the $t\bar{t}$ and $Zb\bar{b}$ background to the ZZ^* signal. The leptons in these background processes originate from a b quark and are thus accompanied by jet particles. Tracker isolation requiring no charged tracks above p_T thresholds of 2, 2.5 or 3 GeV in isolation cones of ΔR of 0.2 and 0.3 has been studied in [66]. For the high luminosity studies (10^{34} cm^{-2}s^{-1}) 15 minimum bias events were superimposed to each signal event. The effect of the pile-up at the low luminosity (10^{33} cm^{-2}s^{-1}) is assumed negligible. Here, the results corresponding to the p_T threshold of 2.5

GeV in the isolation cone of 0.2 for the high luminosity, and to the p_T threshold of 3.0 GeV in the isolation cone of 0.3 for the low luminosity are presented.

Impact parameter cut To further discriminate between the prompt leptons from a Z boson decay and the secondary leptons from a b quark decay, a cut can be applied to the measured vertex point on the transverse plane. In the results presented here, no impact parameter cut is applied as its effect on the signal significance is small.

Events in $m_{4\ell} < m_H \pm 2\sigma_{4\ell}$ for 100 fb^{-1}					
m_H (GeV)	$\sigma_{4\ell}$ GeV	Signal	ZZ	$Zb\bar{b}$	$t\bar{t}$
130	0.8 (μ) 1.5 (e)	71.6	8.7	6.2	0.7
150	0.9 (μ) 1.7 (e)	162.7	13.8	6.0	0.9
170	1.1 (μ) 2.4 (e)	31.6	19.9	4.7	1.0
190	1.8	317	88		
200	2.3	352	125		
250	4.4	286	126		
300	7.0	245	113		
350	10.5	243	89		
400	16.0	229	85		
500	31	125	72		
600	53	67	66		

Table 6.9: Event rates for 100 fb^{-1}collected at high luminosity.

Events in $m_{4\ell} < m_H \pm 2\sigma_{4\ell}$ for 30 fb^{-1}					
m_H (GeV)	$\sigma_{4\ell}$ GeV	Signal	ZZ	$Zb\bar{b}$	$t\bar{t}$
130	0.8 (μ) 1.5 (e)	37.2	4.3	2.7	2.3
150	0.9 (μ) 1.7 (e)	73.2	5.2	1.1	2.3
170	1.1 (μ) 2.4 (e)	13.0	6.2	0.5	2.8

Table 6.10: Event rates for 30 fb^{-1}collected at low luminosity.

Event rates The event rates for the signal and the background are presented in table 6.9 for integrated luminosity of 100 fb^{-1}collected at high luminosity. Table 6.10 shows the event rates for 30 fb^{-1}collected at low luminosity. Only the masses corresponding to the ZZ^* channels are shown for low luminosity as in these cases the isolation criteria changes; the rates for 30 fb^{-1}of the ZZ channel can in the first approximation be scaled down from the values of table table 6.9. The lepton efficiency is assumed to be 0.9 for both electrons and muons. The mass resolution for the 4ℓ signal is given in the table.

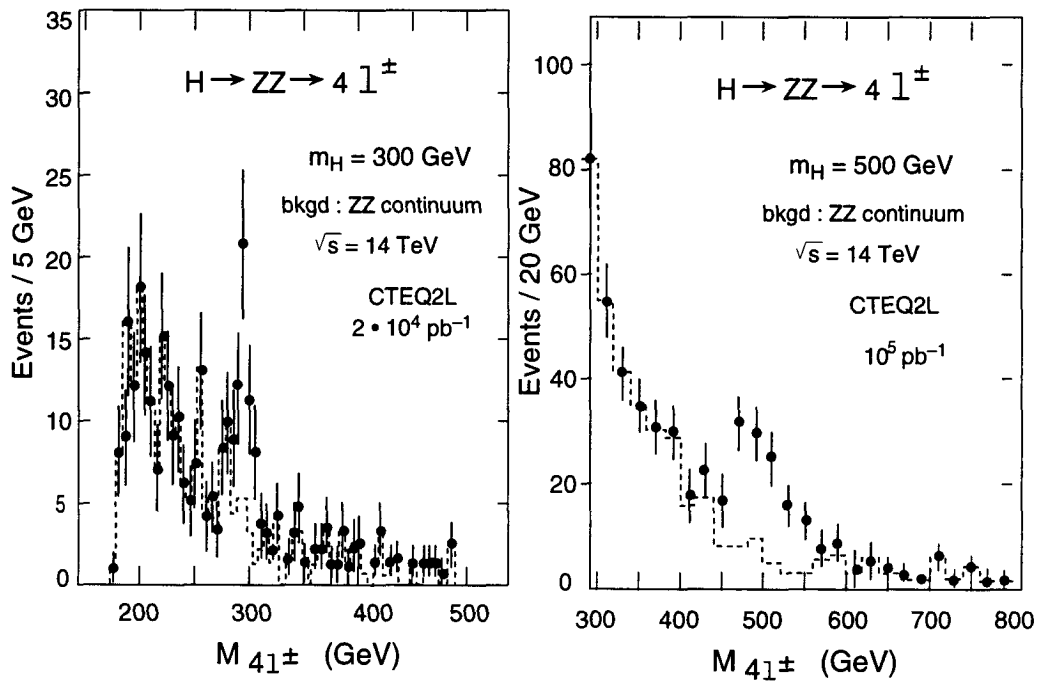

Figure 6.22: $H \rightarrow 4\ell$ signal on the top of the background[93].

The four lepton resolution is affected, apart from the natural width of the Higgs boson which is the dominating effect for $m_H > 300$ GeV, by the internal radiation and the muon momentum resolution in the muon channel, and by the internal radiation, Bremsstrahlung in the tracker material and the electron energy resolution for the electron channel.

Significance at CMS

Figure 6.22 shows the four lepton signal superimposed to the background for $m_H = 300$ GeV and 500 GeV. The signal to background ratio and significance is computed from the event rates presented in table 6.9, and the following is obtained for the integrated luminosities of 30 and 100 fb^{-1}:

	$\int \mathcal{L} = 30$ fb^{-1}				$\int \mathcal{L} = 100$ fb^{-1}				min $\mathcal{L}$
m_H	S	B	S/B	$S/\sqrt{B}$	S	B	S/B	$S/\sqrt{B}$	for 5 σ fb^{-1}
130 GeV	37.2	9.5	3.9	12.1	71.6	15.6	4.6	18.1	5.1
150 GeV	73.2	8.8	8.3	24.7	163	20.7	7.9	35.8	1.9
170 GeV	13.0	9.7	1.3	4.2	31.6	25.6	1.2	6.2	43
190 GeV	95.1	26.4	3.6	18.5	317	88	3.6	33.8	2.2
200 GeV	106	37.5	2.8	17.3	352	125	2.8	31.5	2.5
250 GeV	85.8	37.8	2.3	14.0	286	126	2.3	25.5	3.9
300 GeV	73.5	33.9	2.2	12.6	245	113	2.2	23.0	4.7
350 GeV	72.9	26.7	2.7	14.1	243	89.0	2.7	25.8	3.8
400 GeV	68.7	25.6	2.7	13.6	229	85.5	2.7	24.8	4.1
500 GeV	37.5	21.7	1.7	8.1	125	72.4	1.7	14.7	11.6
600 GeV	20.0	19.8	1.0	4.5	66.6	65.9	1.0	8.2	37.2

It should be noted, that in the case of small number of signal or background events the statistical significance is somewhat overestimated or the minimum luminosity to reach 5 σ underestimated. However, this does not change the results essentially. The four lepton signal will be visible in Higgs mass ranges of 130 – 160 GeV and 185 – 600 GeV for 30 fb^{-1}of integrated luminosity, and over the full range of 130 – 600 GeV for 100 fb^{-1}.

6.3.4 Higgs $\rightarrow WW \rightarrow 2\ell 2\nu$ ($\ell = e, \mu, \tau$)

Features of the decay channel

The opening of the dominant WW decay mode at the WW mass threshold causes the branching ratio of the ZZ decay mode to decrease as shown in figure 2.8. As seen in the preceding section, it is difficult to cover this gap in the Higgs mass range with the four lepton signal. In this region, one can profit from the high branching ratio of the WW decay and study the leptonic decays of the W bosons as first discussed in reference [100]. The main features of this decay channel are

- large (≈ 1) branching ratio of the Higgs decay and 0.1 branching ratio of W's into each lepton results in a signal cross-section of order of picobarns
- the Higgs mass cannot be directly reconstructed but it can estimated from the kinematics of the measured two lepton system
- clean experimental signature of isolated electrons or muons, and missing p_T
- signal to background ratio of 1 is feasible.

The results presented in this section rely on the work done by Dittmar and Dreiner in references [100] and [101].

The signal has been generated with PYTHIA and the MRS(A) parton distribution function. The higher order corrections are taken into account by applying the corresponding K-factors.

The simulation has been performed on particle level as resolution effects will not be important in this channel.

Background processes

The background for the $H \rightarrow WW \rightarrow 2\ell 2\nu$ signal originates from

- non-resonant W^+W^- production
- $t\bar{t}$ production with $t \rightarrow Wb$
- W production in association with b or t quarks

The background processes have been generated by PYTHIA with MRS(A) parton distribution function. For the W boson pair production, the NLO contributions are taken into account by applying a K-factor. In this work, a K-factor of 1.1 is applied. This is smaller than the K-factor computed from the LO and NLO total cross-sections (1.6) but it is justified as most of the NLO processes are accompanied by a central jet[79] and these events are rejected by a jet veto.

The NLO corrections to the $t\bar{t}$ production are accounted for by scaling the total $t\bar{t}$ cross-section to 760 pb. In the absence of NLO calculations no K-factor is applied to the $W - t/b$ production.

Event selection criteria

Kinematical and mass cuts The experimental signature of the signal consists of two isolated leptons with the invariant mass different from that of the Z boson and missing p_T caused by the escaping neutrinos.

To choose the event candidates, the leptons are required to be within the reach of the electromagnetic calorimeter or of the muon system ($|\eta| < 2.4$) and to have the transverse momentum larger than 25 GeV for the most energetic lepton and larger than 10 GeV for the softer lepton. The dilepton mass is required to be larger than 10 GeV. If there is a $\mu^+\mu^-$ pair or e^+e^- pair in the event, the dilepton mass is required to differ more than 5 GeV from the Z boson mass.

Jet veto To reduce the $t\bar{t}$ background where the decay tends to be central, the events with jets with $p_T > 20$ GeV in the central region ($|\eta| < 3$) are vetoed.

Further cuts To further improve the signal to background ratio, some other criteria can be applied. The most efficient ones were found to be the following:

- η of the reconstructed dilepton system should be less than 1.3.
- The angle between the leptons is required to be small.

The former criterion exploits the kinematical differences between $gg \rightarrow H \rightarrow WW$ and $q\bar{q} \rightarrow WW$ and reduces the WW background. The latter criterion profits from the V-A nature of the weak interactions which results in a angular correlation between the two charged leptons and W bosons. The left-handed electron is emitted opposite to the W^- spin orientation and right-handed positron along the W^+ spin. When m_H is close to the $2m_W$ threshold, the transverse momenta of the W bosons are small and they are produced preferably back to back. As the W bosons originate from a scalar particle they have opposite spin orientations and, therefore, the angle between the two leptons for the signal events is small. The angular distribution is shown in figure 6.23

Event rates After these cuts, to distinguish the signal from the remaining background the transverse momentum spectra of the leptons are analysed.

The first step is to control if the p_T distribution of the harder lepton shows an excess compared to the expected background. Limits on the p_T of the harder lepton are defined as the region where most of the excess events are. The limit varies as a function of the Higgs mass. Similarly, limits on the p_T values of the softer lepton are defined. The event rates for 30 fb^{-1}are shown in table 6.11. A lepton efficiency of 0.9 is assumed for each of the two leptons.

Although the mass of the Higgs boson in this channel cannot be directly reconstructed, it can be estimated from the p_T distribution of the minimum and maximum energy leptons as shown in figure 6.24 for m_H values of 160, 170, and 180 GeV.

Significance at CMS

The p_T distribution of the signal on top of the background is shown in figure 6.25 for the Higgs mass of 170 GeV. In the absence of a mass peak a good estimate of the expected

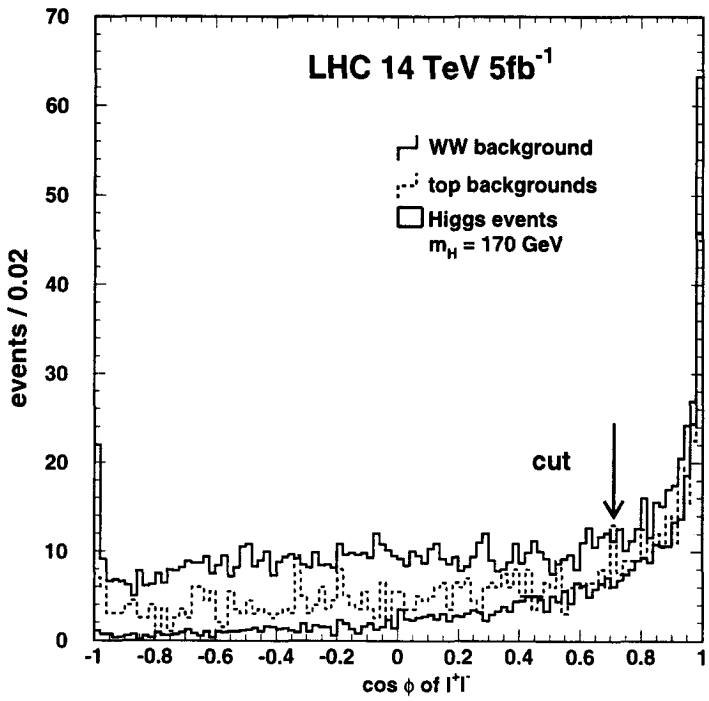

Figure 6.23: Angular distribution between the two leptons in the transverse plane for the Higgs signal (m_H = 170 GeV) and background events[100].

Accepted events for 30 fb^{-1}				
m_H	Signal	W^+W^-	$t\bar{t}$	Wtb
120	75	212	28	51
130	168	324	49	96
140	441	573	92	212
150	497	475	102	198
160	712	210	52	118
170	557	210	52	118
180	812	1092	453	207
200	551	951	531	196
225	378	951	531	196
250	261	754	578	111
300	97	234	277	26
400	135	234	277	26
500	78	234	277	26

Table 6.11: Event rates for 30 fb^{-1}collected at low luminosity..

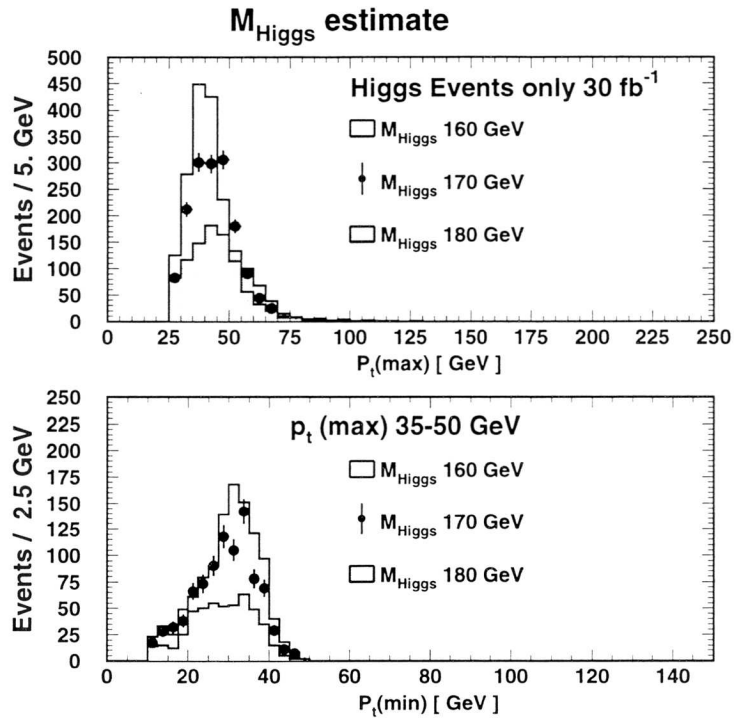

Figure 6.24: Sensitivity of the lepton transverse momentum spectra to the Higgs mass value for m_H = 160, 170 and 180 GeV[100].

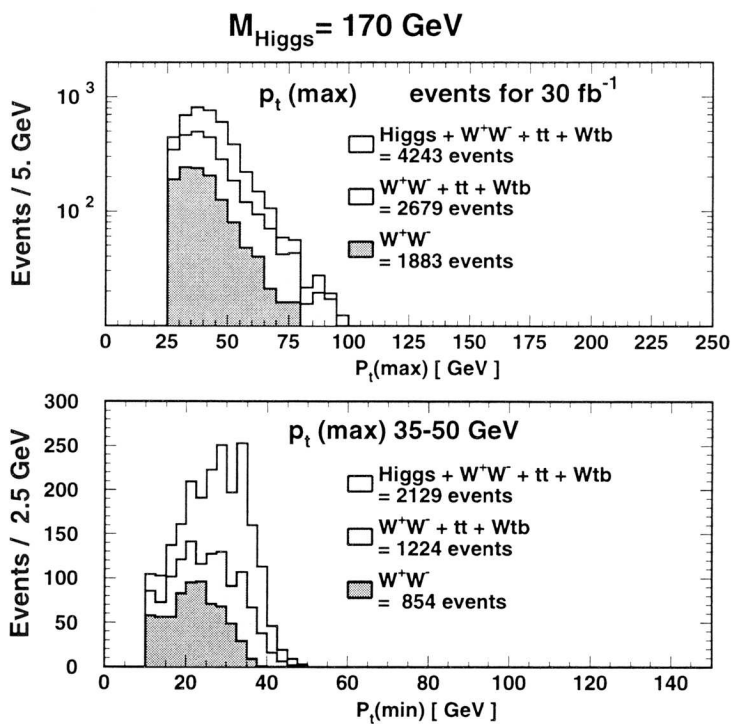

Figure 6.25: The lepton p_T distribution of the $H \rightarrow WW \rightarrow 2\ell 2\nu$ events on the top of the leptons of the background processes[100].

background rate is required to evaluate the number of signal events in excess of the background. For the main WW background, this can be obtained from the distribution of the angle between the leptons as discussed above.

With the signal and background rates from table 6.11 the following statistical significance is obtained for the integrated luminosity of 30 fb^{-1}:

	$\int \mathcal{L} = 30$ fb^{-1}				min $\mathcal{L}$
m_H	S	B	S/B	$S/\sqrt{B}$	for 5 σ fb^{-1}
120 GeV	75	291	0.26	4.4	38.8
130 GeV	168	469	0.36	7.8	12.5
140 GeV	441	877	0.50	14.9	3.4
150 GeV	497	775	0.64	17.9	2.4
160 GeV	712	380	1.87	36.5	0.6
170 GeV	557	380	1.47	28.6	0.9
180 GeV	812	1752	0.46	19.4	2.0
200 GeV	551	1678	0.33	13.5	4.1
225 GeV	378	1678	0.23	9.2	8.8
250 GeV	261	1443	0.18	6.9	15.9
300 GeV	97	537	0.18	4.2	42.8
400 GeV	135	537	0.25	5.8	22.1
500 GeV	78	537	0.15	3.4	66.2

This channel provides the fastest Higgs discovery if the Higgs particle has a mass of 140 – 180 GeV and it gives an important contribution in 130 – 250 GeV. It should be noted that the event selection criteria have been studied assuming the low luminosity running of LHC, resulting in insignificant effect of the pile-up on the jet veto. Therefore, extending the discovery region of this channel beyond 130 – 250 GeV requires further studies.

6.3.5 Heavy Higgs

Features of the decay channel

In the uppermost part of the Higgs mass range ($m_H \approx 1$ TeV) the decreasing production cross-sections makes the discovery with most of the previously discussed channels very difficult. The observable signal can be enhanced by looking for the jet decay channels $H \rightarrow WW \rightarrow \ell\nu 2j$ and $H \rightarrow ZZ \rightarrow 2\ell 2j$. The main characteristics of these channels are

- small production cross-section of less than 1 picobarn which is suppressed by requiring one leptonic decay (BR = 0.2 for the W boson 0.07 for the Z boson) and one hadronic decay (BR = 0.7)
- the possibility of using the typical jet pattern of the vector boson fusion as it gains importance as a production mechanism.

These channels have been investigated in references [102] and [103] where the cuts to optimise the signal to background ratio have been developed and in [104] where the W boson channel has been used as a benchmark for jet-jet reconstruction and forward tagging performance of the CMS detector. The results are somewhat contradictory. In this work, the criticism expressed in [104] of the low p_T limit of the tagging jet (10 GeV) used in [103] is taken into account and results which correspond to p_T limit of 30 GeV[105] are presented.

Of the signal processes, only the vector boson fusion produces a signature with the two tagging jets. Therefore, only the vector boson fusion process has been generated. Although the differences between the cross-sections in [103] and the NLO values[72] are small the cross-sections are scaled to correspond to MRS(R1) values. The scaling factors are shown in table 6.12.

Process	m_H	LO σBR (fb)	NLO σBR (fb)	Scaling factor
$H \rightarrow WW \rightarrow \ell\nu jj$	800 GeV	41.3	34.6	0.84
$H \rightarrow WW \rightarrow \ell\nu jj$	1 TeV	20.7	19.9	0.96
$H \rightarrow ZZ \rightarrow \ell\ell jj$	800 GeV	7.0	5.5	0.79
$H \rightarrow ZZ \rightarrow \ell\ell jj$	1 TeV	3.5	3.2	0.91

Table 6.12: Scaling factors for $H \rightarrow WW \rightarrow \ell\nu jj$ and $H \rightarrow ZZ \rightarrow \ell\ell jj$ from PYTHIA LO results to NLO values for vector boson fusion.

The simulation was performed with CMSJET program[106] taking into account the magnetic field, main cracks in the detector and smearing of the calorimeter resolutions.

Background processes

The main backgrounds are the production of the W or Z boson with an additional jet and the $t\bar{t}$ production in case of $H \rightarrow WW$. The contribution from the vector boson

pair production can be considered negligible for such high invariant masses. However, as pointed out in [107] the non-resonant process where two incoming quarks radiate vector bosons which subsequently scatter off each other may give a sizeable contribution if the presence of two tagging jets is required in the forward region. In [108] cross-sections for the W channel are computed from full QCD matrix elements and the contribution to from the non-resonant process is found to be $\approx 8\%$ with similar event selection that was carried out in [103].

The NLO corrections are taken into account only for $t\bar{t}$ channel where the total cross-section is scaled to correspond to 760 pb[72]. In the absence of NLO calculation, no K-factors are applied to the Z + jet and W + jet production. In [103], these backgrounds were multiplied by 1.5, but here such uncertainties and their consequences are estimated for all channels in section 6.3.6.

Event selection criteria

Kinematical and mass cuts The heavy Higgs events have one or two relatively central high p_T leptons from the leptonic decay of one vector boson and and two jets from the hadronic decay of the other vector boson. Due to the high mass of the Higgs boson, the decay products are boosted and in consequence, the two jets from the hadronic decay are close to each other. The $W/Z \rightarrow jj$ decay is reconstructed from a single large cluster containing two smaller jets.

The following cuts were applied in the central region ($|\eta| < 2.4$):

$H \rightarrow WW \rightarrow \ell\nu jj$:
- $\not{E}_T >$ 150 GeV
- $p_{T,\ell} >$ 150 GeV
- $p_{T,W} >$ 300 GeV
- $p_{T,\ell\nu} >$ 300 GeV
- W reconstructed from a single cluster
- $|m_W - m_{clus}| <$ 15 GeV
- No central jets ($p_T >$ 40 GeV)

$H \rightarrow ZZ \rightarrow \ell\ell jj$:
- $p_{T,\ell} >$ 50 GeV
- $p_{T,Z} >$ 150 GeV
- Z reconstructed from a single cluster
- $|m_Z - m_{\ell\ell}| <$ 10 GeV
- $|m_Z - m_{clus}| <$ 15 GeV
- No central jets ($p_T >$ 40 GeV)

Forward tagging The relative importance of the vector boson fusion as a Higgs production mechanism increases with the increasing Higgs mass: at $m_H = 800$ GeV it results one third and at $m_H = 1$ TeV half of the total cross-section. Therefore, it is hoped that the background can be suppressed by tagging the forward low p_T jets which follow from the outgoing quark line. The forward tagging probabilities reported in [105] are shown in table 6.13. The jet energy is required to be larger than 400 GeV and the jet p_T larger than 30 GeV. The results are shown for two jet sizes: $\Delta R = 0.2$ and $\Delta R = 0.4$. In the following, the signal efficiency is applied to both WW and ZZ channel, and $W + j$ estimate is used also for $Z + j$ background. The size of $\Delta R = 0.4$ for the forward tagging jet will be required.

It is assumed that a presence of the minimum bias events does not affect the tagging efficiency.

Process	$\Delta R = 0.2$	$\Delta R = 0.4$
$H \to WW \to \ell\nu jj$	5.2%	11%
$W + j$	0.12%	0.22%
$t\bar{t}$	0.28%	0.5%

Table 6.13: Double tagging probabilities for signal and background (for the tagging jets $p_T > 30$ GeV and $E > 400$ GeV is required)[105].

WW channel		$m_H =$ 800 GeV	$m_H =$ 1 TeV	$W + j$	$t\bar{t}$	Non-res. WW
30 fb^{-1}	Central cuts	46	54	1024	155	
	Double tagging	5.1	5.9	2.2	0.77	0.4
100 fb^{-1}	Central cuts	153	178	3414	516	
	Double tagging	17	20	7.5	2.6	1.4
ZZ channel		$m_H =$ 800 GeV	$m_H =$ 1 TeV	$Z + j$	ZW	Non-res. ZZ
30 fb^{-1}	Central cuts	20	15	883	< 1	
	Double tagging	2.3	1.6	1.9		0.2
100 fb^{-1}q	Central cuts	68	49	2943	< 4	
	Double tagging	7.5	5.4	6.5		0.6

Table 6.14: Event rates for 30 fb^{-1}and 100 fb^{-1}.

Event rates The event rates after the central region cuts and after the jet tagging are shown in table 6.14 for integrated luminosities of 30 and 100 fb^{-1}. A lepton efficiency of 0.9 is applied to each lepton (0.9 for WW and $(0.9)^2$ for ZZ). The non-resonant vector boson pair contribution is given as 8% of the $m_H = 800$ GeV signal after the double tagging[108], no numbers have been computed after the central cuts only. This contribution is assumed to be of the same size for the WW (for which it was computed in [108]) and ZZ channels.

Significance at CMS

With the event rates of table 6.14 the following statistical significance can be achieved in 30 and 100 fb^{-1}:

m_H		$\int \mathcal{L} = 30$ fb^{-1} S	B	S/B	$S/\sqrt{B}$	$\int \mathcal{L} = 100$ fb^{-1} S	B	S/B	$S/\sqrt{B}$	min $\mathcal{L}$ for 5 σ fb^{-1}
800 GeV	WW	5.1	3.4	1.5	2.8	17	11.5	1.5	5.0	99.5
1 TeV	WW	5.9	3.4	1.7	3.2	20	11.5	1.7	5.9	71.9
800 GeV	ZZ	2.3	2.1	1.1	-	7.5	7.1	1.1	2.8	316
1 TeV	ZZ	1.6	2.1	0.8	-	5.4	7.1	0.8	2.0	609

Almost 100 fb^{-1}of integrated luminosity is required to get a significant signal from the heavy Higgs. With the ZZ channel it is very difficult to reach acceptable event rates even for 100 fb^{-1}. Furthermore, there are large uncertainties in the background rates for such high invariant mass of vector boson pairs.

6.3.6 Conclusion and outlook

The results from previous sections are summarised in figure 6.26 showing the statistical significance in all considered channels for integrated luminosity of 30 fb^{-1}collected at $\mathcal{L} = 10^{33}$ cm^{-2}s^{-1}and for 100 fb^{-1}collected at $\mathcal{L} = 10^{34}$ cm^{-2}s^{-1}. With our present knowledge of signal and background cross-sections and of detector performance, CMS will be able to discover the Higgs particle within 30 fb^{-1}of integrated luminosity collected at low luminosity in the Higgs mass range of 105 – 650 GeV. With 100 fb^{-1}the full m_H range can be covered.

Figure 6.27 shows the integrated luminosity needed to achieve a 5 σ statistical significance in different decay channels. Fast discovery (< 10 fb^{-1}) can be expected if the mass of the Higgs particle is in the range of 150 – 500 GeV. For this region, it is important to have a precise understanding of the background signal and efficiencies before the LHC start as less than a year of running can be enough to reach a level of the discovery.

Whereas the signal cross-sections — including the next to leading order contributions — are well understood and the uncertainties are of 10 – 20 % level, large uncertainties remain in the estimates of the background processes. For several processes, no cross-section calculations are available or they have not been implemented in Monte Carlo generators. In many cases the NLO contributions are unknown. This is the case for all single γ, W or Z productions associated with a jet. Such processes contribute 10 – 20 % of the total background to $H \to \gamma\gamma$, up to 30% to $H \to ZZ^* \to 4\ell$ and $H \to WW \to 2\nu 2\ell$, up 45% to $H \to ZZ \to 2\nu 2\ell$ and 65% to $H \to WW \to \nu\ell 2j$. In addition, many K-factors that are used in the analysis are extrapolated from earlier studies which may have used different assumptions for the centre of mass energy, structure functions and the t quark mass. The effect of such uncertainties is illustrated in figure 6.28 which shows the statistical significance if the total background event rate is further multiplied by 1.5. It can be seen that even with a factor of 1.5 increase in the background rate, CMS is able of fast discovery of the Higgs particle in the Higgs mass range of 130 – 550 GeV.

The higher order corrections tend to change the kinematics of the background events and, therefore, applying a uniform K-factor to the leading order cross-section may result in large errors. The most delicate area is the already difficult heavy Higgs range with $m_H > 600$ GeV. The event selection criteria depend very much on the event topology

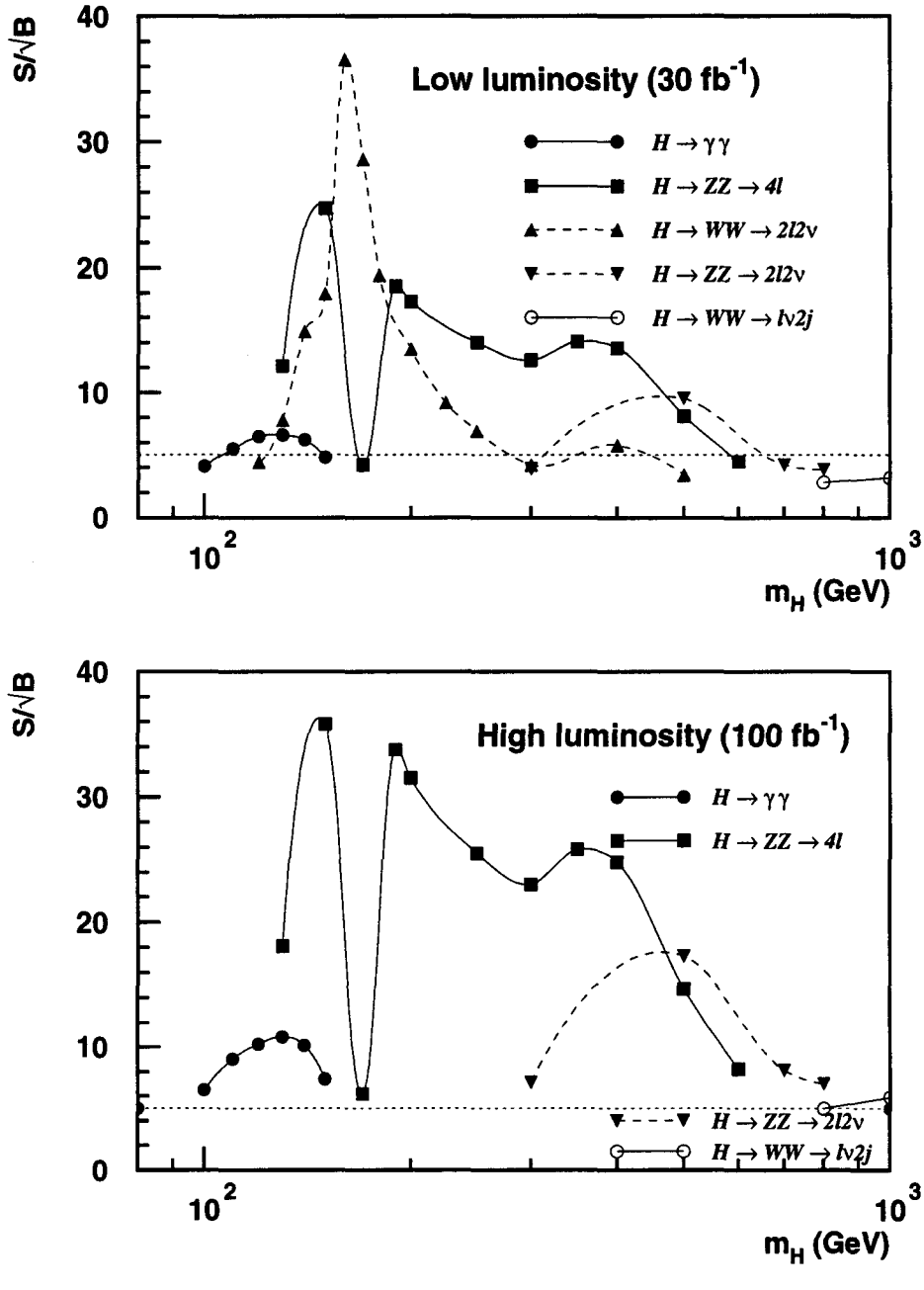

Figure 6.26: Statistical significance of different Higgs decay modes as a function of Higgs mass.

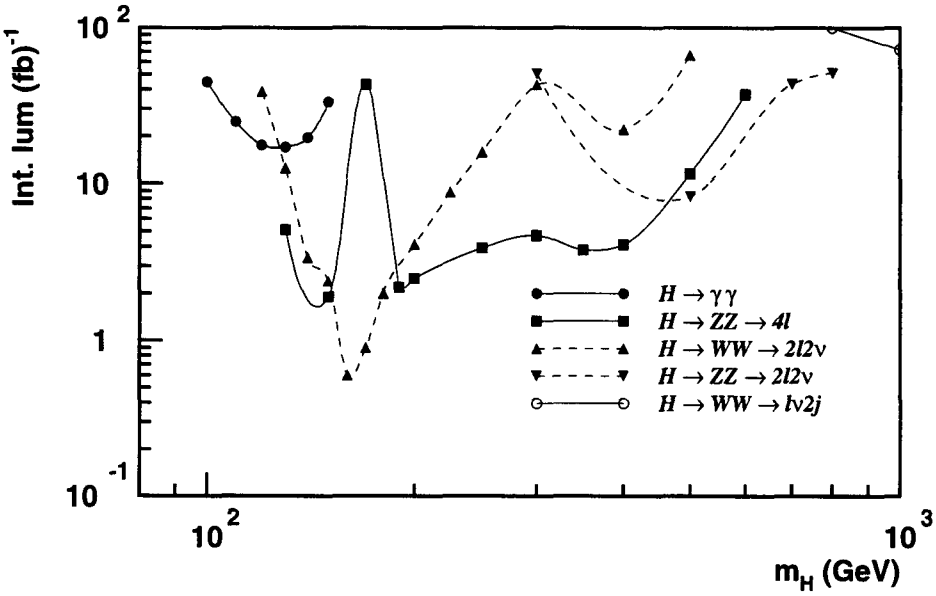

Figure 6.27: Integrated luminosity (in fb^{-1}) required to achieve a 5 σ statistical significance in different Higgs decay modes.

and, at present, are based on the leading order estimates of the processes.

It should be kept in mind that the discovery of the Higgs particle is an important goal but it is the study of its properties on which all effort should be put as soon as its existence can be proved. Therefore, the significance curves are useful only as guidelines in the Higgs searches.

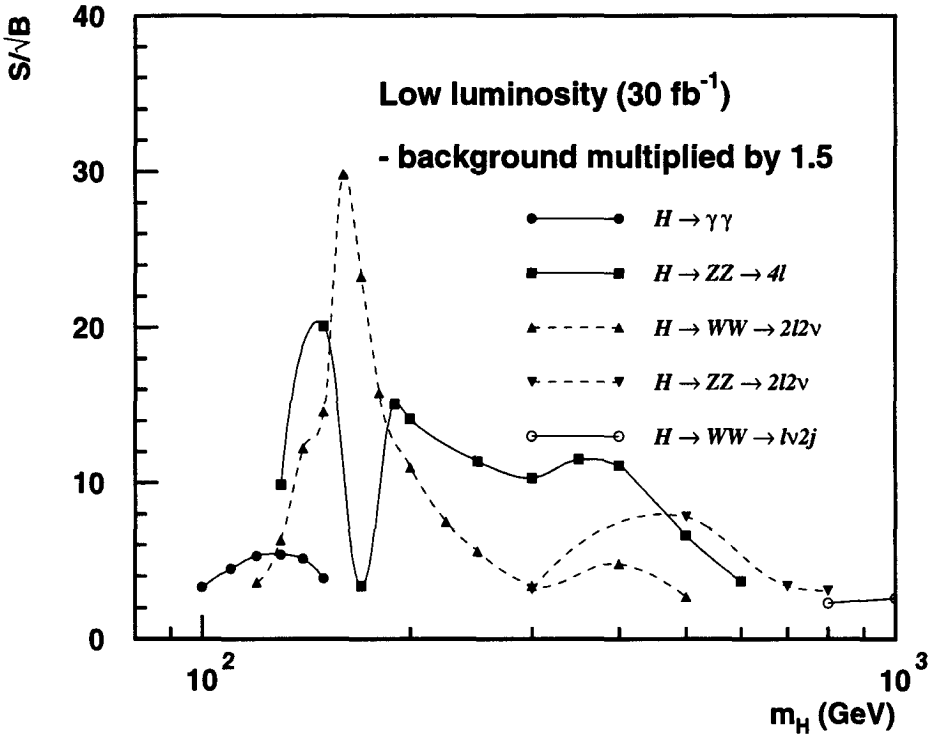

Figure 6.28: The effect of multiplying the background event rates by an additional factor 1.5 on the statistical significance reached with 30 fb^{-1}collected at low luminosity.

Chapter 7

Conclusions

With our present knowledge of the detector performance and the signal and background rates at LHC, the CMS experiment will be able to discover the Standard Model Higgs over the entire m_H range. Less than 10 $fb^{-1}$of integrated luminosity can be enough if the Higgs particle mass is in the range of 150 - 500 GeV. The LHC is expected to deliver this amount of luminosity in its first year of running, assuming $\mathcal{L} = 10^{33}$ $cm^{-2}s^{-1}$and 10^7 s.

The two demanding mass regions for the Higgs discovery are the low mass range below $m_H = 120$ GeV and the high mass end above $m_H = 600$ GeV. In the low mass range, a clean signature of the Higgs is feasible only through the $H \rightarrow \gamma\gamma$ channel. This channel requires an excellent energy measurement in the electromagnetic calorimeter and the results from the beam tests of $PbWO_4$ crystal matrices confirm the required performance can be obtained.

It has been verified by a detailed detector simulation that the CMS electromagnetic crystal calorimeter can reach the excellent two photon mass resolution which is required to establish the clear signal above background. The photon efficiency can be improved by recovering the converted photons with only a minor degradation of the mass resolution. The mass resolution including the recovered conversions is $\sigma = 0.62$ GeV for the low luminosity phase and $\sigma = 0.70$ GeV for the high luminosity phase for $m_H = 100$ GeV.

It has been shown that the $H \rightarrow ZZ \rightarrow 2\ell 2\nu$ channel can contribute up to $m_H = 800$ GeV and it is the fastest discovery channel if $m_H > 500$ GeV. However, there are uncertainties in the background estimates at such high ZZ invariant masses and, in consequence, large uncertainties remain in the signal significance estimates above $m_H = 600$ GeV.

The prospects for the Standard Model Higgs discovery at LHC look promising. Theoretical arguments and fits to the electroweak precision data favour a low mass Higgs and this region can be covered in CMS, mostly with several decay modes. However, such arguments emphasise the importance of the $H \rightarrow \gamma\gamma$ channel and, therefore, care must be taken to include any further theoretical calculations to improve the background estimates for this channel. No concessions can be allowed to the demanding performance requirements of the CMS electromagnetic calorimeter and the amount of material in front of it must be kept at maximum at the level presented in the tracker technical design report.

Appendix A

Test beam setup

The $PbWO_4$ crystals used in 1996 test beam setup were truncated pyramids with a length of 23 cm (25.8 X_0) and with a 20.5 $\times$ 20.5 mm^2 front face. Their shape corresponds to the crystals at $\eta \approx 0$ in the final CMS assembly. The crystal axes were tilted by 3° in the two transverse coordinates with respect to the beam direction in order to achieve the geometry of the final CMS configuration.

All the crystals in the September 1996 setup were produced in Bogoroditsk in Russia or at the Shanghai Institute of Ceramics (SIC) in China. The layout of the crystal matrix is shown in figure A.1. The crystals were wrapped with Tyvek (type 1056, nominal thickness of 160 μm). Before installing the crystals in the beam, the longitudinal non-uniformity of the light collection was measured using a ^{22}Na source (β^+ decay producing 511 keV and 1.275 MeV photons in the annihilation of the positron) and read out with a Philips XP2262B photomultiplier covering completely the crystal rear face. Crystals were uniformised by depolishing the rear face and in some cases also a side face.

1274	1333	1273	1268	1270	1275	1279
1347	1334	1330	1342	1317	1335	1345
1280	1343	1351	1349	1283	1358	1344
1277	1352	1264	1315	1350	1348	1331
1281	1353	1338	1339	1340	1341	1276
1296	1357	1327	1346	1354	1356	1286
1328	1295	1292	1293	1294	1287	1323

Figure A.1: Layout of the September 1996 test beam matrix of 7x7 $PbWO_4$ crystals.

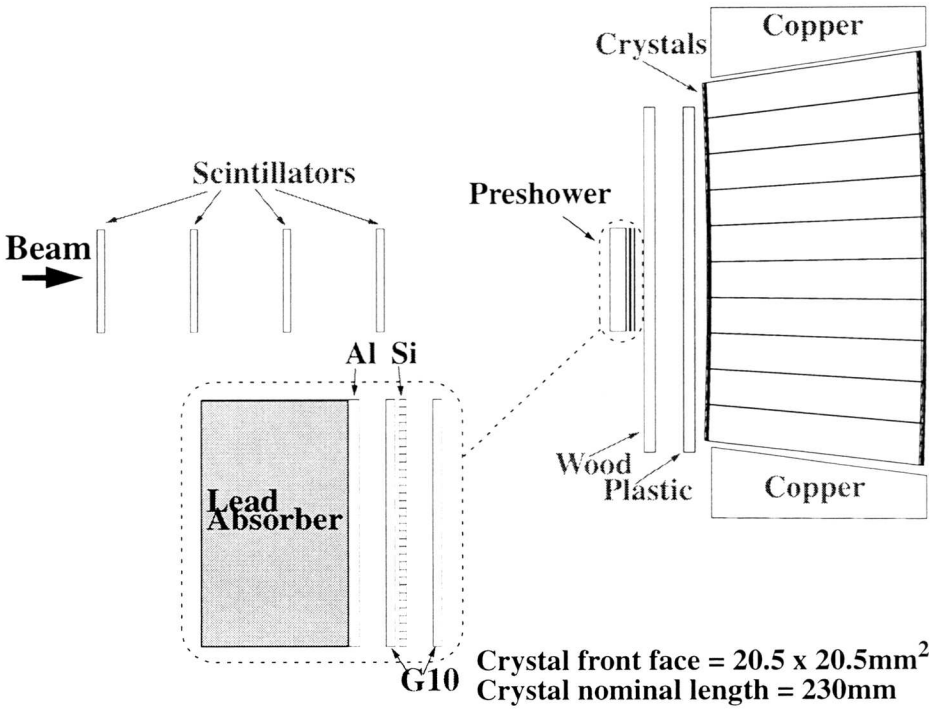

Figure A.2: Schematic view of the testbeam setup.

The matrix of 7x7 crystals was installed in a light-tight wooden box which was internally clad with grounded copper shielding. The box was placed on a remotely controlled moving table, able to rotate the crystal matrix in the two direction perpendicular to the beam axis. A schematic view of the test beam setup is shown in figure A.2[109]. The preshower device was not present in the September 1996 runs.

There were scintillator counters in front of the box. Two orthogonal planes of scintillator fingers were used to adjust the beam position. Halo counters are used off-line to reject events from beam halo. Trigger counters were used to define the beam spot, in most of the cases 20×20 mm^2 corresponding to the crystal front face area. Drift chambers measure the impact point of beam particles.

Temperature control

The light yield of the crystals and the gain of APDs have a strong temperature dependence ($-2\%/^\circ$ for the crystals and $-4\%/^\circ$ for the APDs used in this test). Therefore the temperature of the test beam setup has to be stabilised. The copper plates surrounding the sides of the box were water cooled and the electronics attached to the crystal rear face were in contact with water cooled copper bars. In addition, the six interior surfaces of the box were covered with heat screens consisting of aluminium plates with internal channels where water was circulated.

The temperature on the front and rear face of the crystals were continuously monitored and recorded. With the above described cooling system, it was possible to stabilise the

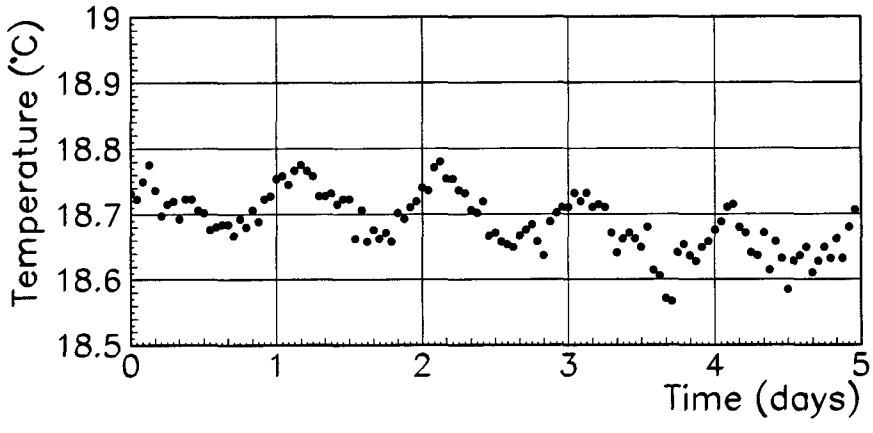

Figure A.3: Temperature monitored on the rear of a crystal near the centre of the matrix.

temperature on the rear face of the crystal to about 0.15° peak-to-peak variation as shown in figure A.3. The variation on the front face was three times smaller.

Readout and electronics

APDs produced by EG&G were used for the light detection. The measuring area of these photodiodes is 5×5 mm^2. The excess noise factor at gain of $M = 50$ is 2.2.

The APD signal is amplified in a preamplifier consisting of a a junction field-effect transistor (JFET) and characterised by high speed and low noise. The measured peaking time is 35 ns and the electronics noise corresponds to 1200 electrons when connected to the EG&G APD. This corresponds to an energy equivalent of noise of 12 MeV/channel. In addition, there was coherent noise due to the poor electronic shielding around preamplifiers resulting to the observed energy equivalent of noise of 120 – 180 MeV for a sum of nine channels.

Monitoring

The crystals were monitored by feeding light pulses in front of each crystal. There were several wave length laser systems which are not used in this analysis, and a light-emitting diode (LED) (SBR5501, peak emission at 660 nm) feeding light pulses of the length of 30 ns. The signals were injected to the crystals and viewed by a silicon photodiodes to stabilise the magnitude of the light pulse. The LED monitoring system achieved a peak-to-peak variation of 0.4% which corresponds to the daily temperature variation of the APD gain. The monitoring signal in a channel is shown in figure A.4.

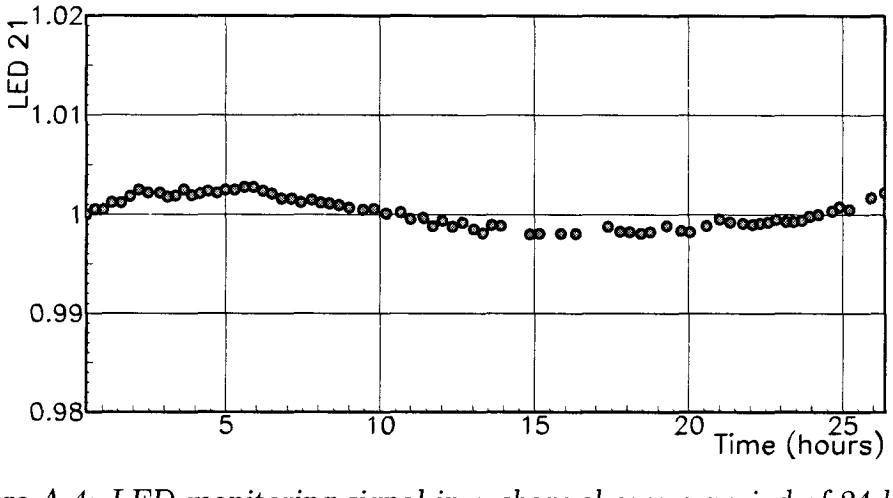

Figure A.4: LED monitoring signal in a channel over a period of 24 hours.

Bibliography

[1] S. Glashow, Nucl. Phys. 22 (1961) 579

[2] S. Weinberg, Phys. Rev. Lett. 19 (1967) 1264

[3] A. Salam in Elementary Particle Theory, ed. by N. Svartholm, Aspenäsgården (1968) 367

[4] G. 't Hooft and M. Veltman, CERN Report 73-9 (1973)
explained in G. 't Hooft, "Under the Spell of the Gauge Principle", World Scientific (1994)

[5] J. Schwinger, Ann. of Phys. 2 (1957) 407

[6] F.J. Hasert et. al., Phys. Lett. B46 (1973) 138

[7] J. Goldstone, Nuovo Cimento 19 (1961) 154
J. Goldstone, A. Salam and S. Weinberg, Phys. Rev. 127 (1962) 965

[8] P. Higgs, Phys. Lett. 12 (1964) 132
P. Higgs, Phys. Rev. Lett. 13 (1964) 508
P. Higgs, Phys. Rev. 145 (1966) 145

[9] M.W. Grünewald, HUB-EP-98/67 to appear in Proc. of the 29th International Conference on High Energy Physics, Vancouver (1998)

[10] e.g. E. Leader and E. Predazzi, "An introduction to gauge theories and modern particle physics", Cambridge University Press, 1996

[11] M. Spira, CERN-TH/97-68

[12] M. Spira and P. M. Zerwas, CERN-TH/97-379

[13] H. Georgi et al., Phys. Rev. Lett. 40 (1978) 692

[14] M. Spira, A. Djouadi, D. Graudenz and P.M. Zerwas, Nucl. Phys. B453 (1995) 17

[15] R.N. Cahn and S. Dawson, Phys. Lett. B136 (1984) 196

[16] T. Han, G. Valencia and S. Willenbrock, Phys. Rev. Lett. 69 (1992) 3274

[17] S.L. Glashow et al., Phys. Rev. D18 (1978) 1724

[18] Z. Kunszt, Nucl. Phys. B247 (1984) 339

[19] T. Han and S. Willenbrock, Phys. Lett. B273 (1991) 167

[20] M. Sher, Phys. Rep. 179 (1989) 273
G. Altarelli, G. Isidori, Phys. Lett. B 337 (1994) 141

[21] M. Lindner, Z. Phys. C 31 (1986) 295
G. Altarelli, Proc. of LHC Workshop, Aachen, ed. by G. Jarlskog and D. Rein (1990) CERN 90-10

[22] T. Hambye and K. Riesselmann, Phys. Rev. D55 (1997) 7255

[23] LEPC presentation, 12.11.1998, CERN

[24] D. Treille, to be published in the Proceeding of 29th International Conference on High Energy Physics, Vancouver, 1998

[25] G. Altarelli, Proc. of LHC Workshop, Aachen, ed. by G. Jarlskog and D. Rein (1990) 153, CERN 90-10

[26] S. Weinberg, Phys. Rev. D13 (1976) 974, Phys. Rev. D18 (1979) 1277
L. Susskind, Phys. Rev. D20 (1979) 2619

[27] R. Casalbuoni et al., Phys. Lett. B155 (1985) 95, Phys. Lett. B282 (1987) 235
R. Casalbuoni et al., Nucl. Phys. B310 (1988) 181

[28] e.g. J.L. Hewett and T. Rizzo, Phys. Rep. 183 (1989) 193

[29] H.P. Nilles, Phys. Rep. 110 (1984) 1

[30] The LHC Study Group, "The Large Hadron Collider, Conceptual Design", CERN/AC/95-05

[31] ATLAS Technical Proposal CERN/LHCC/94-43

[32] CMS Technical Proposal CERN/LHCC/94-38

[33] ALICE Technical Proposal CERN/LHCC/95-71

[34] LHCb Technical Proposal CERN/LHCC/98-4

[35] This is the cross-section for the minimum bias events (MSEL = 1) in Pythia[50]

[36] T. Sjöstrand and M. van Zijl, Phys. Rev. D36 (1987) 2019

[37] CMS Technical Design Reports:
The Magnet Project, CERN/LHCC 97-10
The Hadron Calorimeter Project, CERN/LHCC 97-31
The Electromagnetic Calorimeter Project, CERN/LHCC 97-33
The Muon Project, CERN/LHCC 97-32
The Tracker Project, CERN/LHCC 98-6

[38] T. J. Virdee, Proc. of the 2nd International Conference on Calorimetry in High Energy Physics, Capri (1991) p. 3

[39] Review of Particle Physics, Eur. Phys. J. C3 (1998) 159

[40] J. B. Birks, The Theory and Practice of Scintillation Counting, Pergamon Press (1964)

[41] P. Lecoq et al., CMS-TN/94-308

[42] E. Auffray, K. Lassila-Perini et al., CMS Note 1997/099, Nucl. Instr. Meth. A412 (1998) 223

[43] P. Lecoq, Proc. of the 6th International Conference on Calorimetry in High Energy Physics, Frascati (1996) p. 755

[44] D. J. Graham and C. Seez, CMS Note 1996/002
C. Markou, CMS Note 1997/048

[45] CMS ECAL TDR, CERN/LHCC 97-33, p. 60

[46] R. Y. Zhu et al.,Proc. of the 6th International Conference on Calorimetry in High Energy Physics, Frascati (1996) p. 577

[47] A. Annenkov et al., CMS Note 1997/008, Nucl. Inst. Meth
R. Y. Zhu, CMS Note 1998/007

[48] CMS Simulation and Reconstruction Package http://cmsdoc.cern.ch/cmsim/cmsim.html

[49] CERN Program Library Long Writeup W5013

[50] T. Sjöstrand, CERN-TH/7112/93

[51] CMS ECAL TDR, CERN/LHCC 97-33, p. 306

[52] D. Barney, CMS IN 1006/009

[53] D. Barney and G. J. Davies, CMS Note 1996/006

[54] C. Seez in the open presentation of the CMS ECAL TDR, CERN, 15.1.1998

[55] These numbers can be extracted from figure 14 in D. J. Graham and C. Seez, CMS Note 1996/002

[56] K. Lassila-Perini, CMS Note 1998/031

[57] G.A. Akopdjanov et al., Nucl. Inst. Meth. 140 (1977) 441-445

[58] F. Gautheron and A. Givernaud, CMS Note 1997/037

[59] K. Lassila-Perini, presentation in ECAL test beam analysis meeting 17.10.1997

[60] K. Lassila-Perini, Proc. of the VI International Conference on Calorimetry in High Energy Physics, Frascati (1996) p 487

[61] D. Barney, private communication

[62] C. Seez CMS TN/93-115 (1993)
D.J. Graham CMS TN/95-115 (1995)

[63] CMS ECAL TDR, CERN/LHCC 97-33, p. 325

[64] P. Busson and C. Charlot, CMS-TN 1005/074

[65] Review of Particle Physics, Eur. Phys. J. C3 (1998)

[66] I. Iashvili et al., CMS-TN/95-059

[67] C. Charlot and I. Puljak, CMS Note 1997/043

[68] C. Charlot and I. Puljak, CMS IN 1998/019

[69] CMS Tracker TDR, CERN/LHCC/98-6, p. 558

[70] K. Lassila-Perini, CMS Note 1996/001

[71] J-P. Vialle, M. Lebeau, A. Givernaud, M. Maire, CMS-TN 95-151

[72] M. Spira and M. Dittmar, CMS Note 1997/080

[73] B. Bailey and D. Graudenz, Phys. Rev. D49 (1994) 1486

[74] P. Aurenche et al., Z. Phys. C29 (1985) 459
B. Bailey et al., Phys. Rev. D46 (1992) 2018

[75] J. Ohnemus and J. F. Owens, Phys Rev. D43 (1991) 3626

[76] J. Ohnemus, Phys. Rev. D44 (1991) 1403
S. Frixione, Nucl. Phys. B410 (1993) 280

[77] J. Ohnemus, Phys. Rev. D44 (1991) 3477

[78] T. Han et al., Nucl. Phys. B384 (1992) 59

[79] J. Ohnemus, Phys. Rev. D50 (1994) 1931

[80] E. W. N. Glover and J. J. Van Der Bij, Nucl. Phys. B321 (1989) 561

[81] Chung Kao and D. A. Dicus, Phys. Rev. D43 (1991) 1555

[82] C. Seez and T.S. Virdee, CMS-TN/94-289

[83] P. Mättig in Proc. of Lake Louise Winter Institute on Collider Physics, Lake Louise, Canada (1994), CERN-PPE 93-87

[84] This procedure was proposed by M. Dittmar, unpublished

[85] S. Abdullin et al., INP MSU 98-13/514 (hep-ph/9805341)

[86] D. Rainwater and D. Zeppenfeld, MADPH-97-1023 (hep-ph/9712271)

[87] S. Abdullin and N. Stepanov, CMS-TN/94-179

[88] I. Gaines et al., CMS-TN/95-084

[89] The numbers have been estimated from figures 2b), 7b) and 11b) in J. Ohnemus, Phys. Rev. D50 (1994) 1931

[90] E.W.N. Glover, Phys. Rev. D37 (1988) 3193

[91] S. Banerjee and A. Khan, CMS-TN/96-023
I. Iashvili and A. Kharcilova, CMS-TN/96-100

[92] D. Denegri et al., CMS-TN/93-101

[93] D. Bomeštar et al., CMS-TN/95-018

[94] M. Dželalija et al., CMS-TN/95-076

[95] Ž. Antunović et al., CMS-TN/96-092

[96] E. Barberio et. al., Comp. Phys. Comm. 66 (1991) 115

[97] V. Karimäki et al., CMS-TN/93-62

[98] A. Nikitenko et al., CMS-TN/95-019

[99] The numbers have been estimated from figure 2b) in J. Ohnemus, Phys. Rev. D50 (1994) 1931

[100] M. Dittmar and H. Dreiner, Phys. Rev. D55 (1997) 167

[101] M. Dittmar and H. Dreiner, CMS Note 1997/083

[102] S. Abdullin and N. Stepanov, CMS-TN/93-088

[103] S. Abdullin and N. Stepanov, CMS-TN/94-178

[104] I. Gaines et al., CMS-TN/95-154

[105] S. Abdullin, CMS-TN/94-177

[106] S. Abdullin et al.,CMS TN/94-180

[107] U. Baur and E. W. N. Glover in Proc. of Large Hadron Collider Workshop Vol. II Aachen (1990) 570

[108] K. Iordanidis and D. Zeppenfeld, MADPH-97-1017 (hep-ph/9709506)

[109] D. Barney, CMS CR 1998/004

Acknowledgements

It has been a great pleasure to work in the Laboratory for High Energy Physics of ETHZ. I would like to thank all my colleagues for a motivating working environment, first of all Felicitas Pauss who has been an excellent supervisor. I have learnt enormously from her competence and vision.

I also thank Hans Hofer who has kindly accepted to be co-examiner of this thesis.

Special thanks go to Michael Dittmar who has helped me with PYTHIA simulation and introduced me the mysteries of K-factors. His enthusiasm and truth have encouraged me to try to complete the studies to the best of my ability. I'm also grateful to Frank Behner who has readily helped me with any of my computing problems.

I have enjoyed working in the CMS ECAL collaboration and I'm indebted to many colleagues for their help and advice. I'm grateful to Jim Virdee who helped me get started with the $H \rightarrow \gamma\gamma$ simulation. Especially, I thank Chris Seez for his advice and answers to my numerous questions concerning beam tests, crystals, readout, physics simulation, or anything else. I'm pleased to acknowledge the useful discussions with my colleagues Jon Hays who has readily helped me with the simulation in the endcaps and Dave Barney who has kindly provided me many useful figures.

Finally, I thank Diego for his support and understanding during this time. Although my daughter Elisa has shown a genuine enthusiasm about my Feynman diagrams ("ikks!!") I want to dedicate her a figure she can discuss:

I wish that by the time when my children go to school and learn their physics we have learnt something more to tell about the Standard Model of particles and forces — whatever it will be at that time.

Curriculum vitae

Personal data

Name	Katri Lassila-Perini
Date and place of birth	25th August 1965, Hämeenlinna, Finland
Nationality	Finnish

Education

1972 – 1981	Comprehensive school, Hämeenlinna
1981 – 1984	High School of "Hämeenlinnan lyseon lukio", Hämeenlinna
1984	Matriculation examination
1984	French studies in Rambouillet, France
1985	Italian studies in Venice, Italy
1985 – 1991	Faculty of Technical Physics at the Helsinki University of Technology, Finland
1991	Master of Science Thesis written at the Application Software (AS) group in the Computers and Networks (CN) division at CERN
1992 – 1994	Fellow in the AS group of the CN division at CERN
1994 – 1998	Ph. D. student in the Institute for Particle Physics at the Swiss Federal Institute of Technology, Zurich